Vol. 289, No. 2, April 29, 1994 ISSN 0003-2670

ANALYTICA CHIMICA ACTA

An international journal devoted to all branches of analytical chemistry

ELSEVIER

ANALYTICA CHIMICA ACTA

Scope. *Analytica Chimica Acta* publishes original papers, rapid publication letters and reviews dealing with every aspect of modern analytical chemistry. Reviews are normally written by invitation of the editors, who welcome suggestions for subjects. Letters can be published within **four months** of submission. For information on the Letters section, see inside back cover.

Submission of Papers

Americas

Prof. Harry L. Pardue
Department of Chemistry
1393 BRWN Bldg, Purdue University
West Lafayette, IN 47907-1393
USA

Tel:(+1-317) 494 5320
Fax:(+1-317) 496 1200

Computer Techniques

Prof. J.T. Clerc
Universität Bern
Pharmazeutisches Institut
Baltzerstrasse 5, CH-3012 Bern
Switzerland

Tel:(+41-31) 6314191
Fax:(+41-31) 6314198

Prof. Sarah C. Rutan
Department of Chemistry
Virginia Commonwealth University
P.O. Box 2006
Richmond, VA 23284-2006
USA
Tel:(+1-804) 367 1298
Fax:(+1-804) 367 7517

Other Papers

Prof. Alan Townshend
Department of Chemistry
The University
Hull HU6 7RX
Great Britain

Tel:(+44-482) 465027
Fax:(+44-482) 466410

Prof. Willem E. van der Linden
Laboratory for Chemical Analysis
Department of Chemical Technology
Twente University of Technology
P.O. Box 217, 7500 AE Enschede
The Netherlands
Tel:(+31-53) 892629
Fax:(+31-53) 356024

Prof. Paul Worsfold
Dept. of Environmental Sciences
University of Plymouth
Plymouth PL4 8AA
Great Britain

Tel:(+44-752) 233006
Fax:(+44-752) 233009

Submission of an article is understood to imply that the article is original and unpublished and is not being considered for publication elsewhere. *Anal. Chim. Acta* accepts papers in English only. There are no page charges. Manuscripts should conform in layout and style to the papers published in this issue. See inside back cover for "Information for Authors".

Publication. *Analytica Chimica Acta* appears in 16 volumes in 1994 (Vols. 281–296). *Vibrational Spectroscopy* appears in 2 volumes in 1994 (Vols. 6 and 7). Subscriptions are accepted on a prepaid basis only, unless different terms have been previously agreed upon. It is possible to order a combined subscription (*Anal. Chim. Acta* **and** *Vib. Spectrosc.*).
Our p.p.h. (postage, packing and handling) charge includes surface delivery of all issues, except to subscribers in the U.S.A., Canada, Australia, New Zealand, China, India, Israel, South Africa, Malaysia, Thailand, Singapore, South Korea, Taiwan, Pakistan, Hong Kong, Brazil, Argentina and Mexico, who receive all issues by air delivery (S.A.L.–Surface Air Lifted) at no extra cost. For Japan, air delivery requires 25% additional charge of the normal postage and handling charge; for all other countries airmail and S.A.L. charges are available upon request.

Subscription orders. Subscription prices are available upon request from the publisher. Subscription orders can be entered only by calendar year and should be sent to: Elsevier Science B.V., Journals Department, P.O. Box 211, 1000 AE Amsterdam, The Netherlands. Tel: (+31-20) 5803 642, Telex: 18582, Telefax: (+31-20) 5803598, to which requests for sample copies can also be sent. Claims for issues not received should be made within six months of publication of the issues. If not they cannot be honoured free of charge. Readers in the U.S.A. and Canada can contact the following address: Elsevier Science Inc., Journal Information Center, 655 Avenue of the Americas, New York, NY 10010, U.S.A. Tel: (+1-212) 6333750, Telefax: (+1-212) 6333990, for further information, or a free sample copy of this or any other Elsevier Science journal.
Advertisements. Advertisement rates are available from the publisher on request.

US mailing notice – Analytica Chimica Acta (ISSN 0003-2670) is published 3 times a month (total 48 issues) by Elsevier Science B.V. (Molenwerf 1, Postbus 211, 1000 AE Amsterdam). Annual subscription price in the USA US$ 3035.75 (valid in North, Central and South America), including air speed delivery. Second class postage paid at Jamaica, NY 11431. *USA Postmasters*: Send address changes to Anal. Chim. Acta, Publications Expediting, Inc., 200 Meacham Av., Elmont, NY 11003. Airfreight and mailing in the USA by Publication Expediting.

ANALYTICA CHIMICA ACTA

An international journal devoted to all branches of analytical chemistry

(Full texts are incorporated in CJELSEVIER, a file in the Chemical Journals Online database available on STN International; Abstracted, indexed in: Aluminum Abstracts; Anal. Abstr.; Biol. Abstr.; BIOSIS; Chem. Abstr.; Curr. Contents Phys. Chem. Earth Sci.; Engineered Materials Abstracts; Excerpta Medica; Index Med.; Life Sci.; Mass Spectrom. Bull.; Material Business Alerts; Metals Abstracts; Sci. Citation Index)

VOL. 289 NO. 2 CONTENTS APRIL 29, 1994

(Continued overleaf)

Contents (continued)

Other Topics

ELSEVIER

Analytica Chimica Acta 289 (1994) 125–134

ANALYTICA CHIMICA ACTA

Automated, high-precision coulometric titrimetry Part I. Engineering and implementation

Kenneth W. Pratt

Chemical Science and Technology Laboratory, National Institute of Standards and Technology, Gaithersburg, MD 20899, USA

(Received 17th June 1993; revised manuscript received 22nd November 1993)

Abstract

Automated constant-current coulometry, based on Faraday's Laws, achieves uncertainties (relative standard deviation) of less than 1 part in 20000 without chemical standardization. It is applicable to acid–base, redox, and precipitation titrations of high-purity compounds and solutions. Automation of the technique permits unsupervised operation and reduces operator-dependent errors. Initial setup and sample introduction are the sole manual steps. Each assay consists of a main titration at high, constant current, bracketed by the initial and final endpoint routines, each at a lower current. The coulometric assay is analogous to a conventional titration in which two different concentrations of the titrant are used to attain optimum accuracy. The initial endpoint determination corresponds to the blank determination in a classical titration. Each titration includes a statistical analysis of the random and systematic uncertainties associated with the analysis. Individual steps in the procedure are performed by a hierarchical series of subroutines to reduce program complexity. Results are presented for $K_2Cr_2O_7$, benzoic acid, and solutions of strong acids.

Key words: Coulometry (constant-current); Automated titrimetry; High-precision assays; Primary standards

1. Introduction

High-precision, constant-current coulometry was first developed as an analytical technique by Taylor and Smith [1] for acidimetric assays of acids and bases. The technique was later expanded by Marinenko and Taylor to other high-precision assays: halides [2] by argentimetry, potassium dichromate [3] by oxidimetry, arsenic trioxide by iodimetry [4], benzoic and oxalic acids [5] by a refined version of the technique used in [1], and boric acid [6]. Later work by Marinenko and co-workers further expanded the applicability of high-precision coulometry to uranium assays [7,8].

This paper describes the general plan for automated, high-precision coulometry. The automated procedures described here require operator intervention only for the initial setup of the cell and sample introduction. In contrast, the previous manual techniques require tedious manipulations and constant operator attention throughout the assay. Since the reliability of each component step is improved in the automated

SSDI 0003-2670(93)E0692-Z

procedures, the reliability for the overall analysis is increased. Automation also makes coulometric high-accuracy assays accessible to workers outside the field.

The coulometric assay yields the concentration of the major component on an absolute basis, calculated from Faraday's Laws of Electrolysis. Hence, coulometry provides a direct route for the determination of the purity of primary standard chemicals. In addition, the method provides independent confirmation of purity determinations obtained by subtraction of the known impurities from 100%. These applications both require the high accuracy characteristic of coulometric analyses.

2. General procedure

The general procedure for each automated coulometric titration consists of the initial endpoint routine, sample introduction, the main titration, final endpoint routine, and assay calculation with error analysis. The automated procedures are combined into a single BASIC program, with compound-specific branches included in the program as required. A menu is used for initial selection of the compound to be assayed. The molecular weight M, equivalents per mole of analyte n, the density d and, for weak acids, the acid dissociation constant K_a, are automatically loaded when the analyte is chosen. Compounds

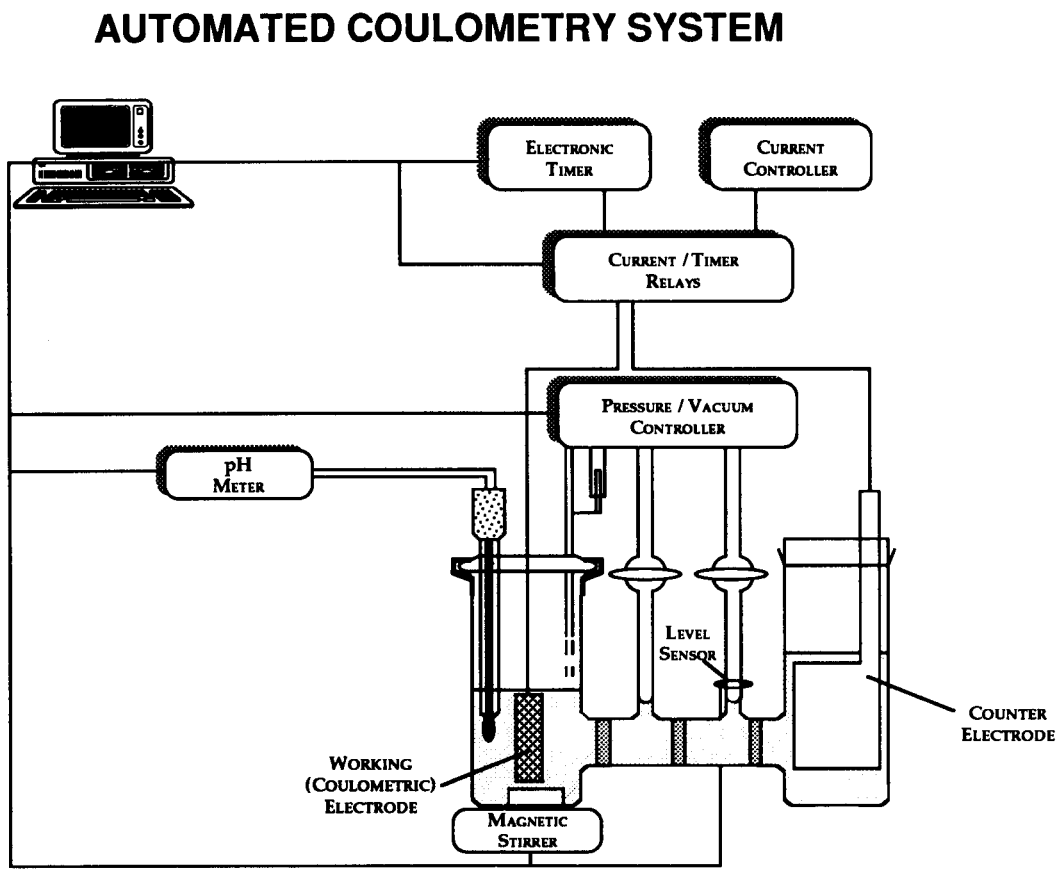

Fig. 1. Block diagram of the automated coulometry system.

not in the menu can be titrated using a separate option, in which all compound-specific parameters are entered manually.

The main titration is performed at high, constant current (I_{main}, 101.8243 mA), for a time t_{main}, and is equivalent to 99.8–99.9% of the added sample. The initial and final endpoint routines bracket the main titration and are identical. Each is recursive, consisting of discrete charge aliquots at a lower, constant current, I_{low}, alternating with indicator electrode (IE) measurements (pH for acidimetry, otherwise amperometric). The initial and final endpoints, t_{init} and t_{final}, are expressed as accumulated times corresponding to the charge added at I_{low} at the given endpoint. The quantity t_f represents the time corresponding to the total charge added at I_{low} in the initial endpoint routine. The total charge passed through the cell between the initial and final endpoints, viz. $I_{low}(t_f - t_{init})$ at the end of the initial endpoint routine plus $I_{main}t_{main}$ in the main titration plus $I_{low}t_{final}$ in the final endpoint routine, yields the overall assay (%) from Eq. 1, where w_{sample} is the sample mass and F is the Faraday constant.

$$\text{assay} = 100M\left[I_{main}t_{main} + I_{low}(t_f - t_{init} + t_{final})\right] / nFw_{sample} \quad (1)$$

Because the identical procedure is used to determine the initial and final endpoints, systematic errors in t_{init} and t_{final} tend to cancel. This increases the accuracy of the final result.

The cells used in the analysis are those used in the previous manual work [1–8]. Each cell (Fig. 1) consists of a sample half-cell, two center compartments (CC) in series, a counter electrode half-cell, and three frits (coarse, medium, and fine porosity, respectively) separating these four sections. The two CCs are emptied or filled pneumatically. A silica gel or agar-agar plug prevents any solution flow through the fine frit. Both CCs are totally filled during the main titration, to reduce the total cell resistance to a value such that the compliance of the I_{main} constant-current supply is not exceeded. The CCs are partially (ca. 10%) filled during the endpoint titrations, to reduce the systematic error associated with the small fraction of excess sample or titrant present in the CCs during the endpoint determination. Analyte or titrant that diffuses into the CCs during titration is returned to the sample half-cell by rinsing the cell after the main titration and during the procedure for endpoint detection.

Sample introduction is performed manually, directly after the center compartments are filled and before the start of the main titration. Sample masses are corrected for air buoyancy, using the sample density entered from the initial menu. Total automation of the sample introduction would require significant robotic hardware and additional programming effort; this may be a future research effort.

Deaeration of the cell electrolyte is effected via miniature dispersion tubes inserted through the covers of the sample and counter electrode half-cells. The dispersion tube for the sample half-cell is automatically raised and lowered, as required, during the course of the titration in order to eliminate spray losses.

Error diagnostics are provided throughout the program. The coulometric generation circuit is tested at the start and end of each titration step. Correct operation of the IE circuit (pH meter or potentiostat) is verified during each measurement. Correct operation of the rinsing procedures is verified at the start of each rinse. Immediately after exiting the menu, an initial test of all systems is performed to check the cell setup, and the electronic balance is automatically calibrated against a 100.0000-g standard mass. Any error at this point generates a user prompt to correct the malfunctioning or missing item. If an error is detected after this initial test, the titration is discontinued, the center compartments are emptied, all systems are initialized, and the program terminates.

Assay calculations are performed using Eq. 1 after the conclusion of the final endpoint determination. The random uncertainty of the titration is estimated by the square root of the sum of squares of all the known random uncertainties. The analytical results, including a summary of the titration data, are stored in a user-selected filename and in a backup file at the end of the titration. Additionally, a detailed data file con-

taining all IE measurements and rinse data is stored separately. A separate program is used for all data output at the conclusion of the program. This same program is used for subsequent output of data from the disk files.

The programming logic and hardware used to implement the above procedures are discussed in greater detail below.

3. Equipment and software: general

The automated coulometric system is controlled by a PC/AT or compatible computer [1]. The interface hardware installed in the computer consists of an IEEE-488 controller card and an analog/digital multifunction input/output (I/O) board (Lab-PC, National Instruments, Bellevue, WA) providing three 8-bit digital I/O ports (A, B, and C) and analog I/O with 12-bit resolution. Individual bits from ports A (input) and B (output) serve several functions, described below. Port C, configured as an output, controls the valve manifold for solution handling via an external 8-bit relay board. The COM1 RS-232 port is used for the pH meter interface. The basic layout of the overall system is shown in Fig. 1.

Coulometric titration times are measured with a precision timer (PM 6665/036, Philips, Eindhoven) with a temperature-compensated crystal time base and IEEE-488 interface. An electronic analytical balance (AE160, Mettler, Herisau) fitted with an IEEE-488 interface is used to weigh liquids. The sample mass is obtained by taring the balance to zero with the filled syringe and reading the negative result obtained after sample delivery. The syringe and its supporting cradle comprise a missile-shaped device that holds the capped syringe erect on the balance pan during weighing. A microbalance (Mettler M5) is used to weigh solid samples. The mass of the Pt boat plus sample is entered initially, and the final boat mass (after sample delivery) is entered during sample dissolution, after completion of the weighing step. A battery-powered pH meter (720, Orion Research, Boston, MA) and combination glass/Ag,AgCl pH electrode are used for all pH measurements.

The main program and the output program are both stored as executable files and require approximately 95 and 14 kilobytes, respectively. An additional 78 kilobytes of memory space is required for the BASIC run-time module for these programs. The main program has a hierarchical structure, with high-level subroutines, described below, used for each major operation in the titration.

At the lowest level, a single subroutine generates all time delays for the entire program, simultaneously displaying the time remaining in the given step. Subroutines of the second-lowest level effect data I/O with the various interfaces. Error detection is performed at this level. Detection of an error signal sets an error flag that successively exits each higher-level subroutine until the main level is reached. The error flag also generates a string message indicating the cause of error, time of day, and time in the titration that the error occurred.

4. Current control, timing, and switching

The hardware for the coulometric current circuit consists of two constant-current supplies, high-accuracy standardization circuitry [9], the precision timer, and a switching circuit. The switching circuit consists of two DPDT Hg-wetted relays, one for I_{main} and one for I_{low}. Each relay is controlled by one line of port B through a 2N6660 IGFET driver. The timer gating circuit, described below, is inserted in the positive lead to the coulometric cell. Other details are similar to those used previously [7,9].

The gating circuit (Fig. 2) consists of an 4N35 optoisolator as current sensor and a debouncing circuit. Three series-connected, forward-biased Si

[1] Certain commercial equipment, instruments, or materials are identified in this paper to specify adequately the experimental procedure. Such identification does not imply recommendation or endorsement by the National Institute of Standards and Technology, nor does it imply that the materials or equipment identified are necessarily the best available for the purpose.

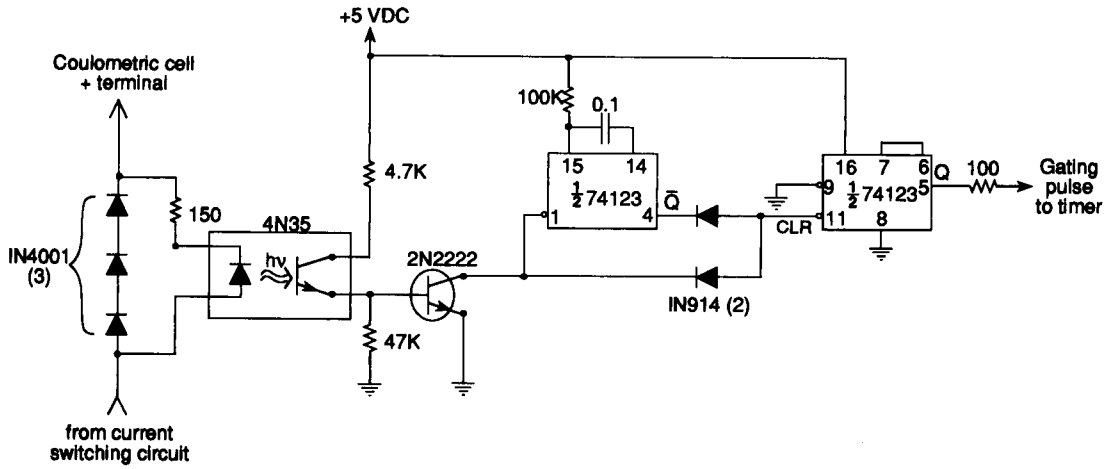

Fig. 2. Timer gating circuit. Values of resistors shown in ohms; capacitors shown in microfarads. Electrolytic capacitors shown in μF/rated DC voltage.

diodes are connected in parallel with the light-emitting diode (LED) of the optoisolator, ensuring relatively constant LED current over a wide range of cell currents (0.4 mA–1 A). The 74123 monostable generates a 3.3-ms pulse at $\overline{Q}$ when triggered by the first flow of current through the cell. This pulse and the output of the optoisolator are digitally summed by the 1N914 diodes and

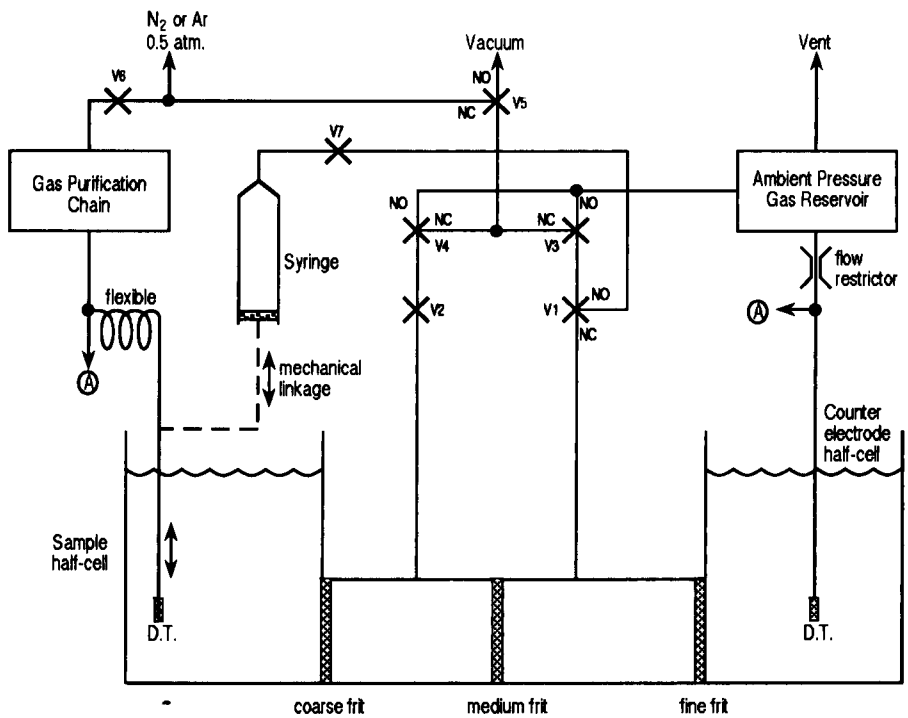

Fig. 3. Valve manifold and associated pneumatic connections. Valve designations: V1–V5, solution control; V6–V7, deaeration control. D.T. = deaeration tube; NC = normally closed; NO = normally open.

then inverted and buffered, yielding a TTL high, debounced signal at Q that is used as the gating pulse for the timer.

This gating circuit eliminates the systematic error associated with the use of separate relay contacts for timer gating and current switching. The circuit has the additional advantage that any interruption of the cell current after the initial 3.3 ms terminates the gating of the timer. The IEEE-488 status byte of the timer, controlled by the gating pulse, thus indicates correct functioning of the coulometric circuit.

A single subroutine, differing only in the output bit sent to the switching circuit, is used both for the main titration and for the charge additions during the endpoint determinations. The subroutine consists of relay actuation, verification of presence or absence of current, the delay routine, and relay opening. The presence of cell current is verified after the relay bit from the computer I/O board is set high. The delay subroutine then decrements for the time corresponding to the required charge. Continuous presence of cell current is verified after the delay routine concludes. The relay bit is then set low, opening the relay, and the absence of current is verified. The exact titration time is read from the timer and is used for all later calculations. Absence or presence of current is verified by a separate serial polling subroutine that sets the error flag if the desired status byte is not obtained within a set time.

5. Solution handling and deaeration

The hardware for solution handling (Fig. 3) consists of a valve manifold and a level sensor. The valve manifold consists of five valves for solution handling and two additional valves for raising and lowering the deaeration tube via a pneumatic syringe. Each valve is controlled by one bit of port C via the relay board. By actuating the appropriate valves, either or both CCs or the pneumatic syringe may be placed in any of four states (gas pressure applied, vacuum applied,

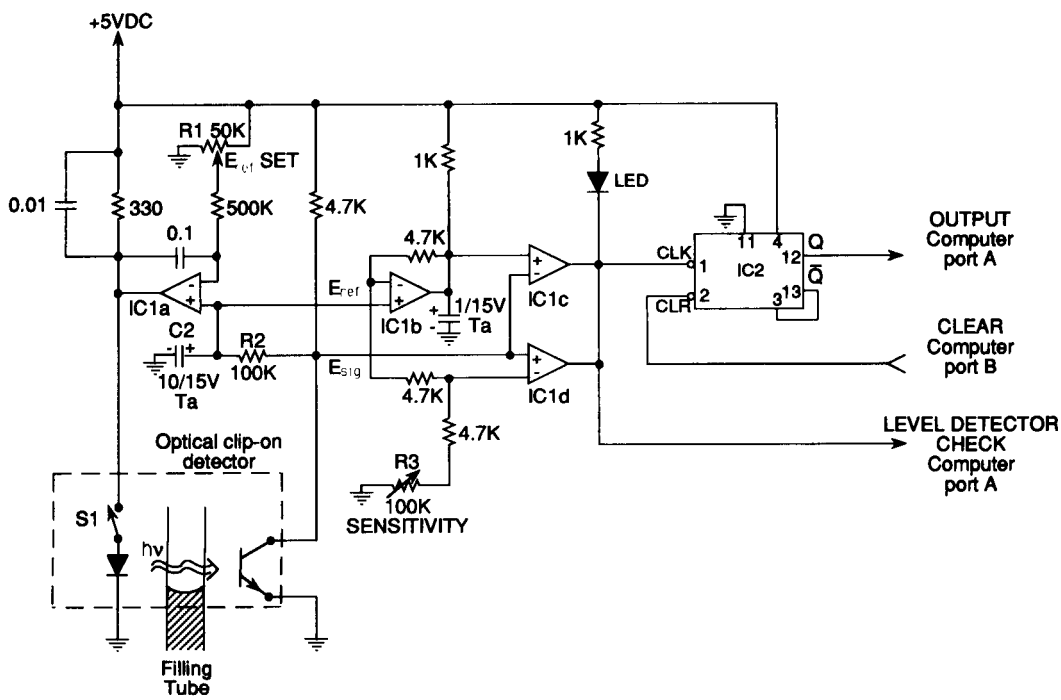

Fig. 4. Level detector. IC1, LM338 quad comparator; IC2, 7473 dual J-K flip-flop. Nomenclature as in Fig. 2.

vented, or sealed off). Pressure in the CCs is equalized by venting them to the ambient-pressure reservoir after each partial fill. This maintains constant level after the CCs are sealed off, while avoiding solution contamination from O_2 or CO_2 from the air.

For a single cell rinse, the CCs are emptied, filled, re-emptied, and partially re-filled. All solution transfer is effected via the coarse and medium frits. Solution in the two CCs always remains at or below the level of the sensor, never contacting the valve manifold. The rinse subroutine consists of two intermediate-level subroutines used to fill and empty the CCs. These two subroutines each consist of a series of individual valve operations, effected by a lower-level valve subroutine. The valve subroutine consists of the actual sending of the selected byte to port C, followed by the delay subroutine. Error detection is performed in the valve subroutine at the start of each filling operation as described below.

The level sensor (Fig. 4) consists of an optical detector, a limit comparator, and a latch. The optical detector clips on to the filling tube of the medium-fine CC, closing switch S1 and establishing the optical feedback loop for IC1a. This circuit is normally in the active state, with E_{sig} equal to E_{ref}, set by R1. An RC filter (R2C2) with a time constant of 1 s limits the frequency response of the feedback loop. Passage of the solution meniscus by the sensor causes a rapid change in the transmittance of the filling tube and generates a pulse at the collector of the photo-transistor. The effects of slow accumulation of deposits on the filling tube or alignment variations are eliminated by the action of the feedback loop and no pulse is generated. R3 controls the sensitivity of limit detector IC1c-d. A TTL low signal is produced if the threshold set by R3 is exceeded, and latch IC2 is set (output bit TTL high) if enabled by the computer (port B; clear input TTL high). An error condition is indicated if the output of IC1c-d is TTL low before the latch is enabled.

The level sensor is enabled for each total filling operation. The output bit-of latch IC2 is read within the delay subroutine. If this bit is high, the delay routine terminates, returning control to the valve subroutine. The valve subroutine then stores the elapsed "fill time" for the next total filling. The ratio of this time to the preceding filling time is used to correct all other emptying and partial filling times proportionately. All times are lengthened by 10% if the latch output remains TTL low throughout the delay routine. In this manner, the program 'self-corrects' for changes in the porosity of the frits or the solution viscosity. This feature is most important for precipitation titrations in which the precipitate slowly clogs the coarse frit.

A cell washdown is performed by vibrating the cell after the main titration and in the endpoint procedures each time the rinse threshold (defined below) is reached. Systematic error from droplets adhering to the upper portions of the sample half-cell is thus minimized. The vibrator is a motor-driven eccentric controlled by a bit from Port C.

A synchronous stirrer is also controlled by the computer (Port B). The constant stirring rate (600 RPM) provides maximum hydrodynamic uniformity for the sample half-cell. The solution is quiescent during sample introduction; otherwise the stirrer is on.

6. Indicator electrode

The pH meter is interfaced to the computer via an optoisolated RS-232 link. Two 4N35 optoisolators are connected in each of the RS-232 data transmission lines (TXD and RXD), with each LED protected against reverse polarity by a series-connected Si diode. The phototransistors are connected in series with 10K load resistors to provide the required RS-232 high and low input signals. Power is obtained from the RTS and DTR lines of the COM1 port, latched at +9 V and −9 V by bit-level commands, and from the CTS line of the pH meter. Data I/O via the RS-232 port also uses bit-level commands to avoid toggling the RTS and DTR lines. The optoisolated RS-232 link and the use of battery power for the pH meter eliminate stray current flow through the pH electrode, thus avoiding any errors from ground loops during coulometric generation of the titrant.

A recursive procedure is used for all pH measurements, to eliminate errors due to the response time of the pH electrode. The pH value is read at the meter-limited rate (1–2 readings/s) and the elapsed time is recorded from the last pH reading in which a change in measured pH occurred. This loop is repeated until the measured pH remains constant for 6 s, corresponding to a maximum drift rate of 0.01 pH units/min. This pH is then taken as the stable value and the loop is exited. Accurate pH values are obtained by this procedure in solutions of weak acids (rapid pH electrode response) or strong acids (slow response) in the minimum time.

An analog potentiostat (PAR 174A, Princeton Applied Research, Princeton, NJ) is used for amperometric detection. The analog output of the potentiostat is connected to an analog input of the computer I/O board. The potentiostat is operated in the 2-electrode mode, with both cell leads connected to the IE through a DPST relay operated from one bit of port B. The relay is closed only during IE measurements. With the relay open, the potentiostat is isolated from the cell, eliminating the ground loop through the IE during coulometric generation of titrant. Each final IE measurement is the mean of ten discrete IE readings. This improves the signal-to-noise ratio of the measurement by averaging out slow variations in the IE reading, e.g. those caused by variations in mass transport to the electrode.

7. Endpoint detection and determination

Two subroutines are used for the endpoint determinations, one for acidimetry and one for titrations with amperometric detection. Each consists of two portions, referred to as endpoint detection and endpoint determination. Endpoint detection consists of the sequence of charge aliquots and cell rinses used to titrate the solution to a threshold value near the endpoint and eliminate any contamination of the frits with titrant or sample. Endpoint determination consists of the sequence of charge aliquots and IE measurements used in the actual calculation of the endpoint. The logic flow is outlined below for the acidimetric procedure.

The recursive procedure for endpoint detection is based on two major branching points, governed by two parameters: the rinse threshold pH_{min} and the maximum change in pH on rinsing, ΔpH_{max}. If the measured pH is greater than pH_{min}, the cell is rinsed; otherwise a charge aliquot is added. Following each rinse or charge aliquot, the pH is again measured. After each rinse, the pH change, ΔpH, is calculated. If ΔpH is greater than ΔpH_{max}, an additional rinse is performed. If the pH decreases below pH_{min} after a rinse, an additional charge aliquot is added and the same decision tree is followed. Rinses are repeated until the pH is greater than pH_{min} and ΔpH is less than ΔpH_{max}, whereupon the procedure proceeds to the endpoint determination.

The logic flow in the amperometric subroutine is similar. The main differences result from the fact that the endpoint cannot be estimated from IE measurements obtained prior to the endpoint. Hence, a constant titration time is used for all aliquots in the endpoint detection, and the rinse threshold corresponds to an IE reading slightly after the equivalence point. Aliquots in the endpoint determination are half as large and yield a linear IE current-time function. A least-squares line is used as the basis for the calculation of the endpoint. The estimated random uncertainty is calculated from the standard deviation of the X-intercept of this line [10].

8. Results and Discussion

Experimental results have been obtained for most of the classes of compounds noted in the Introduction. Representative data are shown in Table 1 for a hydrochloric acid solution and two high-purity chemicals: benzoic acid and potassium dichromate [NIST Standard Reference Material (SRM) 136c], together with the mean sample masses for which the quoted uncertainties in assay were obtained. The automated system achieves uncertainties (based on the relative standard deviation, R.S.D.) equal to or lower than those reported for the same compounds at

Table 1
Assays by automated coulometry

Compound	Assay (units as indicated)	n	R.S.D. (%)	Approximate sample mass (g)	Comparable R.S.D. for manual assay (Ref.)
HCl	49.9078 mmol/kg	10	0.0016	24.1	0.010 [1]
C_6H_5COOH	99.9996%	7	0.0041	0.25	0.004 [1]
$K_2Cr_2O_7$	99.9753%	4	0.0015	0.33	0.002 [3]

similar concentration levels and sample masses by Taylor and co-workers [1,3,5] using the earlier manual techniques. The standard deviation for potassium dichromate is also comparable to that reported by Knoeck and Diehl [11] using a different system and larger samples.

The results for SRM 136c also indicate negligible bias for the automated procedures, based on the earlier value obtained with the manual technique for the same material. The accuracy of the automated method is thus at least as good as the earlier manual technique. Fig. 5 illustrates the agreement of results using the automated technique with the certified value for this SRM, obtained [12] by a combination of manual coulometric analysis and by titrimetric intercomparison with SRM 83c (As_2O_3) and with SRM 136b, the previous issue of $K_2Cr_2O_7$, using weight titration with ferrous ammonium sulfate.

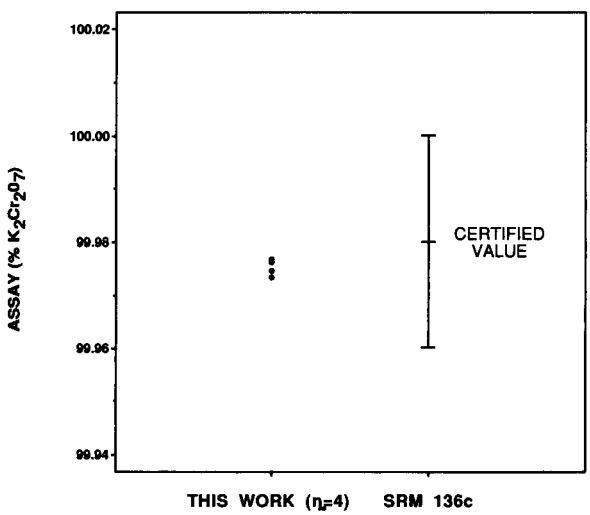

Fig. 5. Analytical results for NIST SRM 136c, potassium dichromate, by automated coulometry. Bracket denotes certified assay for the SRM.

Titration times for a single sample are typically on the order of 2–3 h for analyses with a main titration of 4000 to 7000 s. Shorter times can be obtained using smaller samples, but with increased risk of sample inhomogeneity. In addition, sample masses less than 0.1 g for solid samples or 5 g for solutions can limit the overall precision due to the uncertainty of the mass measurement. Sample throughput on a time-per-analysis basis is increased by only approximately 25% over manual titrations, due to the lengthy main titration. However, the percentage of 'lost' analyses compared to manual titrations is greatly decreased. This factor and the facility for unattended operation yield a significant increase in productivity on a cost-per-analysis basis.

9. Conclusion

Automated, high-precision coulometric titrations are readily performed using the instrumentation and software described. Analytical results uncertain to less than $\pm 0.005\%$ (R.S.D.) are demonstrated for several classes of compounds. Manual intervention is required only for initial setup of the cell and sample introduction.

Future papers in this series will stress the applications of this system to individual compounds. The chemical theoretical basis for the approach to the acidimetric endpoint, calculations associated with the endpoint determination, and estimation of bias and systematic uncertainties will also be discussed in greater detail.

10. References

[1] J.K. Taylor and S.W. Smith, J. Res. Nat. Bur. Stand., 63A (2) (1959) 153.

[2] J.K. Taylor and G. Marinenko, J. Res. Nat. Bur. Stand., 67A (1) (1963) 31.
[3] G. Marinenko and J.K. Taylor, J. Res. Nat. Bur. Stand., 67A (5) (1963) 453.
[4] G. Marinenko and J.K. Taylor, Anal. Chem., 39 (1967) 1568.
[5] G. Marinenko and J.K. Taylor, Anal. Chem., 40 (1968) 1645.
[6] G. Marinenko and C.E. Champion, J. Res. Nat. Bur. Stand., 75A (5) (1971) 421.
[7] G. Marinenko, W.F. Koch and E.S. Etz, J. Res. Nat. Bur. Stand., 88 (2) (1983) 117.
[8] T. Tanaka, G. Marinenko and W.F. Koch, Talanta, 32 (1985) 585.
[9] W.F. Koch and H. Diehl, Talanta, 23 (1976) 509.
[10] J. Neter, W. Wasserman and M.H. Kutner, Applied Linear Regression Models, Richard D. Irwin, Inc, Homewood, IL, 1983, pp. 172–174.
[11] J. Knoeck and H. Diehl, Talanta, 16 (1969) 181.
[12] Certificate for SRM 136c, National Bureau of Standards (U.S.A.), Washington, DC, March 1970.

ELSEVIER

Analytica Chimica Acta 289 (1994) 135–142

ANALYTICA CHIMICA ACTA

Automated, high-precision coulometric titrimetry Part II. Strong and weak acids and bases

Kenneth W. Pratt

Chemical Science and Technology Laboratory, National Institute of Standards and Technology, Gaithersburg, MD 20899, USA

(Received 17th June 1993; revised manuscript received 22nd November 1993)

Abstract

Automated constant-current coulometric acidimetry, based on Faraday's Laws, is uncertain to less than 1 part in 20000 (relative standard deviation) and requires no chemical standardization. It is applicable to strong and weak acids and bases, with bases back-titrated after addition of excess strong acid. Initial setup and sample introduction are the sole manual steps. Assays of HCl, benzoic acid, Na_2CO_3, and tris(hydroxymethyl)aminomethane are presented. In the endpoint determination procedure, a generalized titration equation yields the theoretical charge remaining to the endpoint before each charge addition. The ratio of the experimental to the theoretical charge for the preceding aliquot corrects for experimental deviations.

Key words: Coulometry; Automated analysis; Acidimetry; High-precision assay

1. Introduction

This paper is the second in a series of papers on automated high-precision, constant-current coulometric titrimetry. The first paper in this series [1] presented the engineering and instrumentation of the automated coulometric system. This article presents applications of this system to high-precision acidimetry, based on the original manual procedures of Taylor and Smith [2]. The use of automated coulometric back-titrations, based on work by Koch and co-workers [3,4] and by Marinenko [5] is presented.

The general automated procedure consists of a main titration at I_{main} for a time t_{main}, bracketed by the initial and final endpoint routines. For direct titrations, the assay (%) is calculated from Faraday's Laws on an absolute basis using Eq. 1. The calculation is identical to that described previously [1] except that different current levels, I_{init} and I_{final}, are used in the initial and final endpoint routines for maximum accuracy. F, M, n, and w_{sample} are the Faraday constant, molecular weight, equivalents per mol of analyte, and sample mass. The initial and final endpoints, t_{init} and t_{final}, are expressed as accumulated times corresponding to the charge added at I_{init} or I_{final} at the given endpoint. The quantity t_f represents the time corresponding to the total charge added at I_{init} in the initial endpoint routine.

$$\text{assay} = 100M\left[I_{main}t_{main} + I_{init}(t_f - t_{init}) + I_{final}t_{final}\right]/nFw_{sample} \quad (1)$$

0003-2670/94/$07.00
SSDI 0003-2670(93)E0693-2

The assay calculation for back-titrations, Eq. 2, takes into account the amount (mol) of HCl added, which is calculated from w_{HCl} and C_{HCl}, its mass and concentration in mol/g, respectively. The remaining variables are as in Eq. 1.

$$\text{assay} = 100M\{w_{HCl}C_{HCl} - [I_{main}t_{main} + I_{init}(t_f - t_{init}) + I_{final}t_{final}]/F\}/nw_{sample} \quad (2)$$

2. Theory

The endpoint in coulometric acidimetry can be predicted from prior pH measurements using titration theory. This reduces the total number of charge aliquots and pH measurements in each endpoint routine, reducing the overall time per analysis. The theoretical calculation of titration times is based on Eq. 3, the general equation [6,7] for titration of an acid of analytical concentration C_a and dissociation constant K_a. In Eq. 3, n_{OH} is the amount of OH^- added (in mol per liter of solution), K_w is the dissociation constant of water, and concentrations are denoted by brackets.

$$n_{OH} = C_aK_a/([H^+] + K_a) + K_w/[H^+] - [H^+] \quad (3)$$

The total titrant (mol) required to reach the equivalence point from a given pH is obtained by subtracting n_{OH} from C_a and multiplying by the sample half-cell volume, V_{cell}. Faraday's Laws are then used to obtain $t_{ep,pH}$, the titration time from a given pH to the equivalence point, for a current I:

$$t_{ep,pH} = \{C_a - C_aK_a/([H^+] + K_a) - K_w/[H^+] + [H^+]\}V_{cell}F/I \quad (4)$$

Eq. 4 is valid for both weak and strong (i.e., $K_a \rightarrow \infty$) acids over the entire titration curve. The theoretical time for titration from a given pH, pH0, to any higher pH, pH1, is equal to $t_{ep,pH0} - t_{ep,pH1}$.

In the program, each $t_{ep,pH}$ is calculated from Eq. 4 using $[H^+]$ obtained from the corresponding pH value by exponentiation. Each theoretical titration time after the first aliquot is corrected for the difference between theory and experiment using the ratio of the experimental to the theoretical titration time for the preceding aliquot. This operation is expressed mathematically by Eq. 5, where k is the aliquot number, $t_{prlm,(k+1)}$ is the preliminary titration time for the $(k+1)$th aliquot, and $t_{expt,k}$ is the experimental time for the kth aliquot. The initial and final pH values for the kth aliquot are pH0 and pH1, and pHt is the target pH. The calculation is performed after the end of the kth aliquot; hence, pH1 is the current pH.

$$t_{prlm,(k+1)} = [t_{ep,pH1} - t_{ep,pHt}] \cdot t_{expt,k}/[t_{ep,pH0} - t_{ep,pH1}] \quad (5)$$

The correction factor in Eq. 5 corrects automatically for the activity coefficient of H^+ and for variations in V_{cell}.

Approximate expressions derived from Eq. 3 are used to calculate the endpoint pH (inflection point) for titrations of weak acids and bases and to determine the optimum current level for the endpoint determinations. The endpoint pH, pH_{ep}, is given by Eq. 6.

$$pH_{ep} = (pK_w + pK_a + \log_{10}C_a)/2 \quad (6)$$

Eq. 7 is used to calculate t_{trial}, the theoretical titration time yielding a 0.1-pH change for a weak acid at its endpoint, calculated from the ratio of the buffer capacities, dn_{OH}/dpH [6], of a weak and a strong acid, each at its respective endpoint, and the corresponding time t_{min} for a strong acid.

$$t_{trial} = (C_a/K_a)^{1/2}t_{min} \quad (7)$$

Parallel equations valid for back-titrations of bases are obtained by replacing $[H^+]$ with $[OH^-]$ and C_a and K_a with their basic analogues C_b and K_b in Eqs. 3, 4 and 7.

For weak acids and bases, the inherent deviation between n_{OH} at the endpoint and n_{OH} at the equivalence point ($n_{OH} = C_a$), Δn_{OH}, is given by the Roller equation [8]:

$$\Delta n_{OH}/C_a = -3K_w/C_aK_a \quad (8)$$

Coulometric acidimetry differs from conventional acidimetry in that the solution volume over the course of the titration is virtually constant. Hence, the observations of Meites and Goldman [9] regarding the effects of dilution on the nature of the inflection point are not applicable, and Eq. 8 applies to this system. This was verified experimentally by Marinenko and Champion [10] using the boric acid–mannitol system.

3. Apparatus

The construction of the coulometric cell has been described previously [1,11]. A thin 3% agar–agar + 1.0 mol/l KCl plug on the counter-electrode side of the fine frit prevents transfer of solution from or to the counter electrode half-cell. The initial value of V_{cell} for this work is 65 ml. V_{cell} is updated after sample introduction for use in Eq. 4 in the final endpoint routine. Titration times are thereby increased proportionately.

A splash guard, fashioned from the bottom of a 50-ml PTFE bottle, is inserted into the sample half-cell, fitting snugly around the beaker wall about 1 cm above the solution level. The splash guard, attached to the cell cover and fitted with holes for the pH electrode and deaeration tube, prevents loss of sample during the main titration from H_2 bubbles evolved at the cathode. The pH electrode rests on the cover of the sample half-cell, with a foam rubber cushion for vibrational isolation.

Both half-cells are deaerated with N_2 using miniature deaeration tubes. Trace CO_2 is eliminated from the N_2 by a chain of three scrubbers filled with 0.5 mol/l KOH, 0.001 mol/l HCl, and water. Excess N_2 from the outlet of the ambient-pressure reservoir is used to blanket the cavity between the splash guard and the cell cover. Within the sample half-cell, the deaeration tube, when raised, remains within the cavity formed by the splash guard and the surface of the solution. This arrangement effects a 2-stage shield between the sample solution and the atmosphere, resulting in minimal CO_2 levels in the cell during the procedure.

The supporting electrolyte for the acidimetric titrations is 1.0 mol/l KCl, made from reagent-grade KCl and deionized water with a conductivity below 0.06 μS/cm. The filling solution for the reference element of the pH electrode is AgCl-saturated 1.0 mol/l KCl, substituted for the standard saturated KCl + AgCl normally used. Electrode stability is unaffected by this solution. The filling solution has the advantages of freedom from KCl crystal formation on extended usage and lower Ag^+ concentration. This results in a lower systematic error due to Ag electrodeposition onto the cathode during titration, since seepage from the reference electrode adds less Ag^+ to the cell.

The coulometric electrode for acidimetry is a Pt, Ta, or Au cathode, wound into a 3-cm diameter helix with 5–6 turns. The cathode is placed such that the pH electrode is roughly centered in the helix. This reduces the error from the electrical field during the main titration to less than 60 mV (1 pH). The counter electrode is an Ag rod with a surface area of ca. 45 cm^2, sufficient for titrations of up to 10 mmol H^+ without acidifying the KCl solution in the counter electrode half-cell.

4. Procedure

The detailed procedure has been described previously. Only those steps not described in [1] are presented here.

The entire cell is deaerated for 15 min after the initial cell test and before the start of the analysis. The pH of the electrolyte in the sample half-cell, nominally 7.0 when deaerated, is lowered by adding 2.5 μmol HCl before the start of the titration. This accelerates removal of dissolved CO_2 and facilitates the initial endpoint determination. The pH of the solution typically increases from about pH 5.5 to pH 5.8 during the deaeration. After this step, the deaeration tube is lowered only when (a) the solution pH is less than $\pm 2pH_{range}$ (defined below) from the endpoint or (b) during carbonate back-titrations.

Liquid samples are introduced by lifting the pH electrode out of the cell and inserting the outlet tube of the syringe through the holes in the

cell cover and splash shield. This reduces contamination from CO_2 in analyses of liquid samples. The pH electrode is replaced immediately after the sample introduction.

For back-titrations, excess titrant is added by syringe, immediately prior to the sample introduction. Advance coulometric standardization of the excess titrant, typically HCl, is required prior to the start of the back-titration.

At the end of the delay routine in the main titration, the program enters a pH measurement loop. The measurement loop is exited when a single measurement exceeds a preset target value, and the main titration concludes. The target value, $pH_{ep} - 2$ for weak acids and $pH_{ep} - 4$ for strong acids, takes into account the measurement errors due to the potential field from the coulometric current and the response time of the pH electrode. This procedure shortens the titration time required in the final endpoint routine. This routine is not used in the endpoint routines, since the pH electrode responds too slowly to avoid overshoot.

For weak acids or bases, a value of C_a or C_b is first available after sample introduction. Values of pH_{ep} and t_{trial} are calculated at this point from Eqs. 6 and 7 (or the basic analogues). I_{final} is set to 9.6486 mA if t_{trial} is greater than 5 s; otherwise it remains 0.96486 mA. For strong acid titrations, I_{final} is 0.96486 mA and $C_a = 0$, yielding the same result as $K_a \rightarrow \infty$ in Eq. 4. I_{init} is always 0.96486 mA, corresponding to $t_{min} \approx 1$ s in Eq. 7.

The value of I_{main} is fixed at 101.8243 mA for all titrations. Assay values are calculated using a value of 96486.04 NIST C/mol for the Faraday constant. Molecular weights for the various compounds are calculated using 1987 IUPAC atomic weights.

Table 1
Results for replicate titrations by automated coulometric acidimetry

Compound	n	Mean	S.D.	R.S.D. (%)
HCl	10	49.9078 mmol/kg	0.00079 mmol/kg	0.0016
C_6H_5COOH	7	99.9996%	0.0041%	0.0041
Na_2CO_3	5	99.9823%	0.0028%	0.0028
Tris	6	99.9238%	0.0051%	0.0051

Assays yielding the data in Table 1 were performed using high-purity sodium carbonate and reagent-grade benzoic acid and tris(hydroxymethyl)aminomethane (Tris). The sodium carbonate was a high-purity material certified for trace-metal content. Data in Table 1 were obtained using samples dried as follows: Na_2CO_3, 5 h at 300°C; benzoic acid and Tris, 24 h over $Mg(ClO_4)_2$ at less than 100 Pa.

5. Compound-specific features

In carbonate back-titrations, the sample reacts with the excess acid to yield CO_2. This CO_2 must be quantitatively eliminated from the sample half-cell before the final endpoint determination. Hence, the deaeration tube is lowered from the end of sample dissolution until the start of the final endpoint determination. A 15-min deaeration period is also inserted after sample dissolution, to eliminate CO_2 at acidic pH. The final endpoint detection and determination are those of a strong acid, since H_2CO_3 and CO_2 have been quantitatively eliminated at this point in the procedure. The value of n is 2 for the assay calculation.

Benzoic acid does not dissolve completely at sample introduction, yet must be quantitatively dissolved before rinsing the cell or beginning the final endpoint routine. Hence, a final dissolution step is inserted immediately after the main titration. The center compartments are emptied, and the cell is vibrated until a stable pH ($|dpH/dt|$ below 0.01 pH/min) is obtained. The alkaline pH (initially 10–11, final value near 7) at this point increases the rate of dissolution. This step is followed by the first rinse and the final endpoint routine.

6. Endpoint routines

The endpoint routine consists of endpoint detection and endpoint determination. The main parameters for the endpoint routine are pH_{ep},

the preliminary endpoint; ΔpH_{max}, the maximum pH change on rinsing; and pH_{range}, the pH range for the endpoint determination. The rinse threshold, pH_{min}, is equal to $pH_{ep} - pH_{range}$.

Endpoint detection consists of the sequence of charge aliquots and cell rinses used to titrate the solution to pH_{min} and eliminate any contamination of the frits with titrant or sample. Charge aliquots are added using t_{prlm} values calculated from Eqs. 4 and 5 as described above. Exact titration times are obtained from the precision timer after each aliquot. Cell rinses are performed only if the pH of the sample solution is greater than pH_{min}; otherwise a charge aliquot is added. Endpoint detection is completed when the measured change in pH on rinsing falls below ΔpH_{max} and the final pH is above pH_{min}.

Endpoint determination consists of the sequence of charge aliquots and pH measurements used in the actual calculation of the endpoint. The procedure consists of a series of discrete charge aliquots that yield a set of equally spaced pH–time points. The titration time for each aliquot is calculated from the slope (dpH/dQ) for the preceding charge aliquot and the desired change in pH, set as $pH_{range}/4$. No rinses are performed during the endpoint determination, and the deaeration tube is raised to avoid interference of bubbles with the pH measurements.

The endpoint determination for strong acids or bases is terminated when the pH exceeds 7.000. The "best value" for the endpoint is estimated by linear interpolation between the two last pH–time points.

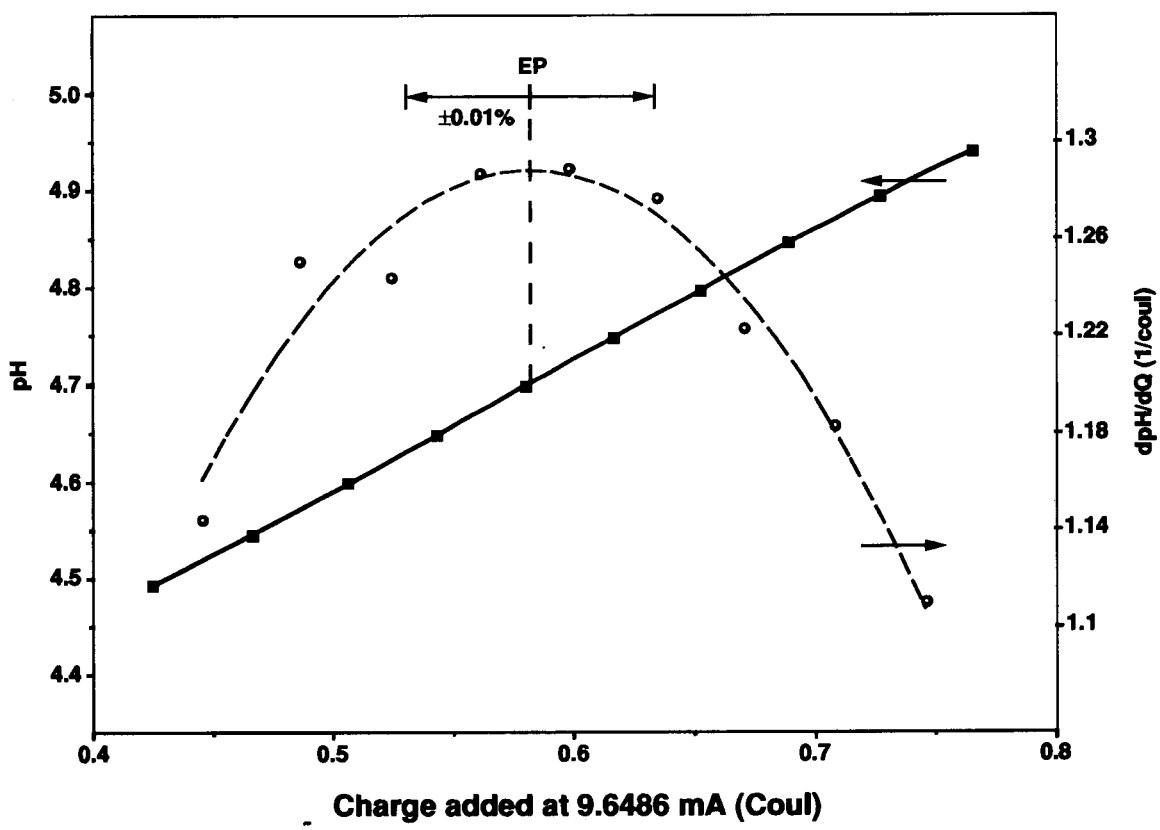

Fig. 1. Final endpoint determination for back-titration of Tris. ■, experimental pH–time points; solid line, least-squares cubic polynomial curve fit to the pH–time points; ○, $\Delta pH/\Delta Q$ points calculated from experimental pH–time points; broken line, first derivative of least-squares cubic curve fit. Start of final endpoint routine defines $Q = 0$.

In the endpoint determinations of weak acids or bases, a set of pH–time points symmetrically bracketing the endpoint is generated. To obtain these, a "sliding" endpoint is used. The value of pH_{ep} is updated to the mean of the last two pH values if the slope from the present aliquot is greater than the maximum slope for all the preceding aliquots; otherwise it remains unchanged. Charge aliquots are added until the solution pH is greater than $pH_{ep} + pH_{range}$. The initial endpoint determination also uses this procedure, in order to correct for any initial contamination of the frits with weak acid or base from a preceding titration. In direct titrations of weak acids, an initial pH_{ep} of 7 and the "sliding" endpoint routine automatically locate the initial endpoint. For back-titrations of weak bases, the initial pH_{ep} is set to pH 6.6 in order to avoid overshooting the actual endpoint.

The "best values" for t_{init} and t_{final} for weak acids and bases are calculated from the second derivative of the least-squares third-degree polynomial calculated [12] from the set of pH–time points generated as described above. Setting the second derivative equal to zero yields t_{init} or t_{final}, from which pH_{ep} is back-calculated using the cubic polynomial. The effect of errors in the individual pH measurements is minimized through use of the entire set of pH–time points from the endpoint determination. Fig. 1 illustrates the accuracy of fit obtained using this technique for the final endpoint in a back-titration of Tris, a weak base with $pK_b = 5.92$. Location of this endpoint to the requisite uncertainty (0.002%) using the classical point-by-point technique is difficult.

7. Estimation of uncertainties

Standard uncertainties u_i [13] are calculated for t_{init} and t_{final} in the corresponding endpoint routine, using a root-sum-of-squares calculation of uncertainty (a), due to incomplete rinsing of the frits; and uncertainty (b), due to pH measurement. Both of these uncertainties are Type B [13], with an assumed normal distribution and estimated lower and upper limits x_- and x_+ such that there is about a 67% probability that the value of the quantity lies in the interval x_- to x_+, where $u_i \approx x$. Uncertainty (a) is estimated from the experimental change in pH for the final rinse and the buffer capacity (dn_{OH}/dpH) at the endpoint. This estimate assumes that the uncertainty is equal to the experimental change which would have resulted from omission of the last rinse. Uncertainty (b) is currently estimated from the product of 0.01 pH (the assumed maximum uncertainty for the pH measurement, based on the maximum $|dpH/dQ|$) times dn_{OH}/dpH at the endpoint. This Type B estimation of uncertainty (b) will be replaced in the future by a Type A [13] estimate, calculated from the set of experimental pH–time points and the least-squares third-degree polynomial obtained in the endpoint determination. This calculation will be reported in a future publication.

The combined standard uncertainty u_c for a single titration is estimated by root-sum-of-squares combination [13] of the estimated component u_i values. Individual u_i components are calculated from the following estimated Type B uniform distributions: sample weighing (5 μg for solids, 0.2 mg for liquids); the electrical standards (10 ppm); and the uncertainty due to variations in the amount and concentration of the solution in the center compartments in the initial and final endpoint determinations (10 ppm). These uniform distributions are each divided by $\sqrt{3}$ to yield estimates of u_i for each component before combination with the uncertainties for the initial and final endpoints (see previous paragraph) and, for back-titrations, $u_c/k^{1/2}$ for the standardization of the excess acid, obtained from the mean of the set of k titrations used to standardize the acid. The result of this calculation provides an estimate of the combined uncertainty u_c which includes all known instrumental u_i components. It does not include the contribution of any u_i components due to chemical effects. The u_c value obtained from the above calculation is useful in the absence of a valid Type A estimate of the random uncertainty of a set of independent assays.

Chemical effects specific to coulometric acidimetry are potential sources of bias in the

reported result. These include the deposition of Ag onto the cathode during electrogeneration of OH^-; incomplete removal of CO_2 from the electrolyte; and, for weak acids, the inherent deviation of the endpoint from the equivalence point [8]. Quantitative measurements of the bias due to Ag^+ deposition, using anodic stripping voltammetry at a Ta cathode after a coulometric HCl assay, yielded an estimate of less than 1 ppm with an estimated uncertainty of 0.5 ppm for titration of a 25-g sample of 0.05 mol/l HCl. The bias due to incomplete removal of CO_2 from the electrolyte in the sample half-cell can be estimated from experimental values of dpH/dQ for titrations of strong acids, in which the value of dpH/dQ observed at the endpoint provides an estimate of the CO_2 concentration. Based on such measurements, this bias is estimated at less than 10 ppm with an maximum uncertainty of 5 ppm for a 1000-s titration of 0.05 mol/l HCl. The bias due to the inherent negative deviation of the endpoint from the equivalence point for weak acids is given by Eq. 8. Using C_a and K_a values for acids analyzed in this work, this theoretical bias is less than 0.4 ppm (calculated from Eq. 8) for all assays performed in this work. The above three sources of bias are deemed negligible compared to the other sources noted above. The final result is not corrected for these sources of bias, nor are their uncertainties included in the calculation of u_c.

8. Results and discussion

Results of replicate coulometric assays of 0.05 mol/kg HCl, benzoic acid, sodium carbonate, and Tris are presented in Table 1. These represent typical data for a strong acid, weak acid, strong base (as titrated here) and weak base, respectively. R.S.D. values from this work and from the literature at similar concentration levels are summarized graphically in Fig. 2. In most cases, the RSD from the present work is smaller than the corresponding value obtained by Taylor and Smith [2], Koch and co-workers [3,4], or

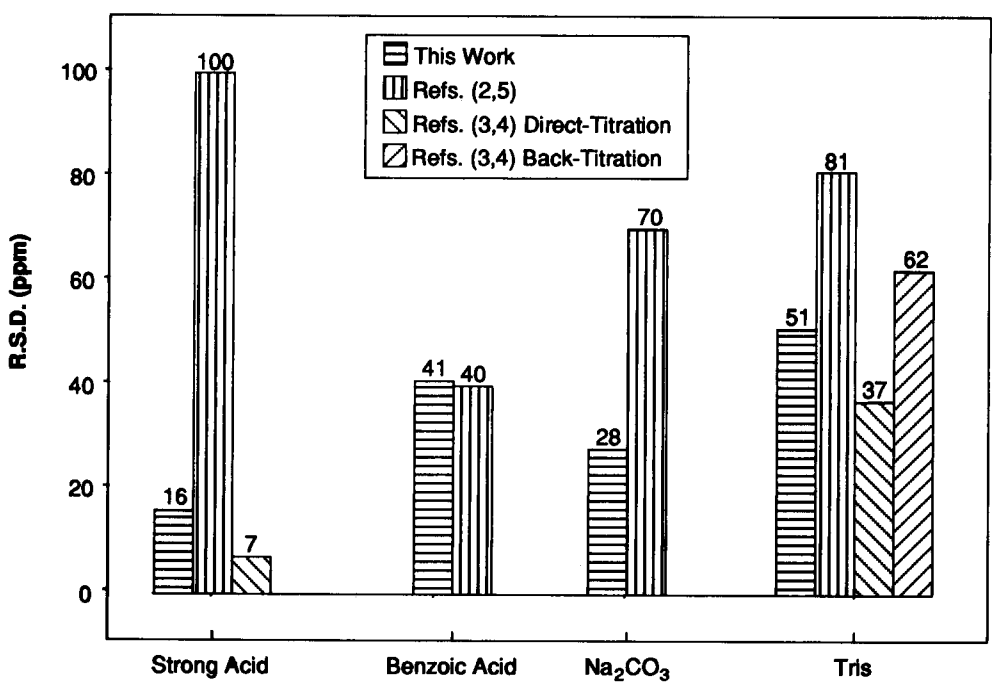

Fig. 2. Comparative uncertainties (stated as R.S.D.) for automated coulometric acidimetry (this work) and coulometric acidimetry (Refs. as shown). All values given as ppm.

Marinenko [5] using the corresponding manual technique. Slightly lower R.S.D. values of 0.0007% for titrations of $HClO_4$ [4] and 0.0037% for Tris [3] reported by Koch and co-workers result from the use of larger samples and a direct titration for Tris.

Evidence for accuracy has also been obtained for the automated system. The 0.05 mol/kg HCl results listed in Table 1 were used for the results reported for the sodium carbonate back-titrations. The value near 100% for the Na_2CO_3 assay demonstrates internal consistency for these two assays, providing evidence for the accuracy for these two determinations. A slow decrease in individual assay values with increasing assay number (first assay = 99.9874%, fifth assay = 99.9807%) results from slow takeup of moisture by the Na_2CO_3 during the successive openings of the weighing bottle used to store the compound.

A separate control titration for NIST Standard Reference Material (SRM) 723 performed concurrently with the data shown in Table 1 yielded 99.9716% Tris, in agreement with the certified value of 99.969 ± 0.003% (95% confidence interval of the mean, based on 30 determinations) for this SRM by Marinenko [5]. The lower assay reported (99.9238%) for the reagent-grade material is due to mother liquor occluded in the crystals of this material. In support of this conclusion, three titrations of the reagent-grade material, assayed after grinding in an agate mortar for 10 min, yielded a value of 99.952% Tris with an R.S.D. of 0.003%. Such occlusions have previously been detected in Tris by optical microscopy and manual coulometry at levels up to 0.7% [3].

9. Conclusion

Acidimetric assays uncertain to less than 0.005% (R.S.D.) are readily obtained using automated coulometry as presented herein. Basimetric assays are also possible via back-titration. Operator intervention is required only for the initial setup and for sample introduction. The theory and practical aspects of the prediction of the endpoint from prior pH measurements are described and their use in automated coulometry is described.

10. References

[1] K.W. Pratt, Anal. Chim. Acta, 289 (1994) 125.
[2] J.K. Taylor and S.W. Smith, J. Res. Natl. Bur. Stand. (U.S.), 63A (2) (1959) 153.
[3] W.F. Koch, D.L. Biggs and H. Diehl, Talanta, 22 (1975) 637.
[4] W.C. Hoyle, W.F. Koch and H. Diehl, Talanta, 22 (1975) 649.
[5] G. Marinenko, Natl. Bur. Stand. (U.S.) Technical Note, 543 (1970) 56.
[6] D.D. Van Slyke, J. Biol. Chem., 52 (1922) 525.
[7] E.D. Eastman, J. Am. Chem. Soc., 47 (1924) 332.
[8] P.S. Roller, J. Am. Chem. Soc., 50 (1928) 1.
[9] L. Meites and J.A. Goldman, Anal. Chim. Acta, 29 (1963) 472.
[10] G. Marinenko and C.E. Champion, Anal. Chem., 41 (1969) 1208.
[11] G. Marinenko and J.K. Taylor, Anal. Chem., 40 (1968) 1645.
[12] W.F. Koch, D.P. Poe and H. Diehl, Talanta, 22 (1975) 609.
[13] B,N. Taylor and C.E. Kuyatt, Natl. Inst. Stand. Technol. (U.S.) Technical Note, 1297 (1993) 1.

ELSEVIER

Analytica Chimica Acta 289 (1994) 143–153

ANALYTICA CHIMICA ACTA

Electrochemical immobilization of glucose oxidase in poly(amphiphilic pyrrole) films and its application to the preparation of an amperometric glucose sensor

Liliane Coche-Guérente *, Alain Deronzier, Pascal Mailley, Jean-Claude Moutet

Laboratoire d'Electrochimie Organique et de Photochimie Rédox, URA CNRS 1210, Université Joseph Fourier Grenoble 1, BP 53, 38041 Grenoble Cedex 9, France

(Received 20th September 1993; revised manuscript received 22nd November 1993)

Abstract

A glucose sensor has been realized by the electropolymerization on a platinum electrode of a pre-adsorbed coating of glucose oxidase (GOD) mixed with the amphiphilic substituted pyrrole **1**. In the presence of glucose and molecular oxygen, this biosensor has a fast response time and provides a low detection limit (0.1 μM). The stability, pH, temperature response of the sensor and its kinetic parameters have been studied. The preparation procedure enables the control of the amount and the activity of entrapped enzyme. Multilayered assemblies could be easily obtained by sequential electropolymerization. These structures allowed to increase notably the linear part of the calibration curves, from 2.5 to 5 mM in glucose, and to minimize the electrochemical interferences due to endogenous electroactive substances. Preliminary attempts at the preparation of miniature glucose sensors have demonstrated the potential interest of this new biosensor construction technique.

Key words: Amperometry; Biosensors; Glucose sensor; Electropolymerization; Polypyrrole

1. Introduction

Since the first report in 1962 by Clark and Lyons [1] on a glucose oxidase (GOD) based electrochemical sensor, a large amount of work has been devoted to amperometric glucose electrodes and their development continues to receive considerable attention [2]. Particular efforts have been directed to the realization of sensors for biomedical analysis. The final goal of these researches is the construction of a glucose electrode offering the possibility of continuously self-monitoring of blood glucose levels by diabetics [3]. An important consideration in the future development of practical devices is how to develop efficient and straightforward techniques for enzyme immobilization on electrodes surfaces. The main conventional approaches include physical adsorption at a solid electrode surface, covalent bonding to a reactive insoluble support, entrapment in polymeric gels, carbon paste or within microcapsules and cross-linking by means of bifunctional reagents such as glutaraldehyde, often

* Corresponding author.

SSDI 0003-2670(93)E0660-Y

in combination with adsorption or physical entrapment [4]. Recently, incorporation of GOD in a Langmuir-Blodgett films [5], its covalent attachment to a redox polymer [6] and the copolymerization of a pyrrole-substituted GOD with pyrrole [7] have also been reported.

Electrochemical entrapment in a conducting polymer film provides an attractive alternative for the facile immobilization of enzymes on electrodes surfaces. Numerous studies have demonstrated that GOD may be incorporated in electrochemically deposited films of polypyrrole [8–19] and its derivatives [20–23], polyaniline [24–26], polyphenols [27] and polyindole [28]. Such immobilization provides a simple one-step approach for controlling the amount of deposited polymeric material by monitoring the current consumed during the electropolymerization. However, this procedure suffers from severe limitations. High amounts of monomer and enzyme must be used. It must be emphasized that if the size of the coating can be controlled by coulometry, the amount, thus the real activity of immobilized enzyme molecules, cannot be determined. We have recently described [29] a novel monomer and enzyme saving procedure for the deposition of enzyme–polymer layers on Pt and C disc electrodes. This procedure is based on the oxidative electropolymerization in an aqueous electrolyte of an adsorbed layer of enzyme mixed with the amphiphilic substituted pyrrole **1**.

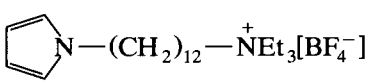

1

It has been demonstrated that glucose oxidase and choline oxidase [29], and tyrosinase [29,30] can be effectively immobilized this way. This paper is a full account of our work on the elaboration of a Pt/poly**1**–GOD electrode and its response in the presence of glucose and molecular oxygen as electron acceptor. The hydrogen peroxide produced by the enzymatic reaction is amperometrically determined by monitoring the current due to its electrochemical oxidation at the metal–film interface. The effect of enzyme loading, temperature and pH on the electrode response has been studied. A calibration curve for glucose obtained with an optimized electrode and its operational stability are presented. We report also the characteristics of glucose sensors based on different arrangements (mono- and multilayered structures). The effect of electrochemical interferents such as ascorbic acid and uric acid on the electrode response has been investigated. We demonstrate that these interferences are minimized by using bilayered films. Preliminary attempts at the preparation of miniaturized enzymes electrodes are also presented.

2. Experimental

2.1. Apparatus

Electrochemical experiments were performed with a PAR Model 173 potentiostat equipped with a Model 179 digital coulometer, a Model 175 programmer and a Sefram TGM 164 xy/t recorder. Electrochemical polymerizations and measurements were carried out in a three-compartment electrochemical cell, using a saturated calomel reference electrode and a platinum wire counter electrode separated from the electrolyte by a salt bridge. The cell was thermostated with a Colora calorimeter. Poly**1**-enzyme films were deposited on 5 mm platinum discs (sealed in glass) polished with 1 μm diamond paste. Platinum microelectrodes were prepared by sealing a Pt fiber (Johnson Matthey, 50.8 μm diameter) into a 3 mm diameter glass tube. Sealing was accomplished with epoxy resin. The tip of the electrode was polished with fine sand paper and 1 μm diamond paste. Electrical contact was provided with a copper wire and mercury droplet.

Spectrometric measurements were performed with a Varian Cary 1 UV–visible spectrophotometer. The amphiphilic monomer **1** was ultrasonically dispersed in pure water using a Branson 200 W generator coupled to a thermostated Cup Horn transducer.

2.2. Chemicals

Monomer **1** was synthesized as previously described [31]. Glucose oxidase (GOD) from *As-*

pergillus niger (Type VII, 150 U mg^{-1}) and β-D-glucose were obtained from Sigma. Stock solutions of glucose (prepared in phosphate buffer, pH 7) were allowed to mutarotate overnight before use. Others reagents were from analytical grade.

2.3. Procedures

The enzyme electrodes were fabricated as follows. Monomer **1**, which has a very low solubility in water ($\leqslant 10^{-5}$ M [31]) was ultrasonically dispersed in pure water to give a stable, optically transparent dispersion to which GOD was added. A drop of the aqueous mixture (30–40 μl) containing 0.1 to 0.3 μmol of **1** and 10 to 68 units of GOD was spread on a 5 mm diameter Pt disc. Water was removed under vacuum. Polymerization of the dry, adsorbed monomer **1**-enzyme film was performed at 0.76 to 0.85 V in deaerated aqueous 0.1 M $LiClO_4$ to zero current.

The amount of enzyme truly trapped in the polymeric film was measured from the difference between the quantity of enzyme initially spread on the electrode surface and the quantity of enzyme lost in the electrolyte during the polymerization step. This last value was obtained from the enzymatic activity of the polymerization electrolyte and determined spectrophotometrically using the standard *o*-dianisidine Sigma procedure, based on the increase in absorbance at 500 nm, carried out on 50 to 100 μl samples of electrolyte. The activity of immobilized enzyme molecules was estimated from the same spectrophotometric assay, with the rotating tip of the electrode immersed in the test mixture.

3. Results and discussion

3.1. Enzyme immobilization

Fig. 1, curve a, shows the cyclic voltammogram of a Pt/poly**1**–GOD electrode prepared by electropolymerization at 0.76 V, which exhibits the well defined response ($E_{1/2} = 0.53$ V) of the polypyrrole matrix. The amount of pyrrole, i.e., of ammonium units fixed on the electrode surface could be estimated from the charge recorded under the oxidation wave, assuming that one in three pyrrole units is oxidized [32].

Table 1
Elaboration [a] and characteristics of Pt/poly**1**–GOD electrodes

Entry	E_{app}/ V vs. SCE	Polymerization time (min)	Charge consumed (mC)	GOD retained [b] (%)	Electrode activity/mU (mU cm^{-2})	Residual activity [c] of trapped GOD (%)	Electrode response [d] to 1 mM glucose/μA (current density, μA cm^{-2})
1	0.76	19	15.6	22	17 (87)	0.40	1.8 (9.2)
2	0.76	15	15.6	23	16 (82)	0.35	2.3 (11.7)
3	0.76	19	15.6	25	18 (92)	0.37	2.4 (12.2)
4	0.76	25	15.6	25	17 (87)	0.35	2.5 (12.7)
5	0.85	24	18	99	59 (301)	0.33	2.9 (14.8)
6	0.85	6	18	46	43 (219)	0.47	0.9 (4.6)
7	0.85	4	18	99	13 (66)	0.07	0
8	0.85	6	18	99	35 (178)	0.19	0.8 (4.1)
9	0.85	12	18	59	43 (219)	0.36	2.0 (10.2)

[a] Electropolymerization of a coating containing 20 U of GOD and 0.15 μmol of **1**, deposited on a 5 mm diameter Pt disc electrode, in H_2O + $LiClO_4$ 0.1 M.
[b] Percentage of GOD molecules retained in the polymer film, determined from the activity of the polymerization electrolyte; see the Experimental section.
[c] Average activity of immobilized GOD molecule, as compared to the activity (100%) of the free enzyme.
[d] Measured at 0.5 V in stirred 0.1 M phosphate buffer (pH 7) at 24°C.

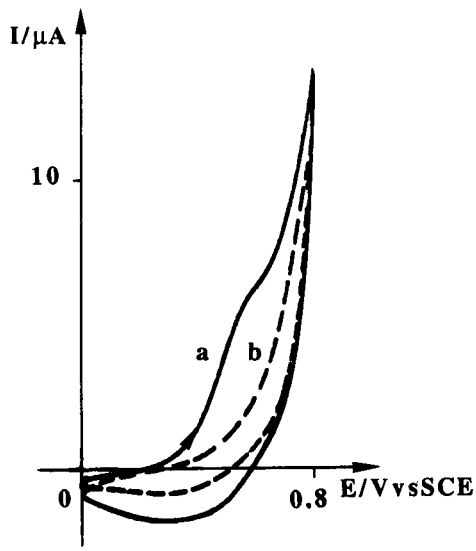

Fig. 1. Cyclic voltammograms in $H_2O+0.1$ M $LiClO_4$ for Pt/poly**1**–GOD electrodes prepared by electropolymerization at 0.76 V (a) and 0.85 V (b) of 0.15 μmol of **1** and 20 U of GOD coated on a Pt disc (5 mm diameter); $v = 2$ mV s^{-1}.

Spectrophotometric assays (see the Experimental section) carried out on polymerization electrolytes in which a series of Pt/poly**1**–GOD electrodes has been elaborated at 0.76 V, from 0.15 μmol of **1** and 20 U of GOD, have shown that 22 to 25% of preadsorbed enzyme molecules were retained in the polymeric films (Table 1, entries 1–4). From the enzymatic activity at the electrodes it could be calculated that the average activity of immobilized enzyme molecules had dropped down to 0.35–0.40% of that of the free enzyme (Table 1, entries 1–4). Despite this low residual enzymatic activity, rather fair response currents were obtained in the presence of 1 mM glucose, from 1.8 to 2.5 μA.

Direct electrical communication between GOD and a platinum surface through an oxidized, conductive polypyrrole has already been observed [11,23,33]. We found that such phenomenon took place in an oxidized, conductive poly**1** matrix. Very low currents were obtained at $E_{app} = 0.5$ V in a carefully deaerated electrolyte, following the addition of 5 mM glucose. We have checked that glucose is not oxidized at this potential, on both Pt and Pt/poly**1** electrodes. This current response appeared unstable, especially in the presence of oxygen. This is probably due to the oxidative degradation of the conductivity of poly**1** by the enzymatically produced hydrogen peroxide. Therefore, we chose to over-oxidize the polypyrrole to destroy its conductivity [34] before use, simply by cycling it several times up to 1.2 V.

We tried to improve the immobilization procedure by using a higher polymerization potential (0.85 V), in order to promote a faster electropolymerization and to retain more enzyme molecules in poly**1** films. Fig. 1, curve b, shows that a polymeric film prepared in this way is non-conductive, since no reversible oxidation wave can be seen. This is not surprising, since the high potential applied leads to a quick degradation of the electroactivity of the polypyrrole as soon as it is formed, due to its overoxidation [34]. Data from Table 1 (entries 5–9) demonstrate that the use of this higher oxidation potential leads to scattered and poorly reproducible results. First of all the polymerization time, i.e., the time required to pass a charge of 18 mC varies from 4 to 24 min. As expected, more enzyme was retained in the polymeric film, from 46 to 99%. However, the electrode activity is not a function of the amount of trapped enzyme molecules, whose average activity varies from 0.07 to 0.47% to that of the free GOD. The electrode response to glucose appeared also uncertain. In most cases (entries 6–9) the current measured in the presence of 1 mM glucose is lower than the current obtained on the electrodes prepared at 0.76 V. However, it is noteworthy that the shorter the polymerization time, the higher was the current response. The better results obtained by electropolymerization at 0.76 V could be due to the fact that the polymeric film remains conductive under these conditions. This is responsible for a clean polymerization, to form reproducible enzymatic layers showing a higher catalytic activity. It should be noted that the electrodes activity, from 82 mU cm^{-2} (Table 1, entry 2) to 92 mU cm^{-2} (entry 3), compares well with that measured for conventional polypyrrole–GOD sensors, since values from 1.5 mU cm^{-2} [15] to 125 mU cm^{-2} [8] have been reported in the literature.

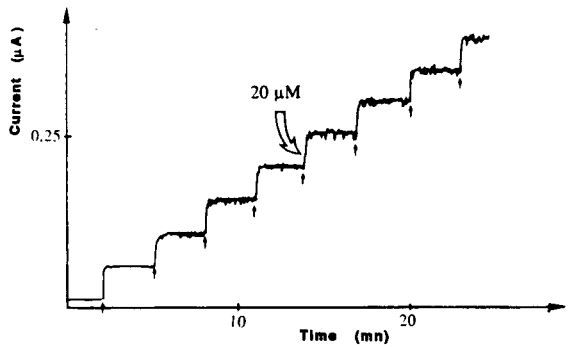

Fig. 2. Response of a poly**1**–GOD (monolayer prepared from 20 U of GOD and 0.15 μmole of **1**) electrode to additions of 20 μM glucose (marked by the arrows) to the bulk solution, obtained at 0.5 V in stirred phosphate buffered solution (pH 7, 27°C).

3.2. Electrodes characteristics

Response to glucose

Fig. 2 shows a typical set of responses to the addition of glucose; the response time for the electrode was of the order of 10 s. A study of the current response in the potential range 0.4 to 0.7 V has shown that the higher responses were obtained from 0.5 V.

Fig. 3 (curve a) shows a plot of the current response as a function of the glucose concentration. A linear relationship was observed for glucose concentrations ranging from 0.1 μM to 2.5 mM, where the reaction was first order with respect to the substrate. These sensors provide a low limit of detection (based on a signal-to-noise ratio of 3) for glucose, namely 10^{-7} M. The response saturated at about 30 mM. The response at high glucose concentration can be limited by either the reaction of the molecular oxygen with the enzyme or by the saturated enzyme–substrate kinetics. In order to investigate this, measurements were made in both air-saturated and oxygen-saturated buffer. Fig. 4 shows the responses to glucose at a C/poly**1**–GOD electrode under these two experimental conditions. The current clearly saturated at a lower level in the air-saturated buffer. This indicates that the current at high glucose concentrations under these conditions was limited by the rate of re-oxidation of the enzyme by the oxygen, as it was already observed for GOD immobilized in a polyphenol film for example [35].

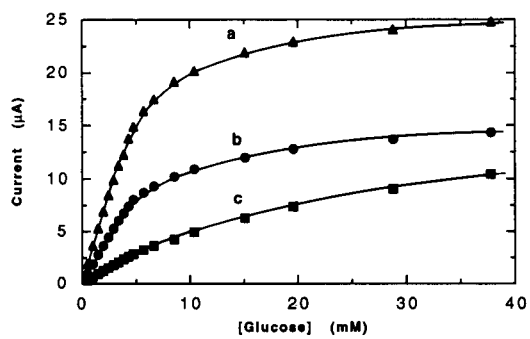

Fig. 3. Calibration curves for glucose obtained in stirred phosphate buffer, pH 7; the steady-state current was recorded at 0.50 V on a modified Pt disk, (a) monolayer prepared from 20 U of GOD and 0.12 μmole of **1**, (b) bilayer structure 20 U (GOD)–0.12 μmole (**1**)/0.12 μmole (**1**), (c) sandwich structure 0.04 μmole (**1**)/20 U (GOD)/0.16 μmole (**1**).

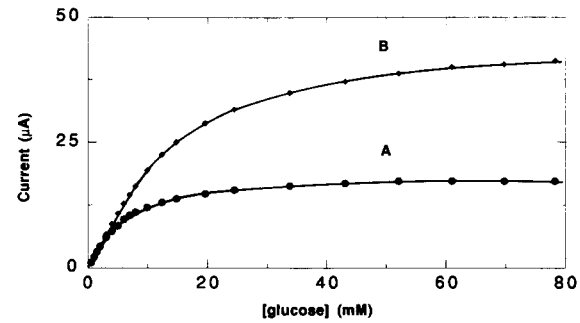

Fig. 4. Response to glucose for a Pt/poly**1**–GOD electrode prepared as described in Table 1 (entries 1–4) in (A) air-saturated and (B) oxygen-saturated buffered solution.

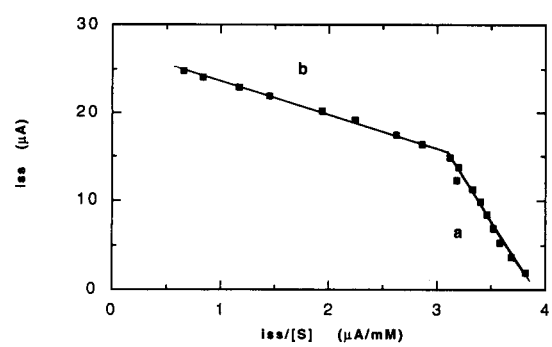

Fig. 5. Eadie-Hofstee plot obtained from the data in Fig. 3a.

The electrochemical Eadie-Hofstee type plot which is given in Fig. 5 is characterized by two straight lines. A strong positive deviation is observed for glucose concentrations lower than 6 mM. The equation of the straight lines corresponds to:

$$i_{ss} = i_{max} - K'_M i_{ss}/[s]$$

where i_{ss} is the steady-state current, i_{max} the maximal current under saturating glucose conditions, [s] is the glucose concentration in the air saturated solution and K'_M is the apparent Michaelis-Menten constant. The coefficients of correlation (r^2) were 0.992 and 0.989 for the straight lines *a* and *b* respectively. From their slopes, apparent Michaelis-Menten constants of 20.2 and 3.5 mM were determined at low and high (> 6 mM) glucose concentration, respectively.

Non-linear Eadie-Hofstee plots have also been observed for polypyrrole–GOD sensors [36]. The lack of linearity was related to some modification of the film structure. At high concentration of glucose, glucose oxidation occurred at the film/solution interface; and for higher glucose concentration, it occurred in a thicker layer of the polypyrrole–GOD film. A similar explanation can be propounded for poly**1**–GOD films. The existence of two different kinetics could be due to different conformations and/or environments for the immobilized enzyme. For high glucose concentration, glucose is transported deeper in the enzymatic film, thus is oxidized in a thicker layer of the poly**1**–GOD film where enzyme molecules are blocked in a polymeric phase which is more reticulated, thus less permeable and less accessible to substrate molecules. A lower K'_M (3.5 mM) value confirms this hypothesis [37].

The apparent Michaelis-Menten constant could also be estimated by considering the substrate concentration at which the electrode response is half the saturation value ($i_{max}/2$). In this case, we found K'_M = 3.8 mM (i_{max} = 25 μA). It should be noted that Eadie-Hofstee plots for various electrodes differing in film composition always showed two straight lines, j_{max} varying from 50 to 210 μA cm^{-2} according to the monomer on enzyme ratio used for their preparation (vide infra).

3.3. Effect of film composition on the electrochemical response of the enzyme electrode. Multilayered structures

Enzyme on monomer ratio

The amperometric response of a GOD electrode depends on several factors including enzyme concentration in the polymer layer, mass transport of the substrates (glucose, O_2) and products (H_2O_2, gluconolactone) through the polymer film, and the kinetics of the enzyme reaction. First, we have investigated the effect of the enzyme on monomer **1** ratio in the pre-adsorbed layer (before polymerization) on the steady-state electrochemical response of the glucose sensor. For these experiments, several en-

Table 2
Effect of GOD/monomer **1** ratio on the response of the enzyme electrode

Entry	Initial composition of the coating [a]		Charge consumed [b] (mC)	Electrode response [c] to 0.2 mM glucose (μA)	Sensitivity (μA mM^{-1})
	GOD/U	**1**/μmol			
1	15	0.19	22	0.46	2.3
2	15	0.12	8	0.81	4.1
3	20	0.12	8	0.70	3.5
4	22	0.14	13.4	0.66	3.3
5	30	0.12	8	0.83	4.2
6	56	0.24	8.8	1.15	5.8
7	68	0.27	8.5	1.31	6.6

[a] Deposited on a 5 mm diameter Pt disc electrode.
[b] Charge consumed during the polymerization of the adsorbed coating.
[c] Measured at 0.5 V in stirred phosphate buffer (pH 7) at 25°C.

zyme electrodes have been prepared by electropolymerization on platinum discs of GOD–**1** coatings of different compositions and their responses towards a low concentration of glucose (0.2 mM) have been studied.

With the lowest GOD to monomer ratio, we have obtained the best electropolymerization, as judged by the high charge consumed during the preparation of the enzymatic films (Table 2, entry 1). Taking into account that the polymerization of a pyrrole group requires 2.3 electrons (this corresponds to the two-electron oxidation of the pyrrole group, plus the oxidation of the pyrrole ring (0.3 electron) in the resulting polymer [32]), it can be estimated that 50% of the monomer **1** initially deposited on the electrode surface has been polymerized. This enzyme electrode gave the lowest current response to glucose (2.3 μA mM^{-1}). This is related to the limitation of the response imposed by diffusional constraints, due to the entrapment of the enzyme in a thick polymer film. Similar observations have been made for poly(pyrrole)–GOD [13] and poly(*N*-methyl pyrrole)–GOD [20] electrodes elaborated by electrochemical polymerization of pyrrole or *N*-methylpyrrole in the presence of GOD. It was observed that the electrode response diminished with increasing film thickness.

Increasing the enzyme to monomer ratio results in a poor electropolymerization, as judged by the weak maximum charge (around 8 mC) which could be consumed, but it increases the sensitivity of the resulting enzyme electrode (Table 2, entry 2). This is probably due to the formation around the enzyme molecules of a thinner polymer film in which the diffusional constraints are minimized. Comparison between enzyme electrodes prepared from similar small amounts of **1** (0.12–0.14 μmol) and increasing amounts of GOD (15, 20, 22 and 30 U: entries 2–5 in Table 2) shows that similar sensitivities to glucose were obtained, from 3.3 to 4.2 μA mM^{-1}. Again, the lowest sensitivity was observed with the enzyme electrode prepared from the larger amount of monomer **1** (0.14 μmol, entry 4). Further increase in the enzyme to **1** ratio inhibits strongly the electropolymerization process, leading to uncertain results mainly as a consequence of the poor mechanical properties of the resulting enzymatic films.

Enzyme electrodes showing the best responses were obtained by increasing in the same proportions the amounts of monomer **1** and enzyme in the pre-adsorbed film (Table 2, entries 6 and 7). Low polymerization charges, close to that measured during the polymerization of thinner monomeric films were also observed. Obviously, the use of higher amounts of both monomer **1** and enzyme allows to retain more enzyme molecules in polymer films which present a good permeability to substrates and products of the enzymatic reaction.

Multilayered structures

The linear part of the calibration curve can be extended by using multilayered films. Discrete layered structures (Scheme 1) have been synthesized by sequential electropolymerization. Fig. 3 shows calibration curves for three different electrodes prepared with the same amount of GOD. As described previously, curve a depicts the electrochemical response to glucose of a regular Pt/poly**1**–GOD electrode, prepared from 20 U of GOD and 0.12 μmol of monomer **1**. A linear relationship is observed for glucose concentrations up to 2.5 mM. The bilayered structure was prepared by electropolymerization of a pure poly**1** layer (prepared with 0.12 μmol of **1**) onto a poly**1**–GOD layer previously prepared from 0.12 μmol of **1** and 20 U of GOD. We have checked that the same amount of GOD was trapped in

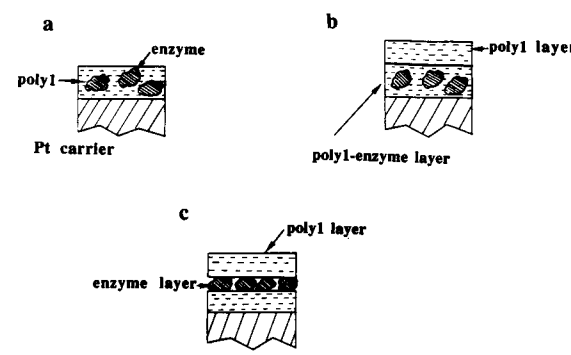

Scheme 1. (a) Monolayer, (b) bilayer and (c) sandwich structures.

the enzymatic films of the mono- and bilayered electrodes. The overlying film is responsible for a lower sensitivity and an increase of the linear part of the calibration curve, up to 4 mM in glucose (curve b). This result is not surprising, since it is well known that the linearity of the response of an enzyme electrode can be extended by means of a specific membrane possessing high diffusion limitation with respect to the substrate and separating the immobilized enzyme layer from the medium [38–40].

Just like for the monolayered electrode, the Eadie-Hofstee plot for the bilayered electrode is characterized by two straight lines, from which were calculated two Michaelis-Menten constants ($K'_M = 26$ and 4.9 mM). These K'_M are higher than those found for the monolayered electrode ($K'_M = 20.2$ and 3.5 mM). It has already been demonstrated that the coating of an enzyme layer with an additional membrane or polymer layer results in an increase of the K'_M [41]. Since the protecting membrane limits the transport of glucose to the enzyme sites, the overall kinetics are controlled by this diffusion process leading to a lower sensitivity, an extended linear response range and a higher K'_M.

Further increase of the linear part of the calibration curve could be achieved with a "sandwich" structure. This film was prepared by spreading and drying a drop of water containing 20 U of GOD on a poly**1** film elaborated from 0.04 μmol of **1**, then covering the enzyme layer with another thin poly**1** film by electropolymerizing 0.16 μmol of **1**. With this arrangement, the sensitivity of the enzyme electrode is lower in comparison with the ones of mono- and bilayer electrodes, but the linear part of the calibration curve is increased up to 5 mM in glucose (curve c). This behaviour may also reflect a more difficult diffusion of glucose to the enzyme sites, due to the presence of the upper poly**1** film which acts as a barrier between the solution and enzyme layer. The decrease of the electrode response can be related to the fact that a fraction of the hydrogen peroxide cannot reach the Pt surface and does not contribute to the current.

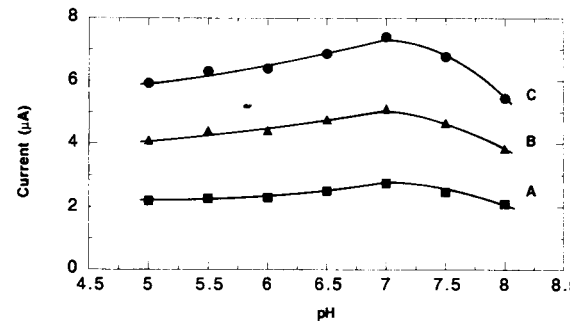

Fig. 7. Effect of the pH on the current response of a Pt/poly**1**–GOD electrode. The response to 1 mM (A), 2 mM (B) and 3 mM (C) glucose was evaluated at 0.7 V/ECS in a phosphate buffer.

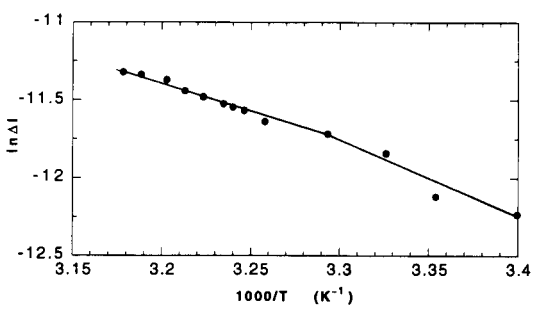

Fig. 6. Arrhenuis-Van't Hoff plot for a glucose oxidase electrode. [Glucose] = 10^{-2} M.

3.4. Effect of the temperature on the response of the enzyme electrode

The effect of the temperature at which the assay was carried out on the response of the GOD electrode to 10 mM glucose, was studied over the range 12–47°C. The current response of the electrode increased gradually from 12 to 47°C, after which the current decreased. The Arrhenius-Van't Hoff plot is characterized by two straight lines intersecting at 28°C (Fig. 6). Such behaviour has been already observed with glucose oxidase [42] and xanthine oxidase [43] electrodes. It has been attributed to the existence of different temperature conformations for the immobilized enzyme. Two activations energies were calculated from the two slopes of the Arrhenius plot and were found to be 44 kJ mol^{-1} (below room temperature) and 31 kJ mol^{-1} (above room tem-

perature). These values compare well with that found (31–50 kJ mol^{-1}) for GOD immobilized in different matrices [13,44,45].

3.5. Effect of the pH on the enzyme electrode response

The effect of the pH on the steady state current response of an electrode was examined from pH 5 to 8 for three different glucose concentrations, i.e. 1, 2 and 3 mM. We have verified that the amperometric current for electrochemical oxidation of hydrogen peroxide at a bare platinum electrode and at a poly1 modified electrode, is pH-independent in the range of our study. As shown in Fig. 7, the Pt/poly1–GOD electrode displayed optimum responses at pH 7. This is quite different to the value of pH 5.6 reported for soluble glucose oxidase [46]. In the present case, the poly1 matrix gives rise to a charged micro-environment that can affect the catalytic behaviour of the enzyme in such a way that the optimal pH is displaced towards a more alkaline value. Such changes in optimal pH have previously been observed for GOD bound to polyacrylic acid and polyacrylamide derivatives [44]. In addition, we have found that poly1 films protect trapped redox anions against changes in the pH of the electrolyte, as demonstrated by the differences in their redox behaviour in solution and in the polymeric phase [31b].

3.6. Shelf life and operational stability of the enzyme electrode

The stability of the Pt/poly1–GOD electrode has been examined for three different experiments which define the lifetime and the operational stability of the electrode. The operational stability was first evaluated by recording over 30 assays the current response to increasing concentrations of glucose in the 0.1 to 2 mM concentration range, which corresponds to the linear part of the calibration curve. We found that the current response on the whole was stable, within 15%. The operational stability was also studied on 18 assays, with glucose concentrations ranging from 0.1 to 1 mM. In this last experiment, each

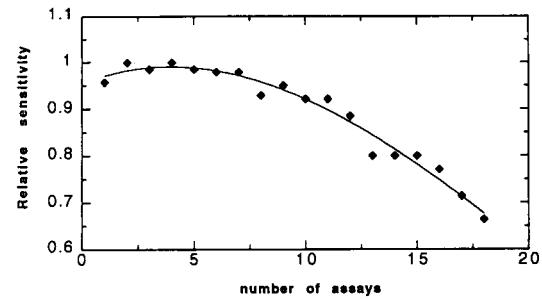

Fig. 8. Operational stability of a Pt/poly1–GOD electrode.

measurement was carried out in a fresh electrolyte. This implied that the enzyme electrode must be preconditioned each time for a few minutes at 0.5 V until a stable background current was achieved, before the addition of glucose. In this case, we found that the electrode has lost 8.5 and 34% of its initial activity after 10 and 18 assays, respectively (Fig. 8). Thus, the first experiment demonstrates that the enzymatic reaction is responsible for a weak deactivation. On the other hand, a larger decrease of the current response to glucose was found when the enzyme electrode was preconditioned before each measurement. This additional deactivation could be due to an electrochemical transformation and/or destruction of the polymeric material.

The lifetime of an electrode was measured by keeping it in a dry box at −18°C for 42 days, measuring the current response to a glucose concentration of 0.2 mM each week. Results have shown that 94% of its initial activity was maintained after two weeks, 72% after three weeks and 47% after 42 days.

3.7. Interferences

A main application of glucose sensors is in the analysis of biological fluids. The electrochemical oxidation of a number of endogenous electroactive substances, e.g., ascorbic acid and uric acid, can interfere at the potential where the hydrogen peroxide is monitored. This is especially true for ascorbic acid (AA), which is extracted and concentrated by the cationic poly1 matrix. AA itself is strongly adsorbed at a Pt electrode and its

oxidation causes slow electrode fouling [47–49]. These phenomena are responsible for a lower and unstable current response of the Pt/poly**1**–GOD electrode to glucose, in the presence of a low concentration of AA (0.1 mM). Several studies have been reported in the literature, where successful elimination of interferents was accomplished either by coating the enzyme layer with a polyanionic layer [41,50,51], or by trapping the enzyme in an over-oxidized polypyrrole film [17].

The addition of AA causes a considerable lowering of the current response of the enzyme electrode. As an example, the current measured at 0.5 V on a regular Pt/poly**1**–GOD electrode with 1 mM glucose is reduced with 40% after the addition of 0.1 mM AA. This interference could be largely minimized by coating the enzyme layer on an underlayer of pure polypyrrole. Then, this bilayered film has been overoxidized. The underlayer of over-oxidized polypyrrole acts as a permselective, antifouling membrane capable of rejecting AA [17]. With this Pt/polypyrrole/poly**1**–GOD electrode, the response to glucose is only decreased with 8% after the addition of 0.1 M AA.

In addition, the response of this electrode is identical with or without uric acid.

3.8. Attempts to prepare miniaturized sensors

Miniaturized glucose sensors are particularly attractive in connection with ex vivo and in vivo clinical applications, including measurements of glucose in small volumes or the monitoring of localized events [52]. Preliminary experiments were undertaken to explore the ability of our immobilization technique to fabricate enzyme microelectrodes. Enzyme layers were coated on 50 μm diameter Pt discs (sealed in 3 mm glass tubes), using the procedure described for 5 mm diameter Pt discs and starting with the deposit of 25 μl of water containing 0.1 μmol of **1** and 12 U of GOD. Satisfactory responses to glucose were observed with these microsensors. Electrode characteristics are equivalent to those of larger sized electrodes, with regard to K'_M and linearity of the calibration curves. It must be emphasized that high current densities to 1 mM glucose were obtained, i.e., up to 54 μA cm^{-2}. This is much higher than the current densities observed on 5 mm diameter electrode, prepared with higher amounts of **1** and enzyme (see Table 1). In a separate experiment, we found that current densities for H_2O_2 oxidation on 5 mm and 50 μm diameter Pt disc electrodes were similar. Thus, the higher current response obtained on the miniaturized sensor could be attributed to a higher glucose transport to the enzyme electrode.

4. Conclusion

This paper demonstrates that a glucose sensor can be prepared by a simple, one-step and controlled procedure, by electropolymerization in an aqueous medium of pre-adsorbed GOD-amphiphilic pyrrole monomer layers. Compared to conventional electropolymerization procedures carried out in an electrolyte containing solubilized enzyme and monomer, this procedure presents several advantages, including enzyme and monomer saving, and determination of both the amount and the activity of the immobilized enzyme. In addition, this procedure allows the construction of multilayered structures to increase the linear part of the calibration curves and to minimize the effect of interferents. Extension of this work to poly(amphiphilic pyrrole) films functionalized by redox groups to achieve mediated electron transfer from the enzyme to the electrode is under way.

5. References

[1] L.C. Clark Jr. and C. Lyons, Ann. N.Y. Acad. Sci., 102 (1962) 29.
[2] J. Wang, Anal. Chem., 63 (1991) 235R.
[3] P.D. Home and K.G.M. Alberti, in A.P.F. Turner, I. Karube and G.S. Wilson (Eds.), Biosensors: Fundamentals and Applications, Oxford University Press, Oxford, 1987, p. 723
[4] S.A. Barker, in A.P.F. Turner, I. Karube and G.S. Wilson (Eds.), Biosensors: Fundamentals and Applications, Oxford University Press, Oxford, 1987, p. 85.
[5] S. Sun, P.H. Ho-Si and D.J. Harrisson, Langmuir, 7 (1991) 727.
[6] B.A. Gregg and A. Heller, Anal. Chem., 62 (1990) 258.

[7] S.E. Wolowacz, B.F.Y. Yon Hin and C.R. Lowe, Anal Chem., 64 (1992) 1541.
[8] N.C. Foulds and C.R. Lowe, J. Chem. Soc., Faraday Trans 1, 82 (1986) 1259.
[9] M. Umana and J. Waller, Anal. Chem., 58 (1986) 2979.
[10] C. Iwakura, Y. Kajiya and H. Yoneyama, J. Chem. Soc., Chem. Commun., (1988) 1019.
[11] S. Yabuki, H. Shinohara and M. Aizawa, J. Chem. Soc, Chem. Commun., (1989) 945.
[12] D. Belanger, J. Nadreau and G. Fortier, J. Electroanal. Chem., 274 (1989) 143.
[13] G. Fortier, E. Brassard and D. Belanger, Biosensors Bioelectron., 5 (1990) 473.
[14] P. Janda and J. Weber, J. Electroanal. Chem., 300 (1991) 119.
[15] Y. Kajiya, H. Sugai, C. Iwakura and H. Yoneyama, Anal. Chem., 63 (1991) 49.
[16] M. Marchesiello and E.M. Genies, Electrochim. Acta, 37 (1992) 1987.
[17] D. Centonze, A. Guerrieri, C. Malitesta, F. Palmisano and P.G. Zambonin, Fresenius' J. Anal. Chem., 342 (1992) 729.
[18] J.M. Hämmerle, W. Schuhmann and H.L. Schmidt, Sensors Actuators B, 6 (1992) 106.
[19] Z. Sun and H. Tachikawa, Anal. Chem., 64 (1992) 1112.
[20] P.N. Bartlett and R.G. Whitaker, J. Electroanal. Chem., 224 (1987) 37.
[21] N.C. Foulds and C.R. Lowe, Anal. Chem., 60 (1988) 2473.
[22] P.N. Bartlett, Z. Ali and V. Eastwick-Field, J. Chem. Soc., Faraday Trans., 88 (1992) 2677.
[23] C.G.J. Koopal, M.C. Feiters, R.J.M. Nolte, B. de Ruiter and R.B.M. Schasfoort, Bioelectrochem. Bioenerg., 29 (1992) 159.
[24] H. Schinohara, T. Chiba and M. Aizawa, Sensors Actuators, 13 (1988) 79.
[25] C. Malitesta, F. Palmisano, L. Torsi and P.G. Zambonin, Anal. Chem., 62 (1990) 2735.
[26] M. Shaolin, X. Huaiguo and Q. Bidong, J. Electroanal. Chem., 304 (1991) 7.
[27] P.N. Bartlett, P. Tebbutt and C.H. Tyrrel, Anal. Chem., 64 (1992) 138.
[28] P.C. Pandey, J. Chem. Soc., Faraday Trans. 1, 84 (1988) 2259.
[29] L. Coche-Guérente, S. Cosnier, C. Innocent, P. Mailley, J.-C. Moutet, R. Morelis, B. Leca and P. Coulet, Electroanalysis, 5 (1993) 647.
[30] S. Cosnier and C. Innocent, J. Electroanal. Chem., 328 (1992) 361.
[31] (a) L. Coche-Guérente, A. Deronzier, B. Galland, P. Labbé, J.-C. Moutet and G. Reverdy, J. Chem. Soc., Chem. Commun., (1991) 386; (b) L. Coche-Guérente, A. Deronzier, B. Galland, J.-C. Moutet, P. Labbé, G. Reverdy, Y. Chevalier and J. Amhrar, Langmuir, in press.
[32] G.K. Chandler and D. Pletcher, Electrochemistry, 10 (1985) 117.
[33] C.G. Koopal, B. de Ruiter and R.J.M. Nolte, J. Chem. Soc., Chem. Commun., (1991) 1691.
[34] S. Cosnier, A. Deronzier and J.F. Roland, J. Electroanal. Chem., 285 (1990) 133.
[35] P.N. Bartlett and D.J. Caruana, Analyst, 117 (1992) 1287.
[36] D. Belanger, J. Nadreau and G. Fortier, Electroanalysis, 4 (1992) 933.
[37] T. Tatsuma and T. Watanabe, Anal. Chim. Acta, 242 (1991) 85.
[38] W.J. Aston, in A.P.F. Turner, I. Karube and G.S. Wilson (Eds.), Biosensors: Fundamentals and Applications, Oxford University Press, Oxford, 1987, p. 276.
[39] T. Schalkhammer, E. Mann-Buxbaum, F. Pittner and G. Urban, Sensors Actuators B, 4 (1991) 273.
[40] P. Vadgama and P.W. Crump, Analyst, 117 (1992) 1657.
[41] L. Gorton, H.I. Karan, P.D. Hale, T. Inagaki, Y. Okamoto and T.A. Skotheim, Anal. Chim. Acta, 228 (1990) 23.
[42] B.A. Gregg and A. Heller, J. Phys. Chem., 95 (1991) 5976.
[43] E. Lorenzo, E. Gonzales, F. Pariente and L. Hernandez, Electroanalysis, 3 (1991) 319.
[44] G.G. Guilbault and G.L. Lubrano, Anal. Chim. Acta, 64 (1973) 439.
[45] P. Coulet, R. Sternberg and D.R. Thévenot, Biochim. Biophys. Acta, 612 (1980) 317.
[46] B.E.P. Swoboda and V. Massey, J. Biol. Chem., 240 (1965) 2209.
[47] P. Karabinas and D. Jannakoudakis, J. Electroanal. Chem., 160 (1984) 159.
[48] K. Takamura and M. Sakamoto, J. Electroanal. Chem., 113 (1980) 273.
[49] F. Palmisano and P.G. Zambonin, Anal. Chem., 65 (1993) 2690.
[50] D.J. Harrisson, R.F.B. Turner and H.P. Bates, Anal. Chem., 60 (1988) 2002.
[51] C.J. Chen, C.C. Liu and R.F. Savinell, J. Electroanal. Chem., 348 (1993) 317.
[52] D. Bindra, Y. Zhang, G.S. Wilson, R. Sternberg, D.R. Thévenot, D. Moatti and G. Reach, Anal. Chem., 63 (1991) 1692.

ELSEVIER

Analytica Chimica Acta 289 (1994) 155–162

ANALYTICA CHIMICA ACTA

Electrochemical biosensors for glucose, lactate, urea, and creatinine based on enzymes entrapped in a cubic liquid crystalline phase

Valdemaras Razumas *[,a], Julija Kanapieniené [a], Tommy Nylander [b], Sven Engström [b], Kåre Larsson [b]

[a] *Institute of Biochemistry, Mokslininku 12, 2600 Vilnius-MTP, Lithuania*
[b] *Department of Food Technology, Chemical Center, POB 124, S-221 00 Lund, Sweden*

(Received 20th August 1993; revised manuscript received 25th November 1993)

Abstract

A novel method to construct enzyme-based biosensors, where the enzyme is entrapped in a lipid matrix (cubic liquid crystalline phase) is presented. The cubic phases were made of monoolein (1-monooleyl-glycerol) and 35% (w/w) of water-based enzyme solutions. The biocatalytic layers of the sensors consisted of a thin layer of the cubic phase with entrapped enzyme, which was coated with a dialysis membrane. The idea was used to construct and investigate the performance of amperometric β-D-glucose and L-lactate, and pH-sensitive urea and creatinine bioelectrodes based on glucose oxidase, lactate oxidase, urease, and creatinine deiminase. The amperometric enzyme electrodes generate an anodic biocatalytic current due to the oxidation of H_2O_2 at the Pt electrode. Using the urease- and creatinine deiminase-based pH electrodes, proton consumption in the enzymatic reactions is measured. The data for the amperometric sensors are presented on the influence of substrate concentration, potential, pH, and temperature upon the electrodes. Urease- and creatinine deiminase-pH electrodes are tested in relation to the substrate and enzyme concentration, and the buffer capacity. Results of the electrodes long-term stability are discussed in relation to the structural features of the cubic phase and the enzyme.

Key words: Amperometry; Potentiometry; Biosensors; Enzyme electrodes; Glucose; Lactate; Urea; Creatinine; Entrapment; Cubic phase; Monoolein

1. Introduction

The pioneering work of Clark and Lyons [1] stimulated a tremendous growth in the development of the enzyme-based electrochemical sensors. A comprehensive analysis regarding the construction and applications of the electrochemical biosensors has recently been extensively reviewed [2–4]. Undoubtedly, the way the enzyme layer is formed on the surface of the transducer is of paramount importance in the construction of biosensors. Among the methods most generally employed are the entrapment of the enzyme be-

* Corresponding author.

hind a membrane or within a gel, the covalent glutaraldehyde-mediated cross-linking with a supporting membrane [5]. Direct attachment or adsorption on the transducer surface is also possible [5]. Some methods of immobilisation work well with certain enzymes, but not with others. For instance, oxidoreductases are very sensitive and usually the immobilised enzymes have the specific activities that are 5–20% of that in solution [4]. Therefore, the development of efficient new methods of immobilisation must always be given much attention.

In this paper we present the functioning of electrochemical biosensors where the enzymes are entrapped in a thermodynamically stable cubic liquid crystalline phase composed of monoolein and water.

Cubic lipid–water phases form remarkable structures with perfect long-range three-dimensional periodicity, although the molecules exhibit a dynamical disorder at atomic distances, like that in liquids [6]. Monoolein is an example of a lipid forming such a phase, which can contain up to 40% (w/w) of water [7]. It is transparent, very viscous, and can coexist in equilibrium with excess of water. Due to the short-range disorder, these phases are called liquid crystals, although they really are plastic crystals. The cubic phase is assumed to be bicontinuous [6,8], i.e. there are congruent networks of both water and lipid channels. Monoolein has been shown to form a cubic phase in the presence of proteins with a wide variation in size [9]. It was proposed that the protein molecules are located in the water medium, i.e. in the water channel system of the cubic structure [9]. They were also found to keep their native structure, as proved by thermal analysis of the entrapped proteins as well as measurements of the enzymatic activity [10]. The stability of the enzyme has even been shown to increase upon the entrapment in the cubic phase, for instance, in case of glucose oxidase when it is entrapped in a cubic phase based on an ethoxylated fatty alcohol $C_{16-18}(OCH_2CH_2)_{80}OH$ [11].

This earlier study also provides an unique example of the analytical application of an enzyme entrapped in the cubic phase. A cubic phase based on the ethoxylated fatty alcohol and 50% (w/w) of a buffer solution with glucose oxidase, peroxidase and dianisidine was prepared. The pre-formed cubic phase was applied in six hollows of a PVC slab and a known volume of glucose solution was then added on the top of the cubic phase. The aqueous solution swelled rapidly into the cubic phase and the reaction started, as shown by a reddish-brown colour appearing in the cubic phase.

The purpose of the present study is to explore the possibility to use monoolein-based cubic phases, containing glucose oxidase (GO), lactate oxidase (LO), urease, and creatinine deiminase (CD), to prepare the biosensors for the determination of β-D-glucose, L-lactate, urea and creatinine, respectively. The first two enzyme containing cubic phases were applied on the surface of platinum electrodes for the amperometric determination, whereas the urease- and CD-based cubic phases were applied on flat pH electrode for potentiometric determination.

2. Experimental

2.1. Reagents and solutions

Glucose oxidase (GO), type X-S from *Aspergillus niger* (E.C. 1.1.3.4), lyophilised, with the specific activity of ca. 100–150 U mg^{-1} lyophilisate, was a product of Sigma. L-Lactate oxidase (LO) from *Pediococcus* sp. (E.C. 1.1.3.2), lyophilised, with the specific activity of ca. 20 U mg^{-1} lyophilisate, was obtained from Boehringer Mannheim. Lyophilised Jack Bean urease (E.C. 3.5.1.5), type IX, with specific activity of 53 U mg^{-1} lyophilisate, was obtained from Sigma. Creatinine deiminase (CD) from *Corynebacterium lilium* (E.C. 3.5.4.21), lyophilised, with the specific activity of ca. 45 U mg^{-1} lyophilisate, was a product of Boehringer Mannheim. D-(+)-Glucose, L-(+)-lactic acid, urea, creatinine (Sigma) and monoolein (glycerol, 1-mono(9-octadecenoate)) (Grindsted, Denmark) were used as received. Glucose solutions were stored overnight to allow equilibration of α- and β-anomers. All other chemicals used were of analytical grade.

A 10 mM phosphate buffer solution, containing 0.1 M KCl and 1 mM EDTA, served as a supporting electrolyte in studies of the glucose-, lactate- and urea-sensitive electrodes. Phosphate buffer (0.1 M, pH 8.7), containing 0.1 M KCl and 1 mM EDTA, was used in case of the CD-based system. Water used was ion-exchanged, distilled and passed through a Milli Q water purification system (Millipore).

2.2. Preparation of the cubic phases with entrapped enzymes

The cubic phases with entrapped enzymes were prepared in glass ampoules at 38°C by slow addition of 35% (w/w) of the aqueous GO or standard buffer-based LO, urease, and CD solutions on the top of melted monoolein. Samples were sealed and allowed to equilibrate at room temperature for a minimum of 24 h (or until no change could be detected when viewed in the polarising microscope).

The prepared cubic phases contained 0.07, 0.875, 0.42–3.5, and 0.7–8 mg of GO, LO, urease, and CD per gram of monoolein, respectively.

A one-phase region of the cubic phase is simpler to identify than other mesophases. This phase is completely transparent, very viscous and optically isotropic. Still it was checked by centrifugation (8000 *g* during 8 h) that no phase separation can be achieved especially that no excess protein solution was present.

2.3. Preparation of the enzyme electrodes

The transducers in the glucose- and lactate-sensitive biosensors were the platinum discs (0.3 cm^2) soldered in the glass tubes. The surfaces of the electrodes were polished using a polishing kit PK-4 (BAS). After thoroughly rinsing with pure water the electrodes were dried with a stream of nitrogen gas, and finally plasma cleaned for 5 min in low pressure air (0.3 Torr), using a radiofrequency glow discharge apparatus Harrick PDC-3XG (Harrick Sci. Co.).

The combined flat pH-glass electrode (Metrohm) was used for the construction of the urease- and CD-based biosensors. The electrode was rinsed with pure water and dried with filter paper.

Thin layers of the viscous cubic phases with entrapped enzymes were applied on to the surfaces of the Pt or flat pH electrodes over which a ca. 0.1-mm thick nylon netting had been stretched. The layer of the cubic phase was subsequently covered with 30-μm thick dialysis membrane (MW cut-off 6000–8000, Spectrum Medical Industries). Both nylon netting and dialysis membranes were held in place by O-rings.

After preparation and between experiments, the electrodes were stored in the standard electrolyte solution at room temperature.

2.4. Electrodes operation and procedure

Amperometric measurements were performed with VersaStat potentiostat–galvanostat (Princeton Applied Research) in a thermostated glass cell (20 cm^3) using a three-electrode circuit with a platinum wire coil (surface area of ca. 2 cm^2) as an auxiliary electrode and a saturated calomel electrode, SCE, (Radiometer) as a reference. All potentials (E) in the text are referred to the SCE.

To record the current of glucose or lactate oxidation, the enzyme electrode was immersed into the buffer solution and a fixed potential was applied to the electrode until a constant residual current was established. After this pretreatment a solution of glucose or lactate in buffer was introduced into the cell and the current increase was recorded. The catalytic current (I_{cat}) was estimated by the difference between the electrode current in the presence of substrate and that which is established in the blank buffer solution.

The pH-glass electrode coated with the urease- or CD-based cubic phase was connected to a pH-meter PHM82 (Radiometer) supplied with an x–t recorder. The above-mentioned glass cell was used. The potentiometric response of the electrode (ΔE) was estimated by the difference between the E values in the presence of substrate and that which is established in the pure buffer solution. All potential readings were expressed in terms of a pH by using the formula $\Delta E(\text{mV}) = -59.16\ \Delta\text{pH}$.

The solutions were mixed with a magnetic disc stirrer (rotation speed ca. 300 rpm).

3. Results and discussion

3.1. Amperometric β-D-glucose- and L-lactate-sensitive electrodes

The catalytic oxidation of β-D-glucose at the Pt electrode covered with the layer of the GO-containing cubic phase (GO-CP-Pt) proceeds at potentials (E) higher than 0.2 V (Fig. 1). The voltammogram exhibits constant catalytic current (I_{cat}) at $E > 0.45$ V (Fig. 1, curve 2). The catalytic oxidation of L-lactate versus E of the LO-CP-Pt electrode is similar to that described for the GO-CP-Pt electrode. On the basis of these data a potential of 0.6 V was chosen to study the other characteristics of the enzyme electrodes. Under the condition mentioned, the residual current makes up about 14% of the total oxidation current in the 10 mM solutions of glucose or lactate. The electrodes show a fairly rapid response time where 90% of the steady-state current was reached within ca. 2 min.

Figs. 2 and 3 present the dependencies of a steady-state catalytic current of the GO-CP-Pt and LO-CP-Pt electrodes on the concentration of

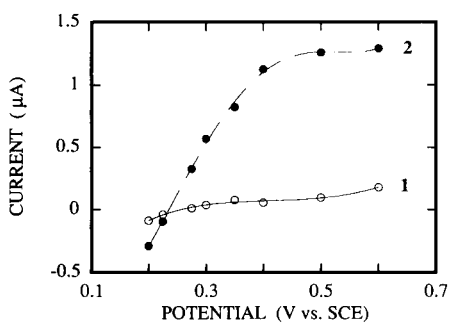

Fig. 1. Dependence of the residual current (1) and steady-state current of D-glucose oxidation (2) on the potential of the Pt electrode coated with the monoolein-based cubic phase with entrapped glucose oxidase (70 ng enzyme per gram of monoolein). D-Glucose concentration was 10 mM in 10 mM phosphate buffer (pH 7.0), containing 0.1 M KCl and 1 mM EDTA, 25°C. Disc stirrer rotation speed was ca. 300 rpm, geometric surface area of the electrode was 0.3 cm^2.

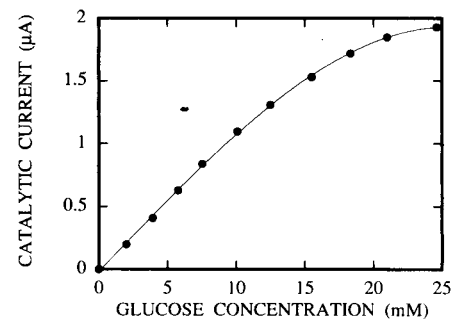

Fig. 2. Catalytic steady-state current calibration curve for the glucose oxidase-based Pt electrode at 0.6 V vs. SCE, pH 7.0 and 25°C. Other conditions are the same as in Fig. 1.

D-glucose and L-lactate, respectively. The measurements were carried out in air-saturated solutions. As may be seen from the data in Figs. 2 and 3, the GO-CP-Pt and LO-CP-Pt electrodes gave rather good linear I_{cat} responses up to 12 mM D-glucose and 10 mM L-lactate. The linear portions can be expressed by the following equations, respectively:

$$I_{cat}(\mu A) = 0.11(\pm 0.01)[S](mM),\ r = 0.9991 \quad (1)$$

$$I_{cat}(\mu A) = 0.13(\pm 0.01)[S](mM),\ r = 0.9994 \quad (2)$$

where [S] is the bulk concentration of substrate (D-glucose or L-lactate) and r is the correlation coefficient.

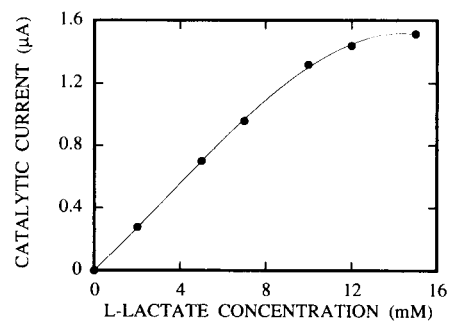

Fig. 3. Catalytic steady-state current calibration curve for the L-lactate oxidase-based Pt electrode at 0.6 V vs. SCE, pH 7.0 and 25°C. The Pt electrode surface was coated with the monoolein-based cubic phase containing 875 ng enzyme per gram of monoolein. Other conditions are the same as in Fig. 1.

The effect of pH on the response of the glucose- and lactate-sensitive electrodes was investigated over the clinically relevant range pH 5–8. The steady-state catalytic currents of the GO-CP-Pt and LO-CP-Pt electrodes are only slightly dependent on pH, with dI_{cat}/dpH of 41(±19) and −60(±20) nA, respectively.

Fig. 4 shows the influence of temperature on the response of the GO-CP-Pt ([S] = 10 mM) and LO-CP-Pt ([S] = 5 mM) electrodes. In case of the GO-CP-Pt electrode, an Arrhenius plot of the data (ln I_{cat} versus $1/T$, where T is the absolute temperature) gives an apparent activation energy (E_a^{app}) equal to 15(±2) kJ mol^{-1}. As seen from Fig. 4 (curve 2), a minor decrease in I_{cat} of the LO-CP-Pt electrode is evident above 25°C. However, an Arrhenius plot of the data in the range 16–25°C gives E_a^{app} the value of about 19 kJ mol^{-1}. Interestingly, similar activation energies (16–21 kJ mol^{-1}) are typical for the diffusion processes in aqueous media [12].

The LO-CP-Pt electrode displayed significantly higher long-term stability than the GO-CP-Pt electrode, when stored in the standard buffer solution at room temperature (Fig. 5). The response of the LO-CP-Pt electrode retained more than 85% of the initial value after two months of storage, while the I_{cat} value of the GO-CP-Pt electrode was reduced to 18% after two weeks. However, it should be noted that if the GO-containing cubic phase was stored separately in a sealed glass ampoule at room temperature for 18 days, 85% of the initial activity was retained.

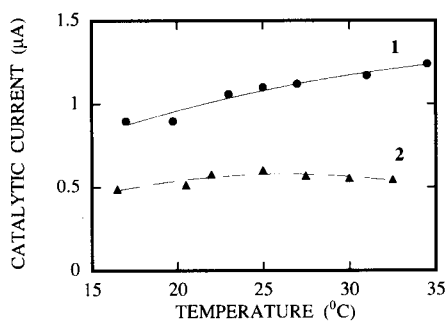

Fig. 4. Effect of temperature on the catalytic steady-state current of the glucose oxidase- (1) and L-lactate oxidase-based (2) electrodes at 0.6 V vs. SCE and pH 7.0. D-Glucose and L-lactate concentrations were 10 and 5 mM, respectively. Other conditions are the same as in Figs. 1 and 3.

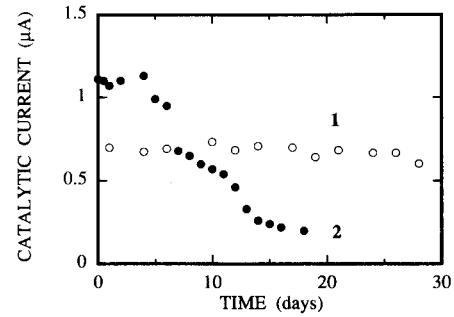

Fig. 5. Long-term stability of the L-lactate oxidase- (1) and glucose oxidase-based (2) electrodes at room temperature. Other conditions are the same as in Fig. 4.

From the above results it is clear that the biosensors presented serve as examples of "unmediated amperometric enzyme electrodes" [4]. Their action can be explained on a basis of the following reactions:

$$S + O_2 \xrightarrow{GO(LO)} P + H_2O_2 \quad (3)$$

$$H_2O_2 \xrightarrow{Pt} O_2 + 2H^+ + 2e^- \quad (4)$$

where S is the substrate, and P is gluconic acid or pyruvate. The anodic response currents of both biosensors are associated with the amperometric detection of H_2O_2.

Fairly long linear calibration ranges, minimal sensitivity to change in pH and temperature mean that the electrodes operate in the diffusion mode. Long-term stability of the LO-CP-Pt electrode also supports this conclusion. However, in this context, a fairly rapid decrease of the GO-CP-Pt electrode response is somewhat inconsistent. It is not improbable that the observed result is determined by the dimensions of the enzyme molecules. The molecular weight of GO is about two times higher than that of LO (160 kDa[13] and 80 kDa [14], respectively). Considering the relatively rigid structural organisation of the cubic phases [6–8], the incorporation of large enzyme molecules (e.g. glucose oxidase) into the water channel system may induce some disorder of the matrix thus decreasing its capacity to fix and to stabilise the enzyme molecules. The following results of the

urease- and CD-based electrodes action provide support for this view.

3.2. Potentiometric urea- and creatinine-sensitive electrodes

Four types of monoolein-based cubic phases, containing 0.42, 0.85, 1.75, and 3.5 mg of urease per gram of monoolein, were prepared in an effort to construct the urea-sensitive pH electrodes. On injection of urea into the pure buffer solution, the increase in pH was monitored by the flat pH-glass electrode covered with the layer of the corresponding urease-containing cubic phase. The response is based on the consumption of protons according to reaction 5:

$$CO(NH_2)_2 + 2H_2O + H^+ \xrightarrow{\text{urease}} HCO_3^- + 2NH_4^+ \quad (5)$$

However, all the electrodes showed a slow response time reaching 90% of the stationary pH in 10–15 min. It is believed that this is because the cubic phase or monoolein penetrates and/or blocks the H^+-sensitive membrane of the pH electrode. Therefore, the response of the urease-based pH electrodes was measured at $t = 3$ min after the substrate sample was injected.

The calibration graphs for the cubic phase-based urea-sensitive electrodes, containing different amounts of urease in the matrix, are shown in Fig. 6 (curves 1–4). Over the whole urea concentration range the calibration curves are like Michaelis-Menten dependence, and apparent kinetic parameters (ΔpH_{max} and K_m^{app}) can be calculated.

The electrode sensitivity ($\Delta pH_{max}/K_m^{app}$) and ΔpH_{max} depend on the amount of urease entrapped in the cubic phase. For the electrodes, containing 0.42, 0.85, 1.75, and 3.5 mg of enzyme per gram of monoolein, the $\Delta pH_{max}/K_m^{app}$ values are equal to $14(\pm 7)$, $20(\pm 6)$, $52(\pm 21)$ and $97(\pm 19)$ M^{-1}, respectively. The ΔpH_{max} values for the corresponding electrodes equal $0.11(\pm 0.04)$, $0.33(\pm 0.14)$, $0.74(\pm 0.47)$ and $1.62(\pm 0.07)$. The values obtained suggest that the parameters $\Delta pH_{max}/K_m^{app}$ and ΔpH_{max} are almost directly proportional to the amount of urease in the cubic phase.

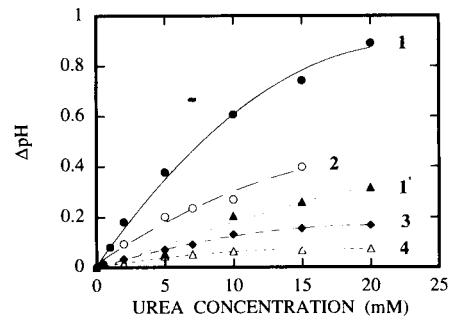

Fig. 6. Dependence of urease-based pH electrode response on urea concentration in 10 mM phosphate buffer (pH 7.4), containing 0.1 M KCl and 1 mM EDTA, 25°C. Enzyme content in the monoolein-based cubic phase (mg per gram of monoolein): (1, 1') 3.5, (2) 1.75, (3) 0.85 and (4) 0.42. Curve (1'), calibration data for the electrode (1) after one day of operation. Response was determined at $t = 3$ min after injection of urea sample. Disc stirrer rotation speed was ca. 300 rpm.

It is important to test to what extent the buffer capacity of the solution (β) would diminish the response of the urease-based pH electrodes since this could severely restrict the wider applicability of such systems. The pH response as a function of β of the phosphate-based buffer solution was therefore tested using the urea-sensitive pH electrode, containing 1.75 mg urease per gram of monoolein. The results can be expressed by the following equation:

$$\Delta pH = 0.391(\pm 0.014) - 0.043(\pm 0.003)\beta(\text{mM}), \quad r = 0.9964,\ n = 4 \quad (6)$$

(n is the number of datapoints used for the fit.) Thus a high value of β is clearly undesirable.

Three types of monoolein-based cubic phases, containing 0.7, 1.4, and 8 mg of CD per gram of monoolein, were prepared in an effort to construct the creatinine-sensitive pH electrodes. The response (ΔpH) of the CD-based pH electrodes was measured at $t = 3$ min after the substrate sample was injected. It is based on the consumption of protons according to reaction 7:

$$\text{Creatinine} + H_2O + H^+ \xrightarrow{\text{CD}} N\text{-Methylhydantoin} + NH_4^+ \quad (7)$$

The creatinine-sensitive electrodes, containing 0.7, 1.4, and 8 mg of CD per gram of monoolein,

gave linear responses between 0.05 and 2 mM creatinine, which is the clinically relevant range [15]. The resulting linear fit to the experimental data (not shown) can be expressed by the following equations, respectively:

$$\Delta pH = 0.022(\pm 0.001)[S](mM),\ r = 0.9989\ n = 4 \quad (8)$$

$$\Delta pH = 0.044(\pm 0.002)[S](mM),\ r = 0.9943\ n = 4 \quad (9)$$

$$\Delta pH = 0.068(\pm 0.002)[S](mM),\ r = 0.9975\ n = 5 \quad (10)$$

where [S] is the bulk concentration of creatinine.

According to Eqs. 8 and 9 the slopes of the calibration plots for the creatinine-sensitive electrodes, containing 0.7 and 1.4 mg of enzyme per gram of monoolein, are directly proportional to the amount of creatinine deiminase in the cubic phase. However, the slope increased only by a factor of 1.6 when the amount of CD in the cubic phase was increased from 1.4 to 8 mg per gram of monoolein (Eqs. 9 and 10). The change of the electrode action mechanism from kinetic to diffusion mode is the most probable reason of this effect.

The long-term stability of the urea- and creatinine-sensitive electrodes, containing 3.5 and 8 mg of enzyme per gram of monoolein, respectively, is shown in Fig. 7.

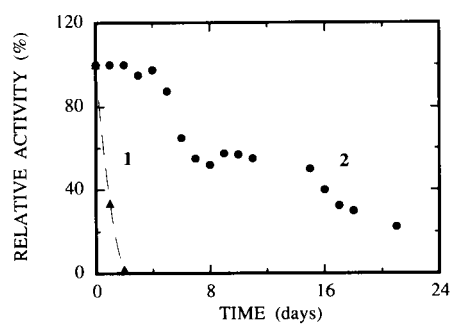

Fig. 7. Long-term stability of the urease- (1) and creatinine deiminase-based (2) pH electrodes at room temperature. Enzyme content in the monoolein-based cubic phase (mg per gram of monoolein): (1) 3.5 and (2) 8. Urea concentration was 10 mM in 10 mM phosphate buffer (pH 7.4) containing 0.1 M KCl and 1 mM EDTA. Creatinine concentration was 1 mM in 0.1 M phosphate buffer (pH 8.7) containing 0.1 M KCl and 1 mM EDTA. Other conditions are the same as in Fig. 6.

The urea-sensitive pH electrodes are not nearly so stable as the amperometric glucose-, lactate-, or creatinine-sensitive electrodes. For instance, curve 1′ in Fig. 6 shows the calibration data for the electrode containing 3.5 mg urease per gram of monoolein after one day of operation. The sensitivity $\Delta pH_{max}/K_m^{app}$ was decreased by a factor of 4.5. There was practically no response after two days of operation, while the response of the CD-based electrode retained 23% of the initial value after three weeks of storage in the standard buffer solution at room temperature (Fig. 7). The high molecular weight of urease (590 kDa [16]) may be responsible for the low stability of the urea-sensitive electrode, i.e. urease may create more dramatic structural changes of the cubic phase in comparison, say, with creatinine deiminase (200 kDa, as stated by the manufacturer) or glucose oxidase. Furthermore, the hexameric urease molecules [16] may dissociate in the relatively narrow water channels of the cubic phase.

4. Conclusions

The results presented provide an unique example of the electroanalytical applications of enzymes entrapped in the cubic lipid–water phase. The high viscosity of cubic phases with entrapped enzymes enables easy formation of the biocatalytic layers on the transducer surface. The data of the action of the amperometric glucose and lactate, and potentiometric urea and creatinine bioelectrodes demonstrate that the immobilisation of the corresponding enzymes in the cubic phase permits the determination of substrates over a wide range of concentrations. The minimal sensitivity of the amperometric biosensors to change in pH and temperature, together with their comparatively high stability mean that it may be possible to incorporate them in devices with a wide range of applications. Clearly this aim invites further investigation. An additional point to emphasise is that the developed systems will also be available for studying the functioning and interactions of proteins incorporated in highly organised lipid–water structures. This is of imme-

diate interest in terms of the biological relevance of the lipid–water cubic phases [6].

5. Acknowledgements

The authors are indebted to Ronnie Wallin for valuable discussions. Valdemaras Razumas and Julija Kanapienienė gratefully acknowledge the support given by The Royal Swedish Academy of Sciences, The Swedish Institute, and The Nils Hörjel Research Foundation. Tommy Nylander acknowledges the financial support from The Swedish Council for Forestry and Agricultural Research.

6. References

[1] L.C. Clark and C. Lyons, Ann. N.Y. Acad. Sci., 102 (1962) 29.
[2] K. Mosbach (Ed.), Methods in Enzymology, Academic Press, New York, 1988, Vol. 137.
[3] A.P.F. Turner, I. Karube and G.S. Wilson (Eds.), Biosensors: Fundamentals and Applications, Oxford University Press, New York, 1987.
[4] A.E.G. Cass (Ed.), Biosensors. A Practical Approach, Oxford University Press, New York, 1990.
[5] K. Mosbach (Ed.), Methods in Enzymology, Academic Press, New York, 1987, Vol. 135.
[6] K. Larsson, J. Phys. Chem., 93 (1989) 7304.
[7] S.T. Hyde, B. Ericsson, S. Andersson and K. Larsson, Z. Kristallogr., 168 (1984) 213.
[8] K. Fontell, Colloid Polym. Sci., 268 (1990) 264.
[9] B. Ericsson, K. Larsson and K. Fontell, Biochim. Biophys. Acta, 729 (1983) 23.
[10] W. Buchheim and K. Larsson, J. Colloid Interface Sci., 117 (1987) 582.
[11] R. Wallin, S. Engström and C.F. Mandenius, Biocatalysis, 8 (1993) 73.
[12] L.G. Longsworth, J. Phys. Chem., 58 (1954) 770.
[13] S. Nakamura, S. Hayashi and K. Koga, Biochim. Biophys. Acta, 445 (1986) 294.
[14] F. Scheller and F. Schubert, Biosensoren, Akademie-Verlag, Berlin, 1989, p. 127.
[15] G.G. Guilbault and P.R. Coulet, Anal. Chim. Acta, 152 (1983) 223.
[16] N.E. Dixon, C. Gazzola, C.J. Asher, D.S.W. Lee, R.L. Blakeley and B. Zerner, Can. J. Biochem., 58 (1980) 474.

ELSEVIER

Analytica Chimica Acta 289 (1994) 163–167

ANALYTICA CHIMICA ACTA

Investigations on bioanalytical chemistry Part V. Adsorption voltammetry of adenine

Xin Zhao, Wenrui Jin *

Chemistry Department, Shandong University, Jinan 250100, China

Jiangxiong Chen, Zuquan Gao, Funing Wang

Biology Department, Shandong University, Jinan 250100, China

(Received 25th October 1993)

Abstract

The adsorptive and voltammetric behaviour of adenine on a hanging mercury drop electrode was investigated in 0.1 mol/l acetic acid–sodium acetate buffer (pH 3.6). The influences of the preconcentration potential and preconcentration time on the peak current as well as the optimum experimental conditions were discussed. The linear relationship between the peak current and the concentration of adenine was tested. To decrease the detection limit, the 1.5th order derivative technique was used and a detection limit for adenine of 1.8×10^{-9} mol/l was reached when the preconcentration time was only 60 s. This method was applied to determine the adenine content in the hydrolytic product of yeast RNA with satisfactory results.

Key words: Voltammetry; Adenine; Adsorption; Bioanalysis; Nucleic acids; Trace analysis

1. Introduction

The determination of purine and pyrimidine bases is very important in nucleic acid research. Most methods of analysis are based on the absorption of UV light at certain wavelengths [1]. The most suitable concentration range for the UV–spectrophotometric determination of the bases is of the order of magnitude of 10^{-5} mol/l. At lower concentrations, this method is not suitable.

The ability of nucleic bases to yield anodic polarographic currents in an alkaline medium was discovered thirty years ago [2–4]. In 1962, Smith and Elving [5] reported the first systematic and detailed study of the electrochemical reduction of adenine. They found that adenine gives a single, large, pH-dependent and largely diffusion-controlled polarographic wave. Coulometry revealed that six electrons were involved in the complete reduction of adenine, and spectrophotometric and chemical investigation of the production solution revealed that ammonia was pres-

* Corresponding author.

SSDI 0003-2670(93)E0659-U

ent. Dryhurst and Elving [6] studied the cyclic voltammetric behaviour of adenine at a hanging mercury drop electrode (HMDE) and the single, pH-dependent cathodic peak of adenine gave no evidence for reversibility of the electrochemical process. A differential pulse polarographic determination of adenine was used by Temerk and Kamal [7] and a detection limit of 2.2×10^{-6} mol/l was found. Cummings et al. [8] used the same method to determine adenine with a detection limit of 5×10^{-8} mol/l.

Adsorption voltammetry is a newly developed technique for determination of trace and ultratrace metal ions and organic compounds [9–11]. Lower concentrations can be determined by accumulation of the compound at an HMDE before applying voltammetric detection.

In this paper, the adsorption voltammetric characteristic of adenine on an HMDE was studied. The optimum detection conditions were selected. When 1.5th-order derivative adsorption voltammetry was used, a detection limit of 1.8×10^{-9} mol/l was reached when the preconcentration time was only 60 s. The method was used to test the content of adenine in the hydrolytic product of yeast RNA with satisfactory results.

2. Experimental

2.1. Apparatus

A Model 83-2.5 voltammetric analyzer (Ningde Analytical Instrument Factory) coupled with a Model 3086-11 X–Y recorder (Yokogawa Hokuskin) was used in connection with a cell, using potentiostatic control of the electrode potential by means of a three-electrode system, consisting of a Model SH-84 HMDE (Department of Chemistry, Shandong University) as the working electrode, a Pt plate as the counter electrode and an SCE as the reference electrode. The SCE was connected to the analyte via a salt bridge filled with buffer to the same level as in the electrolytic cell. During each determination, the solution was stirred with a PTFE-covered stirring bar, rotated by a Model Lab-Line 1250-2 magnetic stirrer.

2.2. Reagents and solutions

A 1 mg/ml stock solution of adenine was prepared by dissolving an appropriate amount of adenine (> 95%, Shanghai Dongfeng Biochemical Technological Co.) in water and standard solutions were obtained by diluting the stock solution. The stock solution was stored in a refrigerator at 4°C. Sodium acetate (NaOAc) and acetic acid (HOAc) were analytical reagent grade. All solutions were prepared from doubly distilled water.

2.3. Procedure

The supporting electrolyte consisted of 0.1 mol/l NaOAc–HOAc (pH 3.6). The solution was deaerated for 20 min with pure nitrogen. Measurements were made after a preconcentration time, in which the solution was left to rest for a certain time, t_a, and a preconcentration potential, E_a, was applied. The response curve was recorded by scanning the potential from E_a to -1.80 V, with a scan rate of 120 mV/s. Each measurement was performed with a fresh drop. All potentials were measured against the SCE.

3. Results and discussion

3.1. Adsorption characteristics of adenine

The electrocapillary curve of adenine in 0.1 mol/l HOAc–NaOAc buffer (pH 3.6) is shown in Fig. 1. After adenine is added to the buffer, the surface tension of the dropping mercury electrode (DME) decreases resulting in a shorter drop time, because of the adsorption of adenine on the surface of the DME.

In 0.1 mol/l HOAc–NaOAc buffer (pH 3.6), a reduction peak of adenine at -1.18 V can be observed. The voltammograms of the reduction of adenine at different preconcentration times, t_a, are shown in Fig. 2. The peak current increases with increasing t_a. It shows the adsorption of adenine on the HMDE. The faster the scan rate, the larger the peak current of adenine. The relationship between the peak current of adenine and the square root of scan rate is shown

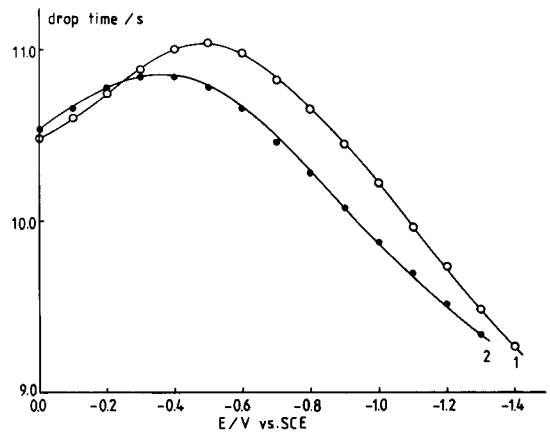

Fig. 1. Electrocapillary curve of adenine in HOAc–NaOAc buffer. (1) 0.1 mol/l HOAc–NaOAc buffer (pH 3.6); (2) 0.1 mol/l HOAc–NaOAc buffer + 4.12×10^{-4} mol/l adenine.

in Fig. 3. The curve has a positive deviation with increasing scan rate, because of the adsorption of adenine on the HMDE.

The relationship between the adsorption peak current of adenine and the preconcentration potential, E_a, is shown in Fig. 4. The peak currents are different at different E_a, which is characteristic for organic materials adsorbed on the surface of the HMDE.

3.2. Optimum experimental conditions

The adsorption/reduction voltammograms of adenine in three different solutions are studied. In 0.1 mol/l NH_3–NH_4Cl buffer (pH 8.9), no reduction peak of adenine on the HMDE can be observed. This confirms that the non-protonated form of adenine is electrochemically irreducible, as Ref. 5 has suggested. In both citric acid–Na_2HPO_4 and HOAc–NaOAc buffer, reduction peak of adenine at around -1.20 V can be observed. The peak potentials of adenine tested in these two solutions are summarized in Table 1. The relationship between the peak current of adenine and the pH of HOAc–NaOAc buffer is shown in Fig. 5. When the pH is between 3.2 to 3.6, a higher peak current can be obtained. HOAc–NaOAc buffer of pH 3.6 is selected for subsequent experiments.

3.3. Analytical application

A linear relationship between the reduction peak current and the concentration of adenine can be obtained in the concentration range of 4.3×10^{-8}–7.6×10^{-7} mol/l for $E_a = -0.70$ V, $v = 120$ mV/s, and $t_a = 30$ s by adsorption voltammetry on the HMDE. When $t_a = 60$ s, the detection limit is 2.2×10^{-8} mol/l. The deviation, calculated from 10 successive measurements of 4.34×10^{-7} mol/l adenine, is $\pm 2.0\%$.

It has been proved that a 1.5th (or 2.5th) order derivative technique has the advantage of further

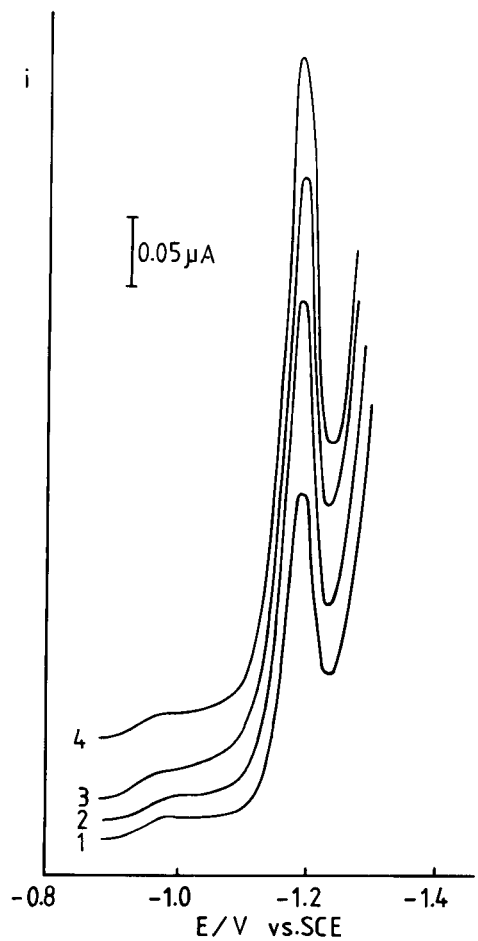

Fig. 2. Adsorption voltammograms of adenine at different preconcentration times, t_a: (1) 0; (2) 30; (3) 60; (4) 120 s. 0.1 mol/l HOAc–NaOAc buffer (pH 3.6), 4.34×10^{-7} mol/l adenine, $E_a = -0.70$ V, $v = 120$ mV/s.

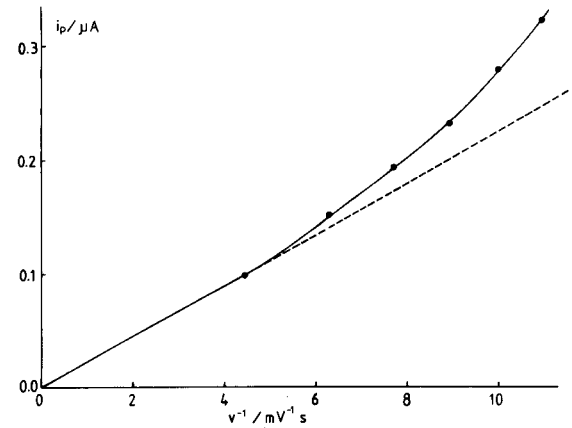

Fig. 3. Relationship between the peak current of adenine and square root of scan rate. Conditions as in Fig. 2.

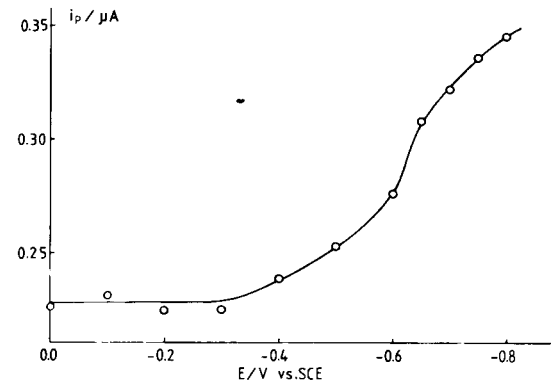

Fig. 4. Relationship between the peak current of adenine and pre-concentration potential. $t_a = 30$ s, other conditions as in Fig. 2.

improvement of the resolution and to increase sensitivity in comparison to conventional linear sweep voltammetry for both the solution phase and the amalgam phase [12–14]. In our previous studies, the theory of 1.5th or 2.5th order derivative adsorption voltammetry has been derived [15] and the technique has been applied to adsorptive voltammetric measurements to increase sensitivity [16,17]. In this work, the 1.5th-order derivative technique is used. Voltammograms of the normal curve and the 1.5th-order derivative curve tested at the same concentration of adenine are shown in Fig. 6. The peak-to-peak e'_{pp} value, obtained by 1.5th-order derivative adsorption voltammetry is much higher than the value of the peak current, i_p, by normal adsorption voltammetry. Using this technique, the concentration of adenine is in agreement with e'_{pp} in the range of 2.2×10^{-8}–1.7×10^{-7} mol/l for $E_a = -0.70$ V, $v = 100$ mV/s and $t_a = 30$ s. When $t_a = 60$ s, the limit of detection is 1.8×10^{-9} mol/l. The deviation calculated from ten successive measurements of 6.52×10^{-8} mol/l adenine is ±5.1%.

Samples of pure yeast RNA (20.0 mg) and 5 ml HCl (1 mol/l) were put in a sealed glass ampoule. After heating in a boiling water bath for 80 min, the solution were transferred into a 25-ml

Table 1
Reduction peak currents and peak potentials of adenine in Na_2HPO_4–citric acid and HOAc–NaOAc buffer ($t_a = 30$ s, other conditions as in Fig. 2)

pH	Na_2HPO_4–citric acid buffer (0.2 mol/l)		HOAc–NaOAc buffer (0.1 mol/l)	
	i_p (μA)	E_p (V)	i_p (μA)	E_p (V)
2.2	0.110	−1.20	0.235	−1.05
2.6	0.092	−1.25	0.253	−1.09
3.2	0.152	−1.29	0.322	−1.12
3.6	– [a]	– [a]	0.322	−1.20
3.8	– [a]	– [a]	0.244	−1.24
4.0	– [a]	– [a]	0.193	−1.25
4.2	– [a]	– [a]	0.175	−1.26
4.6	– [a]	– [a]	– [a]	– [a]

[a] The peak was covered by discharge peak of buffer.

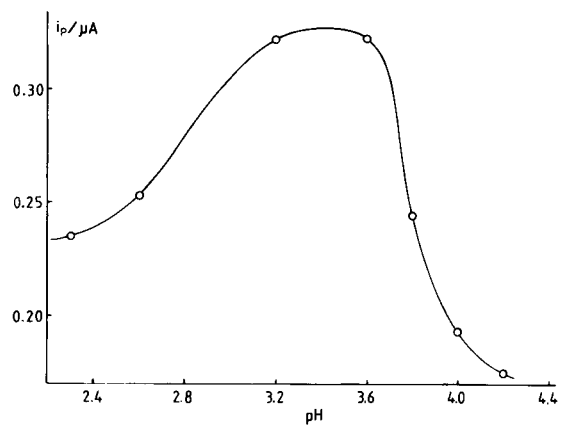

Fig. 5. Relationship between the peak current of adenine and the pH of buffer solution. $t_a = 30$ s, other conditions as in Fig. 2.

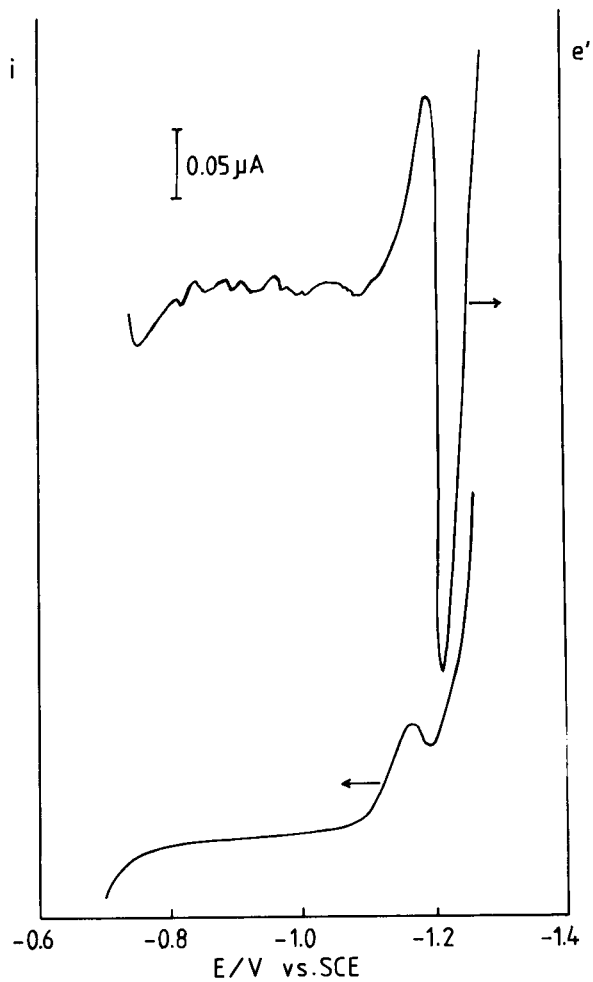

Fig. 6. Linear sweep adsorption voltammogram of adenine and its 1.5th-order derivative curve. 4.34×10^{-8} mol/l adenine, $t_a = 30$ s, other conditions as in Fig. 2.

flask and diluted to the mark with water. 10 μl of the solution was added to 25 ml HOAc–NaOAc buffer (pH 3.6). Cathodic adsorption voltammetry was applied and the standard addition method was used to determine the content of adenine in the hydrolytic product of yeast RNA. A result of 23.8% was obtained which coincides with the standard content of 25.4% reported in the literature.

4. References

[1] G.H. Beaven, E.R. Holiday and E.A. Johnson, in E. Chargaff and J.N. Davidson (Eds.), The Nucleic Acids, Academic Press, New York, 1955, p. 493.
[2] O. Manousek and P. Zuman, Chem. Listy, 49 (1955) 668.
[3] E. Palacek, Naturwissenschaften, 45 (1958) 186.
[4] E. Palacek, Collect. Czech. Chem. Commun., 25 (1960) 2283.
[5] D.L. Smith and P.J. Elving, J. Am. Chem. Soc., 84 (1962) 1412.
[6] G. Dryhurst and P.J. Elving, Talanta, 16 (1969) 855.
[7] Y.M. Temerk and M.M. Kamal, Fresenius' Z. Anal. Chem., 305 (1981) 200.
[8] T.E. Cummings, J.R. Fraser and P.J. Elving, Anal. Chem., 52 (1980) 558.
[9] Y.X. Zhang, Fenxi Huaxue, 13 (1985) 313.
[10] W.R. Jin and K. Liu, Huaxue Xuebao, 43 (1985) 923.
[11] W.R. Jin and W. Jiang, YingYong Huaxue, 2 (1985) 1.
[12] M. Goto, T. Hirano and D. Ishii, Bull. Chem. Soc. Jpn., 51 (1978) 470.
[13] G.Y. Zhu and E.K. Wang, Acta Chim. Sin., 40 (1982) 879.
[14] G.Y. Zhu and E.K. Wang, Sci. Sin. (Ser. B), 4 (1983) 309.
[15] W.R. Jin, H. Cui and S.R. Wang, Anal. Chim. Acta, 268 (1992) 301.
[16] W.R. Jin, H. Cui, L.X. Zhu and S.R. Wang, J. Electroanal. Chem., 340 (1992) 315.
[17] W.R. Jin and X.X. Li, Anal. Chim. Acta, 236 (1990) 453.
[18] W.R. Jin, S.L. Shi and J.Y. Wang, J. Electroanal. Chem., 291 (1990) 41.

ELSEVIER

Analytica Chimica Acta 289 (1994) 169–176

ANALYTICA CHIMICA ACTA

Novel mercury-coated carbon fibre voltammetric detector for use in adsorptive stripping flow analysis

José Amez del Pozo, Agustín Costa-García, Paulino Tuñón-Blanco *

Departamento de Química Física y Analítica, Universidad de Oviedo, 33006 Oviedo, Asturias, Spain

(Received 6th August 1993; revised manuscript received 12th November 1993)

Abstract

The preparation and application of a novel mercury-coated carbon fibre flow microelectrode are reported. The possibility to use this device in a flow system combined with alternating current (ac) stripping voltammetry is also demonstrated using mitoxantrone (MXT) as probe compound. The electrode is easy to prepare. Special analytical advantages have been observed when a.c. stripping voltammetry is applied to the adsorbed molecule on the electrode due to the reversibility of the electrochemical process. Once the operating system has been optimized a limit of detection for mitoxantrone of 4.5×10^{-11} M was found. Manipulation of flow conditions allows the study of different concentration ranges. The direct analysis of serum samples without sample pretreatment, is also discussed and provided a linear calibration range between 4.5×10^{-7} M and 4.5×10^{-6} M.

Key words: Voltammetry; Flow system; Mercury-coated carbon fibre; Mitoxantrone

1. Introduction

Microelectrodes have some well known advantages: quick steady-state mass transport, short charging times and extremely low ohmic drop values [1,2]. Further advantages in flow measurements have also been reported, in particular if a microelectrode array system is available [3]. The advantages of microelectrodes for microcolumn liquid chromatography (LC) are obvious especially when taking into account the possibility to use a mobile phase without electrolyte which increases the number of applications of electrochemical detection [4,5]. Recently, Soucaze-Guillous et al. [6] have shown the analytical advantages of using an amperometric and a fast scan-rate cyclic voltammetric detector based on the use of a platinum microelectrode which allowed the analysis of fullerenes by gel permeation chromatograpy (GPC).

Recently, the application of carbon fibre electrodes in electrochemical analysis has attracted great attention [7,8]. Moreover, the passive carbon fibre electrodes can be reactivated by simple electrochemical pretreatment [9]. The use of a single graphite fiber as working electrode in LC has been reported by several groups [5,10–14].

* Corresponding author.

SSDI 0003-2670(93)E0651-M

The possibility of using a mercury-coated carbon fibre to carry out adsorptive stripping voltammetry has been demonstrated recently [15,16]. Special analytical advantages, such as high sensitivity and ease of use, have been shown when folic acid, mitoxantrone (MXT), or related antitumour drugs were analyzed. These compounds exhibit the common characteristics of strong adsorption onto conventional mercury electrodes. However, an increased resolution in terms of selectivity enhancement of the analytical signal can be achieved when a mercury-coated carbon fibre is used. In fact, under optimum conditions for mercury film deposition, excellent reproducibility can be achieved. Once the analytical strategy to make proper mercury film-coated carbon fibre micoelectrodes has been established, the device shows good performance allowing their use in cells for the adsorptive stripping analysis of folic acid and MXT.

Although the most common electrochemical techniques used in flow systems are potentiometric or amperometric, other techniques such as pulse and square wave voltammetry, have proven to be effective [3,13]. Some workers have coupled flow injection and adsorption–preconcentration methods to improve the characteristics of the former method [17–20], but a.c. voltammetry has never been used for the stripping of the analyte. In the case of MXT, because it is reversibly reduced on mercury [21] or carbon paste electrodes [22], the use of a.c. voltammetry as a detection method, when applied to a flow-through system, provided a more selective method of analysis with the adsorption of the analyte on the electrode as a step prior to the analytical measurement [23].

In this paper a simple T-piece set-up consisting of three adjustable plastic fittings for a low dead volume cell is used as voltammetric detector. The flow cell system is different to those previously reported [24,25]. It is simpler and flexible, and allows to change the microelectrode easily. The flow conditions to generate the mercury film and (or) the rest of the technical and measuring conditions were found to be suitable in such a way that the adsorptive stripping voltammetry of MXT was carried out. This new procedure showed good analytical performance and will increase the use of mercury-coated microelectrodes in flow systems.

2. Experimental

2.1. Apparatus

All experiments were performed using a Metrohm Model E-506 Polarecord in conjunction with a Metrohm Model VA-663 voltammetric stand.

Carbon fibre microelectrodes were prepared from carbon fibres (Donnay Belgium Sport Tennis, Brussels) having a nominal diameter of 7.5 μm. The fibres were immersed in 10% nitric acid, rinsed with distilled water, soaked in acetone, rinsed again with distilled water and finally dried in an oven at 70°C. A single fibre was inserted into a 100-μl standard micropipette to a length of ca. 2 cm and sealed with low-viscosity resin (A.R. Spurr). The pipette was filled with mercury and electrical contact was established with a copper wire. A layer of epoxy resin was then placed over the mercury to prevent any leakage from the microelectrode assembly.

Further details can be found in a previous paper [26].

2.2. preparation of carbon-fibre flow electrodes

A conventional flow-injection analysis (FIA) apparatus arrangement was used.

Flow-injection experiments were carried out using a Millipore (Waters) Model 510 pump. A six port injection valve (Rheodyne 5060) with a 100-μl loop was used for sample injection. All connections were made with 1 mm i.d. PTFE tubing and the distance between valve and detector was 50 cm.

The diagram (Fig. 1) shows the electrode arranged in a T shape. The flow first passes the working electrode (microfibre) before reaching a cell containing the reference (Ag/AgCl) and auxiliary electrode. The auxiliary electrode (steel tube) also acts as a flow outlet. The T-piece set-up consists of adjustable plastic fittings allow-

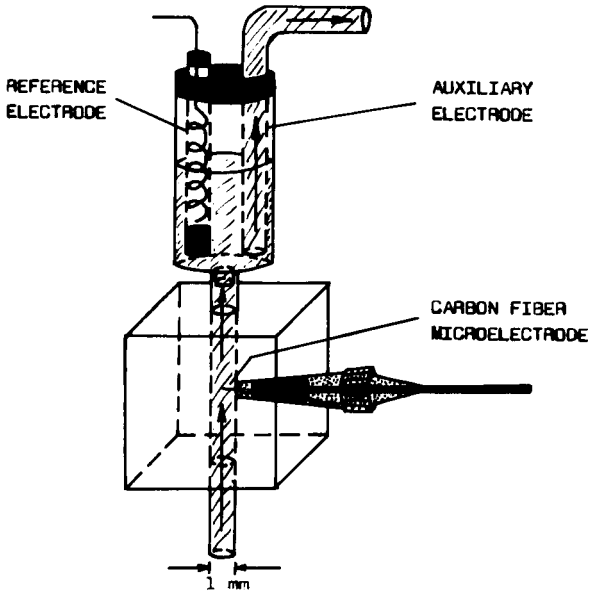

Fig. 1. Schematic illustration of the carbon fibre electrode in the flow cell.

ing for a low dead volume cell which makes it easy to change the fibre when necessary.

2.3. Procedures

Two different mercury coating procedures were developed depending on whether the carrier contained the mercury salt or not. This lead to the arrangement of two different analytical procedures. Moreover, since amperometric detection proved to be useless (poor and non-reproducible results), a.c. voltammetric detection under controlled adsorptive accumulation was employed.

In both cases, parameters affecting the film formation such as carrier composition, deposition time, potential applied, etc. or from the flow system, flow rate, accumulation time, etc., were optimised.

When the Hg(II) ions are included in the carrier solution, the mercury film was formed passing a solution of 0.1 M perchloric acid containing Hg(II) nitrate from 1.0×10^{-2} to 1.0×10^{-4} M and holding the cell under the appropriate reduction potential. The response was evaluated as the a.c. voltammetric signal obtained when 0.1 ml of the carrier solution containing 9×10^{-8} M MXT was injected into the flow system; a.c. voltamperograms were recorded by scanning the potential (10 mV s^{-1}) from the initial potential (+0.200 V) to −1.400 V. The optimum a.c. monitoring conditions: amplitude of the superimposed potential (DE) of 30 mV, phase angle of detection of 90° and fixed frequency of 75 Hz as they have been previously reported [15], were used.

In another procedure, the film was produced first by injection of the Hg(II) salt into the carrier containing 0.1 M perchloric acid and holding the cell under an appropriate mercury reduction potential while the mercury salt (1×10^{-2} M) volume passed through the cell. Then the analytical response was evaluated as indicated above.

2.4. Activation of the electrode

When the same fibre is successively used for coating with mercury films, an activation procedure was necessary between each measurement. For this purpose a potential of +0.740 V was applied to the working electrode for 30 s in a flowing stream containing the carrier solution at constant rate of 1 ml min^{-1} in order to ensure the oxidation of mercury.

3. Results and discussion

3.1. Mercury film electrodeposition

The stability and reproducibility of the mercury film using both procedures were tested. Optimum conditions for the mercury electrodeposition were evaluated in terms of maximum a.c. signal for a known amount of MXT solution introduced into the flowing stream.

3.2. Mercury film electrogeneration using carrier solutions containing mercury

Using this procedure the optimization of parameters affecting the film electrodeposition were more difficult to obtain. When the influence of both the electrodeposition potential and deposition time on the stripping signal were studied, Fig. 2 shows that this influence was almost negli-

gible. However, an electrodeposition potential of +0.200 V was preferred since the baseline of the FIA peaks showed a baseline which is more appropriate for proper measurements of peak currents. An electrodeposition time of 60 s was chosen.

3.3. Influence of flow rate

Since the analyte has to be accumulated on the electrode from a flowing stream and a scanning voltammetric technique is used, tuning of both the starting scanning potential and the flow rate of the system is extremely important. Fig. 3 shows the influence of the flow rate on the stripping signal of MXT when the sample is injected into the system at the same instance the scanning potential is started (initial potential = −0.100 V). The observed behaviour can be explained taking into account both effects, the accumulation period which is shorter when higher flow rates are used and the washing period which is increased when higher rates are used. It explains the shape of the graph with positive and negative slopes at both sides of the plot. Consequently a flow rate of 2.0 ml min^{-1} was found to be suitable. These results confirmed the need to synchronize the scan rate with the necessary period for accumulation of the analyte on the microelectrode surface. Once the flow parameters were established, the influence of the mercury concentration in the carrier was also studied. Proper FIA peaks were only obtained for a concentration of about 1×10^{-4} M. Large noise or lack of resolution of the stripping peaks can be noticed if higher concentrations are used.

3.4. Reproducibility and stability of the mercury film

The reproducibility of the stripping measurements was evaluated by measuring the a.c stripping current after 17 successive injections of 0.5 ml carrier containing 1.0×10^{-4} M mercury salt,

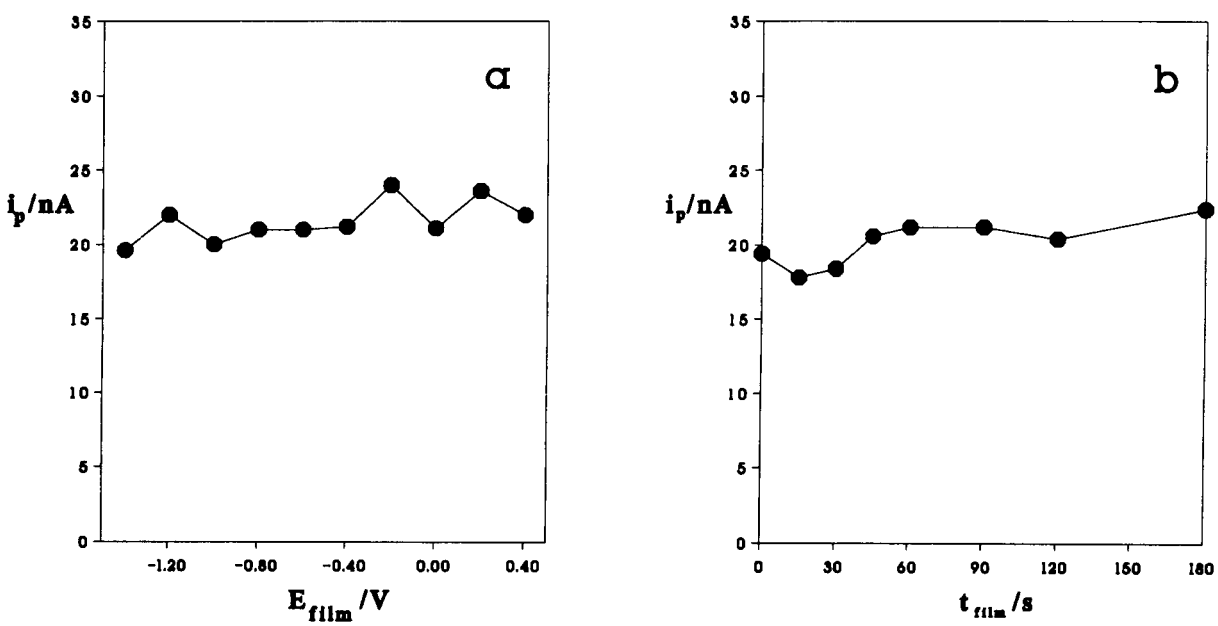

Fig. 2. Influence of the electroplating potential, E_{film} (a) and the electrodeposition period, t_{film} (b) on the a.c. stripping current of MXT 9.0×10^{-8} M introduced into the carrier containing 1×10^{-4} M $Hg(NO)_3$, and 0.1 M $HClO_4$. Conditions: flow rate = 1 ml min^{-1}; film conditions are t_{film} = 60 s (a), E_{film} = +0.200 V (b); ac stripping parameters: accumulation time, ($t_{acc.}$) = 6 s, DE = 30 mV, frequency = 75 Hz, phase angle = 90°, initial potential (E_i) = −0.000 V, final potential (E_f) = −1.500 V, scan rate = 10 mV s^{-1}; activation conditions: activation period, (t_{act}) = 30 s, activation potential, (E_{act}) = +0.740 V.

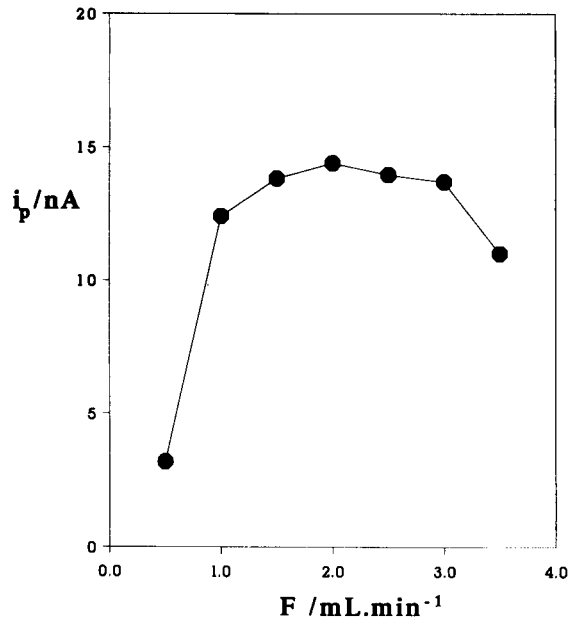

Fig. 3. Influence of flow rate on the a.c. stripping current of a 9.0×10^{-8} M MXT carrier solution. $E_{film} = +0.200$ V, $t_{film} =$ 60 s. The rest of the conditions is as described in Fig. 2.

0.1 M perchloric acid and 9.0×10^{-8} M in MXT under optimum flow and operating conditions. The film was electrodeposited at +0.200 V for 60 s and the activation procedure shown above was followed between each measurement. The reproducibility reached was about 1.7%. However, when this procedure was repeated with a single coated-mercury microelectrode (without renewing the mercury film), the cleaning procedure necessary to renew its surface by applying a potential of −1.500 V, produced a decrease in the signals showing the instability of the film. For further improvement the procedure below was used to develop the analytical method.

3.5. Film mercury electrogeneration in the absence of mercury

The way in which the mercury film is electrodeposited had strong influence on the stability and sensitivity of the stripping signal. In fact when the film was generated first by direct injection of the mercuric salt in 0.1 M perchloric acid, the stripping responses showed always better baseline and higher peak current than those obtained when the mercury is already in the carrier. Using this procedure the improved conditions for the mercury film formation were studied as follows.

3.6. Electrolysis parameters

Composition of the supporting electrolyte and electrodeposition potentials were the main parameters under study when working at fixed flow rate conditions (2 ml min^{-1}). For this purpose 0.5 ml of different concentrations of the salt in 0.1 M $HClO_4$ were injected into the system using a range of different electroreductive potentials for 180 s in each case. The different mercury films formed were tested by measuring the a.c. stripping signal created by a carrier containing 9.0×10^{-9} MXT in 0.1 M $HClO_4$ which was always injected at the same instance in which the scanning potential was initialized at +0.000 V. The results summarized in Fig. 4 show how the signal increases with increasing concentrations of the salt similar to the application of increasingly negative potentials. For these reasons a potential of −1.200 V was considered as most suitable since the ratio of peak height to half peak width was better. Also a salt concentration of 1.0×10^{-2} M was chosen since higher concentrations produced increasing baseline noise.

3.7. Flow conditions

The flow conditions need to be controlled since they affect both the characteristics of the mercury film and the adsorption of the analyte. Regarding the film formation, the electrodeposition period is the main parameter which should be fixed; it is always dependent on the flow rate. By varying both parameters, a flow rate of 2 ml min^{-1} was found to be suitable since it provided reasonable electrodeposition periods (15 s) and reproducible peak currents.

When the analyte adsorption is taken into account the carrier flow rate is extremely important and must be controlled. Fig. 5 shows the influence of the flow rate on the a.c. stripping voltammetric peak measured when 0.5 ml of a

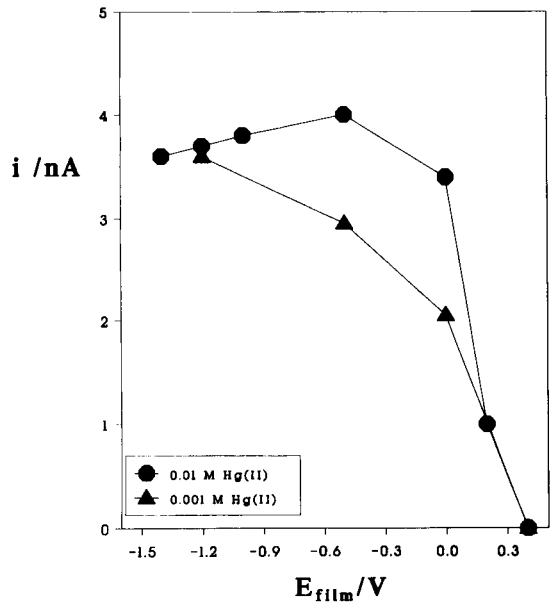

Fig. 4. Influence of both mercury salt concentration and electroplating potential on the a.c. stripping current of 9.0 $\times 10^{-9}$ M MXT. Conditions: carrier solution: 0.1 M $HClO_4$, flow rate = 2 ml min^{-1}; film conditions: $t_{film} = 180$ s, $E_{film} = -1.200$ V; stripping parameters: $t_{acc} = 15$ s, rest of a.c. technical parameters as in Fig. 2; activation conditions: $t_{act} = 60$ s, $E_{act} = +0.400$ V.

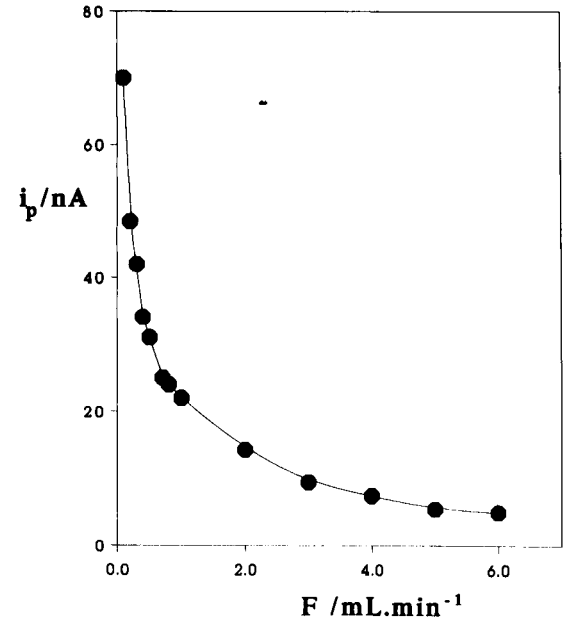

Fig. 5. Influence of flow rate on the a.c. stripping current of 9×10^{-9} M MXT under optimum mercury film conditions. For the rest of the operating conditions see Fig. 4.

carrier containing 9.0×10^{-9} M MXT in 0.1 M $HClO_4$ were injected into the system once the mercury film was previously generated onto surface microfibre. For each flow rate the starting potential was varied in such a way that no washing period was introduced. In this way it can be concluded that the adsorption behaviour of the molecule is better at low flow rates (producing higher peak currents). In order to determine the influence of the washing period (t_w), estimated as the overall time which the analyte adsorbed at the microelectrode is subjected to the carrier stream before it is voltammetrically reduced (i.e., for a flow rate of 2 ml min^{-1}, $t_w = 30$ s), Fig. 6 shows how the voltammetric signal is reduced to half its value for washing periods of 240 s while it remained constant for washing periods less than 30 s.

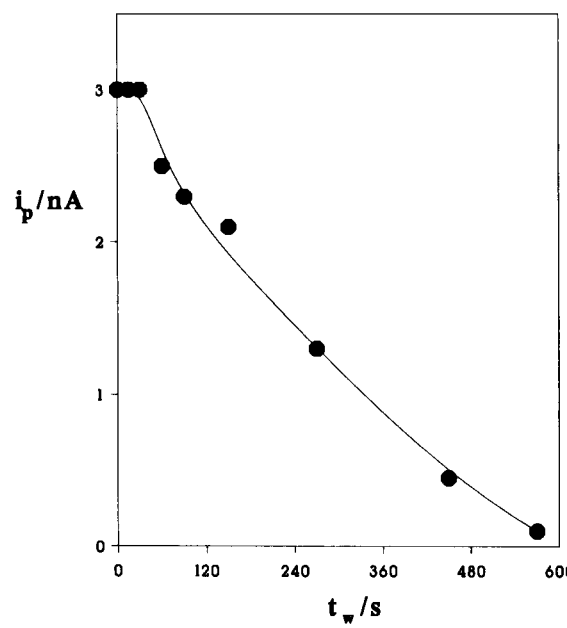

Fig. 6. Influence of the washing period (t_w) on the a.c. stripping voltammetric signal of 9.0×10^{-9} M MXT. The rest of the experimental conditions are as described in Fig. 4.

3.8. Reproducibility and stability of the mercury coated microelectrode

The reproducibility of the measurements was studied by introducing several 0.5-ml aliquots of a carrier containing 9.0×10^{-9} M of MXT in 0.1 M perchloric acid and using a constant flow rate of 2 ml min^{-1}. The film was previously formed introducing 0.5 ml of the mercury salt in 0.1 M $HClO_4$ and keeping the electrode under an appropriate potential. Activation of the surface microelectrode was always necessary and the procedure consisted of applying a potential of +0.400 V for 60 s. When using these conditions together with the same fiber a reproducibility expressed in terms of relative standard deviation was found of 1.62% ($n = 8$). Activation is necessary after each recording.

Finally, the stability of the film was tested by coupling different coated fibres to different flow rates for different lengths of time. The films were stable since their anodic stripping peaks remained constant and the reproducibility achieved was notably improved when the film was held under electrolysis.

3.9. Calibration graphs

Excellent calibration graphs could be obtained by using different flow conditions. Two flow rates were tried and the mercury film was always previously generated by electrodeposition at −1.200 V in a 1.0×10^{-2} M mercury salt solution for 180 s under a constant flow of 2 ml min^{-1}. When a low flow rate was used: 0.2 m min^{-1}, the starting scan potential was delayed for 270 s when 0.5 ml of the sample carrier was introduced into the system. Working like this the accumulation time, taken as the time spent by the sample volume at the detector, was 15 s. No real washing period was used and the lower MXT concentrations could be measured. In fact, two orders of magnitude were covered by the straight calibration from 4.5×10^{-11} to 4.5×10^{-9} M and an excellent linear relation according to the equation:

$$i(\text{nA}) = 5.798 \times 10^{9} C_{\text{MXT}}(\text{M}) + 0.121(\text{nA})$$

$$r = 0.9998,\ n = 7$$

could be obtained. The detection limit (S/N = 3) is 4.5×10^{-11} M.

Using flow rates which are ten times higher (2 ml min^{-1}), higher concentrations (9.0×10^{-10} to 2.25×10^{-8} M) could be determined. The calibration graphs covered one and a half orders of magnitude according to the equation:

$$i(\text{nA}) = 9.953 \times 10^{8} C_{\text{MXT}}(\text{M}) - 0.168(\text{nA})$$

$$r = 0.9992,\ n = 5$$

and a detection limit of 9.0×10^{-10} M was found.

3.10. Analytical approach to MXT determination in human serum

An attempt to determine MXT in serum samples was made. A pool of different serum samples from healthy individuals was spiked with a known amount of MXT. Different aliquots diluted with perchloric acid were assayed and then 0.5 ml of the diluted sample was introduced into the system. The mercury electrodeposition and the rest of the operating conditions were as reported before. The best results were obtained when 1 ml of the spiked sample was diluted up to 2 ml with 0.2 M $HClO_4$ and then introduced into the system. Successive injections, using a flow rate of 0.2 ml min^{-1}, gave FIA responses which varied linearly with the MXT concentration with a drug concentration higher than 4.5×10^{-7} M. The linearity range was tested from this concentration up to 4.5×10^{-6} M and was adjusted according to the equation:

$$i(\text{nA}) = 1.457 \times 10^{5} C_{\text{MXT}}(\text{M}) + 0.184(\text{nA})$$

$$r = 0.9991,\ n = 4$$

A limit of detection of 4.5×10^{-7} M was found.

The main inconvenience of this method is that it is impossible to use the same fibre for making more than one calibration graph. This was also proven using longer washing periods between each injection. It means that the mercury film is seriously distorted and the loss of film stability caused poor reproducibility of the measurements.

4. Conclusions

In this paper the possibility to use a single micro carbon fibre coated with a mercury film as an analytical tool in FIA has been demonstrated. The ability of a.c. adsorptive stripping voltammetric analysis in a flow system, which allowed the determination of MXT, showed interesting advantages over measurements under static conditions previously reported [15]. An important advantage of using a flow-injection system is the better reproducibility of the measurements. The method is more versatile and provides lower limits of detection. Finally, because a carrier is used the mercury film seemed to be more resistant to interferences arising from the matrix when real samples were analyzed. It opens up a very promising research area although much more work has to be done. A logical step would be the development of better pretreatment regimes or the search for better support materials that would lead to more stable mercury film electrodes.

The use of this device as LC detector seems to be foreseeable in the near future. This will increase the importance of voltammetric techniques coupled to LC which has noticeable advantages over the use of conventional mercury electrodes.

5. Acknowledgements

The authors acknowledge DIGYCIT (Project No PB-87-1041) for financial support. Thanks are also due to Dr. J. Barreira Rodriguez and Mr. Michael Malone for their valuable technical assistance.

6. References

[1] T.E. Edmons, Anal. Chim. Acta, 175 (1985) 1.
[2] M. Fleischmann, J. Ghoroghchian and S. Pons, J. Phys. Chem., 89 (1985) 5330.
[3] K. Stulik, Analyst, 114 (1989) 1519.
[4] D.L. Lumscombe and A.M. Bond, Talanta, 38 (1991) 66.
[5] W. Hou, H. Ji and E. Wang, Anal Chim. Acta, 230 (1990) 207.
[6] B. Soucaze-Guillous, W. Kutner and K.M. Kadish, Anal. Chem., 65 (1993) 669.
[7] R.M. Wightman, Anal. Chem., 53 (1981) 1125A.
[8] S. Pons and M. Fleischmann, Anal. Chem., 59 (1987) 1391A.
[9] T.J. O'Shea, A.C. García, P.T. Blanco and M.R. Smyth, J. Electroanal. Chem., 307 (1991) 63.
[10] J.G. White, R.L. St Clair and J.W. Jogerson, Anal. Chem., 58 (1986) 293.
[11] M. Goto and K. Shimada, Chromatographia, 21 (1986) 631.
[12] L.A. Knetch, E.J. Guthrie and J.W. Jogerson, Anal. Chem., 56 (1984) 479.
[13] S.P. Kounaves and J.B. Young, Anal Chem., 61 (1989) 1469.
[14] H. Chi, Y. Wang, C. Jin and T. Zhou, Anal. Chim. Acta, 235 (1990) 273.
[15] J. Amez del Pozo, A. Costa-García and P. Tuñón-Blanco, Anal. Chim. Acta., 273 (1993) 101.
[16] M. Malone, A. Costa-García, P. Tuñón-Blanco and M.R. Smyth, Analyst, 118 (1993) 649.
[17] J. Wang and A.F. Bassam, Anal. Chem., 55 (1983) 1285.
[18] E.N. Chaney Jr. and R.P. Baldwin, Anal. Chim. Acta, 176 (1985) 105.
[19] J. Wang and H.D. Dewald, Anal. Chim. Acta, 153 (1983) 325.
[20] M. Kopanica and V. Stará, J. Electroanal. Chem., 214 (1986) 115.
[21] J.C. Cortina-Villar, A. Costa-García and P. Tuñón-Blanco, Talanta, 40 (1993) 333.
[22] J.C. Cortina Villar, A. Costa-García and P. Tuñón-Blanco, Talanta, 40 (1993) 325.
[23] J.C. Cortina-Villar, A. Costa-García and P. Tuñón-Blanco, Anal. Chim. Acta, 256 (1992) 231.
[24] H. Huiliang, C. Hua, D. Jagner and L. Renman, Anal. Chim. Acta, 193 (1987) 61.
[25] M. Malone, A.P. Doherty, M.R. Smyth and J.G. Vos, Analyst, 117 (1992) 1259.
[26] A.L. Suárez-Fernández, J.A. García-Calzón, A. Costa-García and P. Tuñón-Blanco, Electroanalysis, 3 (1991) 413.

ELSEVIER

Analytica Chimica Acta 289 (1994) 177–186

ANALYTICA CHIMICA ACTA

Flow-injection immunosensor for triazine herbicides using Eu(III) chelate label fluorescence detection

Monika Wortberg *,[a], Cornelia Middendorf [b], Andreas Katerkamp [b], Thomas Rump [b], Jörg Krause [a], Karl Cammann [a,b]

[a] *Chair of Analytical Chemistry, Wilhelm Klemm-Str. 8, D-48149 Münster, Germany*
[b] *Institut für Chemo- und Biosensorik, Wilhelm Klemm-Str. 8, D-48149 Münster, Germany*

(Received 12th October 1993)

Abstract

An immunochemical flow-injection system for the determination of triazine herbicides based on principles of immunoaffinity chromatography was developed. Triazine herbicide derivatives immobilized on oxirane acrylic beads serve as the affinity column. They are saturated with fluorescently labelled monoclonal anti-herbicide antibodies prior to the assay. The label used is the fluorescent Eu(III) chelate W8044-Eu. A fraction of the fluorescent antibodies is replaced when exposed to analyte and this fluorescence is detected in a postcolumn mode by means of a special laser-based fluorimeter. With the reusable affinity column a detection limit of 1 $\mu g\ l^{-1}$ for the herbicide atrazine was obtained.

Key words: Chromatography; Flow injection; Fluorimetry; Sensors; Herbicides; Immunosensors; Triazine herbicides

1. Introduction

The determination of water pollutants by means of immunoassay instead of gas chromatography (GC) or liquid chromatography (LC) has become an important and widely applied technique [1]. One group of analytes receiving major attention is pesticides, especially herbicides [2–8]. For any analytical technique used to determine pesticides in environmental samples, high sensitivity is required, as tolerable herbicide concentrations in drinking water are in the sub-$\mu g\ l^{-1}$ range. This criterion can be satisfied with immunoassays.

The class of herbicides of interest in this work are triazine herbicides, the most important of which is atrazine. Others frequently used are, e.g., cyanazine, propazine, prometryn, simazine and terbutryn. These herbicides are used as weed-control agents in agriculture.

An immunoassay is in general only for single use and is not applicable for continuous analyte monitoring. It is desirable to replace the discontinuous assay with a sensor system that can be operated continuously. Sensors have been developed on the basis of enzymes. If enzymes are

* Corresponding author. Present address: Department of Entomology, University of California at Davis, Davis, CA 95616, USA.

SSDI 0003-2670(93)E0657-S

tagged to either an antibody or an antigen/hapten as a label to visualize the binding reaction, their stability may become the lifetime-limiting part of a sensor, although not limiting their application in immunoassays. For a sensor, multiple use of bio-components is required. Therefore, avoiding enzymes as labels but replacing them with more stable fluorophores is advantageous. Only a few fluoroimmunoassays for herbicides without enzymatic enhancement have been described [9,10]. In most instances the fluorophore is produced enzymatically instead of being tagged to a component [11], because most fluorophores cannot be detected easiliy at sufficiently low concentrations. In contrast, Eu(III) chelates as a special class of fluorophores exhibit an extremely large Stokes shift (> 260 nm) and a long fluorescence decay time (up to 1 ms). This permits the easy separation of the specific Eu(III) fluorescence from background interference. Hence, measuring in the time-resolved mode, the limit of detection using an Eu(III) chelate can be as low as 10^{-13} mol [12]. Therefore, Eu(III) chelates are widely applied as fluorescent labels in clinical immunoassay [12–15].

Another factor effecting the lifetime of an immunosensor, even if there is no enzyme present, is the stability of the antibody (or the antigen). In a common immunoassay configuration, antibodies are immobilized on a solid support and the analyte and a labelled analyte (tracer) are added. If this configuration is applied to an immunosensor, any loss of immobilized antibody activity, e.g., after regeneration steps, will lower the signal and thus result in poor reproducibility and reliability. This problem can be circumvented by immobilizing a more stable molecule. In a hapten determination this can be a hapten derivative provided that it is more stable than its corresponding antibody. This principle has already been demonstrated in fibre-optic immunosensors for pesticides [16,17].

For the present sensor, immunoaffinity chromatography [18] was combined with flow-injection analysis (FIA) [19]. The general principle, utilizing affinity membranes or beads, has already been applied to herbicides [20] and to other analytes [21–23], but in these systems either the use of enzymatic enhancement or the presence of the natural protein fluorescence was required. However, some work is based on fluorescein-labelled haptens which are replaced by analytes during the immunoanalysis [24,25], while another approach utilizes liposomes filled with a fluorescent dye [26]. In the present approach, oxirane acrylic beads with immobilized hapten derivatives serve as the affinity part in the set-up. If these haptens are saturated with Eu(III) chelate-labelled antibodies, some of the antibodies can be replaced from the solid-phase haptens after addition of analyte. A replacement occurs according to the affinity characteristics of the antibodies.

2. Experimental

2.1. Materials

Monoclonal K1F4 anti-triazine antibodies [27] were kindly provided by B. Hock (TU Weihenstefan, Germany) and the Eu(III) chelate W8044-Eu by I. Hemmilä (Wallac, Turku, Finland). The atrazine derivative 2-chloro-4-isopropylamino-6-carboxypentylamino-1,3,5-triazine was synthesized as described [28]. Oxirane acrylic beads (250 μm in diameter), poly-L-lysine (molecular weight 150000–300000), the coupling agent 1-ethyl-3-(3-dimethylaminopropyl) carbodiimide (EDC), the detergent Tween 20 and pig albumin were obtained from Sigma Chemie (Deisenhofen, Germany). Dimethylformamide (DMF) of LC grade was obtained from Aldrich, (Milwaukee, WI). Buffer reagents of analytical-reagent grade were obtained from Merck (Darmstadt) and guanidine hydrochloride (99% purity) from Fluka (Buchs). Doubly distilled water was used throughout all experiments. For purification of the antibody–fluorophore conjugate, Presto columns were used (Pierce, Rockford, IL). Econo columns (4 cm × 0.8 cm i.d.) for immunoassays were purchased from Bio-Rad (Munich) and microtitre strips from Labsystems (Pultittie, Finland).

2.2. Preparation of the antibody–fluorophore conjugate

The coupling of the fluorophore W8044-Eu to K1F4 anti-triazine antibodies and conjugate pu-

rification have been described elsewhere [9]. The conjugate was stored at −20°C and at 4°C for short-term use.

2.3. Coupling of the atrazine derivative 2-chloro-4-isopropylamino-6-carboxypentylamino-1,3,5-triazine to oxirane acrylic beads

The principle of immobilization involves coupling of the synthetic protein poly-L-lysine to the epoxy groups of the beads as the first step. This is followed by the formation of peptide bonds between amino groups of poly-L-lysine and carboxyl groups of the hapten derivative. This principle is shown in Fig. 1. The first immobilization step was adapted from a standard procedure [18] and the second is a modified version of the method developed previously [9].

A 500-mg amount of oxirane acrylic beads was filled into a suitable wide-necked vessel and 3 ml of poly-L-lysine solution (2.5 mg ml^{-1}) in 1 M phosphate buffer (pH 7.4) were added. After 1–2 days of gently moving the suspension with a shaker, the beads were washed on a sintered-glass funnel with 10–20 ml each of water, 1 M NaCl solution and water. A 10-mg amount of the atrazine derivative 2-chloro-4-isopropylamino-6-carboxypentylamino-1,3,5-triazine was dissolved in 300 μl of dimethylformamide (DMF). This solution was added dropwise to 15 ml of phosphate-buffered saline (PBS). The PBS solution, now containing the atrazine derivative, was cautiously poured on to the beads and 15 mg of the solid coupling agent EDC were added. The mixture was gently shaken for $\geqslant$ 2 h. After coupling, the beads were rinsed three times with 10–20 ml of PBS and twice with water. For deactivating the remaining epoxy groups, 10 ml of a 5% solution of mercaptoethanol in water, adjusted to pH 8.0, were added to the beads for 8–12 h. After rinsing with water and PBS, the beads were incubated with a 0.5% (w/v) solution of pig albumin in PBS for 1 h for further blocking. The pig albumin was washed off thoroughly with PBS and the beads were stored at 4°C in a PBS solution containing 0.05% NaN_3.

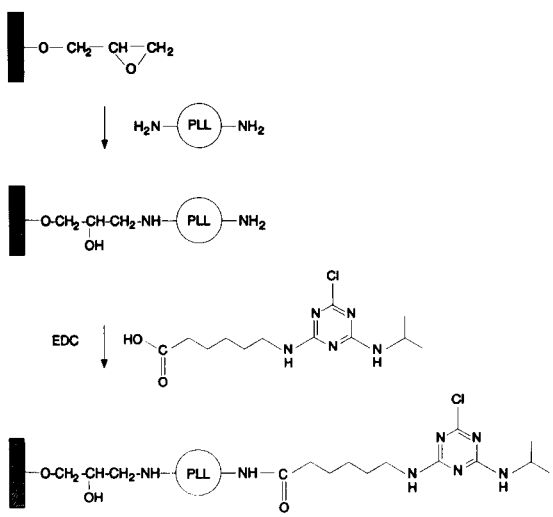

Fig. 1. Immobilization of the hapten derivative to oxirane acrylic beads. Poly-L-lysine (PLL) is coupled to the solid-phase epoxy groups first. Subsequently, a peptide bond is formed between the functionalized atrazine derivative and an amino residue of poly-L-lysine, using the coupling agent 1-ethyl-3-(3-dimethylaminopropyl) carbodiimide (EDC).

2.4. Preparation of affinity columns

Glass tubes of 1.5 mm i.d. were cut into pieces 30–80 mm long. One end of the column was sealed with a nylon net and a piece of silicone-rubber tube. The column was filled with oxirane acrylic beads by pumping the suspension into the tube, then the other end was stoppered as described. The column was connected with PTFE tubes and integrated into the flow-injection system. Affinity beads were stable at room temperature for at least 2 weeks when stored in PBS solution containing 0.05% NaN_3.

2.5. Batch immunoassay with affinity columns

For establishing a suitable protocol for the flow-injection analysis, batch immunoassays were performed using individual Econo columns for each triazine concentration. The assay principle was to replace labelled anti-triazine antibodies from their binding to the solid-phase hapten by adding analyte molecules.

Each column was filled with 15 mg of pretreated oxirane acrylic beads. The moist beads were weighed out quickly to prevent changes in specific gravity due to evaporation of remaining

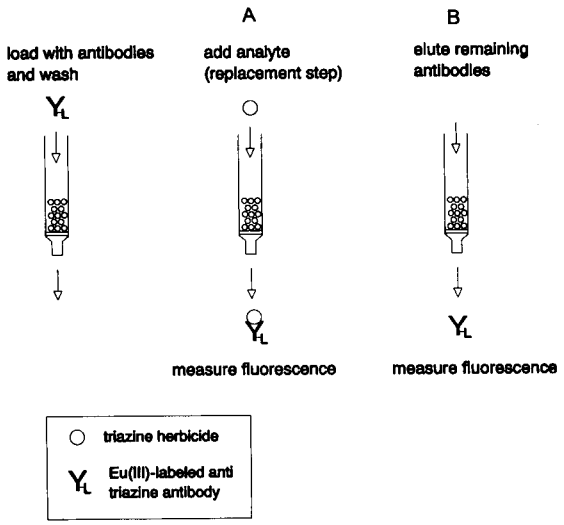

Fig. 2. Two different assay approaches for fluorescence detection in the replacement mode. Either the replaced fraction of previously bound fluorescent antibodies is washed into the detector (A), or in a second step the remaining fraction of bound antibodies is eluted from the beads with a denaturating agent such as guanidine hydrochloride solution (B).

moisture. Incubation steps were performed in stoppered columns, using a plate shaker as in conventional immunoassays. To remove reagents and to rinse the beads, all solutions were pumped through the sintered-glass funnel at the bottom of the columns. For reading convenience the buffers used in the assays are numbered as follows: buffer 1 = PBS solution containing 0.01% Tween 20 and buffer 2 = PBS solution containing 0.1% Tween 20 and 2% pig albumin. Herbicide working standard solutions were prepared by diluting stock standard solutions containing 1 mg ml^{-1} in DMF with buffer 1.

Two different approaches to performing the replacement assay are shown schematically in Fig. 2. For the replacement approach A, 300 μl of a solution containing 1 μg ml^{-1} Eu(III)-labelled K1F4 antibodies in buffer 2 were pipetted on to each column to saturate the solid-phase haptens. After 30 min of incubation the beads were washed four times with 2 ml of buffer 1 to remove non-bound labelled antibodies. A 500-μl volume of herbicide solution in buffer 2 was incubated for 2 h and the effluent from each column was collected in a separate vial. The effluents contained Eu(III)-labelled antibodies that had been replaced from the solid-phase haptens by binding herbicide molecules of the analyte solution instead. Aliquots of 175 μl of the effluents were pipetted into the wells of microtitre strips. The fluorescence was detected in an Arcus 1230 fluorimeter (LKB Wallac, Turku, Finland), which is specially designed to determine Eu(III) chelate fluorescence.

For the replacement approach B, an elution step followed the replacement: 500-μl aliquots of an aqueous 4 M guanidine solution were pipetted on to each column. After 30 min of incubation, the fluorescence of the eluate was measured as described above. This eluate contains the fraction of Eu(III)-labelled antibodies that had remained on the solid phase after the replacement step. Thus, in contrast to approach A, the fluorescence signal is inversely proportional to the herbicide concentration.

2.6. Laser-based fluorimeter

The custom-built fluorescence detector system is shown in Fig. 3. The excitation source was a pulsed nitrogen laser operated at 337.1 nm (Laser 2000) that was triggered externally at 6, 12 or 24 Hz. The pulse width was 0.5 ns with a pulse

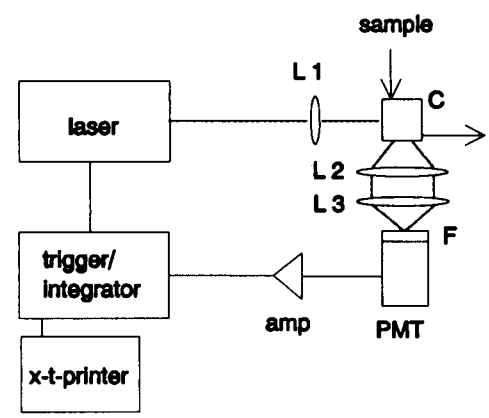

Fig. 3. Set-up of the fluorescence detector. The system is specially designed for the detection of Eu(III) chelates. Amp = amplifier; C = cuvette; F = interference filter (610 nm); L1–3 = lenses; PMT = photomultiplier tube.

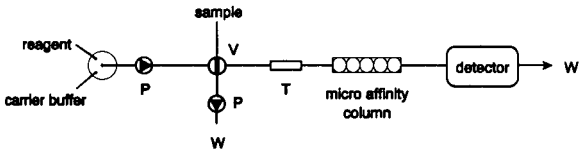

Fig. 4. Set-up of the single-channel FIA system. The selector supplies the system with either carrier buffer or labelled antibodies (reagent). P = peristaltic pump; T = air trap; V = injection valve; W = waste.

energy of 300 kW. The laser beam was focused on the flow channel of a rectangular-shaped quartz cuvette by means of a biconvex quartz lens (Spindler and Hoyer). The flow-through cuvette had inner dimensions of 1×1 mm.

The detection system consisted of an R 923 side-on photomultiplier tube (PMT) (Hamamatsu) equipped with a 610-nm interference filter (LOT), a 1-MΩ amplifier and an electronic integrator. The integrator was synchronized with the laser trigger and summed a maximum of eighteen fluorescence signals, using 3-ms gated sampling intervals after each laser pulse. The fluorescence light was focused on the PMT window by means of a cylindrical and a biconvex glass lens (Spindler and Hoyer). The integrated fluorescence signal was recorded with an x–t printer.

2.7. FIA apparatus

The flow-injection apparatus was an Eppendorf Variables Analysensystem (EVA) (Eppendorf, Hamburg). Fig. 4 shows the set-up used for the single-channel FIA. It consisted of an eight-port selector, two of which were in use, a six-port injection valve, a four-channel peristaltic pump equipped with a clutch and a master as computing unit. Labelled antibodies (= reagent) and carrier buffer (PBS) were pumped alternately according to two selector positions. By using the clutch it was possible to fill the injection valve with analyte parallel to a washing cycle. The fluorescence detector was activated only during the appearance of the fluorescence peaks at the end of the complete FIA cycle by a signal generated from the master unit.

The FIA cycle for the replacement concept involving stopped-flow intervals consisted of the following steps: (1) loading the affinity column with labelled antibodies (1–10 μg ml^{-1} in PBS buffer, stopped flow for 15 min) and washing; (2) injection of 100–200 μl of atrazine solution in PBS and stopped flow for 20–40 min; and (3) postcolumn fluorescence detection. The flow-rate in all flow steps was 0.25 ml min^{-1}. FIA parameters were first adapted from batch immunoassays and were subsequently optimized with respect to incubation times, antibody concentration and column volume. A complete FIA cycle including steps 1–3 required 45–75 min.

3. Results and discussion

3.1. Hapten immobilization

First, the immobilization procedure needs a further explanation. As both the oxirane acrylic beads and the atrazine derivative to be linked by covalent bonding were electrophiles, a bifunctional nucleophilic reagent was required for coupling. In the first experiments it proved to be disadvantageous simply to apply a diamine such as diaminohexane. With diaminohexane as spacer, strong non-specific binding of Eu(III)-labelled antibodies was observed so no assay was possible. Therefore, poly-L-lysine (M_r 150000–300000) was chosen as a bulky "bifunctional" reagent. These protein molecules have the size of an antibody and hence can penetrate pores in the beads of similar size as can labelled antibodies. The advantage of this procedure is that, on the one hand, small pores are already blocked, whereas on the other, the hapten derivatives will be preferably immobilized on the outer surface of the beads rather than inside the inaccessible cavities. Hence, the haptens are more efficiently presented to the antibodies. The overall effect is a decrease in the non-specific binding of antibodies, as will be discussed later. Additionally, pig albumin (M_r ca. 60000) was used as a blocking agent for smaller pores.

3.2. Batch immunoassays

After the immobilization procedure had been established, different assay concepts were compared in batch immunoassays using individual columns. As the K1F4 antibody showed the highest affinity to terbutryn and a lower cross-reactivity to atrazine [27], first experiments were carried out with terbutryn instead of atrazine as analyte. With the functionalized atrazine molecule coupled to the affinity beads, two possible strategies can be applied for the performance of the analysis. For the first approach, triazine herbicide molecules (the analyte) are incubated simultaneously with anti-triazine antibodies. Competitive binding takes place, resulting in a distribution of the labeled antibodies between both analyte in solution and column-bound analyte derivatives. As binding events on the column cannot be visualized, the bound fraction of labelled antibodies has to be removed (eluted) with a suitable reagent and subsequently detected in the postcolumn mode. The fluorescence signal obtained on elution is inversely proportional to the analyte concentration.

The second strategy is based on the concept of replacement, as demonstrated in Fig. 2A and B. Here, the column is preloaded with labelled antibodies. After addition of analyte a fraction of the previously bound antibodies is released from the solid phase, now binding to the analyte in solution instead. These antibodies are detected in the postcolumn mode as in the competitive binding approach, but in contrast no additional reagent is required (Fig. 2A). The fluorescence signal is directly proportional to the analyte concentration. The replacement may additionally be followed by elution (Fig. 2B). In this instance the antibody fraction that had remained on the column is detected, and the signal is therefore inversely proportional to the analyte concentration.

The replacement concept is only feasible with antibodies of sufficiently low affinity to the immobilized herbicide derivative. If the affinity is too high, the amount of replaced antibodies will be too low. The affinity must not be too low either, as a low affinity will result in a non-specific release of labelled antibodies simply to addition of buffer, according to the law of mass action. Therefore, the use of medium-affinity antibodies is necessary. As monoclonal antibodies have a uniform affinity they should be preferred to polyclonal antibodies.

Several eluting agents commonly used in affinity chromatography were tested for removing antibodies from the column: 0.1 M glycine–HCl (pH 2.0–3.0), 4 M guanidine hydrochloride solution, 8 M urea and 6 M KSCN solution. As the acidic eluent glycine–HCl destroyed the Eu(III) complex it was not applicable for fluorescence detection. The three chaotropic and denaturating agents were of similar eluting quality, but the high salt concentrations adversely affected the polymer beads and are disadvantageous for an FIA system: high salt concentrations will increase crystal formation in the valves and tubes. Therefore, 4 M guanidine solution was chosen as the least concentrated but effective eluent.

As it was found that the competitive binding approach followed by guanidine elution gave a relatively low sensitivity (data not shown), only the replacement approaches were tested further. Fig. 5 shows two calibration graphs for the triazine herbicide terbutryn obtained with one column per concentration. The fluorescence of each fraction was measured in duplicate. The results should only be regarded qualitatively as the experimental error was not quantified. The curve with triangles represents the amount of replaced labelled antibodies whereas that with circles corresponds to the amount of antibodies that was still bound to the beads and was eluted subsequently with guanidine. The former curve yields a large dynamic range from ca. 0.8 to 100 $\mu g\ l^{-1}$ terbutryn. The latter curve B, representing the eluted antibodies after the replacement step, covers an approximately linear concentration range from 1 to 50 $\mu g\ l^{-1}$ terbutryn. As the slope of this curve is lower than that of the former curve, the assay sensitivity achieved with elution instead of replacement is decreased.

The linear dynamic range covered by these batch immunoassays was larger than the range observed in conventional assays in microtitre strips [9]. This can be attributed to a much larger active surface area available when using porous

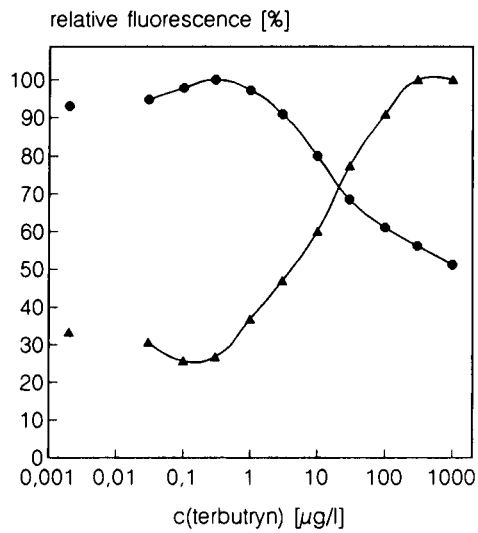

Fig. 5. Calibration graphs for terbutryn obtained in batch immunoassays performed on oxirane acrylic beads with immobilized atrazine derivative. ▲ = Fluorescence of the replaced fraction of labelled antibodies which emerged from the column after addition of analyte; ● = remaining fraction of labelled antibodies, which is subsequently eluted with guanidine solution in a further assay step. All data points represent only single determinations; the single points on the left indicate the blank values.

beads rather than polystyrene cavities. It should be mentioned that the data points shown for the same concentrations on both curves in Fig. 5 were obtained with the same columns. Ideally, the sum of both curves would yield a straight horizontal line as the sum of fluorophores (eluted fraction + replaced fraction) should be identical for all concentrations, which is not the case here. The fluorescence of the sum curve (not shown) increases, which might be attributed to the characteristics of the elution process. During guanidine elution some antibodies are removed that had only been bound non-specifically to the beads, whereas during replacement only relatively few antibodies are released non-specifically. This explains why the lowest eluent fluorescence at high terbutryn concentrations is still relatively high (50% of the maximum value for the curve with circles in Fig. 5). In contrast, the corresponding blank fluorescence in the replacement mode without guanidine elution is only 30% of the maximum value.

From these qualitative investigations, it is concluded that measuring the fluorescence of replaced antibodies yields a lower background signal than guanidine elution. The FIA concept of choice will therefore be based on replacement without any eluting agent.

3.3. FIA investigations

The replacement concept applied in the batch immunoassays was adapted to FIA conditions. This required the implementation of stopped-flow intervals in the FIA protocol. The set-up for the sequential FIA, requiring only one flow channel for the assay buffer, is shown in Fig. 4.

First, the influence of the column volume on the calibration graph was tested. Fig. 6 shows two calibration graphs for atrazine obtained with a 50- and a 75-µl column. The calibration graphs do not exhibit the typical sigmoidal shape of immunoassays. Instead, they stay linear over a range of three decades towards the upper limit, which is given by the solubility of the herbicide in

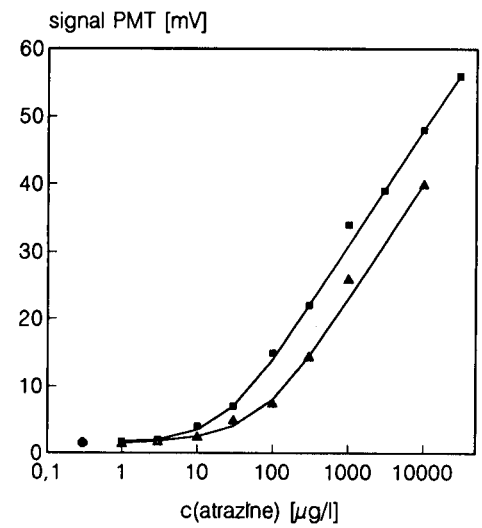

Fig. 6. FIA calibration graphs for terbutryn with two different volumes of the affinity column. The decrease in detection limit associated with the increase of bead volume is shown. For each graph the same charge of beads was used. ▲ = 50-µl column volume; ■ = 75-µl column volume; ● = blank.

buffer solutions. For all data points on each graph the same column material was used for all measuring cycles. As only single data points were available in this experiment, no detection limit is indicated, but the tendency for a shift can be observed. It can be concluded that the larger the bead volume, the lower is the detection limit, while the slope of the calibration graph remains the same. The linear dynamic range covers three orders of magnitude for the 75-μl column. With the 50-μl column the dynamic range is smaller owing to the increase in detection limit. The dynamic range is exceptionally extended compared with conventional immunoassays, which usually only cover a maximum of two concentration decades. As was mentioned above, this can be attributed to the large surface area of the beads. Additionally, the upper concentration limit of the graph is given by the solubility of atrazine in PBS buffer. As a concentration of 30000 μg l^{-1} atrazine is far beyond any real water contamination, this does not mean any restriction.

The sensitivity and the detection limit of the system were optimized by varying several parameters. To minimize the number of experiments, only two standard concentrations were used, namely PBS buffer yielding the blank value and a concentrated atrazine solution of 100 μg l^{-1}. The blank value indicates the minimum fluorescence signal of a calibration graph and the high atrazine concentration represents the behaviour of the (arbitrarily chosen) maximum value. The optimization process is best described as a compromise between gain in sensitivity and decrease in speed of analysis due to the extended incubation time.

A higher antibody concentration increased the efficiency of column loading and hence the amount of antibodies to be replaced, but the time required for washing off the excess during the FIA cycle also increased. The fluorescence signal for a labelled antibody concentration of 1 μg l^{-1} is shown in Fig. 7A, and a tenfold increase to 10 μg l^{-1} yields Fig. 17B. With a 125- instead of a 75-μl column the absolute signals increased (Fig. 7C) according to the observations already made in Fig. 6, comparing a 50- and a 75-μl column. However, as here a larger volume of antibody and

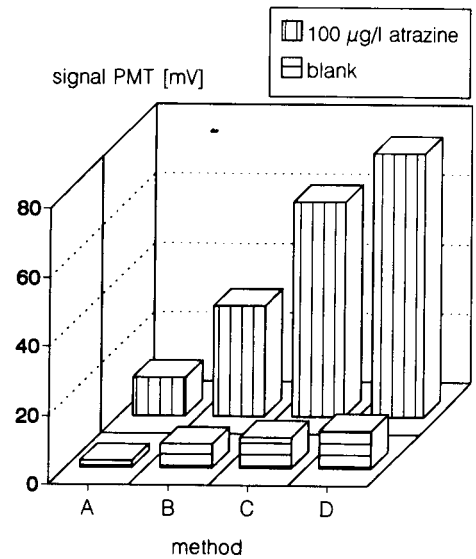

Fig. 7. Optimization process for FIA, varying different parameters. The maximum and minimum fluorescence signals obtained after parameter variations were recorded. In each subsequent variation an additional parameter was changed with the previous changes fixed. (A) Antibody concentration 1 μg l^{-1}, column volume 75 μl, replacement time 20 min; (B) antibody concentration increased to 10 μg l^{-1}; (C) column volume increased to 125 μl; (D) replacement time extended to 40 min.

analyte solution was required, the cycle time increased and all time parameters had to be adapted to a 200-μl reagent and injection volume instead of a 100-μl volume. On increasing the time for the replacement step from 20 to 40 min, it was found that the relative increase in the blank value was stronger than that of the maximum signal (Fig. 7D). This indicates that non-specific (antibody-releasing) events cannot be neglected. The release of non-specifically bound antibodies in pure buffer solution is in fact a washing process. Simple washing off has different time characteristics to a "real" replacement. The specific replacement is a function of the affinity constant: if the affinity of the antibodies to the solid phase hapten is low, cleavage of the antibody–hapten complex will occur even when no hapten is present in solution, as is expected according to the law of mass action. The cleavage continues until the equilibrium concentrations (distribution of the antibody molecules between solid and liquid

phases) are adjusted. This effect could be termed a non-specific antibody release: for the specific replacement concept it is assumed that one atrazine molecule present in the sample causes one antibody molecule to emerge from the beads. This is only an approximation valid for high-affinity antibodies with a low (virtually zero) equilibrium antibody concentration in solution. With high-affinity antibodies the replacement process would be slow and hardly observable. In terms of affinity, a large extent of non-specific antibody release is a result of a low affinity between the hapten on the solid phase and the labelled antibody. Therefore, an increase in the time allowed for replacement was not suitable for improving the detection limit, besides being a disadvantage owing to the decrease in assay speed. The best compromise is the set of parameters in Fig. 7C, with a total cycle time of 75 min.

The influence of assay buffer composition on the non-specific cleavage of the hapten–antibody complex was also examined. First, any detergent present in buffers will lead to an increased blank fluorescence. Using a citrate–phosphate buffer (pH 5.0) instead of PBS buffer (pH 7.4) to dilute the triazine standards, the amount of released antibodies was much larger (data not shown). However, this was also true if no analyte was present in this buffer. Hence the blank value increased enourmously in the pH 5.0 buffer. As the acidic buffer is rather an eluent than a buffer, it cannot be recommended for use in FIA.

Additionally, if the concentration of organic solvents present in the sample exceeded 1%, the non-specific cleavage of the hapten–antibody complex also increased. It was found that the addition of 1% DMF to the PBS buffer (pH 7.4) doubled the blank signal. Therefore, it has to be ensured that the replacement signal observed is not simply caused by alterations in the buffer or sample composition. To avoid false-positive assay results or even artefacts when examining water samples containing organic solvents, one possibility is to spike the buffers with ethanol or DMF prior to use.

To examine the reproducibility of the FIA signals, triple determinations for each atrazine concentration were performed. An example is

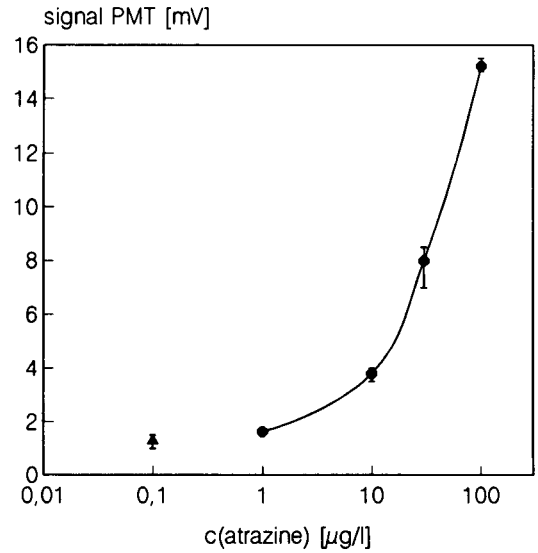

Fig. 8. Reproducibility of the FIA signals. The error bars represent the range of triplicate determinations (●) performed in arbitrary order. All data points were obtained with the same column, which was only reloaded with fresh antibodies. ▲ = Blank.

given in Fig. 8. The error bars indicate the range of three determinations, with range defined as being equal to two standard deviations. To avoid systematic errors, the herbicide concentration was changed after each determination. Thus, high and low analyte concentrations were applied to the column alternately. As in the previously described experiments, all data points were obtained with the same batch of bead material. The reproducibility was high with deviations of $< 10\%$. The detection limit, based on three standard deviations (or 1.5 times the range), was 1 $\mu g\ l^{-1}$.

As the FIA set-up consisted of only one affinity column, all steps had to be performed subsequently. It is also possible to use several columns in a parallel mode, switching them alternately into the buffer and reagent stream: while one column is loaded with antibodies, another column can be incubated with analyte, a third one is rinsed while at the same time a further column produces a fluorescence peak which is recorded in the fluorimeter. With this improvement, the number of samples per hour can be increased

although the time required for a single determination remains unchanged. If a sufficiently large column is used, the reloading step can be omitted for several subsequent determinations. The excess of antibodies on the column serves as a reservoir, and hence the time per FIA cycle can be decreased significantly to about 20 min.

The use of other hapten derivatives immobilized on the affinity beads would result in alterations in affinity. Preferably, a lower affinity of the hapten to the antibody is desired, because with this approach the detection limit for atrazine might be lowered further.

4. Conclusions

A flow-injection analysis method for triazine herbicides was developed based on affinity chromatography with postcolumn fluorescence detection. The Eu(III) chelate W8044-Eu was used as a fluorescent label attached to the anti-triazine herbicide antibodies. By imitating the FIA conditions in batch immunoassays with the same carrier bead material, an appropriate FIA cycle was developed. With the FIA system, the detection limit for atrazine was 1 μg l^{-1} and the linear dynamic range of the calibration graph covered three orders of magnitude. The affinity column proved to be stable at room temperature for at least 2 weeks and provided good data reproducibility. To the authors' knowledge, this system is the only FI immunosensor for triazine herbicides based on affinity chromatography that is reusable without the necessity to remove all bound species. Additionally, only few systems exhibit a comparably large dynamic range.

5. Acknowledgements

The authors thank Professor B. Hock and Dr. T. Giersch for providing the monoclonal K1F4 antibodies. They also thank Dr. I. Hemmilä for supplying W8044-Eu. Financial support by the Fonds der Chemischen Industrie and the Bundesministerium für Forschung und Technologie, No. 322-4004-0319508A, is gratefully acknowledged.

6. References

[1] J.M. van Emon and V. Lopez-Avila, Anal. Chem., 64 (1992) 79A.
[2] F. Jung, S.J. Gee, R.O. Harrison, M.H. Goodrow, A.E. Karu, A.L. Braun, Q.X. Li and B.D. Hammock, Pestic. Sci., 26 (1989) 303.
[3] C. Wittmann and B. Hock, Z. Wasser Abwasser Forsch., 24 (1991) 2.
[4] M.G. Weller, L. Weil and R. Niessner, Microchim. Acta, 108 (1992) 29.
[5] P. Schneider and B.D. Hammock, J. Agric. Food Chem., 40 (1992) 525.
[6] M.H. Goodrow, R.O. Harrison and B.D. Hammock, J. Agric. Food Chem., 38 (1990) 990.
[7] J.-M. Schlaeppi, W. Föry and K. Ramsteiner, ACS Symp. Ser., 442 (1990) 199.
[8] B. Hock, Z. Wasser Abwasser Forsch., 22 (1989) 78.
[9] M. Wortberg and K. Cammann, Fresenius' J. Anal. Chem., 346 (1993) 757.
[10] M. Wortberg, K. Strupat, F. Hillenkamp and K. Cammann, Fresenenius' J. Anal. Chem., in press.
[11] P. Ulrich, L. Weil and R. Niessner, Fresenius' J. Anal. Chem., 343 (1992) 50.
[12] I. Hemmilä, Applications of Fluorescence in Immunoassays, J. Wiley, New York, 1991.
[13] I. Hemmilä, Anal. Chem., 57 (1987) 1676.
[14] T.K. Christopoulos and E.P. Diamandis, Anal. Chem., 64 (1992) 342.
[15] F.J. Lüke and W. Schlegel, Clin. Chim. Acta, 189 (1990) 257.
[16] F.F. Bier, W. Stöcklein, M. Böcher, U. Bilitewski and R.D. Schmid, Sensors Actuators B, 7 (1992) 509.
[17] M.A. Northrup, L.H. Stanker, M. Vanderlaan and B.D. Watkins, NATO ASI Ser., Spectrosc. Inorg. Biochem., 280 (1989) 229.
[18] P.G.D. Dean, W.S. Johnson and F.A. Middle, Affinity Chromatography, IRL Press, Oxford, 1991.
[19] J. Ruzicka and E.H. Hansen, Anal. Chim. Acta, 78 (1975) 145.
[20] P. Krämer and R. Schmid, Biosensors Bioelectron., 6 (1991) 239.
[21] I.H. Lee and M.E. Meyerhoff, Anal. Chim. Acta, 229 (1990) 47.
[22] W. Stöcklein, V. Jager and R.D. Schmid, Anal. Chim. Acta, 245 (1991) 1.
[23] M. Nilsson, H. Hakanson and B. Mattiasson, Anal. Chim. Acta, 249 (1991) 163.
[24] R.A. Ogert, A.W. Kusterbeck, G.A. Wemhoff, R. Burke and F.S. Ligler, Anal. Lett., 25 (1992) 1999.
[25] A.W. Kusterbeck, G.A. Wemhoff, P.T. Charles, D.A. Yeager, R. Bredehorst, C.-W. Vogel and F.S. Ligler, J. Immunochem. Methods, 135 (1990) 191.
[26] L. Locasio-Brown, A.L. Plant, V. Horváth and R.A. Durst, Anal. Chem., 62 (1990) 2587.
[27] T. Giersch and B. Hock, J. Agric. Immunol., 2 (1990) 85.
[28] B. Dunbar, B. Riggle and G. Nieswender, J. Agric. Food Chem., 38 (1990) 433.

ELSEVIER

Analytica Chimica Acta 289 (1994) 187–194

ANALYTICA CHIMICA ACTA

Automatic study of selectivity by the flow-rate gradient technique

Bernhard Lendl [a,1], Angel Ríos [a], Miguel Valcárcel *,[a], Manfred Grasserbauer [b]

[a] *Department of Analytical Chemistry, University of Córdoba, E-14004 Córdoba, Spain*
[b] *Institute for Analytical Chemistry, Technical University of Vienna, A-1060 Vienna, Austria*

(Received 21st September 1993; revised manuscript received 11th November 1993)

Abstract

An automatic flow methodology was developed to study the selectivity of analytical flow methods. The methodology is characterized by its simplicity, rapidity, precision and flexibility. The flow-rate gradient technique was used to establish interferent concentration gradients along the manifold where the main photometric reaction took place. By continuously monitoring the absorbance, the maximum tolerated foreign species to analyte concentration ratio was automatically determined. The aluminium(III)–Eriochrome Cyanine R system was chosen to test the performance of the new methodology.

Key words: Flow system; Automation; Flow-rate gradient technique; Selectivity

1. Introduction

Selectivity is one of the main analytical properties on which quality of the analytical results relies [1]. In contrast to such properties, like precision and sensitivity, selectivity is difficult to quantify. A mathematical, essentially theoretical, approach leading to a definition of selectivity was developed by Kaiser in 1972 [2]. Interferences can have various origins. They can be caused by individual species as well as by many species acting in conjunction, giving rise to the so-called "matrix effects", which include not only chemical effects, but also factors such as the ionic strength and viscosity. As regards flow-injection methods, Hansen et al. [3] developed an approach to quantifying the interference produced by a foreign species in the form of a selectivity coefficient.

The flow-rate gradient technique [4] has proved to be widely applicable for solving ordinary analytical problems such as those faced in automated titrations [5,6] or simultaneous determinations [7,8], as well as less common ones such as those met in automatic determinations of physicochemical parameters [9]. The main advantage of this technique is the ability to establish concentration gradients within the flow system in an automatic and reproducible way. By producing concentration gradients of foreign species in the chemical system used for a given determination, one can determine how each foreign species influences the analytical response, and thus easily obtain information on the selectivity of the

* Corresponding author.
[1] Present address: Institute for Analytical Chemistry, Vienna University of Technology, A-1060 Vienna, Austria.

SSDI 0003-2670(93)E0644-M

method concerned. This principle was used in this work to study, in an automatic way, the selectivity of the aluminium(III)–Eriochrome Cyanine R system employed for the photometric determination of aluminium [10–13].

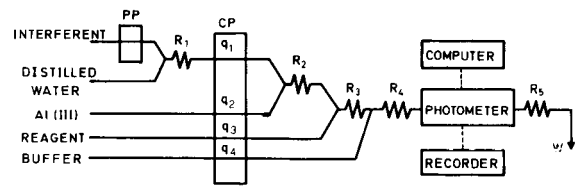

Fig. 1. Manifold used to deliver interferent concentration gradients and providing a constant flow-rate ($q_1 = 0.9$, $q_2 = q_3 = q_4 = 0.7$ ml min^{-1}; $R_5 = 200$ cm, i.d. = 0.8 mm). For further details see text.

2. Experimental

2.1. Reagents

A stock solution of aluminium(III) was prepared by dissolving 0.528 g of $Al(NO_3)_3 \cdot 9H_2O$ (Merck) in distilled water, adding 17.25 ml of concentrated HCl and making up to 250 ml. A 3.37×10^{-5} M aqueous solution of Eriochrome Cyanine R (Merck) was used as reagent, and 0.2 M MES (2-[*N*-morpholino]ethanesulfonic acid, from Sigma) as buffer. All interferent solutions were prepared from P.A. grade chemicals.

2.2. Apparatus

An UNICAM 8625 UV–visible spectrophotometer connected to both a Radiometer REC 80 recorder and a personal computer via a serial RS 232C interface was used. This experimental setup permitted the acquisition and the processing of the data obtained. A Gilson Minipuls-3 peristaltic pump controlled by a Commodore-64 microcomputer via a laboratory-made interface was used to provide the flow-rate gradients [4], whereas a Minipuls-2 peristaltic pump was used to produce a constant flow-rate. A Tecator TM II chemifold and a Hellma 178.12 QS flow-cell of 10 mm light-path and 18 μl inner volume were also used.

2.3. Manifold and procedure

The manifold used is depicted in Fig. 1. The key to this manifold is the location of the programmable pump (PP), providing variable flow-rates, before the conventional pump (CP), operated at constant flow-rate. This arrangement allowed that the resulting flow-rate through channel q_1 (channel of the CP) to be kept constant even though PP delivered a variable flow-rate, thanks to the water channel merging with the PP channel, which equilibrated the resulting flow-rate. During the work, water was propelled by the additional channel, and its pH was adjusted to that of the solution propelled by PP. Doing this minimizes pH changes caused by running a flow-rate gradient experiment. The essential condition was that the maximum flow-rate of PP should be lower than the flow-rate of the resulting CP channel. As interferent species were propelled through PP and the additional water channel always contributed to the difference between the flow streams of the programmable and constant pump, an interferent concentration gradient was created from channel q_1 of CP with no significant change in the resulting flow-rate. The interferent concentration gradient stream was then merged with aluminium, reagent, and buffer streams in succession. The reaction product was formed in reactor R_4 and the effect of interferents was studied photometrically.

2.4. Performance and calibration of the flow-rate gradient system

First, a brief study of the resulting flow-rate, q_1, was carried out. By inserting a flow-meter in the channel, a variation from 0.81 to 0.86 ml min^{-1} in q_1 was observed when the PP was operated between zero and its maximum speed (a maximum increase in flow-rate q_1 of 6.2%). Considering the complete manifold, even this slight increase in q_1 vanishes due to the pressure caused by the manifold after the CP. To increase this pressure, an additional reactor was introduced after the flow-cell, so that no change in the over-

all resulting flow-rate was observed. Linear flow-rate gradients were used throughout the work. The duration of one gradient was roughly 320 s. A linear relationship between the speed of the PP (as %) and time was performed, thus interferent concentration and time data were obtained in a single experiment. As the concentration of Al(III) in the system is not changed during the flow-rate gradient experiment, the establishment of the foreign species to aluminium ratio was simple. The experimental setup permitted recording one data point per second and storing the measurements as a file. The establishment of the foreign species to aluminium ratio was achieved using a calibration file stored on the personal computer.

q_{Al} and $q_{I,i}$ are the respective flow-rates for Al(III) and interferents (time-dependent) as a percentage of the resulting flow-rate used to calibrate the system. Calibration runs were performed by introducing a dye into the system (an acidic solution of K_2CrO_7 was used), they were scaled to 1, and a mean of all runs was calculated, yielding a value f_i at every experimental time $t_{e,i}$. Access to the desired [I]/[Al] (I = interferent) concentration ratio as a function of the experimental time was realized for every second of the measurement by a direct relationship between $([I]/[Al])_i$ and $t_{e,i}$ using f_i from the calibration runs:

$$([I]/[Al])_i = (C_I^\circ q_{I,i})/(C_{Al}^\circ q_{Al}) f_i$$

Reproducibility studies were conducted over three consecutive days by scaling measurements to their maxima and plotting the mean of each day. Fig. 2a shows very good consistency and thus a high reproducibility of the proposed manifold. Fig. 2b shows more detailed recordings, while Fig. 2c illustrates the variance of deviation from the daily mean.

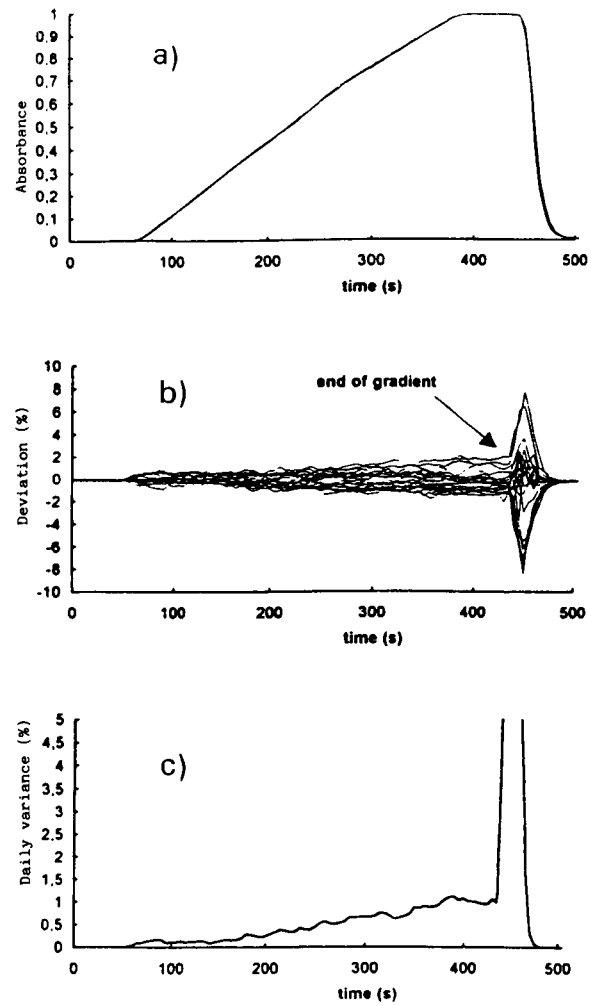

Fig. 2. Calibration plots and reproducibility experiment performed with the manifold used to deliver interferent concentration gradient (a dye was used in this case): plot of the scaled mean of the calibration runs from three different days (a); plots of the deviation from the daily mean of the calibration runs (b); and variance of daily scaled gradients as a function of the experimental time (c).

3. Results and discussion

There are several methods available for the determination of aluminium with Eriochrome Cyanine R (ECR) that differ essentially in the pH at which formation of the coloured complex is monitored [10–13] by measuring the absorbance at 534 nm.

Reactor coils R_1 and R_2 in Fig. 1 were both 60 cm long each (0.5 mm i.d.) and allowed efficient mixing of aluminium(III) and the interferents. The influence of the length of the reactor coils R_3 and R_4 was investigated. In R_3, the mixture of Al(III) and foreign species merged at pH 2.5 (the pH at which the Al(III) solution was pre-

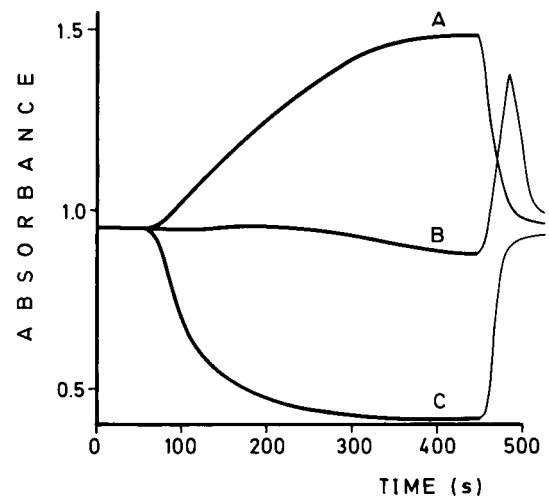

Fig. 3. Original recordings obtained for the influence of Fe(III) (curve A), Pb(II) (curve B), and fluoride (curve C) on the Al(III)–ECR spectrophotometric signal.

pared) with ECR. The length of this reactor did not affect the final absorbance, thereby supporting our previous assumption that no reaction between Al(III) and ECR occurred at this pH. A length of 50 cm was chosen for R_3. As in R_4 the reaction product was formed slowly, increasing its length increased the measured absorbance. By using an R_4 length of 300 cm, a compromise was made between high sensitivity and rapidity. This resulted in ca. 20% sensitivity being lost, but the dead time of the flow-rate gradient experiment was kept at 70 s.

As noted before, the pH was a key variable. Its dramatic influence on the final absorbance recorded was due to the severe pH-dependence of the absorbance of the excess reagent used. The reaction was faster in slightly acidic media. Classical phosphate, and di- or tricarboxylic acid buffers were unusable with this chemical system as they severely interfere. MES was chosen as buffer because of its ideal pK_a of 6.1 and its similarity with ECR. It also provided excellent results thanks to its high buffering capacity, as well as enhanced sensitivity. Thus, a 0.2 M MES buffer of pH 6.3 was finally used. Oscillations in the pH of the waste channel during each flow-rate gradient experiment (Fig. 1) were of ca. 0.01–0.04, but a change of 0.05 in pH resulted in a variation in absorbance of ca. 0.03, thus showing the enor-

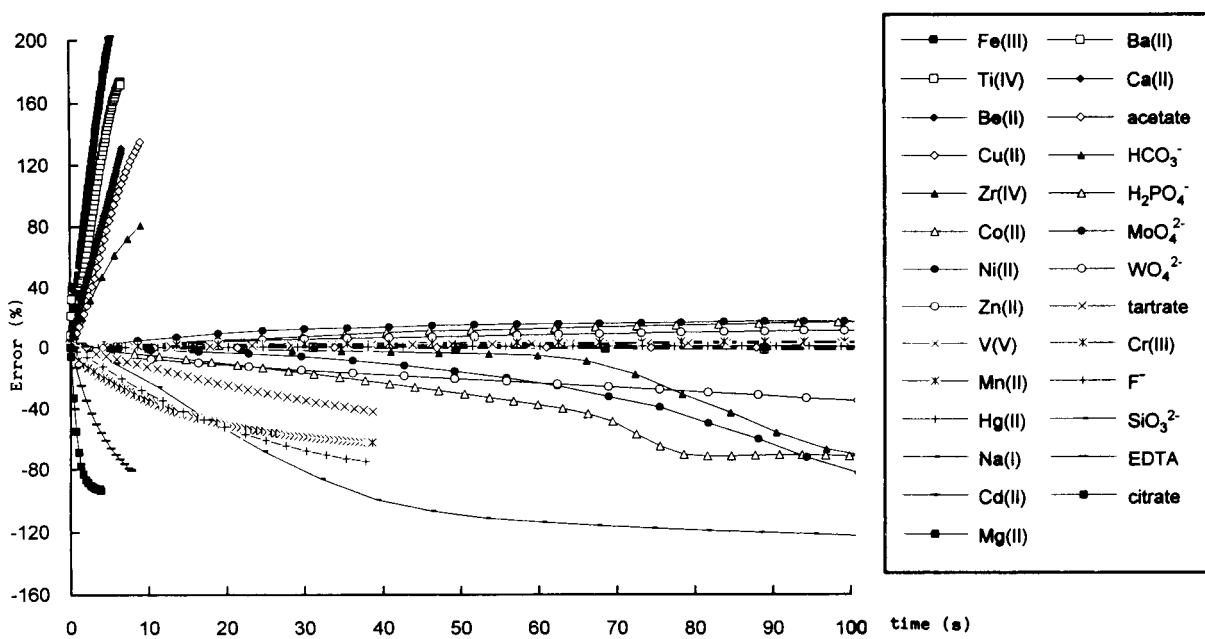

Fig. 4. General overview of the effects caused by the foreign species studied on the Al(III)–ECR system.

Table 1
Classification of interferents with the Al(III)–ECR system according to the type of effect produced

Group	Species	Type of effect
I	Fe(III), Be(II), Ti(IV), Cu(II), Zr(IV)	Severe positive error
II	Cr(III), F^-, citrate, tartrate, EDTA	Strong negative error
III	HCO_3^-, SiO_3^{2-}, $H_2PO_4^-$, MoO_4^{2-}, WO_4^{2-}	Negative error
IV	Mg(II), Ca(II), Ba(II), Cd(II)	Slight negative error
V	Mn(II), Ni(II), Co(II), Zn(II), Hg(II)	Slight positive error
VI	Na(I), K(I), NO_3^-, SO_4^{2-}	No influence
VII	Sn(II), Pb(II), V(V), acetate	Not classified in previous groups

mous influence of pH on the reaction under study.

The linear range of the calibration graph for aluminium determination was obtained by performing flow-rate gradient experiments with the manifold depicted in Fig. 1. A continuous absorbance vs. aluminium concentration linear graph was obtained between 0 and 2 μg ml^{-1} Al(III), with a relative standard deviation (R.S.D.) of $\pm 1.4\%$ for 0.91 μg ml^{-1} ($n = 6$).

3.1. Study of the influence of foreign species

Over 30 different ionic species were tested by continuously scanning an interferent to aluminium weight ratio up to 1200. The original recordings obtained for three different species (Fe(III), F^-, and Pb(II)) are shown in Fig. 3. The validity of these experiments was limited by the condition that no precipitation should occur within the tubes during the process. Otherwise, results that were difficult to quantify were obtained. By way of example, the recording for Pb(II) is given in Fig. 3 (curve B). Unreliable results can easily be identified by the increase of absorbance after the PP was stopped (no foreign species were introduced into the system). This additional peak after the proper flow-rate gradient experiment arose from precipitation or from flushing of adsorbed particles on the tube walls out the system. This effect was only recorded for lead, tin, titanium, zirconium and high concentrations of ammonium. For the most foreign species studied the absorbance returned rapidly to its initial value (signal of the Al(III)–ECR complex) after the PP was stopped (see Fig. 3). In order to express the different measurements in a comparable way, the percent error of the signal relative to that provided by the Al(III)–ECR complex alone was used on the y-axis, whereas the foreign species the [interferent]/[Al(III)] concentration ratio was used on the x-axis. Fig. 4 illustrates the effect of various species on the Al(III)–ECR system.

Table 2
Selectivity coefficients, $k_{Al,I}$, for the groups I and II of species listed in Table 1

Group	Species	$k_{Al,I}$	Group	Species	$k_{Al,I}$
I	Fe(III)	0.36	II	Citrate	−0.71
	Be(II)	0.20		EDTA	−0.18
	Cu(II)	0.16		F^-	−0.027
	Zr(IV)	0.12		Tartrate	−0.012

3.2. Classification of foreign species

The effects observed in Fig. 4 were used to classify foreign species. Six groups were thus established, plus an additional, seventh group that included species which could not be reasonably classified in any of the previous groups (see Table 1).

Like Al(III), group I formed highly coloured complexes with ECR. These species introduce a

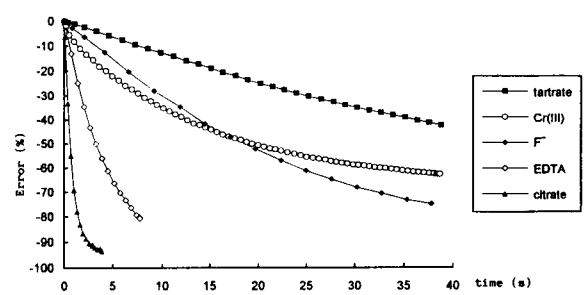

Fig. 5. Graphical results obtained from the flow-rate gradient experiments for the second group of interferents (see text): tartrate (A), fluoride (B), chromium(III) (C), EDTA (D), and citrate (E).

positive error in quantitative spectrophotometric methods where ECR is used as complexing reagent [14]. The selectivity coefficient ($k_{Al,I}$, in this case) defined by Hansen et al. [3] can be used to quantify the interference produced by a foreign species:

$$C'_{Al} = C_{Al} + k_{Al,I}C_I$$

where C_{Al} is the actual concentration of aluminium in the sample, C_I that of interferent, and C'_{Al} that of Al(III) measured in the presence of the interferent (I). Table 2 lists the $k_{Al,I}$ obtained values for the most important interferents. Higher absolute $k_{Al,I}$ values resulted in greater interferences.

Except for Cr(III), the interferents in group II (Table 1) form stable complexes with Al(III) (F^-, citrate, tartrate, and EDTA); hence, they strongly depress the Al(III)–ECR signal. Citrate posed the most serious interference in this group (Fig. 5; the greatest $k_{Al,I}$ absolute value in Table 2), whereas tartrate was the least interfering (the smallest $k_{Al,I}$ value in Table 2). The interference of Cr(III) was due to the formation of a complex with the reagent which resulted in a bathochromic shift.

Only inorganic acid anions were included in group III (Table 1), which caused a negative error. Hydrogencarbonate ion was special as it was the only ion that caused the pH to change during the flow-rate gradient experiment (6.2–6.3) and a dramatic signal decrease (as a negative peak) between 100 and 120 s after the flow-gradient experiment was started. This anomalous behaviour could be due to the pK_1 value of H_2CO_3 (6.37 at $I = 0$). The species in groups IV and V

Table 3
Level of interference for different foreign species expressed as the maximum tolerated ratio of the species studied corresponding to the aluminium concentration used

Species	Reaction time 30 s 1 R.S.D.	Reaction time 30 s 2 R.S.D.	Reaction time 30 s 3 R.S.D.	Reaction time 24 h 3 R.S.D.
Fe(II)	0.02	0.06	0.09	0.45
Ti(IV)	0.01	0.03	0.06	0.1
Be(II)	0.05	0.1	0.15	1
Zr(IV)	0.1	0.18	0.27	2.5
Cu(II)	0.1	0.2	0.32	0.25
Ni(II)	3.5	6	8	5
Co(II)	6	11	17	12
Zn(II)	6	14	22	17
Mn(II)	10	45	150	20
V(V)	30	100	210	75
Hg(II)	200	> 300	> 300	> 300
Ba(II)	75	180	480	200
Ca(II)	80	140	220	> 1200
Mg(II)	150	300	600	220
Na(I)	1100	> 1200	> 1200	> 1200
Citrate	0.01	0.025	0.04	0.025
EDTA	0.1	0.16	0.23	0.005
Cr(III)	0.15	0.27	0.40	0.2
F^-	0.4	0.8	1.35	3
Tartrate	1.3	2.4	3.5	3
Acetate	150	200	260	> 600
WO_4^{2-}	1	2.3	3.8	4.5
$H_2PO_4^-$	3	6	8	0.5
SiO_3^{2-}	7.5	15	22	0.25
MoO_4^{2-}	8.5	16	23	> 80
HCO_3^-	23	37	52	50

gave rise to small errors and can be considered not to interfere at low concentrations.

One other interesting classification of interferents can be made in terms of the time at which analytical readouts were taken. Flow experiments allow one to distinguish the influence of the different species assayed after a reaction time of 30 s (a typical reaction time in FIA), when the Al(III)–ECR complex was not completely formed and kinetic effects may play a prominent role. A second readout was taken ca. 24 h later, by which time equilibrium had been reached. In this way, the thermodynamic effects of the different species were compared to their kinetic behaviour. Thus, the foreign species studied were re-grouped into different categories. The first new group was formed by species whose interfering effect increased at equilibrium: citrate, tartrate, EDTA, F^-, Cr(III), $H_2PO_4^-$, SiO_3^{2-}, Zn(II), Ni(II), Co(II), Mn(II), Mg(II) and V(V). Cations reacting with ECR to form coloured complexes were Cr(III), Zn(II), Ni(II), Co(II), Mn(II), Mg(II) and V(V). The other species form complexes with Al(III) but do not react with ECR (citrate, tartrate, EDTA, fluoride, dihydrogenphosphate and silicate). The second group comprised all the species whose effect was decreased at equilibrium: Fe(III), Be(II), Cu(II), Zr(IV), and MoO_4^{2-}. A third group was formed by all the species for which no clear trend was observed: HCO_3^-, WO_4^{2-}, Ca(II), Cd(II), Ba(II), Ti(IV) and acetate.

3.3. Quantitation of interferences

The maximum tolerated ratios of foreign species to analyte were determined as final results of the work. The ratios depend basically on how large acceptable errors may be. Three different levels were thus defined in terms of precision of the analytical process. The precision of the actual analytical determination, expressed as R.S.D., was compared with the error introduced by the presence of a foreign species. Three different levels were chosen corresponding to one, two and three times that of the R.S.D. An R.S.D. of 1.4% was obtained for the reaction under study, under specified conditions (see above). This resulted in interfering level ranges of $\pm 1.4\%$, $\pm 2.8\%$ and $\pm 4.2\%$ of the analytical result being set (Table 3). For comparison, the results obtained at 24 h for a tolerated error of 3 times the R.S.D. are given. Based on the levels given in Table 3 higher concentrations of a foreign species were tolerated in most cases when the analytical readout was taken under kinetic rather than equilibrium conditions. This was specially obvious with strong masking agents such as citrate, EDTA, silicate and dihydrogenphosphate. By contrast higher concentrations of the strong positive interferents (Fe(III), Be(II), and Cu(II)) were better tolerated under thermodynamic than under kinetic conditions.

4. Conclusions

The proposed automated flow methodology for studying the selectivity of analytical methods is potentially applicable to any of the usual chemicals used in unsegmented flow systems. The new methodology, based on the establishment of interferent concentration gradients improves on existing flow-rate gradient procedures as the resulting flow-rate remains constant throughout the experiment. The recordings automatically obtained clearly show the interferent to analyte concentration ratio at which the foreign species significantly affects the analytical signal used to determine the analyte. Additional information from these recordings can be obtained since a wide interference to analyte ratio range is recorded in each experiment. This information allows foreign species to be classified in groups and each maximum tolerated foreign species to analyte ratio to be quantified. The proposed methodology is characterized by its simplicity, rapidity and precision. Moreover, the information obtained is referred to the specific experimental conditions used for the determination of the analyte in the flow manifold (kinetic conditions), against the conventional selectivity information reported in the literature, which normally involves equilibrium conditions.

5. Acknowledgements

The CICYT is acknowledged for financial support (Grant No. PB93-0717). B. Lendl is also grateful to ERASMUS Program (PIC 92-A-2010/13) for a personal fellowship.

6. References

[1] M. Valcárcel and A. Ríos, Analusis, 18 (1990) 469.
[2] H. Kaiser, Z. Anal. Chem., 260 (1972) 252.
[3] E.H. Hansen, J. Ruzicka, F.J. Krug and E.A.G. Zagatto, Anal. Chim. Acta, 148 (1983) 111.
[4] M. Agudo, J. Marcos, A. Ríos and M. Valcárcel, Anal. Chim. Acta, 239 (1990) 211.
[5] J. Marcos, A. Ríos and M. Valcárcel, Anal. Chim. Acta, 261 (1992) 489.
[6] J. Marcos, A. Ríos and M. Valcárcel, Anal. Chim. Acta, 261 (1992) 495.
[7] J. Marcos, G. del Campo, A. Ríos and M. Valcárcel, Fresenius' J. Anal. Chem., 342 (1992) 76.
[8] J. Marcos, A. Ríos and M. Valcárcel, Analyst, 117 (1992) 1629.
[9] J. Marcos, A. Ríos and M. Valcárcel, Trends Anal. Chem., 11 (1992) 373.
[10] H. Thaler and F.H. Mühlberger, Fresenius' Z. Anal. Chem., 144 (1955) 241.
[11] T. Miller and F. Kúnos, Fresenius' Z. Anal. Chem., 133 (1938) 102.
[12] O. Werner, Beih. Z. Ver. Deutsch. Chemiker, 48 (1944) 92.
[13] B.F. Reis, H. Bergamin, E.A.G. Zagatto and F.J. Krug, Anal. Chim. Acta, 107 (1979) 309.
[14] E. Bishop, Indicators, Pergamon, Oxford, 1972.

ELSEVIER

Analytica Chimica Acta 289 (1994) 195–204

ANALYTICA CHIMICA ACTA

Application of gas chromatography–combustion–isotope ratio mass spectrometry to carbon isotopic analysis of methane and carbon monoxide in environmental samples

Yiqiang Zeng [1], Hitoshi Mukai, Hiroshi Bandow [2], Yukihiro Nojiri *

Global Environment Research Group, National Institute for Environmental Studies, 16-2 Onogawa, Tsukuba, Ibaraki 305, Japan

(Received 19th July 1993; revised manuscript received 16th November 1993)

Abstract

A method for the determination of isotopic composition by combined gas chromatography–combustion–isotope ratio mass spectrometry was examined in order to measure the stable carbon isotope ratios of methane and carbon monoxide in environmental samples. The factors causing deviations in the observed value of $\delta^{13}C$ were studied by analysing a mixed gas sample using different furnace temperatures and sample amounts. The calibration procedure for correcting the measured value is described in detail. The carbon isotopic abundances of gases from biomass burning were determined. A single determination with an accuracy of ca. 0.5‰ as $\delta^{13}C$ took about 10 min. The sample consumption was about 0.2 μl at standard temperature and pressure. The proposed method is simpler and faster than other procedures, permitting a large number of samples to be analysed within a short time while only a small amount of sample is consumed.

Key words: Gas chromatography–mass spectrometry; Isotope dilution methods; Biomass burning; Carbon isotope ratio; Methane

1. Introduction

Recently, the concentrations of many atmospheric trace constituents have been increasing in the troposphere [1]. Major causes of the increases in some trace constituents, such as carbon dioxide and chlorofluorocarbons, are fairly well understood. However, the causes of the increase in other constituents, such as CH_4, N_2O and CO, are not well known because there are many different sources having various emission strengths [1,2].

Isotopic data for these compounds in the source gases and in the atmosphere could facilitate the understanding of the atmospheric budget of these compounds [3–7]. For example, the weighted average of the $\delta^{13}C$ of CH_4 from all sources should be equal to the $\delta^{13}C$ of atmospheric CH_4 when corrected for any fractionation

* Corresponding author.

[1] Present address: Institute of Geochemistry, Chinese Academy of Sciences, Guiyang, Guizhou 550002, China.

[2] Present address: Faculty of Engineering, Osaka Prefectural University, Gakuen-cho, Sakai, Osaka 593, Japan.

SSDI 0003-2670(93)E0654-P

effects in the sink reactions. Isotope data could be useful for evaluating the relative importance of known sources and for discovering overlooked sources. The determination of stable isotopic composition can shed light on the mechanisms for the production and consumption of these compounds, because isotope ratios are excellent tracers [2,5].

A simple and rapid method is desirable for determining the isotopic compositions of a large number of samples. Carbon-containing components should be converted into carbon dioxide, prior to mass spectrometric analysis for stable carbon isotope measurement. This procedure is conventionally done in a separate vacuum system involving complicated processes such as separation, purification and combustion [8,9]. The conventional procedure takes a long time and consumes large amounts of sample. The concentrations of these components in environmental samples are usually low and samples cannot be conveniently obtained and transported in large amounts.

The recent development of gas chromatography–combustion–isotope ratio mass spectrometry (GC–C–IRMS) allows one to make a carbon isotope ratio measurement for volatile organic compounds on smaller samples without pretreatment. This advance makes the carbon isotope measurement simpler and faster than with the conventional method [10–13]. This paper describes carbon isotope measurements of CH_4, CO and CO_2 in gaseous environmental samples with a commercially available GC–C–IRMS system. An example of the application of this method to samples from biomass burning, which is one important source for such compounds, is also reported [14].

2. Experimental

The carbon isotope ratio of a sample is commonly expressed relative to PDB (Pee Dee Belemnite from South Carolina, USA; $R_{PDB} = 0.0112372 \pm 0.0000090$) [15], using the equation $\delta^{13}C = [(R - R_{PDB})/R_{PDB}] \times 1000$ (‰), where R and R_{PDB} are the $^{13}C/^{12}C$ isotopic ratios of for a sample and PDB, respectively. The carbon isotopic data in this study are also expressed as $\delta^{13}C$.

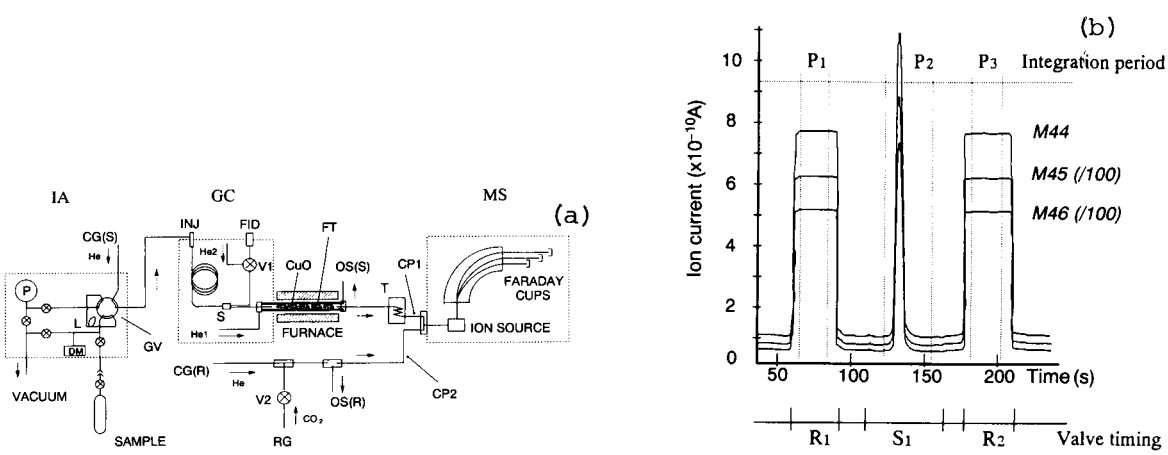

Fig. 1. (a) Schematic diagram of the GC–C–IRMS system and (b) timings of valves on a chromatogram. (a) IA, sample injection apparatus; GV, six-way gas sampling valve; L, sample loop (500 μl); DM, digital manometer; P, pressure gauge; CG(S), CG(R), carrier gases for sample and reference lines, respectively; GC, gas chromatograph with a capillary column; S, splitter, controlling the carrier gas flow to flame ionization detector or combustion furnace; FT, furnace quartz tube packed with CuO; OS(S), OS(R), open splitters for sample and CO_2 reference; T, cryogenic trap to remove water vapour; CP1, CP2, capillaries for sample and CO_2 reference, respectively; RG, reference CO_2 gas; MS, mass spectrometer. (b) R_i, period of V2 opening for recording the isotope ratio of CO_2 reference; S_i, period of V1 closing, to obtain the peak(s) for sample; P_i, period for integrating peaks.

The system employed for isotopic analysis (Fig. 1a) consists of a gas chromatograph (HP5890A; Hewlett-Packard), an interface with a combustion furnace (VG Isotech) and an isotope ratio mass spectrometer (PRISM II; VG Isotech). The PRISM II is a conventional dual-inlet isotope ratio mass spectrometer equipped with three Faraday cups to collect ions of m/z 44, 45 and 46 for CO_2 simultaneously. Ion-current peaks for sample and reference are integrated to calculate $\delta^{13}C$ values. The Craig correction [16] for measured $\delta^{13}C$ values has been included in the program.

A gas-injection line, assembled with a six-way valve, pressure gauges and a sampling loop, is used to inject gas samples quantitatively. The sample pressure in the sampling loop is measured by a digital manometer. The six-way valve injects the gas sample into the GC column. Components in the sample gas are separated using a capillary column (Pora PLOT Q, 25 m × 0.32 mm i.d.) (Chrompack) and then introduced into the flame ionization detector or the combustion furnace by opening or closing a split valve in the interface.

Separated carbon-containing compounds are burnt in the combustion furnace, which is an electrically heated quartz tube (270 mm × 1 mm i.d.) packed with CuO particles. The products of the combustion, CO_2 and H_2O, are carried into a −100°C cryogenic trap to remove water, while CO_2 passes and flows through the capillary into the ion source of the mass spectrometer. CO_2 from a cylinder can be introduced intermittently into the ion source through another capillary as a reference (known isotope ratios of C and O) during the intervals between sample peaks by arranging so-called "window timing" of the reference and the sample. This window timing requires the open time of valves in the interface to be controlled by a computer (Fig. 1b). The carrier gas was research-grade helium, used as received. CuO in the combustion furnace was regenerated, if necessary, overnight at 550–600°C under a small flow of research-grade air.

Before isotopic analysis, the concentrations of CH_4 and CO in sample gases were determined using a gas chromatograph (Shimadzu GC14A) equipped with a thermal conductivity detector, flame ionization detector and a separation column (molecular sieves 13X, 60–80 mesh, packed in a 2 m × 3 mm i.d. stainless-steel column). Those samples which contain concentrations of CH_4 and/or CO higher than 2000 $\mu l\ l^{-1}$ are diluted with research-grade nitrogen gas to about 2000 $\mu l\ l^{-1}$.

Biomass was burnt in the laboratory using a modified domestic incinerator made of steel. Exhaust gases were grab-sampled into 2-l Tedlar bags with a diaphragm pump through stainless-steel pipes which were inserted into the incinerator. The burnt material consisted of stems and leaves of the pine tree (*Pinus densiflora*), and straw and chaff of rice plants, which comprise the biomass most often burnt in Japan. Exhaust gases sampled in the bags were transferred to evacuated glass bottles (0.5 l in volume) within 24 h. It is noteworthy that low molecular-weight compounds such as CH_4, CO, O_2 and CO_2 can penetrate Tedlar film and thus exchange with the surrounding air [17]. Carbon isotope ratios in the biomass materials were also determined by IRMS in combination with a conventional elemental carbon–nitrogen analyser (Carlo Erba NA1500).

3. Results and discussion

3.1. Combustion efficiency and deviation

A commercially available reference gas mixture (CH_4 0.983%, CO_2 1.02%, C_2H_6 0.967%, by volume in N_2) was first analysed with the system to examine the combustion efficiency of the furnace and the precision of the $\delta^{13}C$ measurement by GC–C–IRMS. Table 1 lists the results of the observed peak area of m/z 44 ion current and observed $\delta^{13}C$ values for CH_4 (after conversion to CO_2) and CO_2 under various analytical conditions. The injection volume was ca. 0.02–1 μl under the conditions of standard temperature and pressure (STP) for each compound.

If CH_4 were converted completely into CO_2 during the combustion, the ratio of the peak area of m/z 44 ion current for CH_4 to that for CO_2 should be the same as the ratio of their concentrations (0.96). Lower ratios of the peak areas

(Table 1) indicate incomplete combustion in the furnace. The ratio of the peak areas normalized by the ratio of their concentrations represents the combustion efficiency (Table 1). The combustion efficiency was about 50% at a furnace temperature of 750°C. The efficiency approaches unity at 800°C, although it is less than 90% when the sample amount is large. Higher temperatures may permit a higher combustion efficiency. However, 800°C is the maximum furnace temperature for the equipment used and was also chosen to prolong the lifetime of the CuO particles.

Deviation of $\delta^{13}C$ in the CO_2 sample can be regarded as an intrinsic error associated with this GC–C–IRMS analysis. The $\delta^{13}C$ data for CO_2 (Table 1) indicate an analytical precision of $\pm 0.4‰$ (one standard deviation) under these conditions. Within this analytical precision, this method gives the same $\delta^{13}C$ value for CO_2, independent of the furnace temperature and the sample amount. In contrast, $\delta^{13}C$ observed for CH_4 shows larger deviations at both 750 and 800°C. The average $\delta^{13}C$ values for 750 and 800°C are -29.9 ± 9.9 and $-35.1 \pm 2.7‰$, respectively. This large discrepancy might be caused by incomplete conversion of CH_4 into CO_2 as mentioned above.

The $\delta^{13}C$ of CH_4 depends on peak area at both 750 and 800°C (Fig. 2). The dependence of $\delta^{13}C$ on sample size, is much lower at 800 than that at 750°C. For example, the change in the $\delta^{13}C$ is 0.35 and 22‰ at 800 and 750°C, respectively, for peak areas ranging from 2×10^{-8} to 6×10^{-8} A s. Hence, it is easier to measure CH_4

Table 1
Precision of $\delta^{13}C$ measurements for CH_4 and CO_2 with combustion efficiency of CH_4 in the CuO furnace

Furnace temperature (°C)	CH_4		CO_2		Peak-area ratio (CH_4/CO_2)	Combustion efficiency (%)
	Area [a] ($\times 10^{-8}$ A s)	$\delta^{13}C$ [b] (‰)	Area [a] ($\times 10^{-8}$ A s)	$\delta^{13}C$ [b] (‰)		
750	0.232	−44.78	0.421	−24.82	0.552	57.3
	0.868	−38.76	1.709	−25.49	0.508	52.7
	0.897	−38.00	1.650	−25.63	0.544	57.5
	1.920	−33.87	3.863	−25.58	0.497	51.6
	2.085	−31.87	4.434	−25.19	0.470	48.8
	3.750	−25.39	8.580	−25.60	0.437	45.3
	4.246	−21.86	9.917	−25.88	0.428	44.4
	5.360	−16.43	13.28	−26.25	0.404	41.9
	5.803	−17.82	14.40	−25.67	0.403	41.8
Average		-29.9 ± 9.9		-25.6 ± 0.4		49.0 ± 6
800	1.061	−37.83	1.108	−24.70	0.958	99.4
	1.348	−38.03	1.301	−24.79	1.036	107.4
	1.728	−37.09	1.671	−24.68	1.034	107.3
	3.200	−36.52	3.823	−24.93	0.837	86.9
	3.551	−36.36	3.994	−24.59	0.889	92.2
	3.732	−36.22	3.826	−24.69	0.975	101.1
	3.946	−36.48	4.875	−25.40	0.809	83.9
	4.540	−37.46	5.398	−24.44	0.841	87.3
	5.337	−35.15	6.465	−25.14	0.826	85.7
	6.073	−35.28	7.016	−25.12	0.866	89.9
	7.922	−32.98	9.371	−25.15	0.845	87.7
	8.411	−32.31	9.775	−24.85	0.861	89.3
	11.060	−30.91	14.570	−25.74	0.759	78.8
	11.160	−29.26	14.310	−25.04	0.780	80.9
Average		-35.1 ± 2.7		-24.9 ± 0.3		
		(-36.2 ± 0.8) [c]		(-24.9 ± 0.3) [c]		(90 ± 6) [c]

[a] Peak area of m/z 44 ion current. [b] Real $\delta^{13}C$ values are unknown. [c] The values in the parentheses are the averages and 1σ values for the data within the range of peak areas from 2×10^{-8} to 6×10^{-8} A s.

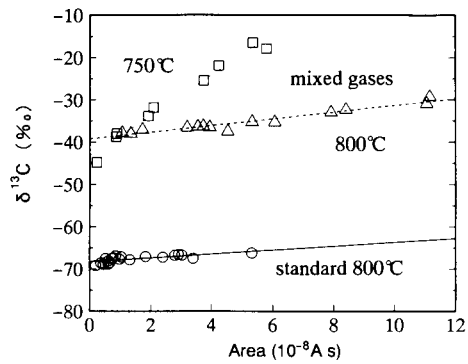

Fig. 2. Results of measurements of $\delta^{13}C$ of CH_4 in mixed sample gases at furnace temperatures of 750 and 800°C, together with the measurements of CH_4 standard gas ($\delta^{13}C = -66.5‰$) at 800°C. These data were plotted against the peak areas.

for $\delta^{13}C$ with an acceptable precision at 800 than at 750°C.

The measurement of the isotopic composition of CH_4 in a standard gas sample, for which $\delta^{13}C$ had been determined as $-66.5‰$ by a conventional method (by courtesy of Mitsubishi Institute of Life Sciences), gave a reasonable value ($-66.77 \pm 0.41‰$, $n = 6$) within the above range of peak area. However, the values became much lower as the peak area of the m/z 44 ion current became smaller than 2×10^{-8} A s. When the peak area was very small ($< 1 \times 10^{-8}$ A s), the deviation from the known reference value increased considerably, as shown in Fig. 3.

These effects can be explained as follows. First, in the present system, m/z 44, 45 and 46 ion currents are collected and amplified simultaneously. The m/z 45 and 46 ion currents are so

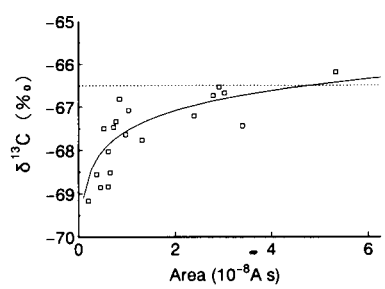

Fig. 3. Measured $\delta^{13}C$ for a CH_4 standard gas. The known value of $\delta^{13}C$ is $-66.5‰$ (dashed line).

small that the programmed calculation of subtracting background current from the observed current would make the ratio (m/z 45/44) smaller because of the non-linearity of the system for small signals. Second, the carbon isotopes were fractionated during incomplete combustion of CH_4 in the CuO furnace. Generally, lighter isotope species are oxidized more easily and the product becomes depleted in heavy isotopes. This is consistent with the measured $\delta^{13}C$ values obtained being smaller than the known value of the CH_4 standard. However, if isotope fractionation were the main factor, it should be enhanced when the conversion efficiency is low at lower furnace temperatures or with larger sample amounts. In fact, the correlation between $\delta^{13}C$ value and peak area (Fig. 2) suggests that other factors affect the $\delta^{13}C$ value in this measurement.

It is highly probable that an ion–molecule reaction occurs in the ion source of the mass spectrometer. Residual CH_4 from incomplete combustion in the furnace is brought into the ion source and could be ionized.

$$CH_4^+ + CO_2 \rightarrow CH_3 + HCO_2^+$$

may occur, resulting in the formation of HCO_2^+ ions [18]. Therefore, $H^{12}CO_2^+$ ions overlap with $^{13}CO_2^+$ ions in the m/z 45 ion current when extra large amounts of sample are injected. $\delta^{13}C$ values larger than the actual values measured under the conditions of low conversion efficiency could be accounted for in part by the contribution of $H^{12}CO_2^+$. Such a process would make the $\delta^{13}C$ increase greater with increase in peak area at lower furnace temperature.

Hence it was concluded that the reproducibility of the measurement of $\delta^{13}C$ with a furnace temperature of 800°C provides an acceptable precision for determining the isotopic composition of CH_4 provided that both a proper sample injection and a suitable calibration are made.

On the other hand, as CO is much more easily converted into CO_2 than is CH_4, there is no serious combustion efficiency problem for CO. In this system, when a prepared sample of mixed CO and CO_2 was analysed, the ratio of peak areas (CO/CO_2) was always equal to the ratio of concentrations over a wide range of furnace tem-

Table 2
$\delta^{13}C$ of CO in a working standard (furnace 700°C, column −60°C)

Area ($\times 10^{-8}$ A s)	$\delta^{13}C$ (‰)	Area ($\times 10^{-8}$ A s)	$\delta^{13}C$ (‰)
5.815	−28.41	3.390	−28.19
10.20	−29.06	8.388	−29.62
6.848	−28.90	8.068	−28.65
7.434	−29.54	10.88	−28.70
4.676	−28.71	16.06	−29.62
7.994	−28.85		

$\delta^{13}C$ average = −28.93‰, σ = 0.48, n = 11.

peratures (550–800°C), which indicates that adequate combustion of CO occurred. The effect of sample amount of CO on the observed $\delta^{13}C$ was examined (Table 2).

In the ion current chromatogram, an extra peak was often observed that overlapped the CO peak. By injecting pure nitrogen under the same analytical conditions, the peak of N_2O was confirmed to have a retention time close to that of CO_2 converted from CO. This indicates that the extra peak might be due to N_2O derived from N_2. Therefore, it is necessary to separate CO from N_2 in order to determine the $\delta^{13}C$ of CO in an air or nitrogen matrix sample using this GC–C–IRMS system. When operating at a column temperature of −55°C, the peak of N_2O from N_2 appears clearly ahead of that of CO_2 from CO (Fig. 4).

3.2. Measurement of samples from biomass burning and correction of observed data

The concentrations of CH_4 in burning biomass samples measured in this study were about one

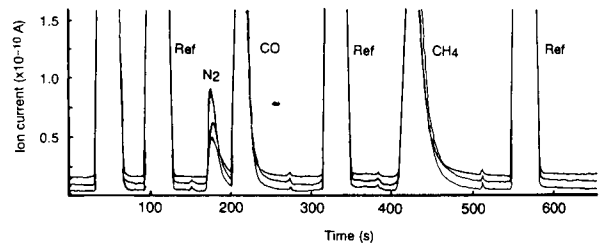

Fig. 4. Enlarged spectrum of the measurement of CO and CH_4 mixture in N_2 at a GC oven temperature of −55°C.

tenth of that of CO (Table 3). Therefore, the $\delta^{13}C$ values for CH_4 and CO were measured separately in order to adjust the amount of sample injected.

The working standard (wstd, $\delta^{13}C = -65.6$‰) was prepared with pure methane. Research-grade nitrogen was used to dilute the pure methane to 2000 μl l^{-1}. A typical amount of working standard injected was 0.4 μl (STP) CH_4 for a single measurement. Working standard sample was introduced intermittently during sample analysis. Measured values can be corrected to exclude the error caused by incomplete combustion in the furnace, which resulted in carbon isotope fractionation as described above.

With the definition of $\delta^{13}C = [(R - R_{PDB})/R_{PDB}] \times 1000$(‰), the $^{13}C/^{12}C$ isotopic ratio of a sample is rewritten as follows:

$$R = (\delta^{13}C/1000 + 1)R_{PDB} \quad (1)$$

As mentioned above, incomplete combustion in the CuO furnace and the ion source of the mass spectrometer can cause a deviation in the measured $\delta^{13}C$ value from the real value. Therefore,

Table 3
Characteristics of biomass materials and composition of burning biomass exhaust samples analysed in this study

Sample	Biomass material			Burning temperature (°C)	Composition of burning biomass exhaust				
	Elemental composition		Water content (%)		O_2 (%)	CO_2 (%)	N_2O (nl l^{-1})	CO (μl l^{-1})	CH_4 (μl l^{-1})
	C (%)	N (%)							
Rice chaff, dry	34.4	0.28	11	470	20.4	0.51	300	1300	80
Ricestraw, dry	36.9	0.43	18	600–800	11.8	8.83	210	10300	1120
Pinetree, live (*Pinus densiflora*)	53.2	0.81	36	75–100	20.4	0.58	380	1020	101
				200–230	19.0	1.76	590	2250	233
				200–360	19.2	1.56	690	2960	302
				450–520	16.4	4.11	–	5400	570

the measured $^{13}C/^{12}C$ ratio for wstd, $R_{obs(wstd)}$, may not be equal to $R_{CH_4(wstd)}$, the actual value for the wstd. If the value $R_{CH_4(wstd)}$ is known, the ratio of $R_{obs(wstd)}$ to $R_{CH_4(wstd)}$ represents a correction factor for this analysis. Using Eq. 1, the correction factor $\alpha = R_{obs}/R_{CH_4}$ is expressed as

$$\alpha_{(wstd)} = \left[\delta^{13}C_{obs(wstd)} + 1000\right] / \left[\delta^{13}C_{CH_4(wstd)} + 1000\right] \quad (2)$$

for working standard CH_4.

When a sample is measured, the same kind of deviation should occur. Under the same analytical conditions, it is reasonable to assume that one can use the same correction factor for sample CH_4 as was calculated for working standard CH_4, i.e., $\alpha_{(sample)} = \alpha_{(wstd)}$. Hence the $\delta^{13}C$ value of CH_4 in samples is corrected using the following equation:

$$\delta^{13}C_{CH_4(sample)} = \left\{\left[\delta^{13}C_{CH_4(wstd)} + 1000\right] \times \left[\delta^{13}C_{obs(sample)} + 1000\right]\right\} \times \left\{\delta^{13}C_{obs(wstd)} + 1000\right\}^{-1} - 1000 \quad (3)$$

where $\delta^{13}C_{CH_4(sample)}$ and $\delta^{13}C_{obs(sample)}$ are the corrected and the observed $\delta^{13}C$ values, respectively, for the sample concerned. The average of the three determinations for each sample was used for $\delta^{13}C_{obs(sample)}$. The average of the nearest two observed values for wstd are used as $\delta^{13}C_{obs(wstd)}$ for each sample in the measurement sequence. The known $\delta^{13}C_{CH_4(wstd)}$ value was $-65.6‰$.

No correction of the isotopic ratios was made for CO in the biomass samples (Table 4). The

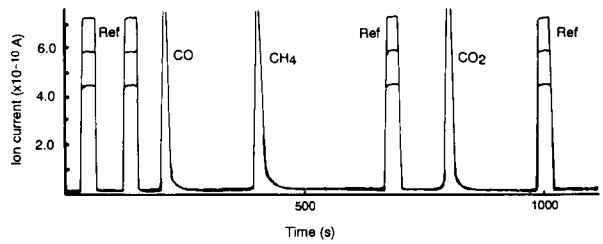

Fig. 5. Arrangement of peaks for sample and reference to measure CO, CH_4 and CO_2 with one injection. GC column temperature, −55°C for 4.6 min, then increased and to 5°C at 70°C min^{-1}.

precision of the $\delta^{13}C$ data for CO was 0.5‰ judged from the data in Table 2. Both CH_4 and CO in the smoke had fairly close $\delta^{13}C$ values to those of the original biomass materials, as shown in Table 4. It is also interesting that the concentration and $\delta^{13}C$ of CO in the burning pine tree exhaust increased as the burning temperature increased, although the reason for the trend is unknown. Although the samples were not sufficient to study the characteristics of biomass burning, this system was found to be very useful for measuring this kind of mixed gas sample, because a single determination of CH_4 or CO takes about only 10 min for the whole procedure from injection to printing out the result.

3.3. Improvements to the method

If the concentrations of components in a mixed gaseous sample are similar, it is possible to determine the isotope ratios of each component with only one injection. For example, two samples, mixtures of CO, $CH_4(\delta^{13}C = -65.6‰)$ and $CO_2(\delta^{13}C = -26.8‰)$ in N_2 with concentrations

Table 4
Isotopic composition of carbon in biomass materials and in burning biomass exhaust samples

Sample	Biomass material (‰)	Combustion temperature (°C)	CO		CH_4	
			$\mu l\,l^{-1}$	$\delta^{13}C$ (‰)	$\mu l\,l^{-1}$	$\delta^{13}C$ (‰)
Rice chaff, dry	−26.57 ± 0.13	470	1300	−28.6	80	–
Rice straw, dry	−27.75 ± 0.29	600–800	10300	−19.9	1120	−20.5
Pine tree, live	−29.80 + 0.96	75–100	1020	−31.5	101	–
(*Pinus densiflora*)		200–230	2250	−31.0	233	−29.7
		200–360	2960	−28.4	302	−30.8
		450–520	5400	−25.8	570	−28.0

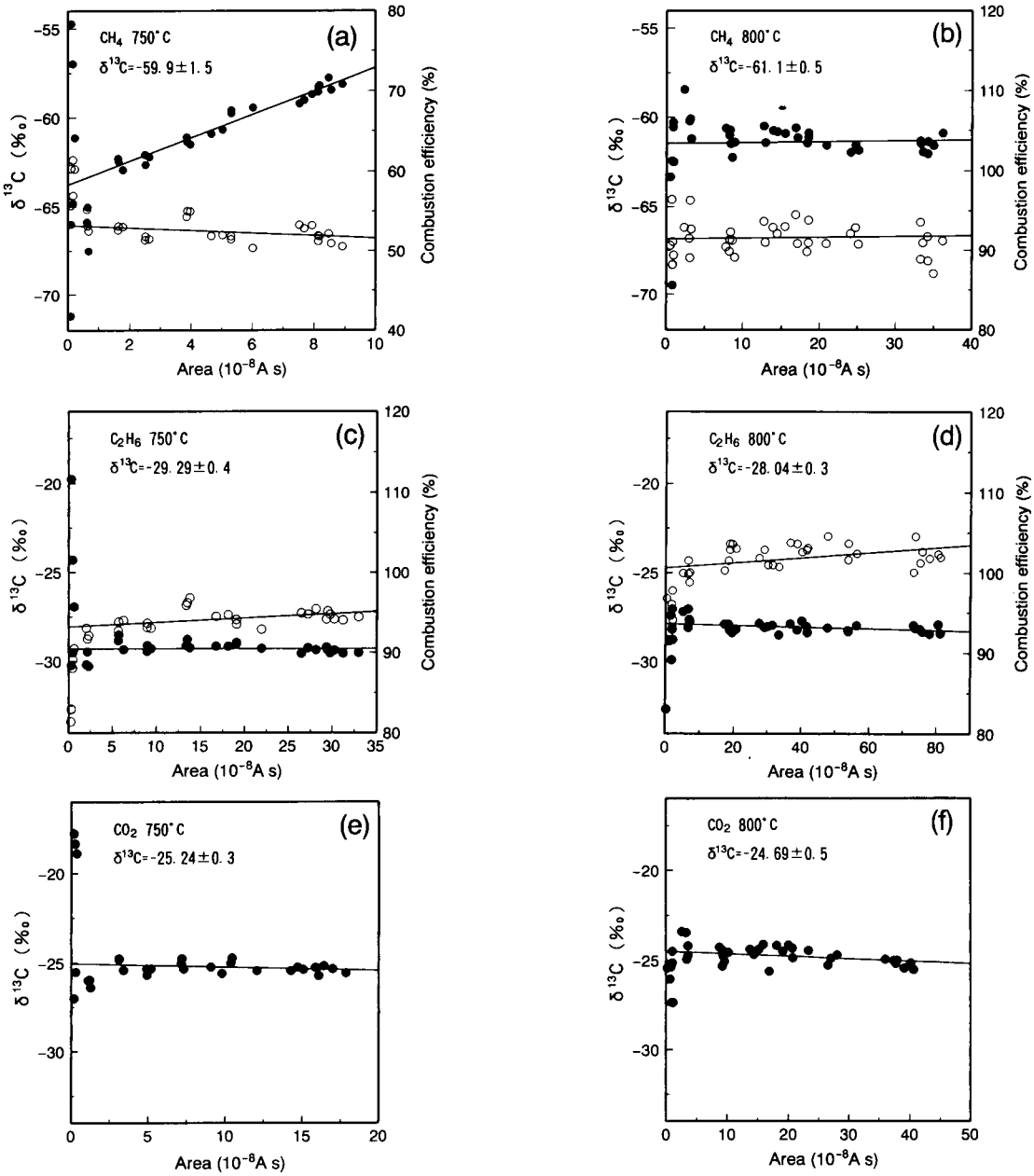

Fig. 6. Correlation between the observed $\delta^{13}C$ value and combustion efficiency vs. peak area at furnace temperatures of 750 and 800°C. Solid circles indicate $\delta^{13}C$ of (a, b) CH_4, (c, d) C_2H_6 and (e, f) CO_2. Open circles indicate the combustion efficiency. The $\delta^{13}C$ data are average values for the points having peak areas larger than 2×10^{-8} A s. (a) CH_4 at 750°C; (b) CH_4 at 800°C; (c) C_2H_6 at 750°C; (d) C_2H_6 at 800°C; (e) CO_2 at 750°C; (f) CO_2 at 800°C.

of 2000 $\mu l\,l^{-1}$, were analysed. The initial temperature of the GC column was kept at −55°C for 4.6 min to separate CO from N_2, then the column temperature was raised to 5°C at 70°C min^{-1}. Subsequently, the peaks of CH_4 and CO_2 could be recorded within 15 min (Fig. 5). A higher GC

Table 5
Measurement of mixed samples in one injection

Canister	$\delta^{13}C$ (‰)		
	CO	CH_4 [a]	CO_2 [a]
A	−27.58	−63.96	−26.47
	−27.74	−64.30	−26.27
	−27.90	−65.66	−27.97
Average	−27.7 ± 0.2	−64.6 ± 0.9	−26.9 ± 0.9
B	−27.52	−64.84	−26.52
	−27.88	−65.13	−26.26
	−27.98	−65.08	−26.19
	−27.89	−64.37	−26.87
Average	−27.8 ± 0.2	−64.9 ± 0.3	−26.5 ± 0.3

[a] $\delta^{13}C$ values of CH_4 and CO_2 should be −65.6 and −26.8‰, respectively.

column oven temperature makes the peaks of CH_4 and CO_2 elute faster, but with a higher background. Data from simultaneous measurements (Table 5) show almost the same precision level for each component as for separate measurements (Tables 1 and 2). It is also found that observed $\delta^{13}C$ values of CO_2 and CH_4 are very close to the values expected. These data (Table 5) were obtained by the analysis of about a 0.4-μl sample amount (STP) for each component with a CuO furnace temperature of 800°C. It is obvious that it takes less time for simultaneous measurements than for separate measurements.

It is important to keep the oxidant (CuO) in good condition, particularly when CH_4 is determined. The relationship between the observed $\delta^{13}C$ and combustion efficiency was scrutinized carefully. When the granular CuO packed previously was replaced with a new type of fresh CuO (columnar type, 0.5 mm i.d. and a few mm long), the combustion efficiency improved and an extended range of sample amount giving stable combustion efficiencies was obtained. Fig. 6 shows the results of combustion experiments with another standard gas mixture of CH_4, CO_2 and C_2H_6 in N_2 gas. The combustion efficiency at 750°C is still poor for CH_4 and the observed values of $\delta^{13}C$ became greater with increase in the amount of sample injected (Fig. 6a), owing to the contribution of $H^{12}CO_2^+$ produced from the ion reaction mentioned above. The combustion efficiency for CH_4 was around 55% in this instance whereas that for C_2H_6 was *ca.* 95% at the same temperature. When the combustion efficiencies are larger than 90% for both CH_4 and C_2H_6, namely at a furnace temperature of 800°C for CH_4 and at 750 and 800°C for C_2H_6, the observed $\delta^{13}C$ of CH_4 and C_2H_6 remain constant within the whole experimental range of sample amount. The effect of the ion–molecule reaction is removed and the dominant factor becomes the isotopic discrimination (lighter isotopic molecules react more readily). As a result, the observed values of $\delta^{13}C$ of C_2H_6 at 750°C appear slightly more negative than the values at 800°C. However, the difference is smaller than with CH_4, as C_2H_6 is more easily converted into CO_2, even at lower furnace temperatures.

The standard deviation of $\delta^{13}C$ of CO_2 (Fig. 6) shows the precision of the system excluding the effects of combustion efficiency. Without conversion, CO_2 passes directly through the furnace into the ion source. Therefore, the observed values at both 750 and 800°C are nearly constant, regardless of the furnace temperature and sample amount, the deviation is 0.3 and 0.5‰ at 750 and 800°C, respectively. This precision is worse than when this system is used as a conventional dual-inlet mass spectrometer, implying other interferences. The background level is a few percent relative to sample signal intensity at a GC oven temperature of 30°C. However, the background increases with increasing oven temperature and reaches an intensity similar to that of the sample signal. Although the background values will be subtracted from the sample signals during calculation, background fluctuations will greatly affect the precision of the observed value. In order to decrease the background noise, it would be helpful to use a suitable column from which less organic compound is flushed out and converted into CO_2 in the furnace.

4. Conclusion

Compared with the conventional method, GC–C–IRMS has an advantage of simplicity and speed so that a large number of samples can be analysed within a shorter time while smaller

amounts of sample are consumed. However, the present data show that further improvements in precision are necessary, especially for environmental samples of low concentration.

5. Acknowledgements

The authors thank Dr. N. Yoshida (Toyama University) for helpful discussions and Dr. A. Sugimoto (Center for Ecological Research, Kyoto University) for providing the standard CH_4 gas and helpful discussions. The authors also are grateful to Dr. A. Tanaka (National Institute of Environmental Studies) and Dr. T. Nakamura (Tokyo University of Fisheries) for providing facilities in the GC–C–IRMS laboratory and Dr. H. Moritomi and Dr. Y. Suzuki (National Institute of Resource and Environment) for their cooperation in carrying out the biomass burning experiments.

6. References

[1] R.T. Watson, H. Rodhe, H. Oeschger and U. Siegenthaler, in J.T. Houghton, G.J. Jenkins and J.J. Ephraums (Eds.), Climate Change, the IPCC Scientific Assessment, Cambridge University Press, Cambridge, 1990, p. 1.
[2] R.J. Cicerone and R.S. Oremland, Global Biogeochem. Cycles, 2 (1988) 299.
[3] S.C. Tyler, J. Geophys. Res., 91 (1986) 13232.
[4] S.C. Tyler, J. Geophys. Res., 92 (1987) 1044.
[5] S.C. Tyler, P.R. Zimmerman, C. Cumberbatch, J.P. Greenberg, C. Westberg and J.P.E. Darlington, Global Biogeochem. Cycles, 2 (1988) 341.
[6] C.M. Stevens and A. Engelkemeir, J. Geophys. Res., 93 (1988) 725.
[7] C.M. Stevens. and F.E. Rust, J. Geophys. Res., 87 (1982) 4879.
[8] C.M. Stevens. and L. Krout, Int. J. Mass Spectrom. Ion Phys., 8 (1972) 265.
[9] D.C. Lowe, and C.A.M. Brenninkmeyer, S.C. Tyler and E.J. Dlugkencky, J. Geophys. Res., 96 (1991) 15455.
[10] M. Bjorøy, K. Hall, P. Gillyon and J. Jumeau, Chem. Geol., 93 (1991) 13.
[11] P.A. Eakin, A.E. Fallick and J. Gerc, Chem. Geol., 101 (1992) 71.
[12] M. Desage, R. Guilluy, J.L. Brazier, H. Chaudron, J. Girard, H. Cherpin and J. Jumeau, Anal. Chim. Acta, 247 (1991) 249.
[13] K.J. Goodman and J.T. Brenna, Anal. Chem., 64 (1992) 1088.
[14] P.D. Quay, S.L. King, J. Stutsman, D.O. Wilbur, L.P. Steele, I. Fung, R.H. Gammon, T.A. Brown, G.W. Farwell, P.M. Grootes and F.H. Schmidt, Global Biogeochem. Cycles, 5 (1991) 55.
[15] J. Koziet, A. Rossmann, G.J. Martin and P.R. Ashurst, Anal. Chim. Acta, 271 (1993) 31.
[16] H. Craig, Geochim. Cosmochim. Acta, 12 (1957) 133.
[17] S. Okada and M. Tezuka, J. Jpn. Assoc. Pet. Technol., 54 (1989) 1.
[18] D. Smith and N.G. Adams, Int. J. Mass Spectrom. Ion Phys., 23 (1977) 123.

ELSEVIER

Analytica Chimica Acta 289 (1994) 205–213

ANALYTICA CHIMICA ACTA

Determination of arsenic compounds in water samples by liquid chromatography–inductively coupled plasma mass spectrometry with an in situ nebulizer–hydride generator

Chorng-jev Hwang, Shiuh-Jen Jiang *

Department of Chemistry National Sun Yat-Sen University, Kaohsiung, 804 Taiwan

(Received 24th September 1993; revised manuscript received 11th November 1993)

Abstract

A preliminary study of an in situ nebulizer–hydride generator as a sample introduction device for an inductively coupled plasma mass spectrometry (ICP-MS) system is described. The samples were ionic arsenic compounds that had undergone chromatographic separation before injection into the hydride generator. L-Cysteine was used instead of potassium iodide as the prereductant. Only mild treatment with nitric acid was necessary to obtain a satisfactory hydride efficiency. The sensitivity, detection limits and reproducibility of a liquid chromatographic (LC)–ICP-MS system with a hydride generator were comparable to or better than an LC–ICP-MS system with conventional pneumatic nebulization or other sample introduction techniques. The limits of detection for various arsenic species were in the range 11–51 ng l^{-1}. The concentrations of various arsenic species in several natural water samples were determined.

Key words: Liquid chromatography; Inductively coupled plasma MS; Arsenic; Hydride generation; Speciation; Waters

1. Introduction

In recent years, it has become recognized that trace metal determinations must involve true metal speciation determination in addition to total metal determination. Biological, biomedical and toxicological properties depend on the specific form in which the metal is present, and combinations of metals have different effects on the environment depending on the nature of the mixture. Information about the various species in a sample can be obtained by a newer form of chromatographic separation with element-selective/specific final detection.

Several reports of liquid chromatography (LC) coupled with inductively coupled plasma mass spectrometry (ICP-MS) for metal speciation determination have appeared [1–11]. In most LC–ICP studies, a conventional pneumatic nebulizer (PN) was employed as the sample-introduction device, although a nebulizer of this type suffers from poor efficiency.

* Corresponding author.

SSDI 0003-2670(93)E0652-N

The hydride generation (HG) sample-introduction technique has been applied in several LC–ICP-MS applications for arsenic speciation determination [12,13]. The use of HG with a gas–liquid phase separator has several advantages. However, a major drawback of these approaches for ICP-MS analysis is that the acid used for the arsenic hydride generation, HCl, forms the molecular ion, $ArCl^+$, which interferes with the determination of arsenic, even when a membrane gas separator is used [14]. In this work, a simple continuous-flow hydride generation system without a conventional gas–liquid phase separator was employed as a sample-introduction device for LC–ICP-MS. An in situ nebulizer–hydride generator has been successfully used in ICP atomic emission spectrometry [15]. With this system, only a minor and inexpensive modification of existing standard equipment was required. Further, L-cysteine was employed as the prereductant, so only a mild nitric acid treatment was required for hydride generation [16–18]. These combinations significantly decreased the interference by $ArCl^+$ molecular ions.

In this study, ionic compounds containing arsenic were separated by reversed-phase LC with a tetrabutylammonium salt as the ion-pairing reagent. The eluate from the LC column was delivered to the hydride generation system and an ICP-MS instrument for arsenic determination. The sensitivity, detection limits and reproducibility of the LC–ICP-MS system with a hydride generator were compared with those obtained with a conventional LC–ICP-MS system with a pneumatic nebulizer. The optimization of the hydride generation LC–HG–ICP-MS technique and its analytical feasibilities, and also its application to the determination of arsenic in riverine water reference sample SLRS-2 and several other natural water samples, are described in this paper.

2. Experimental

2.1. ICP-MS device and conditions

An ELAN 5000 ICP-MS instrument (Perkin-Elmer SCIEX, Thornhill, ON, Canada) was used. Samples were introduced with a cross-flow pneumatic nebulizer with a standard Scott-type spray chamber without a cooling system. ICP conditions that maximized the arsenic ion signal were selected. A solution of 10 $\mu g\ l^{-1}$ arsenic in the mobile phase (to be used for subsequent chromatographic separations) was continuously introduced into the hydride generator. The sensitivity of the instrument may vary slightly from day to day. The operating conditions used throughout this work are summarized in Table 1.

Table 1
Instrumentation and conditions

Plasma conditions	
R.f. power	1100 w
Plasma gas flow-rate	14 l min^{-1}
Intermediate gas flow-rate	0.9 l min^{-1}
Aerosol gas flow	0.75 l min^{-1}
Mass spectrometer settings	
Bessel box lens	10.95 V
Bessel box plate lens	−65.90 V
Photon stop lens	−10.05 V
Einzel lenses 1 and 3	2.97 V
Resolution	Normal
Dwell time	100 ms
Sweeps per reading	2
Reading per replicate	1
Replicate time	200 ms
Points per spectral peak	3
LC conditions	
Column	Vydac 201TP C_{18}, 5 μm, 250 mm × 4.6 mm i.d.
Mobile phase flow-rate	1.0 ml min^{-1}
Mobile phase	2% methanol–1 mM tetrabutylammonium phosphate–2 mM ammonium acetate (pH 5.99)

The data acquisition parameters used for this study are given in Table 1. The element-selected chromatograms were recorded in real time and stored on hard disk with "graphic" software. The dwell time, sweeps per reading and readings per replicate parameters were set so that each data point could be obtained in about 1 s.

2.2. Chromatographic apparatus and conditions

A dual-piston LC pump (Hitachi L-6200), an injector (Rheodyne Model 7125) and various columns comprised the LC system. Samples were

loaded with a syringe on to a 200-μl sample loop. All separations were performed at room temperature under isocratic conditions. Separations were attempted with several combinations of column, organic modifier concentration, type and concentration of counter ion and pH. The conditions given in Table 1 are those which yielded the best chromatographic resolution for the various sets tested. The column outlet was connected to the hydride generation device with Teflon tubing (Fig. 1). The total volume from the column to the spray chamber was only about 0.5 ml.

2.3. Hydride generation system and conditions

A simple and inexpensive continuous-flow in situ nebulizer–hydride generation sample-introduction system was coupled with LC–ICP-MS for arsenic speciation determination in water samples. A schematic diagram of the LC in situ nebulizer–hydride generation system is shown in Fig. 1. Effluent from the hydride generation system was delivered to the pneumatic nebulizer with Teflon tubing and then introduced into ICP-MS instrument for arsenic determination.

The operating conditions for hydride generation were optimized using a flow injection (FI) method. The LC pump and column were removed from the system during these studies. A simple FI system was used for all of the FI work performed in this study. It was assembled from a six-port injection valve (Rheodyne Type 50) with a 200-μl sample loop. Arsenic(III) and arsenic(V) show different behaviours and different sensitivities in the arsine generation process. Because the hydride generation efficiency of arsenic(V) is worse than that of arsenic(III) [19], arsenic(V) was chosen as the model to optimize the operating conditions of the hydride generation system. A 10 $\mu g\ l^{-1}$ stock standard solution of arsenic(V) was prepared. This solution was then loaded into the injection loop and injected into the hydride generation system. Several operating parameters affected the efficiency of hydride formation. The concentration of acids, type and concentration of prereductants, temperature and volume of mixing coil and the concentration of sodium tetrahydroborate ($NaBH_4$) were studied to establish the optimum conditions.

2.4. Reagents

Analytical-reagent grade chemicals were used as received. L-Cysteine was purchased from TCI Chemical (Tokyo) and arsenic(III), arsenic(V) and dimethylarsenic acid (DMAA) from Alfa Chemical (Danvers, MA). Monomethylarsonic acid (MMAA) was obtained from Dr. M.S. Yang (National Tsing Hua University, Hsin Chu, Taiwan). Standard solutions containing 1000 mg l^{-1} (as the element) of each individual species were prepared. These standard solutions were combined and diluted with deionized water obtained with Milli-Q water-purification system (Millipore).

The mobile phases were prepared by dissolving the ion-pairing reagent tetrabutylammonium phosphate (TCI Chemical) and ammonium acetate in LC-grade methanol and deionized water

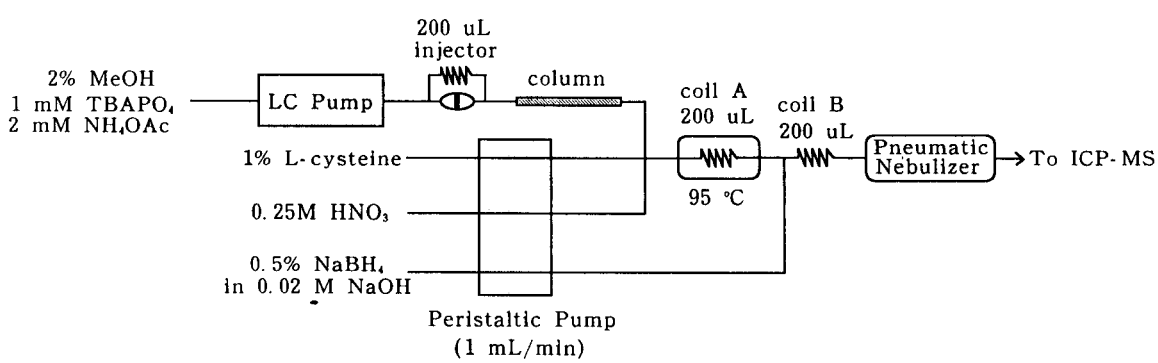

Fig. 1. Schematic diagram of the LC–HG system.

to the desired concentration. Riverine reference material SLRS-2 (National Research Council of Canada, Ottawa) was injected without any sample pretreatment.

3. Results and discussion

3.1. Selection of hydride generation conditions

As tri- and pentavalent arsenic show different behaviours and different sensitivities in the arsine generation process, it is preferred to reduce arsenic(V) to arsenic(III) with prereducing agents before arsine generation. The most popular prereductant is potassium iodide, but it can only be used in strongly acidid media [20,21]. Further, Haring et al. [21] reported that when potassium iodide is used as the prereductant it may take 4–5 h at room temperature to reduce arsenic(V) to arsenic(III) completely.

In this study, L-cysteine was employed as the prereductant. Fig. 2 shows the area of the flow-injection peak as a function of L-cysteine concentration. As the L-cysteine concentration increased, the peak area slowly increased. Because the deposition of solid carbon on the sampling orifice also increased with increasing concentration of L-cysteine, a compromise concentration of 1% (w/v) L-cysteine was used in subsequent experiments.

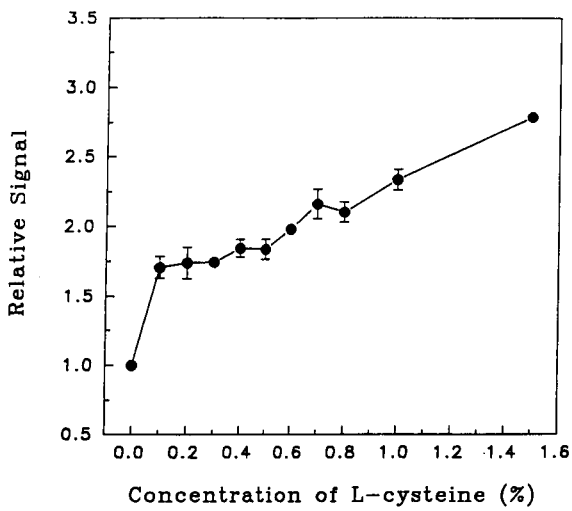

Fig. 2. Effect of L-cysteine concentration on arsenic(V) signal. As concentration, 100 $\mu g\ l^{-1}$; HNO_3 concentration, 0.2 M; $NaBH_4$ concentration, 0.5% in 0.02 M NaOH. All the solution flow-rates were set to 1.0 ml min^{-1}. All the data are relative to the first point. The error bars shown in this and subsequent figures represent the standard deviation for three measurements.

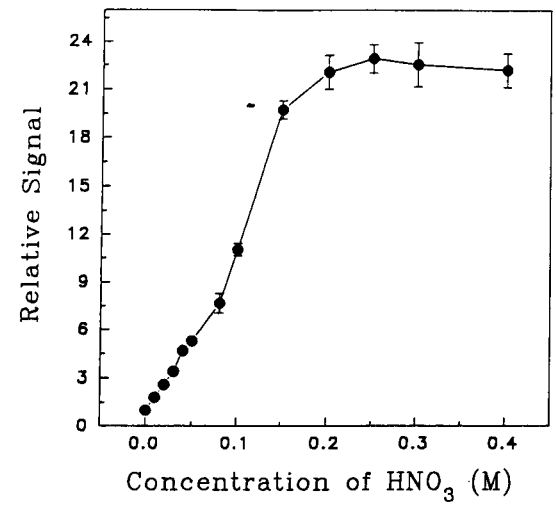

Fig. 3. Effect of acid concentration on the arsenic(V) signal. L-Cysteine concentration, 1%; $NaBH_4$ concentration, 0.5% in 0.02 M NaOH. All the data are relative to the first point.

The acid concentration is critical in the determination of arsenic by hydride generation, hence the effect of acid concentration on the generation of arsine in the presence of L-cysteine was investigated. The results are shown in Fig. 3. In the presence of L-cysteine, arsine production reaches a maximum at an acid concentration of 0.25 M. The low acid concentration required for this technique was an advantage for ICP-MS analysis, as relatively small amounts of hydrogen were produced compared with the amount generated at high acid concentrations.

Fig. 4 shows the area of the flow-injection peaks as a function of the temperature of mixing coil A. As the temperature increased, the peak area increased. An increase in the mixing coil temperature could promote the reduction of arsenic(V) to arsenic(III). For subsequent experiments, the temperature was set at 95°C. Although not illustrated here, it was found in other experi-

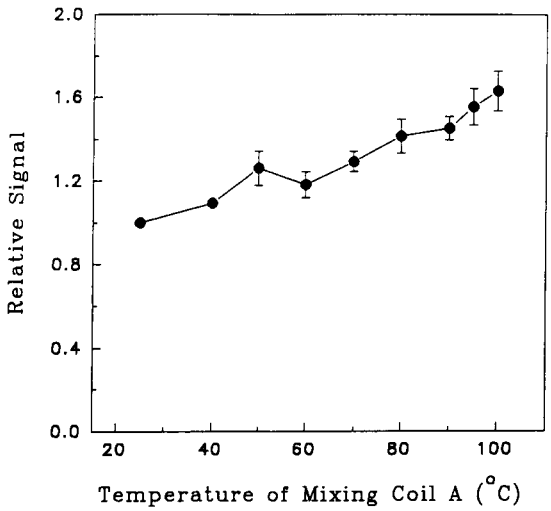

Fig. 4. Effect of mixing coil A temperature on arsenic(V) signal. Other hydride generation operating conditions are given in Fig. 1. All the data are relative to the first point.

ments that the volume of the mixing coils did not affect the arsenic(V) signal significantly.

The optimum sodium tetrahydroborate concentration was 0.5%, as shown in Fig. 5. This concentration is much lower than that used in the conventional method. When the sodium tetrahydroborate concentration increased, the amount of hydrogen generated also increased as well, which appears to have a detrimental effect on the ICP-MS system. When the concentration was higher than 0.5%, the ion signal decreased.

As detection was performed in a flow system, the reduction of arsenic(V) to arsenic(III) was incomplete; the arsenic(V) signal was only about 20% of the arsenic(III) signal. Brindle et al. [17] reported a system in which As(V) was completely reduced to As(III) when HCl (or HNO_3) was used. A summary of the optimum operating conditions for the hydride generation system is given in Fig 1.

3.2. Selection of ICP and LC operating conditions

The effect of an organic solvent on the plasma is generally to decrease its excitation properties significantly [22–25]. Although the signal of $^{75}As^+$ increased when a small amount of organic solvent was present [26,27], the analyte sensitivity decreased as the concentration of the organic modifier in the mobile phase increased to a certain level. Therefore, chromatographic conditions were selected that minimized the concentration of the organic modifier.

The performance of an ICP-MS device is strongly dependent on the operating conditions

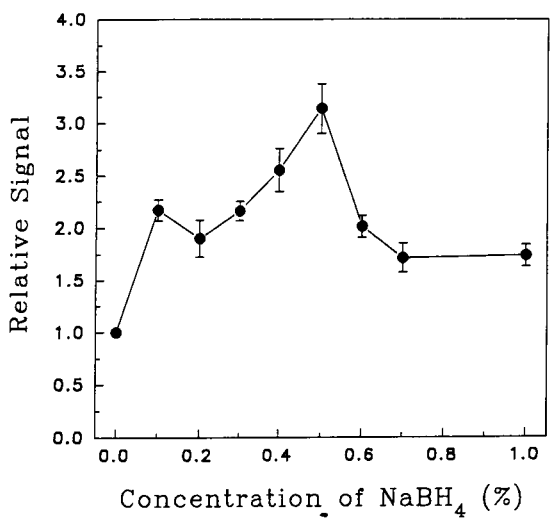

Fig. 5. Effect of sodium tetrahydroborate concentration on arsenic(V) signal. Other parameters are given in Fig. 1. All the data are relative to the first point.

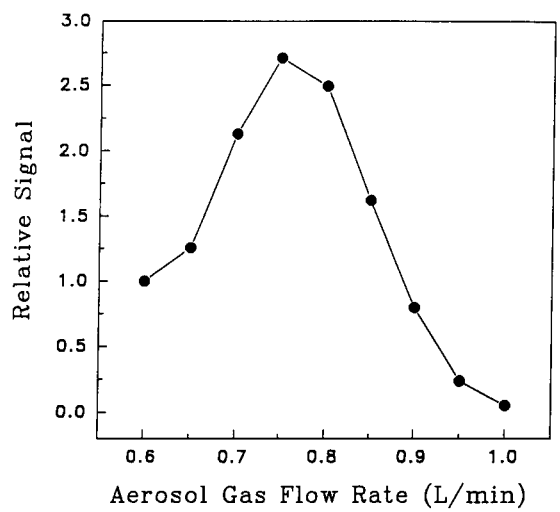

Fig. 6. Effect of aerosol gas flow-rate on arsenic(V) ion signal. All the data are relative to the first point.

[28]. The two key parameters are the aerosol gas flow-rate and the plasma forward power. The dependence of the arsenic ion signal on the aerosol gas flow-rate is depicted in Fig. 6. Although not illustrated here, the dependence of the arsenic ion signal on the plasma forward power is similar to that reported previously [28,29].

3.3. Arsenic speciation determination

A typical chromatogram of a solution containing 80 pg each of arsenic(III), arsenic(V), MMAA and DMAA is shown in Fig. 7. All four species were fully resolved and the separation was complete in less than 10 min. The background at m/z 75 was increased when HG sample introduction was used, which could be due to contamination by traces of arsenic of the reagents ($NaBH_4$ and NaOH) used for hydride generation. Peak-area measurements indicated that the response for arsenic was different for these four arsenic species. This may be attributed to variation of the hydride generation efficiency of the various arsenic species. Similar results were observed when the analyte was determined in the flow-injection mode.

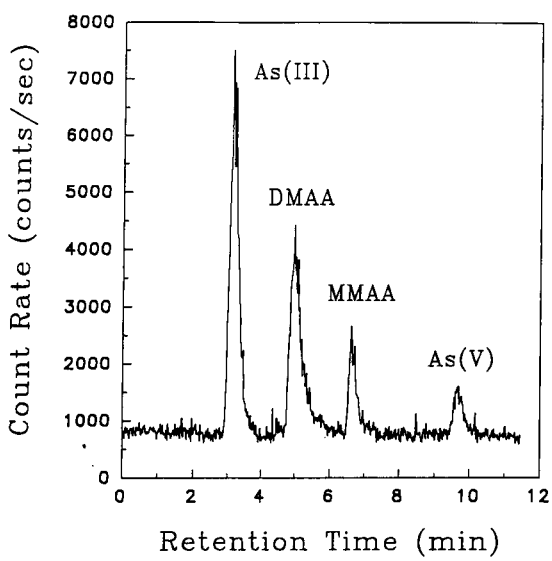

Fig. 7. Arsenic-selective chromatogram for As(III), DMAA, MMAA, and As(V); each species present at 0.40 $\mu g\ l^{-1}$. LC conditions are given in Table 1. Background = 810 ± 40 counts s^{-1}.

Table 2
Calibration parameters (0.2–10 $\mu g\ l^{-1}$) for various arsenic species

Parameter	As(III)	DMAA	NMAA	As(V)
S [a]	9800	6200	3800	2200
r [b]	0.9994	0.9993	0.9989	0.9967
D.L. [c]	11	18	29	51
R.T. [d]	3.2	5.1	6.8	9.8

[a] Sensitivity (counts s^{-1} μg^{-1} l).
[b] Regression coefficient.
[c] Detection limit (ng l^{-1}). Defined as concentration of analyte that gives a peak height equivalent to three times the standard deviation of the background. Sample loop, 200 μl.
[d] Retention time of the LC elution peak (min).

Reproducibility was determined using seven injections of a 10 $\mu g\ l^{-1}$ test mixture. The relative standard deviation of the peak heights was less than 5% for all the species, which is similar to the precision obtained in previous ICP-MS experiments with LC separations using a conventional pneumatic nebulizer [28]. Calibration graphs based on peak heights were linear for each arsenic compound in the range tested (0.2–10 $\mu g\ l^{-1}$). The detection limits were calculated from these calibration graphs and based on the amount (or concentration) necessary to yield a net signal equal to three times the standard deviation of the background. The absolute detection limits were 2.2–10 pg, which corresponds to relative values of 11–51 ng l^{-1} (see Table 2). These results are compared with those for other similar techniques in Table 3. Overall, the detection limits obtained in this work are better than previous results with similar techniques.

3.4. Determination of arsenic in water samples

In order to demonstrate that the system works in practical analyses, several natural water samples were analysed. A riverine water reference sample (SLRS-2) was used as a standard reference. A 200-μl injection of the riverine water was analysed for arsenic without dilution using the LC–hydride generation system. The chromatogram obtained is shown in Fig. 8. There is a

Table 3
Detection limits of the various arsenic species ($\mu g\ l^{-1}$)

Method	As(III)	DMAA	MMAA	As(V)
LC–HG–ICP–MS [a]	0.011	0.018	0.029	0.051
LC–HG–ICP–MS [b]	0.46	–	–	–
LC–DIN–ICP–MS [c]	1.2	1.2	1.0	1.2
LC–PN–ICP–MS [d]	7	3	3	3
LC–PN–ICP–MS [e]	20	8	20	10
LC–HG–ICP–AES [f]	50	105	–	50
LC–HG–AAs [g]	1.0	4.7	1.2	1.6

[a] This work, 200-μl sample loop.
[b] [14].
[c] [1], DIN = direct-injection nebulizer.
[d] [6], PN = pneumatic nebulizer.
[e] [7].
[f] [30].
[g] [31].

slight difference in retention times between the chromatograms shown in Figs. 7 and 8, which could be due to the injection of a highly acidic sample. As shown in Fig. 8, no significant peak was observed at m/z 77 ($Ar^{37}Cl^+$ and $^{77}Se^+$), which indicates that $ArCl^+$ did not interfere. The major arsenic species in the water sample was arsenic(V), as shown in Fig. 8. Smaller amounts of arsenic(III), MMAA and DMAA were also detected. The amount of arsenic present in each of the four species was determined by the standard addition method and the results are given in Table 4. These results agree with the certified value. It should be metioned that the certified value for arsenic in the sample is given for total arsenic only.

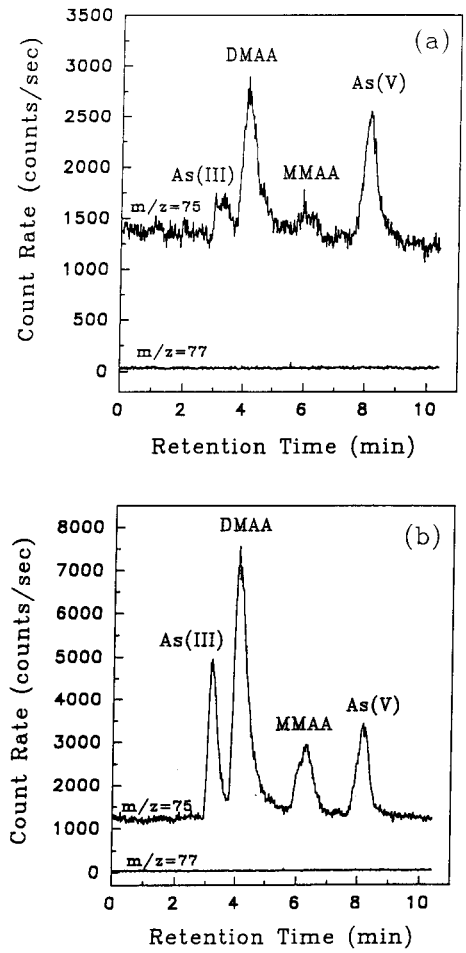

Fig. 8. (a) Arsenic-selective chromatogram of SLRS-2 riverine water reference sample; (b) chromatogram after spiking with 0.40 $\mu g\ l^{-1}$ arsenic mixture. LC conditions are given in Table 1. Concentrations of each arsenic species are listed in Table 4.

Table 4
Concentrations ($\mu g\ l^{-1}$) of arsenic species in natural waters as measured by LC–HG–ICP-MS

Sample	As(III)	DMAA	NMAA	AS(V)	Reference value
SLRS-2	0.05 ± 0.01	0.13 ± 0.01	0.10 ± 0.01	0.44 ± 0.02	0.77 ± 0.09 [a]
Underground water	0.04 ± 0.01	0.05 ± 0.01	0.08 ± 0.01	4.08 ± 0.05	–
Tap water	0.020 ± 0.003	0.10 ± 0.01	0.11 ± 0.01	1.45 ± 0.03	–
Spring water	–	–	–	0.28 ± 0.02	0.29 ± 0.02 [b]

Values are means ± standard deviations for a minimum of three injections of each solution.
[a] NRCC certified value, total arsenic concentration.
[b] [32], Total arsenic concentration, determined by flow-injection ICP-MS after preconcentration on Dowex 1-X8 resin.

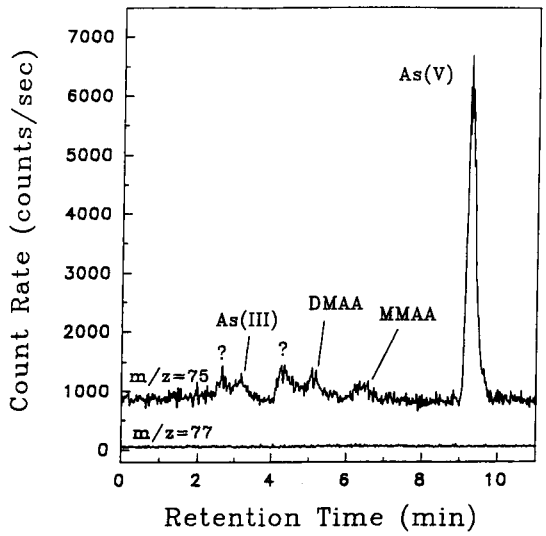

Fig. 9. Chromatogram of underground water taken from National Sun Yat-Sen University. LC conditions are given in Table 1. Concentrations of each arsenic species are listed in Table 4.

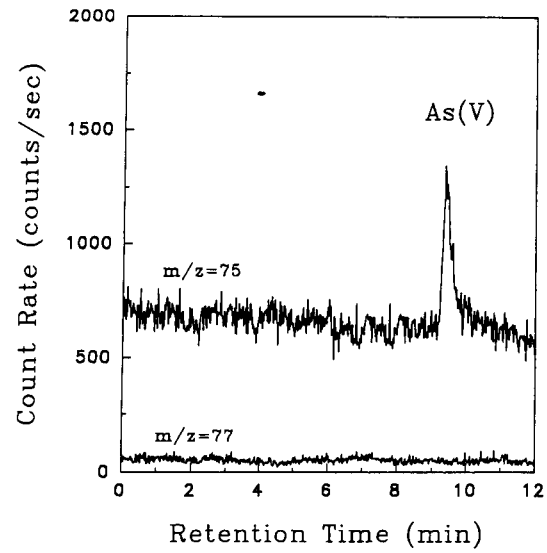

Fig. 11. Chromatogram of spring water taken from Kaohsiung County. LC conditions are given in Table 1. Concentrations of each arsenic species are listed in Table 4.

Black-foot disease is common on the southwestern coast of Taiwan and arsenic pollution of water is suspected to cause this skin disease.

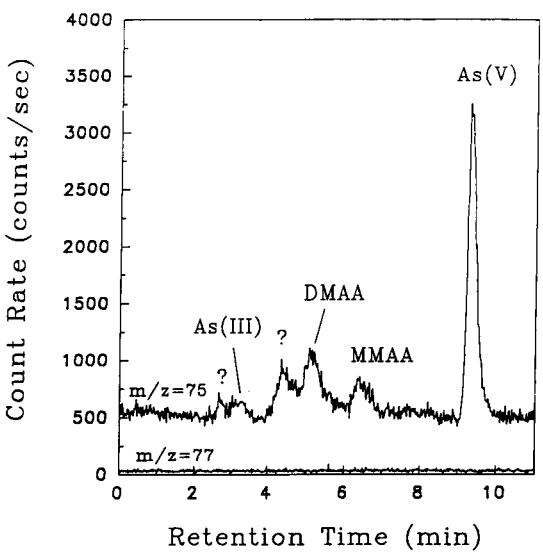

Fig. 10. Chromatogram of tap water taken from National Sun Yat-Sen University. LC conditions are given in Table 1. Concentrations of each arsenic species are listed in Table 4.

From previous arsenic speciation determinations, we demonstrated that the LC–HG–ICP-MS method could provide a reasonable detectability for different arsenic species. Several water samples were collected from different locations in the Kaohsiung area and analysed by LC–HG–ICP-MS. Typical chromatograms of the water samples are shown in Figs. 9–11. Arsenic(V) is the major arsenic species in all the samples. Two other peaks, which did not correspond to any of the four standards used, were also present. Different species were determined by the standard addition method (see Table 4). The precision was better than 20% for all the determinations. These results are much lower than the arsenic content of polluted underground water reported previously [33].

4. Acknowledgement

This research was supported by a grant from the National Science Council of the Republic of China.

5. References

[1] S.C.K. Shum, R. Neddersen and R.S. Houk, Analyst, 117 (1992) 577.

[2] S.C.K. Shum, H.-M. Pang and R.S. Houk, Anal. Chem., 64 (1992) 2444.

[3] J.C. Van Loon and R.R. Barefoot, Analyst, 117 (1992) 563.

[4] A. Al-Rashdan, N.P. Vela, J.A. Caruso and D.T. Heitkemper, J. Anal. At. Spectrom., 7 (1992) 551.

[5] J.W. McLaren, K.W.M. Siu, J.W. Lam, S.N. Willie, P.S. Maxwell, A. Palepu, M. Koether and S.S. Berman, Fresenius' J. Anal. Chem., 337 (1990) 721.

[6] S.H. Hansen, E.H. Larsen, G. Pritzl and C. Cornett, J. Anal. At. Spectrom., 7 (1992) 629.

[7] J.J. Thompson and R.S. Houk, Anal. Chem., 58 (1986) 2541.

[8] B.S. Sheppard, J.A. Caruso, D.T. Heitkemper and K.A. Wolnik, Analyst, 117 (1992) 971.

[9] D. Heitkemper, J. Creed, J.A. Caruso and F.L. Fricke, J. Anal. At. Spectrom., 4 (1989) 279.

[10] D. Beauchemin, K.W.M. Siu, J.W. McLaren and S.S. Berman, J. Anal. At. Spectrom., 4 (1989) 285.

[11] D. Beauchemin, M.E. Bednas, S.S. Berman, J.W. McLaren, K.W.M. Siu and R.E. Sturgeon, Anal. Chem., 60 (1988) 2209.

[12] W.C. Story, J.A. Caruso, D. Heitkemper and L. Perkins, J. Chromatogr. Sci., 30 (1992) 427.

[13] S. Branch, W.T. Corns, L. Ebdon, S. Hill and P. O'Neill, J. Anal. At. Spectrom., 6 (1991) 155.

[14] T. Nakahara, Spectrochim. Acta Rev., 14 (1991) 95.

[15] J.D. Hwang, H.P. Huxley, J.P. Diomiguardi and W.J. Vaughn, Applied Spectrosc., 44 (1990) 491.

[16] H. Chen, I.D. Brindle and X.-C. Le, Anal. Chem., 64 (1992) 667.

[17] I.D. Brindle, H. Alarahi, S. Karshman, X.-C. Le, S. Zheng and H. Chen, Analyst, 117 (1992) 407.

[18] I.D. Brindle, X.-C. Le and X.-F. Li, J. Anal. At. Spectrom., 4 (1989) 227.

[19] R.K. Anderson, M. Thompson and E. Culhard, Analyst, 111 (1986) 1143.

[20] R. Anderson, M. Thompson and E. Culbard, Analyst, 111 (1986) 1153.

[21] B.J. Haring, W. Van Delft and C.M. Bom, Fresenius' Z. Anal. Chem., 310 (1982) 217.

[22] A.W. Boorn and R.F. Browner, Anal. Chem., 54 (1982) 1402.

[23] R.C. Hutton, J. Anal. At. Spectrom., 1 (1986) 259.

[24] G. Kreuning and F.J.M.J. Maessen, Spectrochim. Acta, Part B, 40 (1989) 367.

[25] A. Montaser and D.W. Golightly (Eds.), Inductively Coupled Plasma in Analytical Atomic Spectrometry, VCH, New York, 2nd edn., 1992.

[26] J. Goossens, F. Vanhaecke, L. Moens and R. Dams, Anal. Chim. Acta, 280 (1993) 137.

[27] C.-J. Hwang, Master's Thesis, National Sun Yat-Sen University, Kaohsiung, Taiwan, 1993.

[28] S.-J. Jiang and R.S. Houk, Spectrochim. Acta, Part B, 43b (1988) 405.

[29] C.-W. Huang and S.-J. Jiang, J. Anal. At. Spectrom., 8 (1993) 681.

[30] D.S. Bushee, I.S. Krull, P.R. Demko and S.B. Smith, J. Liq. Chromatogr., 7 (1984) 861.

[31] E. Hakala and L. Pyy, J. Anal. At. Spectrom., 7 (1992) 191.

[32] P.-L. Lu, Master's Thesis, National Sun Yat-Sen University, Kaohsiung, Taiwan, 1993.

[33] S.-R. Wang and S.-J. Jiang, J. Chin. Chem. Soc., 38 (1991) 327.

ELSEVIER

Analytica Chimica Acta 289 (1994) 215–221

ANALYTICA CHIMICA ACTA

Potentiometric stripping analysis of thallium in natural waters

Rob Cleven *, Luuk Fokkert

Laboratory of Inorganic Chemistry, National Institute of Public Health and Environmental Protection, P.O. Box 1, 3720 BA Bilthoven, Netherlands

(Received 1st October 1993; revised manuscript received 19th November 1993)

Abstract

The determination of Tl(I) by potentiometric stripping analysis (PSA) has been studied. Effects of experimental variables such as the plating, deposition and stirring regimes, and the amount of oxidant are described. After optimization of the relevant experimental variables, an amount of $0.35 \cdot 10^{-9}$ mol/l Tl^+ was measured in river Rhine water.

Key words: Potentiometry; Stripping voltammetry; Thallium; Rhine water; Waters

1. Introduction

Thallium is a toxic metal that is introduced in the environment mainly as a waste from the production of lead, zinc and cadmium, and by coal combustion [1–3]. Thallium and its compounds are used in optical systems and in chemical synthesis. Little is known about its systematic occurrence in natural waters. Occasionally, concentrations of thallium in sea water and in rainwater have been reported to be less than $0.5 \cdot 10^{-9}$ mol/l [4–6]. Under E_h and pH conditions usually found in natural waters, Tl^+ is considered to be the predominant thallium species [1]. To determine the low thallium concentration in natural waters, electroanalytical stripping techniques are potentially suited [7,8]. Voltammetric techniques, such as differential pulse anodic stripping voltammetry (DPASV), may be hampered by interferences due to adsorption at the electrode of organic matter present in natural waters, whereas potentiometric stripping analysis (PSA) is expected to be not so sensitive in this respect [9,10]. In this study, the potentialities of PSA for the determination of Tl^+ in natural waters have been studied. Effects of experimental variables such as the plating, deposition and stirring regimes, and the amount of oxidant are described. After optimization of the relevant experimental variables, the concentration of Tl^+ in river Rhine water samples has been measured.

1.1. Potentiometric stripping analysis

Potentiometric stripping analysis is a two-step technique consisting of an electrolysis step and a stripping step. The electrolysis step, commonly performed using a mercury film-coated glassy car-

* Corresponding author.

SSDI 0003-2670(93)E0653-O

bon electrode, is a preconcentration step in which metal ions are reduced to free metal and deposited as amalgam at the working electrode. The electrolysis process is primarily controlled by the concentration and the diffusion coefficient of the metal ions involved, and the thickness of the diffusion layer at the working electrode as imposed by the stirring regime. The measurements are made in the stripping step during which the metals are reoxidized. The reoxidation is essentially a chemical process: during the stripping phase the electric circuitry is interrupted, and a chemical oxidant, such as oxygen or Hg^{2+} ions, will establish the reoxidation. The change in the electrode potential E with time during the reoxidation process is monitored. Computerized equipment enables to sample the potential up to 30 000 times per second. Integration of the dt/dE function between two plateau values of the potential yields the total stripping period t_S for the metal investigated.

An expression of the stripping period t_S given in [8], can be simplified to:

$$t_S \sim k\{[Tl^+]^* \cdot t_D/d_D\}\{[Ox]/d_S\}^{-1} \quad (1)$$

where k is a constant, in which a number of physical constants are incorporated such as the diffusion coefficients of thallium and the oxidizing agent, the hydrodynamic constants depending on the electrode and stirring geometries during the different steps in the analysis, and the ratio of the number of electrons involved in reduction and oxidation of the metal, $[Tl^+]^*$ is the bulk concentration, t_D is the deposition period, [Ox] is the concentration of the oxidant, and d_D and d_S are the diffusion layer thicknesses during deposition and stripping respectively. There exists a domain of experimental values of [Ox], t_D, d_D and d_S, in which t_S and $[Tl^+]^*$ are linearly related.

The stirring regime can be exploited to manage the diffusion layer thickness during electrolysis and stripping, and the purging efficiency can be exploited to manage the amount of oxygen in the sample. In a quiescent solution during stripping, d_S will grow to large values, and accordingly t_S will increase. Obviously, the question whether the linearity of the t_S–$[Tl^+]^*$ function persists is of analytical interest.

2. Experimental

2.1. Instrumentation

A Tracelab system (Radiometer) has been used, consisting of a PSU20 unit, a SAM20 sample station and an Olivetti M240 personal computer. The Tracelab system contains a glassy carbon working electrode (F3600), on which a mercury film is deposited, a platinum counter electrode (P136) and a saturated calomel reference electrode (SCE) (K436). In the SAM20, the 901-974 purge module was mounted. Polypropylene sample beakers of 25 ml have been used.

2.2. Chemicals

Plating solution (Radiometer, S2201) contained 1.3 mol/l HCl, and 800 mg/l Hg^{2+}. Other chemicals used in the investigations, such as thallium(I) nitrate (Merck), lead(II) nitrate (Merck), NaOH (Merck) and EDTA (Merck) were pro analysi quality. Doubly distilled water has been used in the preparation of standard solutions. High quality nitrogen gas has been used for purging sample solutions.

2.3. Procedures

Before each analysis of Rhine water, a new mercury film was prepared, after removing a previously used film with a tissue and rinsing the electrode surface with demineralized water. A solution was prepared containing 20 ml water and 2 ml plating solution. The glassy carbon electrode was plated for a period of 8 min at a potential of −900 mV. The software program TAP2 has been applied, as provided by Radiometer. Standard settings of the system are defined as follows: deposition potential E_D, −900 mV vs. SCE; rest period t_R, 35 s; deposition period t_D, 30 min; stirring mode during deposition, 4. In the case of Rhine water samples and standard solutions, amounts of 0.25 and 2 ml plating solutions have been added respectively.

3. Results and discussion

The number of experimental variables potentially liable to optimization is large. They include the plating, deposition, and stirring regimes, the oxidant characteristics, and the matrix composition. In this study attention is mainly focused on those variables that primarily affect the detection limit.

3.1. Plating regime

The plating procedure as advised by the manufacturer, including a plating time t_{PL} of 8 min, has generally been adopted. It is noted that the plating time t_{PL} in this study is different from the deposition period t_D. Preliminary measurements on the effect of the plating time of the PSA signal, for a thallium(I) nitrate standard solution of 10^{-7} mol/l, resulted in a fast increase in the peak area A_P with increasing t_{PL}, for $0 < t_{PL} < 5$ minutes, whereas for $t_{PL} > 5$ min, the increase in A_P is much slower. The slow increase appears to be approximately linear. These findings support the manufacturers choice of 8 min plating time. This phenomenon, which is principally different from corresponding voltammetric stripping experience, may be understood by considering the combination of two different processes that make up the effect of t_{PL} on A_P. A larger t_{PL} will result in a thicker mercury film at the working electrode. Thus, a larger t_{PL} will yield a lower Tl(Hg) concentration, and thus a correspondingly lower PSA signal is expected, whereas the pathlength over which amalgamated Tl has to diffuse in the reoxidation step will be larger, yielding a higher PSA signal. The effect of a prolonged diffusion process, for $t_{PL} > 5$ min, outweighs the corresponding decrease of the preconcentration factor.

3.2. Deposition regime

To enable a proper choice of the deposition potential E_D, thallium(I) nitrate standard solutions have been measured, applying different deposition potentials. In Fig. 1, plots of the peak area A_P versus the deposition potential E_D are

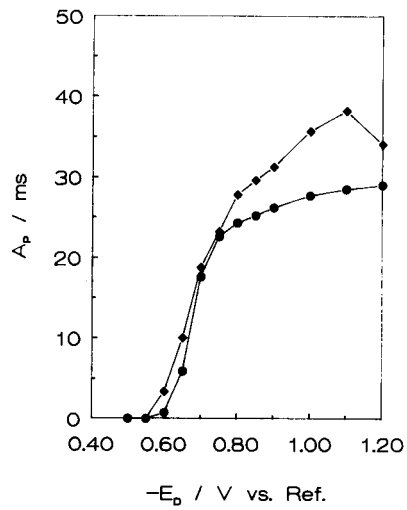

Fig. 1. Peak area A_P of PSA signals for Tl^+ as a function of the deposition potential $-E_D$. $[Tl^+]$: 10^{-6} mol/l (●); 10^{-7} mol/l (♦). In the case of $[Tl^+] = 10^{-6}$ mol/l, $A_P \times 10^{-1}$ is plotted.

presented. An E_D of -900 mV vs. SCE was chosen for the further investigations.

According to Eq. 1, the resulting PSA signal t_S should depend linearly on the deposition period t_D. Obviously, of analytical importance is the domain of experimental conditions under which this linear regime holds. The linearity has been tested adopting the standard settings, except for t_D. The results demonstrate that the linearity holds to a t_D of 40 min, for the thallium(I) standard solution of 10^{-7} mol/l. In Fig. 2, some results for two standard solutions are presented.

3.3. Stirring regime

Stirring of the sample solution during the deposition period obviously enhances the preconcentration of Tl^+ in the mercury film, because of the reduction of the diffusion layer thickness d_D (see Eq. 1). It appeared that A_P linearly increases with the stirring mode values from 1 to 10. However, for values > 8, turbulency occurred in the solutions. Since this turbulency will affect the precision of the measurements, it was decided to use only stirring mode values $\leqslant 8$ during the deposition period. If the stripping step is performed at a stationary electrode, a rest

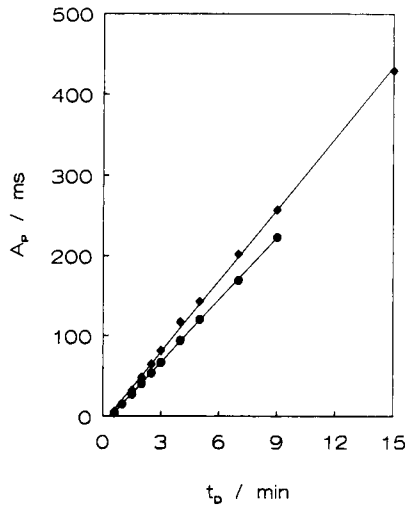

Fig. 2. Peak area A_P of PSA signals for Tl^+ as a function of the deposition period t_D. $[Tl^+]$: 10^{-6} mol/l (●); 10^{-7} mol/l (♦). In the case of $[Tl^+] = 10^{-6}$ mol/l, $A_P \times 10^{-1}$ is plotted.

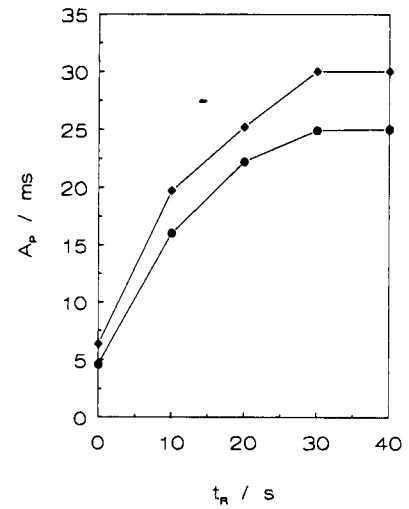

Fig. 3. Peak area A_P of PSA signals for Tl^+ as a function of the rest period t_R before stripping. $[Tl^+]$: 10^{-6} mol/l (●); 10^{-7} mol/l (♦). In the case of $[Tl^+] = 10^{-6}$ mol/l, $A_P \times 10^{-1}$ is plotted.

period between deposition en stripping step is mandatory for the system to settle [11]. An indication of the necessary minimum duration of the rest period t_R resulted from a series of measurements in which the ratio t_D/t_R had been changed, while $t_D + t_R$ was kept constant at 90 s. In Fig. 3, results of these experiments are presented. It appears that under the experimental conditions practised, a rest period of 30 s is necessary for settling the solution hydrodynamics and the transformation of the stagnant diffusion layer. In the further measurements t_R has been set at 35 s.

Effects of stirring during the stripping step have been studied for the available stirring modes 1 – 10, for $t_D = 90$ s and otherwise standard settings, using thallium(I) nitrate of 10^{-6} and 10^{-7} mol/l. In Fig. 4, the corresponding results are presented. It appears that up to stirrer mode 4, the peak area is not affected by the stirring rate. Apparently, for stirring modes < 5, the stagnant layer is sufficiently large to allow the Hg^{2+} ions to reach the electrode by uninfluenced diffusion only, within a period of time smaller then the particular t_S involved. For t_S values of 25–30 ms, see Fig. 4, and applying Einsteins relation for diffusion, this would imply that the stagnant diffusion layer thickness at stirrer mode 4 is about 0.01 mm.

3.4. Amount of oxidant

Eq. 1 demonstrates that the amount of oxidant is inversely proportional to the PSA signal. Thus,

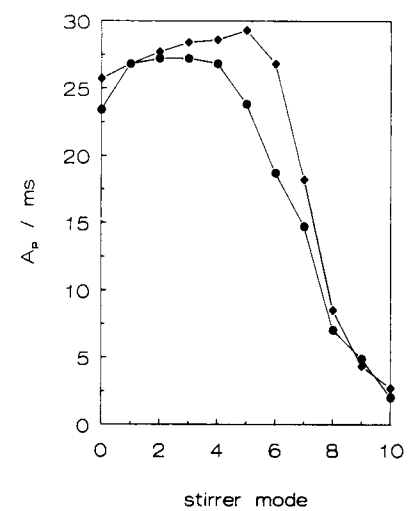

Fig. 4. Peak area A_P of PSA signals for Tl^+ as a function of the stirring rate during stripping. $[Tl^+]$: 10^{-6} mol/l (●); 10^{-7} mol/l (♦). In the case of $[Tl^+] = 10^{-6}$ mol/l, $A_P \times 10^{-1}$ is plotted.

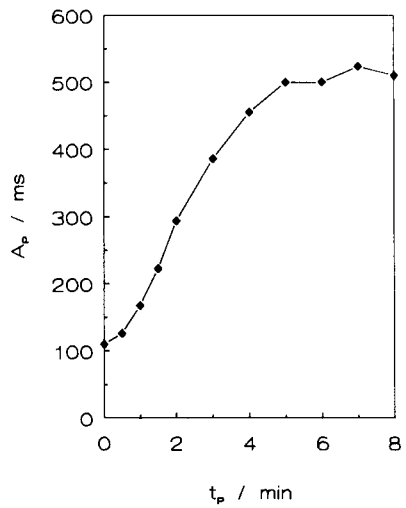

Fig. 5. Peak area A_P of PSA signals for Tl^+ as a function of the purge period t_P. [Tl^+]: 10^{-7} mol/l (◆).

a low concentration of oxidant enables a low detection limit. However, to warrant the linearity of the dependency of t_S on [Tl^+]*, the concentration of oxidant should not appreciably change during the reoxidation process, and should be present in excess over the Tl^+ concentration to be determined.

Either naturally present oxygen or an oxidizing agent to be added to the sample can function as oxidant in the a potentiometric stripping analysis. Unfortunately, to measure trace level concentrations, which is the case for Tl^+ in natural waters, the amount of oxygen naturally present in aerated samples is relatively high. By prior purging the sample solution with nitrogen gas, the oxygen concentration can be diminished, and t_S will correspondingly increase. In Fig. 5, the effect of purging a sample containing a thallium(I) nitrate standard solution of 10^{-7} mol/l, to which no Hg^{2+} ions have been added, is shown. It is concluded that purging with nitrogen gas is an effective tool to increase the PSA signal. However, it also appears that the effect is limited. Purging for more than 6 min does not yield a further increase of the PSA signal, probably due to diffusion of oxygen into the sample. In the determination of Tl^+ in the Rhine water samples, purging has been applied for 7 min. It is clear that to detect Tl^+ at the level present in natural waters, no oxidizing agents have to be added. However, to maintain a stable PSA signal and to level off variations in the remaining oxygen concentration as a result of the purging with nitrogen, a small amount of Hg^{2+} has been added to the Rhine water samples. To estimate a reasonable Hg^{2+} level, peak areas have been determined for the 10^{-6} mol/l thallium(I) nitrate standard solution as a function of the amount of plating solution added to the sample, which has been purged with nitrogen prior to the measurement. The expected inverse relation between t_S and [Hg^{2+}] did not show up perfectly, probably due to interference with competing traces of oxygen. A level of 50 μmol/l Hg^{2+} has been adopted in the measurements of the Rhine water samples. At the chosen level, the peak area was only 15% lower than the area found in the absence of added Hg^{2+}.

3.5. Rhine water samples

Rhine water has been sampled at Lobith at the Dutch/German border. From preliminary experiments it appeared that the Tl^+ concentration in the Rhine water samples was lower than the operational detection limit. Therefore the samples have been concentrated 10-fold by evaporation. Those experimental standard settings, found to be the optimum settings in this study, have been adopted. To 20 ml of the Rhine water concentrate, 0.25 ml plating solution has been added, resulting in a Hg^{2+} concentration of 50 μmol/l. EDTA was added to the solution to a concentration of 0.5 mmol/l, to eliminate inter-

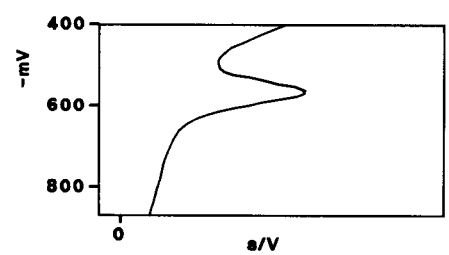

Fig. 6. PSA signal (s/V) Rhine water concentrate as a function of the measured potential $-E$ (mV). The peak maximum is located at -584 mV vs. ref. The peak area corresponds to 1111 ms.

Table 1
PSA results for a Rhine water concentrate and for two standard additions (Δ_P is the peak width at the baseline)

Sample	Addition (nmol/l)	Peak maximum (mV vs. ref.)	Δ_P (mV)	Area (ms)
Rhine water (concentrate)	0.00	−584	195	1111.60
Standard addition 1	2.80	−582	214	1918.25
Standard addition 2	5.61	−584	220	2841.86

Calculated [Tl^+] in the Rhine water concentrate: 3.7 nmol/l ($r = 0.9992$).

ference of lead, and the pH has been adjusted to 5 with NaOH. Dissolved oxygen has been removed by purging with nitrogen during 7 min before the deposition step. During the stripping period, stirring was not applied. To determine the Tl^+ concentration in the original Rhine water sample, the method of standard addition has been applied, using a thallium(I) nitrate solution.

The quality of the thallium peaks for the Rhine water concentrates were good. See the example in Fig. 6. This is also demonstrated by the quality figure of the standard addition calculation, and the potential range Δ_P of the thallium peaks at the baseline. The resulting concentration, corrected for dilution effects, in the original Rhine water sample is calculated to be 0.37 nmol/l. In Table 1, the resulting peak positions and peak area are given for a Rhine water concentrate and standard additions.

3.6. Precision

To estimate the precision, obtained by repetitive plating/stripping, ten measurements have been performed using Rhine water concentrate, applying the settings mentioned above. The resulting average concentration in the original Rhine water samples has been calculated to be 0.35 nmol/l. The relative standard deviation, σ, in the series appeared to be 22%.

A unique detection limit for the PSA analysis of a particular element cannot be defined [12], as it is controlled by the combination of a number of experimental variables, such as the thickness of the mercury film, the deposition period, and the stirring rate, of which the (limiting) values are operationally defined. Under the conditions of the standard settings adopted in this study, the 3σ value for repeated measurements of a low concentration of the standard solution gives an estimate of the operational detection limit for Tl^+ of about 2×10^{-9} mol/l. This detection limit is compatible with those of other techniques: using DPASV, 1×10^{-9} mol/l has been claimed [7], and using liquid chromatography a level of 1×10^{-8} mol/l (based on twice the background level) has been reported [13] as detection limit for Tl.

4. Conclusions

A low PSA detection limit for Tl^+ in natural waters can be achieved by a high stirring rate during the deposition period and by refraining from stirring during the stripping period, and the presence of a relatively low amount of oxidizing agent.

5. References

[1] M. Callahan, M. Slimak, N. Gabel, I. May, C. Fowler, J. Freed, P. Jennigs, R. Durfee, F. Whitmore, B. Maestri, W. Mabey, B. Holt and C. Gould, Water-Related Environmental Fate of 129 Priority Pollutants, Vol. I: Introduction and Technical Background, Metals and Inorganics, Pesticides and PCBs, EPA-440/4-79-029a, Office of Water Planning and Standards, U.S. Environmental Protection Agency, Washington, DC, 1979.
[2] A. Kabata-Pendia and H. Pendias, Trace Elements in Soils and Plants, CRC Press, Boca Raton, FL, 1984.
[3] I. Bodek, W. Lyman, W.F. Reehl and D.H. Rosenblatt (Eds.), Environmental Inorganic Chemstry, Pergamon, New York, 1988.
[4] S. Jaya, T. Prasada Rao and G. Prabhakara Rao, Talanta, 32 (1985) 1061.
[5] J. Struijs, P.M. Wolfs and F.G. van Esseveld, Een Bepalingsmethode voor Thallium in Regenwater met behulp

van Voltammetrie, RIVM Report No. 217702008, Bilthoven, Netherlands, 1985.
[6] A.D. Matthews and J.P. Riley, Anal. Chim. Acta, 48 (1969) 25.
[7] Z. Lukaszewski and W. Zembruski, Talanta, 39 (1992) 221.
[8] Ch. Labar, Electrochim. Acta, 6 (1993) 807.
[9] P. Ostapczuk, Anal. Chim. Acta, 273 (1993) 35.
[10] P. Hansen, Int. Lab., April (1991) 18.
[11] C. Labar and L. Lamberts, Anal. Chim. Acta, 132 (1981) 23.
[12] D. Jagner, Anal. Chem., 50 (1978) 1924.
[13] J.H. Shofstahl and J.K. Hardy, J. Chromatogr. Sci., 28 (1990) 225.

ELSEVIER

Analytica Chimica Acta 289 (1994) 223–230

ANALYTICA CHIMICA ACTA

Interaction between humic acids and copper(II) oxinate

Masami Fukushima, Mitsuhiko Taga, Hiroshi Nakamura *

Division of Material Science, Graduate School of Environmental Earth Science, Hokkaido University, Sapporo 060, Japan

(Received 14th September 1993; revised manuscript received 16th November 1993)

Abstract

The solubility of the fungicide copper(II) oxinate ($Cu(OX)_2$) linearly increased with the concentration of humic acid in aqueous solution. This phenomenon was attributed to the interaction between $Cu(OX)_2$ and hydrophobic domains in humic acid, and the $Cu(OX)_2$ association coefficients with humic acids (K_{doc}) were evaluated. The evaluations of the K_{doc} values were carried out for humic acids extracted from peat and marine sediment. For these humic acids, the K_{doc} values increased at pH 6 with decreasing copper(II) complexing capacity and amount of acidic functional groups. This suggested that the K_{doc} values can be correlated with the polarity of the humic acids. The interaction between $Cu(OX)_2$ and humic acid could be ascribed to the hydrophobic–hydrophobic interaction.

Key words: Humic acids; Copper(II) oxinate; Fungicides; Hydrophobic interactions

1. Introduction

Humic acids, which are widely distributed in the environment, are weak-acid polyelectrolytes. They determine the pH buffering capacity and cation exchange capabilities in natural waters and soils [1–3]. Especially, the complexation reactions of heavy metal ions and humic acids have been studied in connection to their toxicity to phytoplankton [4–6]. In addition, it was also reported that humic acids had points of aggregation such as a critical micellar concentration (CMC) and that they act as surface active agents [7–9]. This suggests that non-polar domains such as aromatic moieties exist in humic molecules. Therefore, hydrophobic organic pollutants (HOPs) such as dichlorodiphenyltrichloroethanes (DDTs) or polychlorobiphenyls (PCBs) could bind with humic acids [10]. This phenomenon is concerned with the fate of HOPs in the environment.

Knowledge about interaction between humic acids and HOPs is important because of the speciation of HOPs in natural waters and soil environments. Although HOPs, insoluble in water, exist in a particle form adsorbed on clay minerals, the solubility of HOPs in water increases in the presence of dissolved organic carbon (DOC), such as humic acids [11,12]. This would promote the diffusion of HOPs. It was found that the water solubility of phenanthrene increased in the presence of DOCs such as humic acids [13]. Furthermore, the water solubility of HOPs such as DDT, PCB and lindane increased

* Corresponding author.

SSDI 0003-2670(93)E0655-Q

in the presence of humic substances [14,15]. These mechanisms were ascribed to a partition-like interaction. Rutherford et al. [16] concluded that the strength of the interaction between HOPs and humic substances depends on the polarity of humic substances. This was supported by experiments using the model compounds such as polyacrylic acid and the polar-to-nonpolar group ratio [(O + N)/C].

On the other hand, metal chelates have been widely used as fungicides [17]. Although the inorganic mixed copper(II) compounds such as $CuSO_4$, CuO and $CuCl_2$ were used for the same purpose, the metal chelate could be used because of excellent permeability through biomembranes [18]. Therefore, the toxicity of the metal chelate to phytoplankton would be higher than when hydrated heavy metal ions appear in aqueous environments. It has been well-known that the toxicity of heavy metal ions is repressed by complexation with humic substances [19–22]. However, it was reported that humic acids had the same effect on the metal chelate as on heavy metal ions. For example, although copper(II)–oxinate, $Cu(OX)_2$, was strongly toxic for Coli type bacilli and killifish, the toxicity was weakened in the presence of humic substances [23]. Recently, the outflow of $Cu(OX)_2$ used as a fungicide in golf links has been a serious environmental problem in Japan. Soil organic matter such as humic substances seems to be involved with the outflow of $Cu(OX)_2$ to the aqueous environment. Therefore, from an environmental and ecological point of view, knowledge about the interactions between $Cu(OX)_2$ and humic acids is required.

In the present study, the association of $Cu(OX)_2$ with humic acid was investigated, and the association coefficients were evaluated by measuring the solubility of $Cu(OX)_2$ in water in the presence of humic acid. Moreover, the evaluation of the association coefficients was performed for various humic acids extracted from peat and marine sediment. The dependence of the association coefficients on pH, ionic strength, copper(II) complexing ability and the amounts of acidic functional groups were investigated, and the interaction between $Cu(OX)_2$ and humic acid was discussed according to these parameters.

2. Evaluation of association coefficients

$Cu(OX)_2$ can dissolve slightly in water, and produce many species such as $CuOX^+$, Cu^{2+}, OX^-, HOX and H_2OX^+. In the presence of humic acid (HA), a hydrophobic–hydrophobic interaction between $Cu(OX)_2$ and humic acid was assumed, assuming the following dissolution and association equilibria:

$$Cu(OX)_2(s) \underset{S_w}{\rightleftharpoons} Cu(OX)_2(aq) \underset{K_{doc}}{\rightleftharpoons} Cu(OX)_2(HA)$$

where S_w and K_{doc} represent the solubility of $Cu(OX)_2$ in water and the association coefficient of $Cu(OX)_2$ between water and HA, respectively. In the absence of humic acid, the water solubility of $Cu(OX)_2$, S_w, can be written as follows,

$$S_w = [Cu(OX)_2]_{aq} + [CuOX^+]_{aq} + [Cu^{2+}]_{aq} \quad (1)$$

where the subscript, "aq", denotes species in aqueous phase. In the presence of humic acid, it was assumed that $Cu(OX)_2$ would also be associated with humic acid according to a dissolution equilibrium. Therefore, the apparent water solubility of $Cu(OX)_2$, S_w^*, could be written as follows,

$$S_w^* = [Cu(OX)_2]_{aq} + [CuOX^+]_{aq} + [Cu^{2+}]_{aq} + [Cu(OX)_2]_{HA} \quad (2)$$

where the subscript, "HA", denotes the species associated with humic acid. The $Cu(OX)_2$ association coefficient can be defined as the ratio of the amounts of $Cu(OX)_2$ associated with humic acid at a unit gram of carbon ($[Cu(OX)_2]/[DOC]$) to the amounts of $Cu(OX)_2$ remains in aqueous solution. The [DOC] (mol l^{-1}) represents the concentration of dissolved organic carbon originating from humic acid. Therefore, the $Cu(OX)_2$ association coefficient, K_{doc}, can be written as,

$$K_{doc} = \frac{[Cu(OX)_2]_{HA}}{[DOC][Cu(OX)_2]_{aq}} \quad (3)$$

The following relationship was derived from Eqs. 1–3,

$$S_w^* = S_w + K_{doc}[Cu(OX)_2]_{aq}[DOC] \quad (4)$$

Eq. 4 represents a linear relationship between S_w^* and [DOC]. K_{doc} can be evaluated from the slope of Eq. 4 and $[Cu(OX)_2]_{aq}$.

Thus, $[Cu(OX)_2]_{aq}$ can be calculated by considering the dissociation equilibria of $Cu(OX)_2$ in the absence of humic acid, and the dissociation equilibria of $Cu(OX)_2$ are as follows:

$$CuOX^+ \rightleftharpoons Cu^{2+} + OX^-$$

$$K_{d1} = \frac{[Cu^{2+}][OX^-]}{[CuOX^+]} \quad (5)$$

$$Cu(OX)_2 \rightleftharpoons CuOX^+ + OX^-$$

$$K_{d2} = \frac{[CuOX^+][OX^-]}{[Cu(OX)_2]} \quad (6)$$

The proton dissociation of oxine (HOX) and the acid dissociation constants, K_{a1} and K_{a2}, can be written as follows,

$$HOX \rightleftharpoons H^+ + OX^-$$

$$K_{a2} = \frac{[H^+][OX^-]}{[HOX]} \quad (7)$$

$$H_2OX^+ \rightleftharpoons H^+ + HOX$$

$$K_{a1} = \frac{[H^+][HOX]}{[H_2OX^+]} \quad (8)$$

From Eqs. 1, 5 and 6, the following equation can be derived,

$$[Cu(OX)_2]_{aq} = \frac{[OX^-]^2 S_w}{[OX^-]^2 + K_{d2}[OX^-] + K_{d1}K_{d2}} \quad (9)$$

The total concentration of oxine in aqueous solution, C_{OX}, can be written as,

$$C_{OX} = 2[Cu(OX)_2]_{aq} + [CuOX^+]_{aq} + [OX^-]_{aq} + [HOX]_{aq} + [H_2OX^+]_{aq} \quad (10)$$

The following cubic equation can be derived from Eqs. 5–10,

$$[OX^-]^3 + K_{d2}[OX^-]^2 + \frac{K_{d1}K_{d2}\alpha - S_w K_{d2}}{\alpha}[OX^-] - \frac{2S_w K_{d1}K_{d2}}{\alpha} = 0 \quad (11)$$

where α is defined as below,

$$\alpha = 1 + \frac{[H^+]}{K_{a2}} + \frac{[H^+]^2}{K_{a1}K_{a2}} \quad (12)$$

$[OX^-]$ can be estimated using Eq. 11. $[Cu(OX)_2]_{aq}$ can be calculated by substituting the $[OX^-]$ value in Eq. 9. The dissociation constants of $Cu(OX)_2$ and the acid dissociation constants of HOX were taken from [24].

3. Experimental

3.1. Humic acids

The humic acids used in the present work were extracted from the Shinshinotsu (SHHA), Bibai (BHA) and Sarobetsu (SAHA) peat and a marine sediment of Funka Bay (FBHA). The humic acids were extracted by sodium hydroxide, sequentially precipitated by hydrochloric acid, and then purified according to the protocol of the International Humic Substances Society (IHSS) [25]. Results from the elemental analyses of these humic acids are summarized in Table 1. The concentration of the dissolved organic carbon originating from humic acid, [DOC], can be calculated by the following equation,

$$[DOC(M)] = \frac{[\text{humic acid}(g\ l^{-1})] \times (\%C/100)}{12.011(g\ mol^{-1})} \quad (13)$$

3.2. Reagents

Copper(II) oxinate dihydrate was prepared by mixing an aqueous solution of copper(II) acetate

Table 1
Elemental analyses of humic acids

Humic acids	% C	% H	% N	% O	ASH
SHHA	51.2	4.72	1.74	40.0	2.44
SAHA	52.9	4.40	3.10	37.9	1.66
BHA	55.1	3.70	1.93	36.8	2.44
FBHA[a]	49.1	6.10	5.48	33.5	2.87

[a] 2.91% S was contained.

with a solution of oxine in ethanol [26]. The stock solution of copper(II) oxinate was the saturated solution of copper(II) oxinate in ethanol. The concentration of copper(II) oxinate in the stock solution was determined by measuring copper(II) using atomic absorption spectrometry (AAS). The $Cu(OX)_2$ concentration in the stock solution was 0.3 mM. Sodium acetate (pH < 5.5), morpholine-*N*-ethanesulfonic acid (MES, pH 6) and *N*-(2-hydroxyethyl)-piperidine-*N'*-ethanesulfonic acid (HEPES, pH 7 and 8) were used as buffering agents (Dojindo Labs.).

3.3. Methods

A 1-ml aliquot of the stock solution of copper(II) oxinate and the buffer solution was put into a 25-ml volumetric flask and was shaken with humic acid for 4 h at 20°C. The solution was filtered through a membrane filter (0.45 μm). The copper(II) species in the filtrate were determined by AAS. The total concentration of copper(II) species in the filtrate represents the apparent water solubility of copper(II) oxinate, S_w^*. The solubility of HOX in water was also measured using the same method as for copper(II) oxinate, and the absorbance of oxine at 310 nm was measured in this case.

The copper(II) complexing capacity and the amounts of acidic functional groups were carried out by the cation-exchange or by conductimetry according to methods described in previous work [27,28].

3.4. Apparatus

A Hitachi 170-50 atomic absorption spectrometer was used to determine copper(II) in the filtrate. A CG-201 PL conductimetric cell and CM-5b conductimeter (TOA Electronics) were used to measure conductivity. A 6366 glass electrode and an M-13 pH meter (Horiba) were used to measure the pH. The infrared spectra were measured using a 1720-X FTIR spectrometer (Perkin Elmer) and the KBr disk method. The UV–visible spectra were measured using a Ubest-30 spectrophotometer (Japan Spectroscopic).

4. Results and discussion

4.1. Dependence of the water solubility of copper(II) oxinate on dissolved organic carbon

The relationships between S_w^* and [DOC] at pH 6 are shown in Fig. 1. As expected from Eq. 4, the values of S_w^* linearly increased with an increase of [DOC]. The *Y*-axis intercepts of these lines (Fig. 1a–d) were in good agreement with the water solubility of $Cu(OX)_2$, S_w, measured in the absence of humic acid. Therefore, the K_{doc} values of humic acids can be evaluated by the slopes of the lines and the value of $[Cu(OX)_2]_{aq}$. These values are summarized in Table 2.

On the other hand, the concentration of the species originating from the dissociation of $Cu(OX)_2$ were calculated by the S_w values in the absence of humic acid (Fig. 2). $Cu(OX)_2$ was the predominant species at pH 6–8, and the concentration of other species were negligible. However, the $[CuOX^+]$, $[Cu^{2+}]$, $[OX^-]$, [HOX] and $[H_2OX^+]$ values could not be neglected for solutions below pH 6. Especially, the complexation of $CuOX^+$ and Cu^{2+} with humic acid would seriously affect to the association of $Cu(OX)_2$ at low pH [29]. However, the linear relationships between S_w^* and [DOC] were maintained at all pH values.

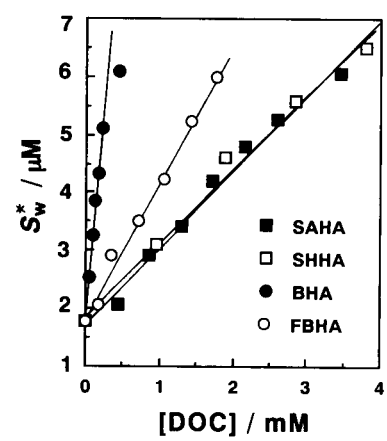

Fig. 1. Typical S_w^* *vs.* [DOC] plots of various humic acids. pH 6, adjusted by 0.01 M MES–NaOH buffer.

Table 2
Partition coefficients and contents of functional groups of various humic acids

	SHHA	SAHA	FBHA	BHA
log K_{doc}	2.82	2.89	3.18	3.91
N [a]	421	410	339	230
A [b]	82.1	64.8	56.3	43.5
(O+N)/C	0.885	0.776	0.795	0.668

[a] Copper(II) complexing capacities measured at pH 6: mmol Cu^{2+} per gram of carbon in humic acid.
[b] Amount of acidic functional groups: mmol H^+ per gram of carbon in humic acid.

4.2. *Effect of association of free oxine and humic acid on the association of copper(II) oxinate*

The free oxine (HOX) was produced below pH 6 as shown in Fig. 2. If the interaction between oxine (HOX) and humic acid is considerable, both the dissociation equilibria of $Cu(OX)_2$ and HOX will change in the presence of humic acid. The HOX association coefficient (K_{doc}^{HOX}) can be written as described for $Cu(OX)_2$,

$$K_{doc}^{HOX} = \frac{[HOX]_{HA}}{[HOX]_{aq}[DOC]} \quad (14)$$

then, by combining Eqs. 3 and 10 with 14, the following equation can be derived:

$$2(S_w^* - S_w) = 2K_{doc}[Cu(OX)_2]_{aq}[DOC] + K_{doc}^{HOX}[HOX]_{aq}[DOC] \quad (15)$$

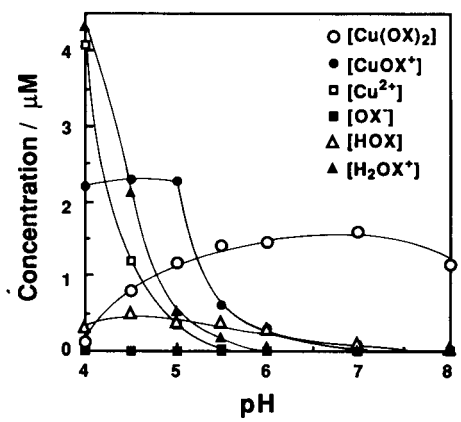

Fig. 2. Distribution curves of species derived from $Cu(OX)_2$ in the absence of humic acids. pH 4–5.5, 0.01 M HOAc–NaOAc buffer; pH 6, 0.01 M MES–NaOH buffer; pH 7–8, 0.01 M HEPES–NaOH buffer.

$Cu(OX)_2$ slightly dissolves in pure water, and this water solubility was 8.0×10^{-7} M (at 20°C). However, the water solubility of HOX was 4.5×10^{-3} M (at 20°C). Because HOX dissolved in the water more easily than $Cu(OX)_2$, HOX seems to have a more hydrophillic character than $Cu(OX)_2$. Hence, it can be predicted that HOX is less distributed into humic acid than $Cu(OX)_2$. If the $S_w^* - S_w$ term will be larger than the $K_{doc}^{HOX}[HOX][DOC]$ term in Eq. 15, the interaction between HOX and humic acid is negligible.

In order to confirm this fact, the HOX association coefficient, K_{doc}^{HOX}, was evaluated. The relationship between the [DOC] and the water solubility of HOX (S_W^{HOX} and S_W^{HOX*}) can be represented as described for $Cu(OX)_2$,

$$S_w^{HOX*} = S_w^{HOX} + K_{doc}^{HOX}[HOX]_{aq}[DOC] \quad (16)$$

According to Eq. 16, K_{doc}^{HOX} could be evaluated by measuring the water solubility of HOX. In the absence of humic acid, the water solubility of HOX, S_w^{HOX}, can be written as follows,

$$S_w^{HOX} = [OX^-]\left(1 + \frac{[H^+]}{K_{a2}} + \frac{[H^+]^2}{K_{a1}K_{a2}}\right) = \alpha[OX^-] \quad (17)$$

$[HOX]_{aq}$ can be calculated by Eq. 17. The association coefficients measured at pH 4.5 are summarized in Table 3. The $S_w^* - S_w$ term and the $K_{doc}^{HOX}[HOX][DOC]$ term were calculated by measuring S_w^* at [DOC] = 0.23 mM (Table 3). From these results, the following inequality can be de-

Table 3
Calculated values of $S_w^* - S_w$ and $K_{doc}^{HOX}[HOX][DOC]$

pH	log K_{doc}^{HOX}	$S_w^* - S_w$ (M)	$K_{doc}^{HOX}[HOX][DOC]$ (M)
BHA; [DOC]: 0.23 mM			
4.5	1.07	1.21×10^{-6}	1.31×10^{-9}
5.0	1.59	2.38×10^{-6}	3.41×10^{-9}
5.5	1.70	3.49×10^{-6}	4.39×10^{-9}
6.0	1.92	3.34×10^{-6}	5.49×10^{-9}
SHHA; [DOC]: 0.95 mM			
4.5	1.07	7.50×10^{-7}	5.41×10^{-9}
5.0	1.59	1.06×10^{-6}	1.41×10^{-8}
5.5	1.70	3.15×10^{-6}	1.81×10^{-8}
6.0	1.92	1.34×10^{-6}	2.27×10^{-8}

rived: $S_w^* - S_w \gg K_{doc}^{HOX}[HOX][DOC]$. Therefore, Eqn. 15 can be reduced to:

$$S_w^* - S_w \approx K_{doc}[Cu(OX)_2]_{aq}[DOC] \quad (18)$$

Eq. 18 is the same as Eq. 4. Therefore, it can be deduced that the HOX association with humic acid is negligible.

4.3. Effect of pH and ionic strength on the association coefficients

The dependence of K_{doc} of BHA and SHHA on pH is shown in Fig. 3. The K_{doc} maximum was at pH 5.5 for both BHA and SHHA. When protonation of functional groups in the polyelectrolyte occurs, the polarity of the polyelectrolyte would decrease [7]. Therefore, the K_{doc} seems to increase with a decrease of pH from 8 to 5.5. However, K_{doc} decreased below pH 5.5. This is due to the decrease of the amounts of $Cu(OX)_2$ caused by dissociation. Furthermore, no binding effects of Cu^{2+} or $CuOX^+$ with humic acids was indicated given the decrease of the K_{doc} below pH 5.5.

On the other hand, dependence of the K_{doc} values on ionic strength (μ) is shown in Fig. 4. K_{doc} increased with μ. With increase of μ, the negative charges of humic acid were shielded by the counter cation (in this case, Na^+). Thus the repulsion between charged groups in humic acid was weakened. Moreover, it was reported that

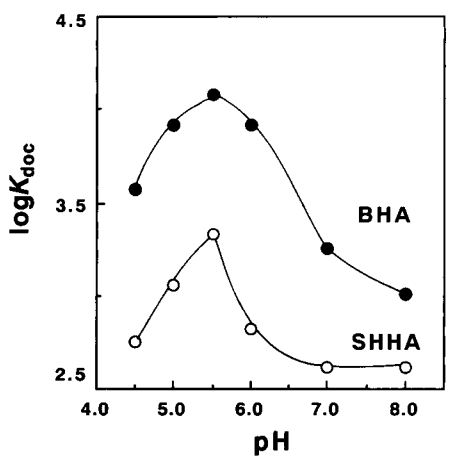

Fig. 3. Effect of pH on K_{doc}.

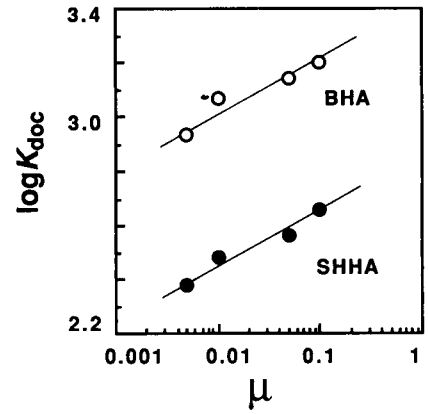

Fig. 4. Effect of ionic strength (μ) on K_{doc}. pH 7, adjusted by 5 mM HEPES–NaOH buffer.

the aggregation point of humic acid decreased by adding inorganic salt with the same trend as CMCs of surfactants [7]. Therefore, the increase of the K_{doc} values with increasing μ values is attributed to the decreasing polarity of humic acid.

4.4. Evaluation of the association coefficients of various humic acids

From the results of pH and ionic strength dependence of the K_{doc} values it can be predicted that the polarity of humic acid affects the association of $Cu(OX)_2$ with humic acid. Factors effecting the polarity of humic acids are the amount of acidic functional groups (A) and the copper(II) complexing capacity (N). In a previous study [27], evaluations of the A and N values were performed by conductimetry and the cation exchange. The A and N values are shown in Table 2. The order of the K_{doc} value was as follows: BHA > FBHA > SAHA ⩾ SHHA. The orders of the A and N values were contrary to those of K_{doc}. The orders of the A and N values correspond to the orders of polarity of humic acids. Therefore, the K_{doc} values increase with a decrease of the amounts of charged groups in humic acids (e.g., acidic functional groups and copper(II) binding sites).

On the other hand, Chiou et al. [15] reported that the ratio of polar elements, such as O and N,

to nonpolar elements such as C corresponded to the polarity of humic acids, and this parameter might effect the association coefficients. The (O + N)/C values of humic acids used in this work are summarized in Table 2. The order of these values was as follows: SHHA > FBHA > SAHA > BHA. This tendency was different from those of the K_{doc}, A and N values. Especially, for the humic acid from the marine sediment, FBHA, it was the highest. The reason will be discussed below.

The absorbance parameter, e_{400}/e_{600}, in Table 4 corresponds to amounts of chromophore or auxochrome in humic acid [30]. The order of this value was as follows: SHHA > SAHA ⩾ BHA > FBHA. This shows that the absorbance of FBHA in the ultraviolet region is the lowest. Since it is known that the chromophores of humic acid are mainly aromatic compounds [31,32], the lower absorbance in the ultraviolet region suggests that the amount of aromatic compounds in FBHA is lower than in the others.

Table 4
Absorbance parameters from UV–visible and FT-IR spectra

Humic acids	e_{400}/e_{600} [a]	A_{1100}/A_{1620} [b]	A_{1100}/A_{3400} [c]
SHHA	9.00	1.131	0.826
SAHA	7.47	1.408	1.514
BHA	7.44	1.407	0.781
FBHA	6.65	2.714	2.427

[a] Ratio of absorbance at 400–600 nm.
[b] Ratio of peak area at ca. 3400–1600 cm^{-1}.
[c] Ratio of peak area at ca. 1100–1600 cm^{-1}. A_{3400}: 3600–3000 cm^{-1}, A_{1620}: 1800–1550 cm^{-1}, A_{1200}: 1300–950 cm^{-1}.

The FTIR spectra of humic acids are shown in Fig. 5. All humic acids showed peaks at about 3400 and 1710 cm^{-1}. These peaks represent the

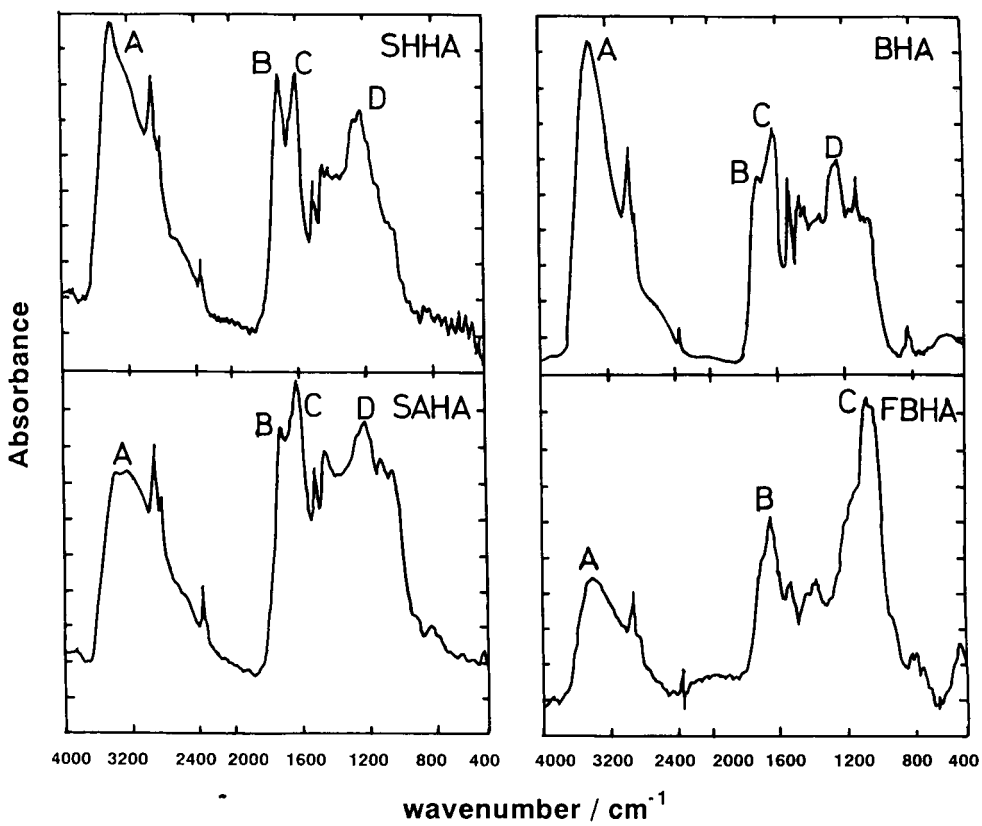

Fig. 5. FT-IR spectra of humic acids. SHHA: (A) 3407, (B) 1718, (C) 1617, (D) 1224. SAHA: (A) 3386, (B) 1708, (C) 1615, (D) 1216. BHA: (A) 3387, (B) 1708, (C) 1615, (D) 1224. FBHA: (A) 3399, (B) 1660, (C) 1085 (cm^{-1}).

O–H stretching vibration of the hydroxyl groups and the C=O stretching vibration of the carboxylic acids, respectively. The absorption maxima at about 1200 cm^{-1} in SHHA, SAHA and BHA shifted to about 1100 cm^{-1} in FBHA. It is generally known that the C–O stretching of aromatic and aliphatic ethers appears at about 1200 and 1100 cm^{-1}, respectively. Therefore, the humic acid from the marine sediment, FBHA, contains smaller amounts of aromatic compounds than the humic acids from peat. The ratios of the peak area at about 1100 cm^{-1} (A_{1100}) to that at about 3400 (A_{3400}) or that at about 1620 cm^{-1} (A_{1620}) are summarized in Table 4. The ranges of the integration are also shown in Table 4. From these results, it is found that the A_{1100}/A_{1620} and the A_{1100}/A_{3400} of FBHA were the largest of all. Thus, in FBHA, the content of hydroxyl groups is smaller but the ether content is larger. Therefore, the K_{doc} values of FBHA became larger.

5. Conclusion

The association coefficients of copper(II) oxinate, K_{doc}, could be evaluated by measuring the water solubility of $Cu(OX)_2$ in the presence of humic acids. The K_{doc} values increased with a decrease of pH and with an increase with ionic strength or functional group content in humic acids. These results suggest that the polarity of humic acid depends on the association of $Cu(OX)_2$ with humic acid. The interaction between $Cu(OX)_2$ and humic acid may be mainly a hydrophobic–hydrophobic interaction.

6. Acknowledgment

The authors are grateful to Dr. S. Tsunogai and Dr. S. Noriki, Department of Chemistry, Faculty of Fisheries, Hokkaido University for providing us with the marine sediment.

7. References

[1] M. Schnitzer and S.U. Khan, Humic Substances in the Environment, Dekker, New York, 1972, pp. 1–7.
[2] G.H. Bolt and M.G.M. Bruggenwert, Soil Chemistry, Elsevier, Amsterdam, 1978, pp. 9–12.
[3] A.M. Ure, Mikrochim. Acta (Wien), II (1991) 49.
[4] T.M. Florence, Talanta, 29 (1982) 345.
[5] D.K. Ryan and H.J. Weber, Anal. Chem., 54 (1982) 986.
[6] I. Ruzic, Anal. Chim. Acta, 140 (1982) 99.
[7] N. Shinozuka, O. Shinji and S. Hayano, J. Jpn. Oil Chem. Soc. (Yukagaku), 31 (1982) 357.
[8] N. Shinozuka and C. Lee, Mar. Chem., 33 (1991) 229.
[9] A.W. Underdown, C.H. Langford and D.S. Gamble, Environ. Sci. Technol., 19 (1985) 132.
[10] R.L. Wershaw, P.J. Burcar and M.C. Goldberg, Environ. Sci. Technol., 3 (1969) 271.
[11] C.T. Chiou, L.J. Peters and V.H. Freed, Science, 206 (1979) 831.
[12] J.C. Means and R. Wijayaratne, Science, 215 (1982) 968.
[13] B.R. Magee, L.W. Lion and T.A. Lemley, Environ. Sci. Technol., 25 (1991) 323.
[14] C.T. Carter and I.H. Suffet, Environ. Sci. Technol., 16 (1982) 735.
[15] C.T. Chiou, R.L. Malcolm, T.I. Brinton and D.E. Kile, Environ. Sci. Technol., 20 (1986) 502.
[16] D.W. Rutherford, C.T. Chiou and D.E. Kile, Environ. Sci. Technol., 26 (1992) 336.
[17] D.C. Torgeson, Fungicides I: Agricultual Applications Environmental Interaction, Academic Press, New York, 1967, pp. 1–37.
[18] D.C. Torgeson, Fungicides II: Chemistry and Physiology, Academic Press, New York, 1969, pp. 105–106.
[19] E.S. Nielsen and S. Wium-Anderson, Mar. Biol., 6 (1970) 93.
[20] E.W. Davey, M.J. Morgan and S.J. Erickson, Limnol. Oceanogr., 18 (1973) 993.
[21] G.A. Jackson and J.J. Morgan, Limnol. Oceanogr., 23 (1978) 268.
[22] N.J.L. Stauber and T.M. Florence, Mar. Biol., 94 (1987) 511.
[23] N. Watanabe, M. Kishi and M. Tsushima, Mizushori-Gijutsu (Technology of Water Treatment, in Japanese), 32 (1991) 541.
[24] D.D. Perrin, Stability Constants of Metal-Ion Complexes (Part B), Pergamon Press, Oxford, 1979, pp. 650–651.
[25] International Humic Substances Society, 1982, Outline of Extraction Procedures.
[26] S.G. Schulman and H.J. Gershon, Inorg. Nucl. Chem., 31 (1969) 2467.
[27] M. Taga, S. Tanaka and M. Fukushima, Anal. Chim. Acta, 224 (1991) 286.
[28] M. Fukushima, S. Tanaka and M. Taga, Nippon Kagaku Kaishi, (1991) 556.
[29] R.F.C. Montoura and J.P. Riley, Anal. Chim. Acta, 78 (1975) 193.
[30] Y. Chen, N. Senesi and M. Schnitzer, Soil. Sci. Am. J., 41 (1977) 352.
[31] J.F. Power and C.H. Langford, Anal. Chem., 60 (1988) 842.
[32] Z.-D. Wang, B.C. Pant and C.H. Langford, Anal. Chim. Acta, 232 (1990) 43.

ELSEVIER

Analytica Chimica Acta 289 (1994) 231–236

ANALYTICA CHIMICA ACTA

Direct determination of sodium, potassium, magnesium, and calcium ions in human saliva by ion chromatography using a taurine-conjugated bile salt micelle-coated stationary phase

Wenzhi Hu *[,a], Hiroki Haraguchi [b]

[a] National Institute for Resources and Environment, 16-3 Onogawa, Tsukuba, Ibaraki 305, Japan,
[b] Department of Applied Chemistry, School of Engineering, Nagoya University, Furo-cho, Chikusa-ku, Nagoya 464-01, Japan

(Received 6th August 1993; revised manuscript received 15th November 1993)

Abstract

Ion chromatography using a taurine-conjugated bile salt micelle-coated stationary phase has been investigated for the direct determination of common metal ions in biological samples. Taurine-conjugated bile salt micelles are reversed aggregates, where the negative charges of sulphonate form the inside of the micelle. The sulphonate charges are acting as the ion-exchange sites for the separation of cations, while the cavity of the helical micelle also acts as a size-exclusion site for the rapid elution of large organic compounds. The combination of ion-exchange and size-exclusion functions provide a new model for the direct determination of inorganic species in biological fluids using ion chromatography. The present system was successfully used for the direct determination of sodium, potassium, magnesium and calcium ions in human's mixed saliva.

Key words: Ion chromatography; Calcium; Magnesium; Potassium; Sodium; Micelles; Saliva; Taurine-conjugated bile salt micelle-coated column

1. Introduction

Determination of the variation of metal ion concentrations in human saliva is of medical interest, because these concentrations are commonly influenced by the conditions of salivary glands [1]. The use of the concentration of calcium ions in saliva to examine the thermodynamic interaction between the dental hard tissue, dental plaque and saliva is another practical application [2,3].

For the determination of metal ions in human saliva, the use of an ion-selective electrode (ISE) seems to be the common technique [2,4]. However, interferences from accompanying metal ions, hydrogen ions, and the differences of ionic strength between sample and standards, usually cause analytical errors [4]. Furthermore, determination of metal ions using ISEs provides quantitative information about a single chemical species only, which is not adequate for the diagnosis of the conditions of salivary glands. For the simple, rapid and simultaneous determination of most metal ions in human saliva, the use of ion chromatography is evaluated. The separation column

* Corresponding author.

SSDI 0003-2670(93)E0656-R

used in this work was a reversed-phase ODS packed column coated with taurine-conjugated bile salt micelles by hydrophobic interaction [5,6]. The present ion chromatographic system shows a retention behaviour different from the conventional ion chromatography in that both cation-exchange and size-exclusion interactions occur in the stationary phase. Separation of cations is due to the negative charges of sulphonate groups present in the inside of the micelle; the size-exclusion function is due to the specific stereohelical structures of bile micelle [7]. The combined functions of cation-exchange and size-exclusion allow biological samples to be directly determined by ion chromatography without sample-pretreatment, such as deproteinization.

2. Experimental

2.1. Apparatus

The microcolumn liquid chromatographic system used in the present experiments was almost the same as in the previous studies [5,6]. It consisted of a microfeeder (Model MF-2; Azumadenki, Kogyo, Tokyo) equipped with a 0.5-ml gas-tight syringe (Model ML-522; Jasco) as the pump, a microvalve injector with 0.02-μl injection volume, a 150 × 0.35 mm i.d. microcolumn packed with Develosil ODS-5 (5 μm, Nomura Chemical, Seto) and a Uvidic-100V UV detector (Jasco). A Chromatopac C-R4AX data processor from Shimadzu (Kyoto) was utilized for the peak area measurement in the chromatograms. In order to confirm the results obtained by the present system, an inductively coupled plasma atomic emission spectrometer (ICP-AES), (Model 075 Plasma Atomocomp MK II; Thermo Jarrell Ash, Franklin, MA) was also used for the determination of the concentrations of metal ions in saliva.

2.2. Reagents

The reagents used were of analytical reagent grade. As bile salts, sodium taurodeoxycholate (NaTDC) and sodium taurocholate (NaTC) were obtained from Sigma (St. Louis, MO), and used to form the bile micelle-coated stationary phase. The metal ions used were obtained as their chloride salts from Wako (Osaka). These reagents were used without furtfier purification. Copper(II) sulphate or cerium(III) chloride dissolved in pure water was employed as the light-absorbing mobile phase for the separations.

2.3. Preparation of bile micelle-coated column

Two columns were prepared as follows: an aqueous solution of 30 mM NaTDC or NaTC was passed through the two microcolumns for 20 min at a flow rate of 2.8 μl/min to adsorb the bile micelles on the ODS surfaces. Then, one of the bile micelle-coated column was conditioned with a 2 mM cerium(III) chloride aqueous solution (pH 4) as the mobile phase for the determination of magnesium and calcium ions. The other bile micelle-coated column was conditioned with a 5 mM copper(II) sulphate aqueous solution (pH 4) as the mobile phase for the determination of sodium and potassium ions.

3. Results and discussion

3.1. Structures of bile micelle-coated stationary phase and size-exclusion function

It was demonstrated in the previous studies [8,9] that bile salt micelles adsorbed on ODS surfaces act as a chiral stationary phase for the recognition of enantiomers. This is because the bile micelles adsorbed on the ODS keep their helical structures as they do in the bile salt micellar mobile phase. When taurine-conjugated bile salt micelles are coated on ODS surfaces, they act as ion-exchange sites for the separation of cations [5,6]. If the taurine-conjugated bile salt micelles coated on the ODS surfaces also keep their micellar structures, the stationary phase should simultaneously act as the cation-exchange sites for the separation of cations and as the chiral stationary phase for the recognition of enantiomers. Fig. 1 shows the chromatogram of (*R*)-(−)-1,1′-binaphthyl-2,2′-diyl hydrogenphosphate (BNDHP) and (*S*)-(+)-BNDHP enan-

tiomers obtained using a NaTDC micelle-coated stationary phase with pure water as the mobile phase. As can be seen, the enantiomers were baseline separated, which demonstrated that the NaTDC micelles coated on ODS stationary phase still keep the helical structure. The bile micelle exhibits reversed aggregation [7], therefore, the cation-exchange groups, viz., sulphonate charges are present in the inside of the helix, as represented in Fig. 2. The particular structures of the taurine-conjugated bile salt micelle-coated stationary phase should provide a specific retention mechanism which does not occur when using conventional ion-exchange stationary phases (for the determination of metal ions in biological samples using a conventional ion-exchange stationary phase, a pretreatment of deproteinization is commonly required). Therefore, we may consider to use the stereohelical structure of the micelle-coated stationary phase as size-exclusion sites for the rapid elution of large organic compounds. Fig. 3 shows a chromatogram of α-amylase obtained when using the NaTDC micelle-coated stationary phase with copper(II) sulphate aqueous solution as the mobile phase. As can be seen, the large organic compound such as α-amylase was eluted within 4 min before sodium and potassium ions appeared. α-Amylase was chosen as the typical protein in this study because α-amylase is the main protein contained in human saliva. This suggests that the present stationary phase also acts as size-exclusion site which causes the large organic compounds to be rapidly eluted from the column. This function may allow the determination of metal ions in biological fluid samples by ion chromatography without deproteinization.

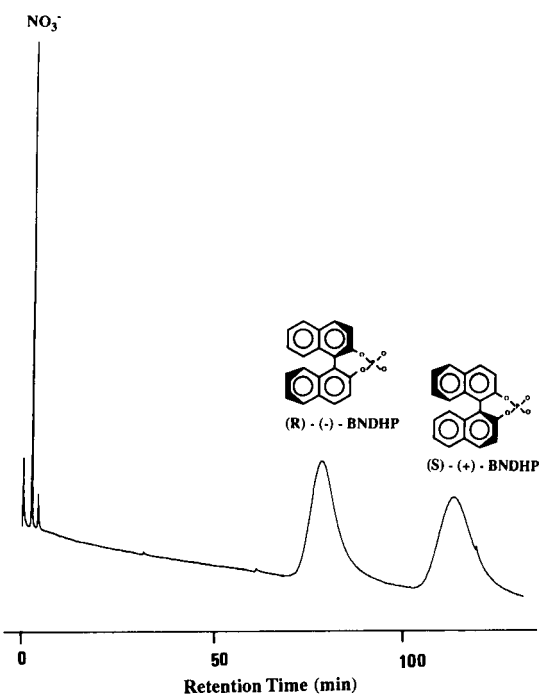

Fig. 1. Separation of BNDHP enantiomers using NaTDC micelle-coated stationary phase. Column: 150×0.35 mm i.d. packed with Develosil ODS-5 coated with NaTDC micelles; mobile phase: pure water; flow rate: 2.8 μl/min; detection at 210 nm.

3.2. Saliva sampling

Twenty-five mixed saliva samples analyzed in the present study were provided from healthy human volunteers. Further information about the sample collection is given in Tables 1 and 2. The saliva samples were taken up by a filter-aid syringe, and then directly injected into the separation column without any sample-pretreatment.

3.3. Conditions of mobile phases

It was experimentally elucidated in previous studies [5,6] that for separation of metal ions by ion chromatography using NaTDC or NaTC micelle-coated stationary phases, a mobile phase containing copper(II) ions is required for the baseline separation of alkali metal ions, while a mobile phase containing cerium(III) ions is effective for the baseline separation of alkaline earth metal ions. Therefore, aqueous solutions of copper(II) ions and cerium(III) ions were respectively used as the mobile phase for the quantitative determination of sodium/potassium ions, and magnesium/calcium ions in saliva. In order to determine the total concentrations of metal ions, the mobile phase pH was fixed at 4 by addition of HCl.

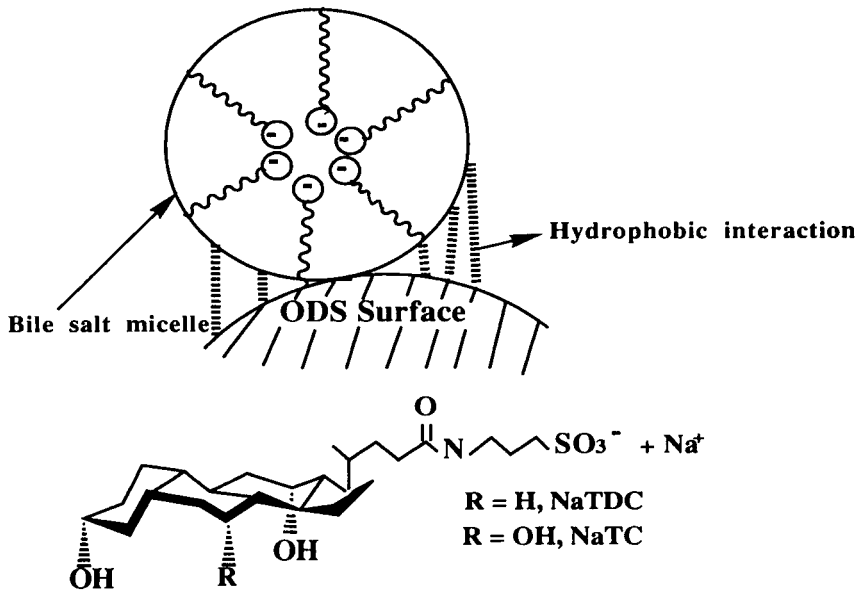

Fig. 2. Representation of taurine-conjugated bile salt micelle-coated stationary phase.

3.4. Analytical figures of merit

The calibration graphs for the determination of sodium, potassium, magnesium and calcium ions were obtained by measuring the peak areas of the analytes. Linear up to 40 mM for sodium and potassium, and linear up to 20 mM for magnesium and calcium, respectively. The relative standard deviation range was 0.1–0.5%, and the analytical recovery was 98–102%, for all cations.

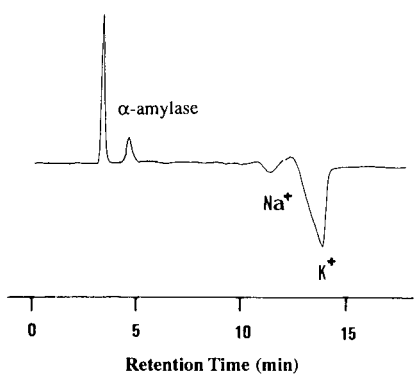

Fig. 3. Chromatogram of α-amylase. Separation conditions are the same as in Fig. 1 except for the mobile phase. Mobile phase: 5 mM copper(II) sulphate aqueous solution.

The detection limits for sodium and potassium ions were 44 μM; for magnesium and calcium were 51 μM per injection (0.02 μl) at a signal-to-noise ratio of 3, respectively.

3.5. Simultaneous determination of sodium and potassium ions

Fig. 4 shows a chromatogram of a human saliva sample obtained when using a NaTDC micelle-coated stationary phase with 5 mM copper(II) sulphate aqueous solution as the mobile phase. As can be seen, sodium and potassium ions present in human saliva were simultaneously and directly determined by using the present method. Sodium and potassium ions were detected by indirect UV-absorption detection using copper(II) as the UV-absorbing mobile phase ions. Several positive peaks appeared before the negative peaks, due to the sodium and potassium ions, which may be attributed to proteins such as α-amylase, and UV-absorbing inorganic anions such as thiocyanate contained in the saliva sample.

Twenty-one individual saliva samples were examined in this study. The concentrations of com-

Table 1
Concentrations of Na^+, K^+, Mg^{2+} and Ca^{2+} in saliva of 21 healthy individuals

Individual	Age	Sex	Concentrations (mM)			
			Na^+	K^+	Mg^{2+}	Ca^{2+}
1 [a]	29	M	3.33	32.9	0.46	2.25
1 [b]	29	M	3.31	33.0	0.46	2.26
1 [c]	29	M	3.33	33.0	0.46	2.26
2 [a]	30	F	3.35	32.3	0.46	2.30
3 [a]	32	F	3.10	33.3	0.47	2.40
4 [a]	33	F	3.41	34.0	0.45	2.35
5 [a]	45	M	3.10	32.0	0.45	2.39
6 [b]	25	M	3.20	33.0	0.46	2.40
7 [b]	25	F	3.10	32.5	0.45	2.40
8 [b]	27	M	3.21	31.0	0.44	2.50
9 [b]	28	M	3.51	30.2	0.39	2.40
10 [b]	36	M	2.98	31.5	0.50	3.01
11 [b]	38	F	3.24	32.0	0.45	2.50
12 [b]	43	F	3.10	32.1	0.46	3.10
13 [b]	46	F	4.10	33.0	0.41	2.95
14 [b]	53	F	3.20	31.0	0.46	3.10
15 [b]	53	F	3.30	32.0	0.46	2.31
16 [b]	54	F	3.30	31.0	0.45	3.10
17 [b]	61	F	4.10	29.9	0.35	2.01
18 [b]	61	F	3.50	31.0	0.40	2.30
19 [c]	63	F	3.60	31.0	0.45	2.41
20 [c]	65	M	2.95	32.0	0.45	2.10
21 [c]	71	M	3.10	31.2	0.43	2.30

Concentrations summarized in this table are the average concentrations of three determinations for each sample.
[a] Before breakfast
[b] After breakfast.
[c] After lunch.

mon metal ions in mixed saliva are summarized in Table 1. The average concentrations of potassium and sodium ions in mixed human saliva were found to be 32.0 mM, and 3.32 mM, respectively. In human saliva, the concentration of potassium ions is about ten-times higher than the concentration of sodium ions. This is in contrast to human serum, where the concentrations of sodium and potassium ions are known to be about 138 mM and 3.8 mM, respectively.

3.6. Simultaneous determination of magnesium and calcium ions

When an aqueous copper(II) sulphate solution was used as the mobile phase, alkaline earth metal ions in saliva could not be eluted from the column, although the sodium and potassium ions were baseline separated, as shown in Fig. 4. For the determination of alkaline earth metal ions in human saliva, an aqueous solution of 2 mM cerium(III) chloride (pH 4) was employed as the light-absorbing mobile phase. Fig. 5 shows a chromatogram of one of the human saliva samples obtained using a NaTDC micelle-coated stationary phase and cerium(III) as the light-absorbing ions. As can be seen, when cerium(III) ions are used as the mobile phase, sodium, potassium, magnesium and calcium ions can be simultaneously separated in human saliva. Magnesium and calcium ions can be quantitatively determined because they were baseline separated from other components in saliva. However, sodium and potassium ions can not be quantified under these separation conditions, because the two components could not be baseline separated, and because other direct UV-absorbing compositions

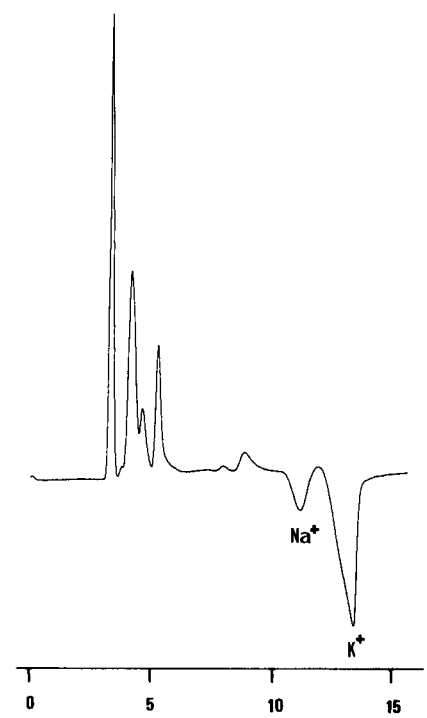

Fig. 4. Simultaneous determination of sodium and potassium ions in human saliva. Separation conditions are the same as shown in Fig. 3.

(the positive peaks shown in Fig. 4) were eluted at the same retention time as sodium and potassium ions.

The average concentrations of magnesium and calcium ions in mixed human saliva (Table 1) were found to be 0.44 mM and 2.48 mM, respectively. The concentrations of magnesium and calcium in mixed saliva are at the same level as they occur in serum.

It should be noted here that the concentrations of metal ions (particularly for calcium) determined under the present separation conditions are the *total* concentrations. This is because the calcium binding in saliva is pH dependent. All calcium is released as free Ca^{2+} ions at pH 4 [2,4]. The same saliva samples (No. 22–25) were also analyzed using ICP-AES (inductively coupled plasma atomic emission spectrometer). The results are summarized in Table 2. As can be seen, the results obtained using the present ion chromatographic system agree well with those obtained using ICP-AES.

Table 2
Comparison with the concentrations determined by ICP-AES

Individual	Age	Sex	Concentration (mM)							
			Present method				ICP-AES			
			Na^+	K^+	Mg^{2+}	Ca^{2+}	Na^+	K^+	Mg^{2+}	Ca^{2+}
22 [a]	22	M	3.25	32.1	0.46	2.31	3.10	32.8	0.47	2.33
23 [a]	23	M	3.30	32.5	0.45	2.32	3.40	33.1	0.47	2.33
24 [b]	23	F	3.23	32.7	0.46	2.34	3.30	33.1	0.46	2.35
25 [b]	30	F	3.30	32.3	0.46	2.32	3.30	32.8	0.45	2.35

[a] After breakfast.
[b] After lunch.

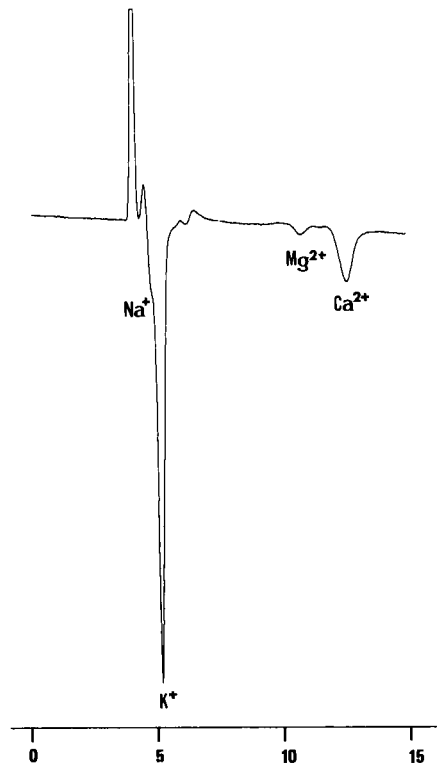

Fig. 5. Simultaneous determination of magnesium and calcium ions in human saliva. Separation conditions are the same as in Fig. 3 except for the mobile phase and the detection wavelength. Mobile phase: 2 mM cerium(III) chloride aqueous solution; detection at 253 nm.

4. References

[1] C. Dawes, Caries Res., 1 (1967) 333.
[2] F. Lagerlof, Clin. Chim. Acta, 102 (1980) 127.
[3] F. Lagerlof and L. Lindqvist, Arch. Oral. Biol., 27 (1982) 735.
[4] F. Lagerlof and S. Matsuo, Clin. Chim. Acta, 198 (1991) 175.
[5] W. Hu, T. Takeuchi and H. Haraguchi, Anal. Chim. Acta, 267 (1992) 141.
[6] W. Hu, T. Takeuchi and H. Haraguchi, Anal. Sci., 8 (1992) 507.
[7] A.R. Campanelli, S. Candeloro De Sanctis, E. Chiessi, M. D'Alagni, E. Giglio and L. Scaramuzza, J. Phys. Chem., 93 (1989) 1536.
[8] W. Hu, T. Takeuchi and H. Haraguchi, Chromatographia, 33 (1992) 63.
[9] W. Hu and H. Haraguchi, Bull. Chem. Soc. Jpn., 66 (1993) 1967.

ELSEVIER

Analytica Chimica Acta 289 (1994) 237–247

ANALYTICA CHIMICA ACTA

Determination of the platinum-group elements in South African kimberlites by nickel sulphide fire-assay and neutron activation analysis

I. McDonald *[a,b], R.J. Hart [b,c], M. Tredoux [a]

[a] *Department of Geology, University of Cape Town, Rondebosch 7700, South Africa*
[b] *Schonland Research Centre, University of the Witwatersrand, P.O. Wits 2050, Johannesburg, South Africa*
[c] *Seconded from the Geological Survey of South Africa, Private bag X112, Pretoria 0001, South Africa*

(Received 23rd November 1992; revised manuscript received 31st August 1993)

Abstract

Ten kimberlites from various localities in South Africa have been analysed for all of the platinum-group elements (PGEs) and gold using a nickel sulphide fire-assay preconcentration followed by neutron activation analysis (NAA). Problems encountered during the analysis of these samples prompted a radio tracer study to test the recovery of the precious metals during firing, and then the subsequent dissolution of the assay button. The results of this study suggest solutions to the potential problems of incomplete melting of MgO-rich and CO_2-rich during fire-assay, and minimising losses of Pt, Pd and Au during dissolution. Furthermore, this improved procedure offers lower limits of detection than previous methods which combined fire-assay and NAA. The concentrations of PGEs determined in this study of South African kimberlites are compared with previous partial analyses from the literature, indicating that earlier analyses may have seriously overestimated the concentrations of some PGEs in kimberlites.

Key words: Neutron activation methods; Platinum-group elements; Kimberlite; Peridotite; Radio tracer; Fire-assay

1. Introduction

Although kimberlites are not of economic interest with respect to the platinum-group metals (PGEs), they can potentially provide useful information on the nature of PGE carriers in the Earth's mantle [1]. For example, some authors have suggested that temperature and the degree of partial melting might play a major role in the fractionation of the PGEs relative to one another during the extraction of some magmas from the mantle [2,3]. As kimberlites are generated by very small degrees of partial melting [4], it was thought that PGE data from kimberlites might help to indicate whether the generation of low partial melt magmas was subject to similar controls. Analyses for the PGEs in kimberlites are rare in

* Corresponding author. Present address: Department of Geology, University of Manchester, Manchester M13 9PL, UK.

0003-2670/94/$07.00
SSDI 0003-2670(93)E0668-W

the geochemical literature. Published results from Siberian kimberlites [5] do not compare well with partial analyses obtained from southern African kimberlites [6,7] and it is generally agreed that the present database cannot be used to model the behaviour of the PGEs in kimberlite melts with any degree of confidence [1,4].

In the earliest study of PGE abundances in southern African kimberlites [6], the analyses were carried out by radiochemical neutron activation analysis (RNAA). Only two PGEs (Pd and Ir), along with Au, were detected in this study. RNAA also suffers from the fact that radiological health considerations place a severe constraint on the amount of material which can be irradiated during RNAA procedures [8]. At most, only a few grams of material can be taken for analysis and the extremely heterogeneous distribution of the PGEs in most rocks, the so-called 'nugget effect' [9], means that this small amount of sample may not be truly representative of the bulk material, making reproducibility of results very difficult.

Since the early 1980s, the combined use of nickel sulphide fire-assay preconcentration on large samples, first with neutron activation, and now more recently with inductively coupled plasma mass spectrometry (ICP-MS), has proved to be the favoured technique for low level analysis of all PGEs [10,11]. Laborious and intricate RNAA procedures have largely been superseded, leading to a more prolific output of high quality data for all six PGEs than was possible before. Nickel sulphide fire-assay, followed by NAA, was used in a study of four South African kimberlites and showed that in addition to Ir, Pd and Au, Os and Pt could also be detected in some samples [7].

The established limits of detection for nickel sulphide fire-assay and NAA procedures [9,12–14] are comparable with the range of PGE concentrations obtained from previous studies of kimberlites [6,7]. In the light of this, we wished to develop a routine analytical procedure based on NAA which could be used to obtain high quality, reproducible data for all six PGEs in kimberlites. First, in order to check the existing analyses from South Africa, and secondly, to establish a technique which could be used to expand the presently sparse database for PGEs in these rocks. Ten samples of kimberlite from various localities in South Africa were selected for this study and the sample locations are shown in Fig. 1.

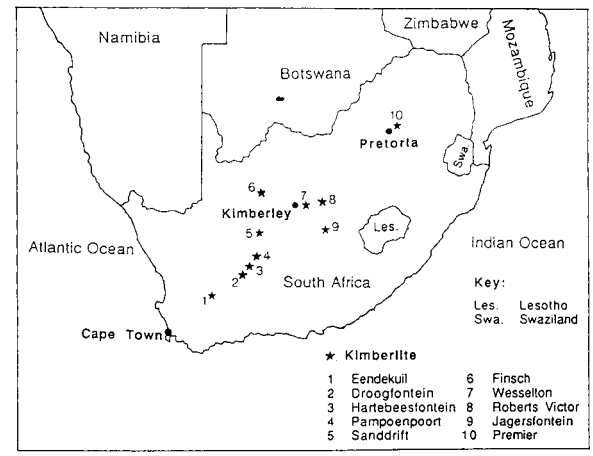

Fig. 1. Map of southern Africa showing the locations of the kimberlites analysed in this study.

2. Experimental

The analysis comprises four steps. These are (1) preparing and crushing of the sample; (2) preconcentration by nickel sulphide fire-assay; (3) acid dissolution of the assay button to leave a PGE sulphide residue which can be filtered; and (4) irradiation and gamma spectrometric analysis of the residue.

In order to account for the possibility that the samples might contain very low levels of PGEs, we designed an analysis procedure which we felt would optimise the collection and subsequent detection of the PGEs. While normal aliquots (i.e. 50 g) of sample material would be treated during the fire-assay stage, two assay buttons would be combined during the dissolution and filtering, leading to double the normal amount of PGE residue on the filter paper prior to irradiation. After activation, the analytical peaks from the residue, shown in Table 1, should then be more easily resolved from background noise during gamma counting. Final concentrations obtained from the kimberlites could then just be divided by

two to correct for the differing amounts of material processed for the kimberlites, compared with the standards.

2.1. Apparatus

The nickel sulphide fire-assay was carried out using a Keegor 42 kW electric furnace. A thermocouple circuit stabilised operating temperatures within 20°C of the set temperature. All filtrations were performed with a Sartorius SM16307 (glass frit) filtration unit using Sartorius 11306 cellulose nitrate filter papers. The filter papers had a diameter of 4.7 cm and a pore size of 0.45 μm.

Irradiations were performed in the Poolside Rotating and Pneumatic facilities of the SAFARI-1 reactor, operated by the Atomic Energy Corporation of South Africa. Thermal neutron fluxes in these facilities were 3×10^{12} n cm^{-2} s^{-1} and 7.5×10^{12} n cm^{-2} s^{-1} respectively. Gamma counting was performed on a dual detector system comprising a coaxial Ge(Li) detector opposite a planar Ge low energy photon detector (LEPD). The coaxial detector had a full width at half maximum (FWHM) value of 1.71 keV at 1332 keV and the planar detector had FWHM of 300 eV at 5.9 keV and 545 eV at 122 keV. The detectors were connected respectively through Canberra 2010 and Ortec 673 spectroscopy amplifiers to Nuclear Data 584 analogue to digital converters and a Nuclear Data 4096 channel micro multichannel analyser. Gamma energy calibrations for the coaxial and planar detectors were 0.5 keV per channel and 0.2 keV per channel respectively. Spectra were processed on an IBM-PC using a modified version of the HEVESY program [15]. A two minute irradiation for ^{104m}Rh was carried out at the reactor site. The gamma spectra were collected using a portable Ge LEPD, with same resolutions as noted above, connected to a Tracor Northern TN7200 multichannel analyser, using 2048 channels and calibrated for 0.1 keV per channel.

2.2. Reagents

During fire-assay, the following reagents were used: finely ground, anhydrous, extra pure sodium carbonate (Merck 6398); fused, GR grade disodium tetraborate decahydrate (borax) (Merck 6308); GR grade nickel carbonate (Labchem 6710); extra pure, 250 mesh silica powder (Halpro Chem.); and ground, sublimed sulphur (Merck 7982). Nickel powder purified by the Mond (carbonyl) process was not used in this study due to its restricted availability in South Africa and the fact that some batches of this material were found to contain abnormally high concentrations (> 50 μg kg^{-1}) of PGEs [7]. Repeated analysis of 8 different batches of locally produced nickel carbonate over a period of 28 months have shown that this nickel has consistently low concentra-

Table 1
Summary of PGE and Au nuclear data

Induced nuclear reaction	% Isotopic abundance of target isotope	Target cross section (barn)	Half life of product radioisotope	γ-Ray used (keV)
^{102}Ru (n,γ) ^{103}Ru [a]	31.6	1.4	38.9 days	497
^{103}Rh (n,γ) ^{104}mRh [a]	100	800	4.41 min	52
^{108}Pd (n,γ) ^{109}Pd [a,b]	26.7	12	13.5 h	88
^{190}Os (n,γ) ^{191}Os [a]	26.4	13	14.6 days	129
^{192}Os (n,γ) ^{193}Os [b]	41.0	2.1	30.5 h	139
^{191}Ir (n,γ) ^{192}Ir [a]	37.3	925	74.2 days	317
^{193}Ir (n,γ) ^{194}Ir [b]	62.7	112	19.2 h	328
^{196}Pt (n,γ) ^{197}Pt [b]	25.3	0.74	18.3 h	191
^{197}Au (n,γ) ^{198}Au [a,b]	100	98.8	2.70 days	412
^{198}Pt (n,βγ) ^{199}Au [a]	7.2	3.7	3.15 days	158

[a] Indicates an analytical radioisotope.
[b] Indicates a radioisotope used for tracer work.

tions (< 10 μg kg^{-1}) of PGEs [16]. However, of the 8 batches we tested, only those which had Ru, Pt and Pd concentrations of < 2.0 μg kg^{-1} and Ir, Os and Au concentrations of < 0.5 μg kg^{-1} were used for the analysis of unknown samples.

During the dissolution step, assay buttons were treated with extra pure, fuming 37% hydrochloric acid (Merck 314). Powdered Os, Ir, Pt, Pd and Au metals (8–50 μm particle size; Johnson Matthey specpure grade) were irradiated and used in tracer experiments.

2.3. Sample preparation and crushing

Fresh rock samples were obtained from drill cores or from surface outcrops. Visible xenolithic fragments were cut out using a diamond saw and the samples were broken into large fragments with a hammer before being crushed to small chips in a jaw crusher. The chips were sorted under a microscope to remove any smaller xenoliths and the separated fraction was crushed to minus 100 mesh between agate rings in a swing mill. It has been suggested that Pt, Pd and Au, which are malleable enough, could smear onto the agate during crushing, generating a source of possible contamination in subsequent samples [7]. Thus, after the crushing of each sample was completed and prior to the next sample being treated, barren quartz was crushed between the rings for several minutes to remove any traces of Au or PGEs which might have been left by the previous crushing. The quartz was then discarded. In reality, the consistently low levels of Pt, Pd and Au which were found in the kimberlites suggests that any cross contamination of samples via the crushing step is likely to be negligible but we consider it wise to include a cleaning step with any unknown material. After, crushing, the sample powders were sealed in screw-top bottles and homogenised on a shaker for one hour each, prior to aliquots being removed for fire-assay.

The standards employed were solid dilutions of the certified noble metal standard SARM7 [17] with high purity silica powder. SARM7, diluted ten, twenty and forty times with silica formed a range of concentrations which was compatible with the range expected in the kimberlite samples. The standards were homogenised on a shaker for 3 h each prior to fire assay. A silicified komatiite sample, Wits-1, was used as an internal PGE standard and high purity silica powder was used for the determination of reagent blanks.

2.4. Nickel sulphide fire-assay

The fire-assay procedure used is a modified version of several previously published procedures [9,12–14,18]. Samples are combined with a flux and melted at 1000°C in a clay assay crucible. During melting of this mixture, nickel sulphide is generated. The PGEs are quantitatively extracted from the silicate into the dense, immiscible sulphide phase as it descends through the melt and are present in the final assay button at the base of the crucible.

Experience has shown that some rock types do not fuse properly under the conditions employed by the above authors (see the Unmodified column in Table 2). With some peridotites ($> 30\%$ MgO and $< 40\%$ SiO_2), a layer of green crystals is sometimes found to be present just above the

Table 2
Summary of reagents used in the modified and unmodified fire-assay mixtures (all masses expressed in grams)

	Peridotite	High carbonate	Unmodified
Sample composition requirements	$< 40\%$ SiO_2 $> 30\%$ MgO	$< 25\%$ SiO_2 $> 15\%$ CO_2	
Sample material	50	50	50
Sodium carbonate	30	30	30
Borax	60	70	60
Sulphur	12.5	12.5	12.5
Nickel carbonate	35	35	35
Silica	10	20	zero

nickel sulphide button. X-ray diffraction analysis indicates that this layer is composed of recrystallized forsteritic olivine (Mg_2SiO_4). Droplets of sulphide are sandwiched between the olivine crystals in this layer. Apparently the olivine crystals may act rather like a filter, trapping some of the nickel sulphide in the silicate slag.

In addition, samples with high levels of carbonate (> 15% CO_2 and < 25% SiO_2) do not form a stable melt at all with the flux components: the highly basic mixture strongly attacks the walls of the clay assay crucible and any sulphide button which forms is generally unstable, disintegrating in air over a period of a few days to leave unconsolidated sulphide flakes. A similar disintegration was noted by Shazali [19] when the ratio of carbonate to borax in the fire-assay charge approached 1:1. For both peridotites and samples rich in carbonate, it is evident that melting of the sample, and therefore collection of the PGEs into the sulphide, may be irregular and probably incomplete.

Kimberlites are peridotitic rocks which may carry variable levels of carbonate [4,20] and we found that both of the above problems arose during fire-assay of our kimberlite samples when the original flux mixture and conditions were employed. Similar effects may occur during fire-assay with other rocks such as Mg-rich dunites, carbonatites and limestones. It was therefore decided to investigate whether the addition of extra acidic components to the flux mixture might neutralise any excess basicity and stabilise the melt.

Irradiated metals were used as tracers to test the extent of transfer of PGEs into the sulphide phase during the firing of different samples. Mixtures of approximately 5 mg each of Os, Pt and Pd and 0.1 mg of Ir and Au were irradiated, allowed to cool for 8 h and the activities of ^{109}Pd, ^{193}Os, ^{194}Ir, ^{197}Pt, ^{198}Au and ^{199}Au were determined with the Ge(Li) detector described previously, using the photopeaks listed in Table 1. Individual mixtures of the metals were then mixed with a standard sample (SARM7 diluted 10 times with SiO2), the internal standard Wits-1, a dunite (RZ4A) and a carbonatite (C/Sovite), which were then subjected to fire-assay using the normal flux mixture.

The activities of the PGE and Au isotopes collected in the sulphide button were measured on the Ge(Li) detector. Geometry and matrix corrections were carried out in a similar manner to that described by Parry et al. [21] except that instead of using PGE salts on a filter paper, irradiated metals were stuck onto clear tape and sandwiched between two halves of a split sulphide button. The recoveries, expressed relative to the initial activities are shown in Table 3. We

Table 3
Transfer of PGE into the nickel sulphide phase during fire-assays carried out on the SARM7 standard, Wits-1, dunite RZ4A, and carbonatite C/Sovite with the unmodified fire-assay flux mixtures (the data are based on the average of two measurements for each sample. n.d.a. indicates no data available)

Sample	% Activity present					
	^{109}Pd	^{193}Os	^{194}Ir	^{197}Pt	^{199}Au	^{198}Au
1:10 SARM7						
Loss to slag	2.0	2.8	1.6	2.9	4.9	5.6
NiS recovery	98.0	97.2	98.4	97.1	95.1	94.4
Wits-1						
Loss to slag	1.4	2.5	2.1	3.5	5.3	5.9
NiS recovery	98.6	97.5	97.9	96.5	94.7	94.1
RZ4A						
Loss to slag	12.3	12.6	8.0	9.7	10.4	15.7
NiS recovery	87.7	87.4	92.0	90.3	89.6	84.3
C/Sovite [a]						
Loss to slag	n.d.a.	n.d.a.	n.d.a.	n.d.a.	n.d.a.	n.d.a.
NiS recovery	n.d.a.	n.d.a.	n.d.a.	n.d.a.	n.d.a.	n.d.a.

[a] No data are available for C/Sovite due to an unstable melt.

found that losses of PGEs and Au to the slag using the unmodified flux mixture varied between 2 and 6% for the SARM7 standard and the internal standard Wits-1, which is in accord with previous studies [12,21]. In addition, the relative losses of PGEs and Au for these samples is very consistent, which indicates that the SiO2-diluted SARM7 standard and Wits-1 behave comparably during fire-assay. However, much higher losses of PGEs and Au (8–12.5%) were encountered with the RZ4A dunite and the unmodified flux, while no button could be formed from the carbonatite using the unmodified flux.

We discovered that the addition of a small amount of silica was sufficient to completely melt any olivine in the peridotite samples. High carbonate samples such as limestones or carbonatites are more unpredictable and can require the addition of both silica and additional borax to form a stable melt. Our recommended peridotitic and high carbonate flux mixtures are shown in the relevant columns of Table 2. The results of tracer experiments on the RZ4A and C/Sovite samples using these modified flux mixtures are shown in Table 4. As this table shows, the use of the modified flux mixtures resulted in similar losses (2–5%) for the dunite and carbonatite samples to those encountered during the firing of the SARM7 and Wits-1 standards with unmodified flux mixture.

It should be stressed, however, that the generalised flux mixtures shown in Table 2 are, at best, guidelines and that a detailed examination of the slag after firing is the only way to ensure that complete melting has indeed occurred. In the case of extremely high carbonate samples (> 25% CO_2) the analyst should be prepared for the possibility of several firings with progressively larger masses of additional silica and borax in order to achieve complete melting of the sample and the formation of a stable assay button.

A carbonatite from the Premier mine required the use of the high carbonate flux but, in general, the other samples in this study had peridotitic compositions with only small amounts of carbonate and most of the fire-assays were performed using the peridotitic mixture. One analysis of Roberts Victor material was carried out using the unmodified mixture for comparison.

2.5. Acid dissolution and filtering

After fire-assay, the buttons were removed from the crucibles. Each was weighed and described before being wrapped in a plastic bag and cracked with a hammer. All of the sulphide chips were emptied into a marked beaker and 500 ml of 37% HCl was then added. Dissolution of the nickel sulphide typically takes 4 to 8 h on a hotplate. The hydrogen sulphide gas generated

Table 4
Recovery of PGE into the nickel sulphide phase during fire-assays carried out on dunite RZ4A, and carbonatite C/Sovite with the modified fire-assay flux mixtures (the data are based on the average of two measurements for each sample. n.d.a. indicates no data available. SARM7 and Wits-1 data are taken from Table 3 for comparison)

Sample	% Activity present					
	^{109}Pd	^{193}Os	^{194}Ir	^{197}Pt	^{199}Au	^{198}Au
RZ4A						
Loss to slag	2.6	2.9	1.9	3.8	5.8	5.0
NiS recovery	97.4	97.1	98.1	96.2	94.2	95.0
C/Sovite						
Loss to slag	2.9	4.0	2.8	4.5	4.1	4.6
NiS recovery	97.1	96.0	97.2	95.2	95.9	95.4
1:10 SARM7						
Loss to slag	2.0	2.8	1.6	2.9	4.9	5.6
NiS recovery	98.0	97.2	98.4	97.1	95.1	94.4
Wits-1						
Loss to slag	1.4	2.5	2.1	3.5	5.3	5.9
NiS recovery	98.6	97.5	97.9	96.5	94.7	94.1

during the reaction maintains a reducing environment within the solution which should inhibit the dissolution of any PGE sulphides [10,22]. These apparently only dissolve under oxidising conditions in HCl solutions and they are etched out of the dissolving nickel sulphide to form a layer of tiny particles on the base of the beaker.

Once dissolution is complete, the beakers are quickly cooled with damp cloths and the solutions are filtered under vacuum through filter papers with a pore-size of 0.45 μm, trapping the PGE sulphide particles as a thin, grey layer. The filter papers are then folded into a triangular shape, packed into polythene vials and dried in a desiccator for several days before irradiation. As noted above, for the kimberlite samples, two assay buttons were dissolved separately and the contents of the two beakers were combined onto one filter paper to yield twice the normal amount of noble metals.

There is considerable debate as to whether losses of PGEs and Au occur during the dissolution step [10,12,14,21,23]. In previously published procedures [9,12,14,18] the hot solutions are allowed to stand for several hours after hydrogen sulphide emissions have ceased and it seems probable that losses could occur at this stage. Early tracer studies [23,24] appear to indicate that there are no major losses of PGEs and Au to the solution while a H_2S-rich environment is maintained, but that significant amounts of PGEs and Au can be dissolved in the HCl in the absence of H_2S. However, more recent studies have suggested that significant losses may take place even with H_2S present [21].

In order to asses this problem, assay buttons containing irradiated PGEs and Au were dissolved, filtered and the activities of ^{109}Pd, ^{193}Os, ^{194}Ir, ^{197}Pt, ^{198}Au and ^{199}Au were determined from the final filter paper. Four buttons were dissolved and filtered as soon as possible after the dissolution was complete. Three other buttons were deliberately left for progressively longer periods after dissolution was complete before they were filtered. The amounts of PGEs and Au on the filter paper relative to the activities initially present in the button are shown in Table 5. We found only small losses (1–3%) of Pd and Au (recorded by both ^{198}Au and ^{199}Au) when filtering took place immediately after dissolution but the losses rapidly increased (up to 10–15%) as the solutions were allowed to stand for longer periods.

Parry et al. [21] suggested that 20% losses of Ru and Au might take place during the dissolution of the nickel sulphide despite the presence of hydrogen sulphide in the solution. We did not perform tracer experiments with Ru therefore we cannot comment on its behaviour but we did not observe losses of Au comparable with those reported by Parry et al. [21]. There are two main procedural differences between our study and theirs. First, Parry et al. [21] used a Ru-rich PGE concentrate as a source of tracers, whereas we used pure metals mixed with rock powders and secondly, that they crushed the assay button prior to dissolution whereas we did not.

The recoveries of PGEs and Au into the sulphide button are comparable in the two studies therefore it does not appear that the use of

Table 5
Recovery of PGE and Au onto the final filter paper after dissolution, relative to the activity initially present in the assay button (the recovery at the dissolution end point is the average of four measurements. The other recoveries are based on single measurements)

	% Activity present					
	^{109}Pd	^{193}Os	^{194}Ir	^{197}Pt	^{199}Au	^{198}Au
Dissolution						
End point	98.6 ± 3.9	102 ± 5.0	99.6 ± 2.4	101 ± 5.1	96.0 ± 3.2	94.7 ± 2.8
End point + 6 h	96.2	105	99.5	103	92.1	92.9
End point + 12 h	92.6	101	99.2	99.4	89.7	88.0
End point + 18 h	89.9	98.9	99.3	94.5	82.6	84.7

different sample matrices is the cause of the discrepancy. Therefore, we tentatively suggest that some losses of PGEs and Au may have taken place during the crushing step, perhaps due to smearing of the metals on the walls of the crusher, and that the losses measured by Parry et al. [21] may not actually reflect losses during the dissolution itself.

Coprecipitation with Te has been used to correct for losses during dissolution [11,17] but this introduces Te into the final residue which, after activation, strongly interferes with the 158 keV peak of ^{199}Au [14,19]. The less sensitive 208 keV peak of ^{199}Au therefore has to be used and this has the effect of raising the limit of detection for Pt by a factor of 3.

As we sought the lowest possible limits of detection for kimberlite analysis, the disadvantage caused by the Te interference on Pt [14] was deemed to outweigh any advantage which could be obtained from Te coprecipitation and it was not used in this study. Instead we adopted the rigorous approach that the hot solutions should be left to stand for as little time as possible after evolution of hydrogen sulphide had ceased. In this manner, any losses of Pt, Pd and Au could be kept to an absolute minimum and the 158 keV peak of ^{199}Au could be employed.

2.6. Irradiation and counting procedures

Batches of 16 to 24 samples, comprising unknowns, standards and blanks, were packed into custom built polythene racks, along with an equal number of tantalum steel wire flux monitors. These were then sealed inside a plastic irradiation container. The container was irradiated for 12 h in the Poolside Rotating facility of the SAFARI-1 reactor.

The samples were allowed to decay for six hours after the end of the irradiation, cleaned with double distilled water, and then counted for one hour each to determine the ^{109}Pd activity. Additional counts were performed: one of two hours per sample, after six days for ^{198}Au and ^{199}Au, and another of three hours per sample after 20 days for ^{103}Ru, ^{192}Ir and ^{191}Os.

For the determination of ^{104m}Rh, samples were individually reirradiated for 2 min in the Pneumatic facility of SAFARI-1. The samples were allowed to decay for 1 min and then counted for 2 min on a planar Ge LEPD. Spectra were temporarily downloaded onto a floppy disk before being returned to the Schonland Centre for processing.

The peak areas of the analytical gamma rays shown in Table 1, corrected for neutron flux,

Table 6
Calculated detection limits and reagent blanks for the NiS fire-assay and NAA procedure detailed in this paper (detection limits estimated from other procedures are shown for comparison. For the blanks, b d l indicates beneath the limit of detection. A values are expressed in μg kg^{-1})

	Os	Ir	Ru	Rh	Pt	Pd	Au
This work (100 g sample)	0.2	0.005	1.0	0.35	2.5	0.8	0.001
This work (50 g sample)	0.4	0.01	1.8	0.60	3.8	1.5	0.002
NAA L.O.D.							
Erasmus [9]	0.5	0.05	2	0.5	5	2	0.05
Hoffman et al. [12]	2	0.1	3	1	5	5	0.1
Shazali et al. [14]	5	0.5	3	2	15	7	0.2
ICP-MS L.O.D.							
Jackson et al. [11]	0.26	0.08	0.35	0.14	0.30	0.33	1.7
Brace and Wilton [25]	0.52	0.05	0.17	0.10	0.20	0.34	1.9
Blank (1)	b d l	0.21	b d l	b d l	b d l	b d l	0.45
Blank (2)	b d l	0.30	b d l	0.41	b d l	b d l	0.67
Blank (3)	b d l	0.24	b d l	0.45	b d l	b d l	0.38
Blank (4)	b d l	0.26	b d l	b d l	b d l	b d l	0.33

Table 7
Summary of PGE and Au concentrations in the South African kimberlites analysed in this study compared with values from the literature (all are expressed in $\mu g\ kg^{-1}$. b d l indicates beneath limit of detection, and n d a indicates no data available for that element at present)

Sample	Concentration present						
	Os	Ir	Ru	Rh	Pt	Pd	Au
1 Endkl-2-1	0.53	0.76	1.8	0.70	11.4	5.4	1.1
1 Endkl-2-2	0.75	0.70	1.9	0.74	13.8	4.7	0.92
2 Drftn-9-1	1.1	1.6	4.1	1.7	10.9	6.0	3.7
2 Drftn-9-2	1.5	1.6	4.3	1.8	10.1	6.3	3.0
3 Hrtbs-16-1	0.85	0.65	2.3	0.60	b d l	0.81	0.58
3 Hrtbs-16-2	0.50	0.60	1.7	n d a	b d l	b d l	0.55
4 Pampn-6-1	1.9	2.2	4.5	1.4	3.8	2.9	0.75
4 Pampn-6-2	2.3	1.8	6.0	1.5	4.0	2.3	0.85
5 Snddft-25-1	1.4	1.1	2.4	0.92	5.7	4.8	1.4
5 Snddft-25-2	1.2	1.1	2.9	n d a	4.1	4.7	1.0
6 Fnsch-445-1	1.6	1.2	2.1	n d a	4.5	6.7	1.8
6 Fnsch-445-1	1.4	1.2	2.6	n d a	4.9	8.0	2.1
7 Wesltn-422-1	2.3	1.4	2.7	n d a	4.9	2.9	2.1
7 Wesltn-422-2	1.8	1.2	2.0	n d a	4.7	4.4	2.6
8 RoVic-112-1	1.9	1.3	2.5	0.65	6.1	0.91	1.3
8 RoVic-112-2	1.6	1.3	1.9	n d a	5.6	0.96	2.2
8 RoVic-112-3	2.0	1.4	1.7	0.30	4.0	b d l	1.6
9 Jagftn-46-1	2.5	2.0	4.0	0.82	b d l	2.3	0.91
9 Jagftn-46-2	2.2	2.0	3.8	n d a	b d l	2.4	0.79
10 Prem-243-1	0.89	0.54	0.95	0.41	3.6	1.5	0.81
10 Prem-243-2	0.47	0.42	0.66	n d a	2.8	b d l	0.67
Range of COV [a]	6–30%	0–12%	3–18%	3–17%	2–17%	2–20%	4–22%
Average COV [a]	14.1%	4.1%	10.6%	6.6%	8.3%	7.5%	10.3%
Previous data							
Jagersfontein [b]	n d a	2.6	n d a	n d a	n d a	8.9	10
Wesselton [b]	n d a	2.8	n d a	n d a	n d a	18	16
Wesselton [c]	2.5	1.5	b d l	n d a	b d l	21	3.1
Finsch [c]	b d l	1.6	b d l	n d a	22.0	b d l	3.7

[a] Coefficient of variation.
[b] Data from Paul et al. [6].
[c] Data from Tredoux [7].

decay time and counting time, were calculated and tabulated. The values from the standards and blanks were used in the preparation of calibration curves for each batch of samples. The fitted regression curves were generally good but most of the curves showed slight negative intercepts on the concentration axis, indicating the presence of small quantities of noble metals in the reagents used for the preirradiation chemistry. This was confirmed by analysis of the blanks and is discussed in the next section. Peak areas obtained from the samples were compared with calibration curves and the concentrations calculated. A correction for the differing masses (and any reagent blank) between the samples and the standards was also applied to this calculation.

3. Results and discussion

The calculated limits of detection for the combined fire-assay and NAA method, defined as the smallest concentration which gives a net peak area of twice the standard deviation of the estimated background beneath the peak of interest, and the values from blank determinations, are

shown in Table 6. The limits of detection obtained in this study offer a substantial improvement on those obtained in earlier NAA procedures [9,12,17] and, for Os, Rh and Pd, begin to approach those attained by recent ICP-MS procedures [11,25]. However, the ICP-MS limits of detection are estimated as three times the standard deviation of the background and these procedures require less sample material for analysis (15–30 g).

Ir, Rh and Au, the most sensitive elements for NAA, gave quantifiable blanks. For the other elements, the reagent blank was below the limit of detection. Detection of Ir, Rh and Au will therefore be strongly constrained by the reagent blank, as sample contributions much smaller than the reagent blank will be very difficult to resolve. The level of reagent blank therefore offers a better representation of the practical limit of detection for Ir, Rh and Au by the fire-assay and NAA procedure.

The method suggested by Asif and Parry [26], based on the use of small masses of nickel and sulphide during the fire-assay, was not employed in this study. Our Os, Ru, Rh Pt and Pd blanks were consistently lower than those reported by Asif and Parry [26] even when a smaller button was employed, but potentially their procedure could significantly reduce the contribution from Ir, Rh and Au in the nickel so that the reagent blank (and hence the real limit of detection) approaches the instrumental limit of detection. Methods of decreasing the blank using smaller assay buttons and other methods, are presently under evaluation.

We found that the absolute concentrations of the PGEs and Au in South African kimberlites are quite low, generally < 10 μg kg^{-1}, as indicated by Table 7. Despite these low concentrations, the average coefficients of variation only range between 4.1 and 14.1%. This is better than the typical precision attainable for SARM7 or Wits-1 using 50 g of sample [16]. The Roberts Victor samples run with different flux mixtures show a reasonable agreement for Os, Ir and Au, but slightly less Ru, Rh, Pt and Pd appear to have been collected by (8 Rovic 112-3), which employed the unmodified flux mixture. This suggests that complete melting and collection probably did not take place during the firing of this sample.

The low concentration of Pt in most of the samples appears to confirm our decision not to employ Te coprecipitation during the dissolution step. It is extremely doubtful whether the use of the less sensitive 208 keV peak of ^{199}Au would have allowed the detection of Pt in most of the samples. The view expressed by Shazali et al. [14] that a coprecipitation step is essential clearly does not apply to all cases, especially those where very low levels of Pt are anticipated. Comparison with previous data [6,7] shows a generally good agreement for Os and Ir but suggests that abundances of Pt, Pd and Au may have been seriously overestimated in the earlier studies.

4. Acknowledgements

The authors would like to thank Anglo American Research Laboratory who kindly made sample material available for this study. K.S. Viljoen and C.B. Smith are thanked for additional samples and for their keen interest and many helpful discussions. Analytical costs were met by the Geological Survey of South Africa through an operating grant to R.J. Hart and by an FRD grant to Marian Tredoux. Iain McDonald acknowledges financial support via a J.W. Jagger scholarship from the University of Cape Town.

5. References

[1] J.H. Crocket, in L.J. Cabri (Ed.), Platinum-Group Elements: Mineralogy, Geology And Recovery, Can. Inst. Min. Metall. Spec. Vol. 23, 1981, p. 47.
[2] M. Tredoux, G. Davies, N.M. Lindsay and J.P.F. Sellschop, Geocongress '86, University of the Witwatersrand (extended abstracts), 1986, p. 625.
[3] D.C. Peck and R.R. Keays, Can. Mineral., 28 (1990) 553.
[4] R.H. Mitchell, Kimberlites, Plenum Press, New York, 1986.
[5] F.V., Kaminskiy, Y.V., Frantesson and V.P., Khvostova, Dokl. Akad. Nauk SSSR., 219 (1974) 190.
[6] D.K. Paul, J.H. Crocket and P.H. Nixon, in F.R. Boyd and H.O.A. Meyer (Eds.), Kimberlites, Diatremes and Diamonds: Their Geology, Petrology And Geochemistry, American Geophysical Union, Washington, DC, 1979, p. 272.

[7] M. Tredoux, PhD thesis, University of the Witwatersrand, 1990.
[8] J.H. Crocket and L.J. Cabri, in L.J. Cabri (Ed.), Platinum-Group Elements: Mineralogy, Geology And Recovery, Can. Inst. Min. Metall. Spec. Vol. 23, 1981, p. 71.
[9] C.S. Erasmus, N.I.M. Tech. Memo. 10928, (1982).
[10] W.C. Lenahan and R. de L. Murray-Smith, S. Afr. Inst. Min. Metall. monograph M6, 1986.
[11] S.E. Jackson, B.J. Fryer, W. Gosse, D.C. Healey, H.P. Longerich and D.F. Strong, Chem. Geol., 83 (1990) 119.
[12] E.L. Hoffman, A.J. Naldrett, J.C. van Loon, R.G.V. Hancock and A. Manson, Anal. Chim. Acta, 102 (1978) 157.
[13] R.V.D. Robért, E. van Wyk and R. Palmer, N.I.M. Report 1371, 1971.
[14] I. Shazali, L. Van't Dack and R. Gijbels, Anal. Chim. Acta, 196 (1987) 49.
[15] H.P. Yule, U.S. NBS Spec. Publ. 312, (1968) 115.
[16] I. McDonald, PhD thesis, University of Cape Town, 1993.
[17] T.W. Steele, J. Levin and I. Copelowitz, N.I.M. Report 1696, 1975.
[18] G. Davies and M. Tredoux, Econ. Geol., 80 (1985) 838.
[19] I. Shazali, PhD thesis, University of Antwerp, 1988.
[20] A. Hall, Igneous Petrology, Longman, Harlow, 1987.
[21] S.J. Parry, M. Asif and I.W. Sinclair, J. Radioanal. Nucl. Chem., 123 (1988) 593.
[22] S. Kallman and C. Maul, Talanta, 30 (1983) 21.
[23] A.P. Kuznetsov, Yu N. Kukushin and D. Makarov, Zh. Anal. Khim., 29 (1974) 2155.
[24] R. Palmer and J.I.W. Watterson, N.I.M. Report 1185, 1971.
[25] T.D. Brace and D.H.C. Wilton, Can. Mineral., 28 (1990) 419.
[26] M. Asif and S.J. Parry, Analyst, 114 (1989) 1057.

ELSEVIER

Analytica Chimica Acta 289 (1994) 249–257

ANALYTICA CHIMICA ACTA

Comparison of structure-thermal property relationships for barium bis(1,1,1,5,5,5-hexafluoro-2,4-pentanedionate) polyether complexes

Halina D. Inerowicz, Thekkekalathil M. Chandrasekhar, Gordon Atkinson, Robert L. White *

Department of Chemistry and Biochemistry, University of Oklahoma, Norman, OK 73019, USA

(Received 2nd September 1993; revised manuscript received 12th November 1993)

Abstract

The thermal properties of $Ba(hfa)_2$, $Ba(hfa)_2$(tetraglyme), $Ba(hfa)_2$(18-crown-6), and $Ba(hfa)_2$(diaza-18-crown-6) are investigated by comparing the results of thermogravimetric analysis (TGA) for these materials. All TGA measurements were made in helium at atmospheric pressure. Infrared, MS, NMR, and x-ray crystallographic measurements are compared for each of the complexes and correlations are made between the structure-specific information derived from these analyses and the thermal properties of the barium complexes.

Key words: Thermometric methods; Barium complexes; Complexes; Bis(1,1,1,5,5,5-hexafluoro-2,4-pentanedionate) polyether complexes with barium

1. Introduction

The recent discovery of ceramics that are superconductive above 20 K [1–3] has led to material science research directed toward developing new products that incorporate these substances. The use of high temperature superconductors in the microelectronics industry is in its infancy. Current research efforts in high temperature superconducting electronics focus on developing new device fabrication methodologies for making hybrid semiconductor/superconductor circuits [4]. Layered thin films must be created in order to produce integrated circuits. Ceramic superconducting thin films can be formed by evaporation [5,6], sputtering [7–11], laser ablation [12–14], and metal–organic chemical vapour deposition (MOCVD) [15–18]. Because it is easier to form thin films on large surface area substrates by MOCVD than by evaporation, sputtering or laser ablation, MOCVD is potentially the best currently available method for commercial production of hybrid semiconductor/superconductor integrated circuits.

The MOCVD process involves the vapour phase transportation of volatile, metal-containing materials that are decomposed to release free

* Corresponding author.

SSDI 0003-2670(93)E0650-V

metal or metal ions in the vicinity of the film substrate [19–22]. For the production of Y–Ba–Cu–O, Bi–Sr–Ca–Cu–O, and Tl–Ba–Ca–Cu–O superconducting thin films, metal β-diketonate complexes are commonly used to transport metals [23–28]. Unfortunately, the thermal properties of barium β-diketonates are poor compared to other metal β-diketones used to make high temperature superconductor thin films by MOCVD [29]. Barium β-diketonates decompose during sublimation and can form oligomeric complexes in the vapour phase [30–34]. These properties result in inefficient and variable barium transport to substrate surfaces during MOCVD thin layer formation. Recent studies have shown that the MOCVD transportation efficiency for barium can be improved by increasing the number of organic ligands coordinated to barium in the volatile complex. This has been accomplished by saturating the barium β-diketone complex carrier gas with oxygen and nitrogen Lewis bases [26,35] and by using barium complexes containing barium ions with higher coordination numbers [36–40].

Barium complexes that sublime at the lowest temperatures are derived from the barium bis(1,1,1,5,5,5-hexafluoro-2,4-pentanedionate) [$Ba(hfa)_2$] complex [29] (**1**) by adding a multidentate ligand. Although fluorinated barium complexes are generally not preferred for MOCVD applications due to the possibility of BaF_2 formation, high quality Y–Ba–Cu–O films can be made from fluorinated barium complexes when appropriate techniques are employed [41]. The synthesis and preliminary characterization of $Ba(hfa)_2$ (tetraglyme) (**2**) and $Ba(hfa)_2$(18-crown-6) (**3**) have been described previously [40,42–45]. In these barium complexes, the barium ion is coordinated to 9 and 10 oxygen atoms respectively. We recently reported the structure of another barium complex of the same type: $Ba(hfa)_2$(diaza-18-crown-6) (**4**) [46]. In order to explain differences in the thermal properties of these $Ba(hfa)_2$-polyether complexes, it is useful to compare the solid-state structural features of **1–4**. Some structural and thermal property information for **1–4** has been published [29,40,42–46]. However, the analysis conditions used to make these measurements varied significantly making correlations between results obtained by different investigators difficult. In order to facilitate the best possible correlations between structural features and the thermal properties of **1–4**, we have augmented structural information previously derived from x-ray crystallographic analyses [43,45,46] with MS, TGA-MS, IR, and ^1H NMR analyses using the same instrumentation and analysis conditions for each substance.

2. Experimental

2.1. Apparatus

Thermogravimetric analyses were performed with a DuPont (Wilmington, DE) Model 951 TGA analyzer. Helium was used as a carrier gas and 5 mg samples were heated at a rate of 10°C/min from 50 to 450°C. TGA-MS measurements were made by connecting the gas outlet of the TGA analyzer to a Hewlett-Packard (Palo Alto, CA) 5985 quadrupole mass spectrometer by means of a Scientific Glass Engineering (Austin, TX) MCVT-1-50 variable splitter valve. The TGA-MS interface was maintained at 240°C by using heating tape. TGA-MS mass spectra were acquired by using 70 eV electron bombardment ionization and scanning from m/z 10 to 1000 at a rate of 2 spectra/min. Ion source pressure was maintained at 5×10^{-6} Torr. Direct insertion probe mass spectra were measured for solid samples with a Hewlett-Packard 5985A quadrupole mass spectrometer. In these measurements, the ionizing electron energy was 70 eV and the ion source temperature was maintained at 200°C. The direct insertion probe was heated from 30 to 300°C at a rate of 30°C/min. ^1H NMR spectra were recorded in $CDCl_3$ on a Varian (Palo Alto, CA) 300XL spectrometer. Infrared spectra (4000–800 cm^{-1}) were measured for KBr pellets (solid samples) and for capillary thin films (liquid samples) with a Mattson (Madison, WI) Sirius 100 FT-IR. Sublimations were carried out in an evacuable glass sublimation apparatus built in our glass shop. Elemental analyses were performed by E + R Microanalytical Lab. (Corona, NY). Hfa vibrations were assigned with the aid of the general

vibrational analysis system software (QCMP 067) obtained from Indiana University through the Quantum Chemistry Program Exchange.

2.2. Reagents

Barium hydride was purchased from Strem Chemicals (Newburyport, MA). $Ba(OH)_2 \cdot 8H_2O$, 2,5,8,11,14-pentaoxapentadecane (tetraglyme), 1,4,7,10,13,16-hexaoxacyclooctadecane (18-crown-6), 1,4,10,13-tetraoxa-7,16-diaza-cyclooctadecane (diaza-18-crown-6), and 1,1,1,5,5,5-hexafluoro-2,4-pentanedione (Hhfa) were obtained from Aldrich (Milwaukee, WI) and were used as received. Tetrahydrofuran (THF) was also obtained from Aldrich and was freshly distilled from Na and benzophenone prior to use.

2.3. Synthesis

$Ba(hfa)_2$ (**1**) was prepared by mixing 139 mg of BaH_2 (1 mmol) with 0.28 ml of Hhfa (2 mmol) under nitrogen for 2 h. $Ba(hfa)_2$ was purified by sublimation at 205–220°C and 10^{-2} Torr.

$Ba(hfa)_2$(tetraglyme) (**2**) was prepared by mixing 70 mg of BaH_2 (0.5 mmol), 111 mg of tetraglyme (0.5 mmol) and 0.14 ml of Hhfa (1 mmol) in 15–20 ml of THF. After stirring the mixture for 3 h under nitrogen, the THF solvent was evaporated. The product was purified by sublimation at 150°C and 10^{-2} Torr. Anal. Calc. for $BaC_{20}H_{24}O_9F_{12}$: Ba, 17.75; C, 31.05; H, 3.13. Found Ba, 17.95; C, 31.28; H, 2.96.

$Ba(hfa)_2$(18-crown-6) (**3**) was prepared by adding 0.28 ml of Hhfa (2 mmol) to a stirred mixture containing 140 mg of BaH_2 (1 mmol) and 264 mg of 18-crown-6 (1 mmol) in 20 ml of freshly distilled THF. The mixture was stirred for 3 h under nitrogen and then the solvent was evaporated. The final product was purified by sublimation at 160–180°C and 10^{-2} Torr. Anal. Calc. for $BaC_{22}H_{26}O_{10}F_{12}$: Ba, 16.83; C, 32.39; H, 3.21. Found: Ba, 16.48; C, 33.07; H, 3.38.

$Ba(hfa)_2$(diaza-18-crown-6) (**4**) was prepared by mixing 70 mg of BaH_2 (0.5 mmol), 131 mg of diaza-18-crown-6 (0.5 mmol) and 0.14 ml of Hhfa (1 mmol) in 20 ml of THF. After 2 h of stirring under nitrogen, the solvent was evaporated and the final product was purified by sublimation at 180–200°C and 10^{-2} Torr. Anal. Calc. for $BaC_{22}H_{28}O_8N_2F_{12}$: Ba, 16.88; C, 32.47; H, 3.47. Found: Ba, 16.68; C, 32.26; H, 3.32.

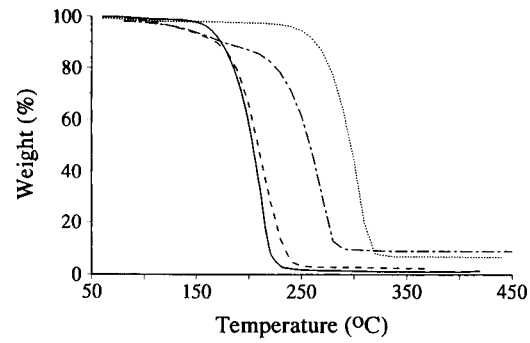

Fig. 1. Thermograms measured for $Ba(hfa)_2$ (dotted line), $Ba(hfa)_2$(tetraglyme) (solid line), $Ba(hfa)_2$(18-crown-6) (long dash–short dash line), and $Ba(hfa)_2$(diaza-18-crown-6) (dashed line).

3. Results

TGA was employed in this study to compare the thermal properties of **1–4**. Thermograms for these materials are shown in Fig. 1. Table 1 lists the temperatures at which the major weight loss step started (T_s) and ended (T_f) as well as the temperature at which the inflection point occurred (T_i) in thermograms for **1–4**. All of the $Ba(hfa)_2$-polyether complexes sublimed at much lower temperatures than $Ba(hfa)_2$. The $Ba(hfa)_2$(18-crown-6) complex was significantly less volatile

Table 1
Thermogravimetric data for Ba complexes [a]

Substance	T_s [b] (°C)	T_i [c] (°C)	T_f [d] (°C)	Residue (% wt.)
$Ba(hfa)_2$(tetraglyme)	160	215	230	1
$Ba(hfa)_2$(18-crown-6)	220	254	280	9
$Ba(hfa)_2$(diaza-18-crown-6)	170	222	240	2
$Ba(hfa)_2$	250	300	310	8

[a] Averages from at least three measurements.
[b] Temperature at which the major weight loss step begins.
[c] Temperature at which inflection point in TGA curve occurs.
[d] Temperature at which weight loss ends.

at 250°C than the other $Ba(hfa)_2$-polyether complexes. In fact, the major weight loss in the thermogram for $Ba(hfa)_2$(18-crown-6) occurred about 40°C higher than the major weight losses for the other two $Ba(hfa)_2$-polyether complexes. The barium complexes were analyzed by mass spectrometry, ^1H NMR, and infrared spectrometry to obtain structural information that might help to explain their thermal properties.

Mass spectra were measured for **1–4** by using a solids direct insertion probe. In addition, mass spectra were obtained for **2–4** by coupling the TGA to the ion source of a mass spectrometer. Mass spectra obtained by TGA-MS were similar to those measured by the direct insertion probe method. Table 2 summarizes some of the fragment ion information derived from probe-MS and TGA-MS measurements of **1–4**. Mass spectra results for **2** and **3** were similar to previously published solid probe mass spectra [42,44]. Molecular ions were not detected in the spectra of any of the complexes. The highest m/z ion detected in $Ba(hfa)_2$-polyether spectra corresponded to the loss of one hfa ligand. The doubly charged ion resulting from the loss of both hfa ligands was also present in all three $Ba(hfa)_2$-polyether mass spectra. In contrast to the $Ba(hfa)_2$-polyether complexes, mass spectra for $Ba(hfa)_2$ contained ion intensity at m/z values above the theoretical molecular weight of the complex. These ions corresponded to species containing two barium atoms. Volatile species containing multiple Ba atoms are commonly found by mass spectrometric analysis of four-coordinate barium β-diketonates [30–34].

Table 2
Mass spectral data for Ba complexes

Substance	m/z	Rel. int.	Ion
$Ba(hfa)_2$	567	77	$[M-L]^+$
(tetraglyme)	379	25	$[(M-2L)F]^+$
	345	44	$[M-L-\text{polyether}]^+$
	180	100	$[M-2L]^{2+}$
	157	79	$[BaF]^+$
$Ba(hfa)_2$	609	38	$[M-L]^+$
(18-crown-6)	421	12	$[(M-2L)F]^+$
	345	20	$[M-L-\text{polyether}]^+$
	201	100	$[M-2L]^{2+}$
	157	55	$[BaF]^+$
$Ba(hfa)_2$	607	54	$[M-L]^+$
(diaza-18-crown-6)	419	7	$[(M-2L)F]^+$
	345	28	$[M-L-\text{polyether}]^+$
	200	100	$[M-2L]^{2+}$
	157	63	$[BaF]^+$
$Ba(hfa)_2$	897	13	$[Ba_2L_3]^+$
	709	10	$[Ba_2L_2F]^+$
	520	24	$[Ba_2LF_2]^+$
	345	85	$[M-L]^+$
	157	100	$[BaF]^+$
	139	12	$[L-CF_3]^+$

Table 3
^1H NMR data for ligands and Ba complexes

Substance	$\delta(CDCl_3)$
Hhfa	6.38 (s; 2H)
Tetraglyme	3.32 (s; 6H)
	3.50 (m; 4H)
	3.58 (m; 4H)
	3.61 (s; 8H)
18-Crown-6	3.67 (s; 24H)
Diaza-18-crown-6	2.28 (s; 2H)
	2.80 (m; 8H)
	3.58 (m; 16H)
$Ba(hfa)_2$(tetraglyme)	3.36 (s; 6H)
	3.48 (m; 4H)
	3.58 (m; 4H)
	3.76 (m; 4H)
	3.80 (m; 4H)
	5.84 (s; 2H)
$Ba(hfa)_2$(18-crown-6)	3.75 (s; 24H)
	5.80 (s; 2H)
$Ba(hfa)_2$(diaza-18-crown-6)	2.77 (m; 4H)
	3.02 (m; 4H)
	3.27 (s; 4H)
	3.44 (m; 2H)
	3.54 (m; 4H)
	3.69 (m; 4H)
	3.84 (m; 2H)
	5.76 (s; 2H)
	9.05 (s; 2H)

The ^1H NMR spectra of **2–4** and Hhfa, tetraglyme, 18-crown-6, and diaza-18-crown-6 ligands are summarized in Table 3. The single Hhfa proton resonance shifted from 6.38 ppm in the neutral ligand to 5.76–5.84 ppm in the barium complexes. Proton NMR signals derived from tetraglyme were slightly shifted in $Ba(hfa)_2$(tetraglyme) compared to the free ligand. The 3.61 ppm singlet observed in the NMR spectrum of

the ligand was split into multiplets at 3.76 ppm and 3.80 ppm in the complex. The 3.67 ppm singlet in the 18-crown-6 spectrum shifted to 3.75 ppm in the NMR spectrum of the $Ba(hfa)_2$(18-crown-6) complex. The proton NMR signals for diaza-18-crown-6 changed significantly when this ligand was coordinated to barium. The NMR spectrum of uncoordinated diaza-18-crown-6 contained a singlet at 2.28 ppm and multiplets at 2.80 and 3.58 ppm. In the $Ba(hfa)_2$(diaza-18-crown-6) complex, these signals were split into two singlets and six multiplets.

The most intense absorption bands found in infrared spectra of **1–4** and Hhfa, tetraglyme, 18-crown-6, and diaza-18-crown-6 are listed in Table 4. Absorption bands at 1086 and 1087 cm^{-1} in $Ba(hfa)_2$-polyether complex spectra correspond to the C–O–C stretching vibration of the polyether. Infrared bands at 1664 and 1670 cm^{-1} in $Ba(hfa)_2$-polyether complex spectra correspond to the C–O stretching vibration of the hfa ligands. The medium and strong absorptions found between 1100 and 1600 cm^{-1} in $Ba(hfa)_2$-polyether complex spectra also arise from the hfa ligands.

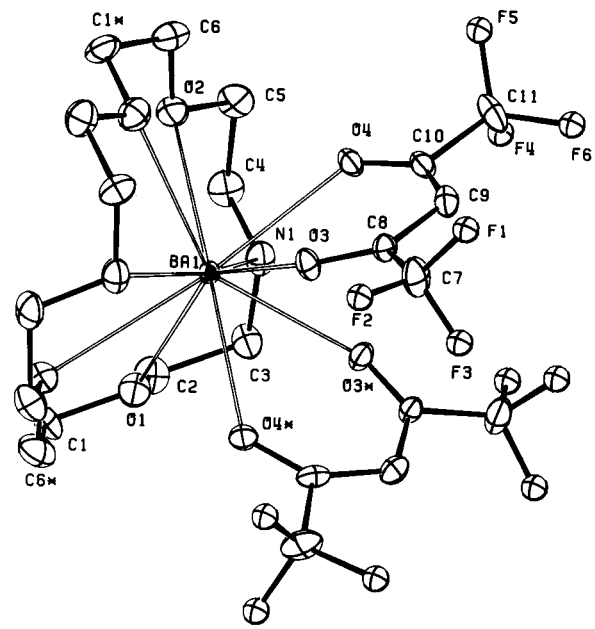

Fig. 2. ORTEP drawing for the molecular structure of $Ba(hfa)_2$(diaza-18-crown-6).

Table 4
Infrared data for Ba complexes and ligands

$Ba(hfa)_2$ (tetraglyme)	$Ba(hfa)_2$ (18-crown-6)	$Ba(hfa)_2$ (diaza-18-crown-6)	$Ba(hfa)_2$
954 [a] (w)	958 (m)	950 (w)	665 (w)
1087 (s)	1087 (s)	1086 (m)	802 (w)
1141 (s)	1137 (s)	1126 (s)	1155 (s)
1199 (s)	1194 (s)	1186 (s)	1201 (s)
1253 (s)	1249 (s)	1251 (s)	1261 (s)
1527 (s)	1529 (s)	1535 (s)	1541 (s)
1664 (s)	1670 (s)	1670 (s)	1666 (s)
2931 (w)	2937 (w)	2914 (w)	
Tetraglyme	18-Crown-6	Diaza-18-crown-6	Hhfa
850 (w)	837 (w)	839 (w)	817 (s)
947 (w)	964 (m)	960 (m)	914 (m)
1107 (s)	1107 (s)	1094 (s)	1082 (s)
1199 (w)	1248 (w)	1249 (m)	1159 (s)
1248 (w)	1348 (w)	1286 (m)	1267 (s)
1350 (w)	1471 (w)	1352 (m)	1359 (m)
1454 (w)	2891 (m)	1452 (m)	1444 (m)
2876 (s)		1637 (m)	1633 (s)
		2881 (s)	1685 (s)

[a] All infrared absorption band frequencies are in cm^{-1}.

4. Discussion

TGA-MS studies indicated that all three $Ba(hfa)_2$-polyether complexes sublime as molecular species. In contrast, $Ba(hfa)_2$ sublimes as oligomers containing multiple barium atoms [30–34]. All three $Ba(hfa)_2$-polyethers sublime at lower temperature than $Ba(hfa)_2$. However, the major weight loss step in the thermogram for $Ba(hfa)_2$(18-crown-6) occurred at significantly higher temperature than for $Ba(hfa)_2$(tetraglyme) or $Ba(hfa)_2$(diaza-18-crown-6), indicating that solid state intermolecular interactions are stronger for $Ba(hfa)_2$(18-crown-6) than for the other polyether complexes.

Complexes containing tetraglyme [43] and 18-crown-6 [45] have similar structures in the solid state with hfa ligands located on opposite sides of the barium atom and the polyether located between the hfa ligands. In contrast, the $Ba(hfa)_2$(diaza-18-crown-6) complex has a solid state

structure (Fig. 2) in which both hfa ligands are on one side of the barium atom and the polyether is on the other side [46]. In addition, whereas the carbon and oxygen atoms in tetraglyme and 18-crown-6 ligands occupy locations that are approximately in the same plane in the $Ba(hfa)_2$-polyethers [43,45], the diaza-18-crown-6 carbon, oxygen, and nitrogen atoms in $Ba(hfa)_2$(diaza-18-crown-6) are not co-planar. For example, N1 and C1 in Fig. 2 are displaced from the polyether mean plane by about 1 Å [46].

The ^1H NMR spectra of tetraglyme, 18-crown-6, and diaza-18-crown-6 are fairly simple and representative of a high degree of symmetry for these uncomplexed ligands. The ^1H NMR spectra of tetraglyme, 18-crown-6, $Ba(hfa)_2$(tetraglyme), and $Ba(hfa)_2$(18-crown-6) summarized in Table 3 compare favourably with previously published data [42,44]. The ^1H NMR spectra of $Ba(hfa)_2$(tetraglyme) and $Ba(hfa)_2$(18-crown-6) differ from the spectra of the uncomplexed polyether ligands only slightly, which is consistent with the x-ray crystallographic measurements that indicate a nearly planar orientation of these ligands about barium. The ^1H NMR spectrum of $Ba(hfa)_2$(diaza-18-crown-6) is significantly different from the spectrum of uncomplexed diaza-18-crown-6. In particular, the N–H proton resonance shifts from 2.28 ppm in the uncomplexed polyether to 9.05 ppm in the complex, indicating that a dramatic decrease in N–H proton shielding occurs when the complex is formed. X-ray crystallographic measurements indicate that uncomplexed diaza-18-crown-6 is approximately planar [47]. Because the diaza-18-crown-6 ring is not planar in $Ba(hfa)_2$(diaza-18-crown-6), a significant distortion of the crown ether ring must occur when diaza-18-crown-6 complexes with barium. This distortion accounts for the increased complexity of the ^1H NMR spectrum of $Ba(hfa)_2$(diaza-18-crown-6) compared to uncomplexed diaza-18-crown-6. The 2.28 ppm and 3.58 ppm multiplets in the free ligand spectrum are split respectively into two and five multiplets in the complex spectrum. In uncomplexed diaza-18-crown-6, the amine hydrogen atoms are located within the crown ether ring and the nitrogen lone pair electrons are located outside the crown ether ring [47]. In order to align the nitrogen lone pair electrons with barium ion orbitals, the amines in the crown ether ring must rotate so that the lone pair electrons move inside the crown ether ring and the hydrogen atoms move outside the ring. The crystallographic and ^1H NMR results described above are consistent with this mechanism.

Infrared vibration frequencies measured for free ligands and **1–4** were compared in order to investigate electron density distortions that occur in $Ba(hfa)_2$-polyether complexes due to coordination of the ligands with barium. Infrared spectra for $Ba(hfa)_2$ and $Ba(hfa)_2$(tetraglyme) were qualitatively similar to previously reported spectra [29,44]. The C–O–C stretching vibration in infrared spectra of **2–4** occurred at lower frequency than the C–O–C stretching vibration of the uncomplexed polyethers. The decrease in this infrared vibration frequency results from electron density being drawn away from ether oxygens by the barium ion in the complex. For $Ba(hfa)_2$(tetraglyme) and $Ba(hfa)_2$(18-crown-6), the C–O–C stretching vibration frequency decreased by 20 cm^{-1} compared to the frequency of the uncomplexed ethers. For $Ba(hfa)_2$(diaza-crown-6), the C–O–C stretching vibration frequency shifted from 1094 cm^{-1} in the uncomplexed ligand to 1086 cm^{-1} in the complex, a shift of only 8 cm^{-1}. The small frequency shift observed for $Ba(hfa)_2$(diaza-18-crown–6) compared to the other $Ba(hfa)_2$-polyethers may indicate that less electron density is withdrawn from crown ether oxygen lone pair electrons by the barium ion in $Ba(hfa)_2$(diaza-18-crown-6). However, it is not possible to attribute this frequency shift entirely to electronic effects because the structure of the diaza-18-crown-6 ligand changes significantly when the ligand is complexed with barium and these structural changes may also affect the frequency of this infrared absorbance band.

Most of the infrared absorptions observed in spectra of $Ba(hfa)_2$-polyether complexes can be assigned to hfa ligand vibrations. By using the relative hfa atom locations derived from x-ray crystallographic measurements, vibration modes for the hfa ligand corresponding to the 1670, 1535, 1251, 1186, and 1126 cm^{-1} bands in the infrared spectrum of $Ba(hfa)_2$(diaza-18-crown-6)

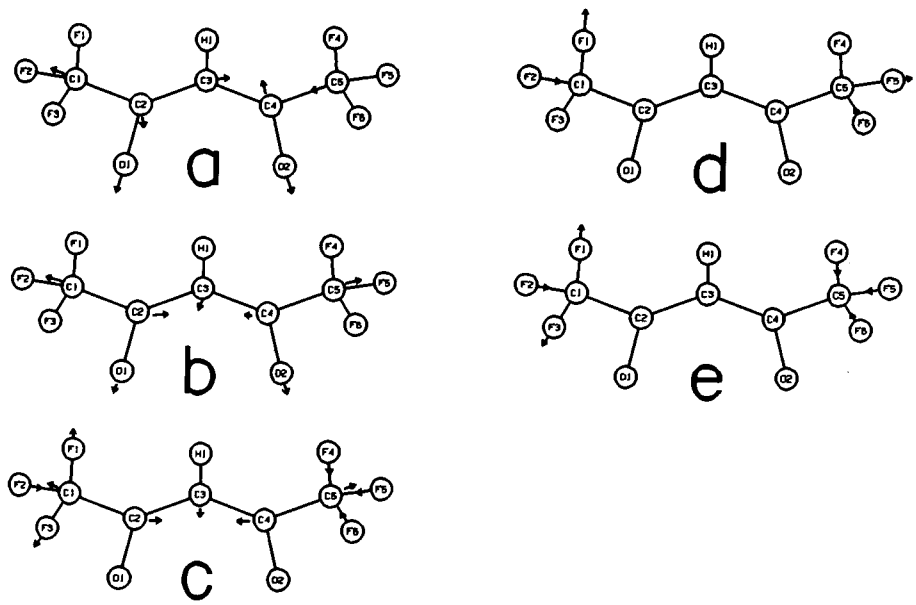

Fig. 3. Vibrational modes of hfa corresponding to infrared absorptions at (a) 1670 cm^{-1}, (b) 1535 cm^{-1}, (c) 1251 cm^{-1}, (d) 1186 cm^{-1}, and (e) 1126 cm^{-1} for the $Ba(hfa)_2$(diaza-18-crown-6) complex. Atom displacements depicted are not to scale.

were assigned (Fig. 3). Because the relative positions of hfa atoms in the other polyether complexes were found to be similar to those measured for $Ba(hfa)_2$(diaza-18-crown-6), the vibrational modes for hfa in $Ba(hfa)_2$(diaza-18-crown-6) are expected to be similar to those in the other complexes. The fact that infrared absorption bands with similar intensities were found at similar frequencies in infrared spectra of **1–4** supports this hypothesis. Little variation was observed in the infrared vibration frequencies corresponding to vibrations involving primarily C–O stretches, indicating that interactions between hfa oxygens and barium ions in **1–4** were similar. However, significant frequency differences were observed for vibrations involving primarily C–F bonds. For example, the vibration depicted in Fig. 3e occurs 30 cm^{-1} lower in $Ba(hfa)_2$(diaza-18-crown-6) than in $Ba(hfa)_2$. Apparently, fluorine atoms in $Ba(hfa)_2$(diaza-18-crown-6) are interacting with moieties that are not available in $Ba(hfa)_2$. The most likely form of this interaction is an intermolecular attraction between hfa fluorines and crown ether methylene hydrogens. X-ray measurements indicate that the separation between fluorines and methylene hydrogens on adjacent molecules is too large for hydrogen bond formation. However, long range electrostatic attraction may be possible.

5. Conclusions

NMR and x-ray crystallographic measurements indicate that the polyether oxygen atoms in **2** and **3** assume near planar orientations. Infrared spectra of **2** and **3** each contain bands corresponding to hfa and polyether C–O–C vibrations that are similar in frequency and intensity, indicating that the molecular environment of the ligands in these complexes is similar. Despite these similarities, **3** requires significantly more energy for sublimation than **2**, even though barium coordination is greater in **3** than in **2**. Infrared spectra of **3** and **4** contain significant differences, especially for vibrations involving hfa fluorines. NMR and x-ray crystallographic measurements indicate that, in contrast to **3**, polyether nitrogens and oxygens are not co-planar in **4**.

Unlike **1**, which is polymeric [48], **2–4** sublime as molecular species because the barium ions in these complexes are better shielded. The fact that the thermal properties of **3** are significantly different from **2** and **4** indicates that barium shielding is not the only factor that dictates sublimation temperatures. Infrared studies indicated that hfa fluorine atoms are affected by the presence of polyether ligands. These effects are presumably electrostatic interactions between hfa fluorines and crown ether methylenes from adjacent $Ba(hfa)_2$-polyether molecules. These H ··· F interactions may be important for maintaining the crystal lattice of these complexes and the strength of these interactions may determine the ease with which **2–4** can be sublimed. It is clear from the results presented here that solid state intermolecular interactions should be considered in addition to the degree of barium ion coordination when attempts are made to synthesize new barium complexes for use in MOCVD processing.

6. Acknowledgement

Support for this work from the Oklahoma Center for Advancement of Science and Technology is gratefully acknowledged.

7. References

[1] J.G. Bednorz and K.A. Muller, Z. Phys. B., 64 (1986) 189.
[2] C.W. Chu, P.H. Hor, R.L. Meng, L. Gao, Z.J. Huang and Y.Q. Wang, Phys. Rev. Lett., 58 (1987) 405.
[3] M.K. Wu, J.R. Ashburn, C.J. Torng, P.H. Hor, R.L. Meng, L. Gao, Z.J. Huang, Y.Q. Wang and C.W. Chu, Phys. Rev. Lett., 58 (1987) 908.
[4] R.P.H. Chang and J.M. Poate, MRS Bull., 11 (1991) 63.
[5] Y. Yasuda, Y. Koide, S. Zaima and N. Sano, Appl. Phys. Lett., 55 (1989) 307.
[6] S. Prakash, D.M. Umarjee, H.J. Doerr, C.V. Deshpandey and R.F. Bunshah, Appl. Phys. Lett., 55 (1989) 504.
[7] G.C. Xiong and S.Z. Wang, Appl. Phys. Lett., 55 (1989) 902.
[8] K. Yamamoto, B.M. Lairson, C.B. Eom, R.H. Hommond, J.C. Bravman and T.H. Geballe, Appl. Phys. Lett., 57 (1990) 1936.
[9] N. Newman, K. Char, S.M. Garrison, R.W. Barton, R.C. Taber, C.B. Eom, T.H. Geballe and B. Wilkens, Appl. Phys. Lett., 57 (1990) 520.
[10] Q.X. Jia and W.A. Anderson, Appl. Phys. Lett., 57 (1990) 304.
[11] J.D. Klein, A. Yen and S.L. Clauson, Appl. Phys. Lett., 56 (1990) 394.
[12] R.K. Singh, J. Narayan, A.K. Singh and C.B. Lee, J. Appl. Phys., 67 (1990) 3448.
[13] K.H. Wu, C.L. Lee, J.Y. Juang, T.M. Uen and Y.S. Gou, Appl. Phys. Lett., 58 (1991) 1089.
[14] P. Tiwari, S.M. Kanetkar, S. Sharan and J. Narayan, Appl. Phys. Lett., 57 (1990) 1578.
[15] R. Singh, S. Sinha, N.J. Hsu, P. Chou, R.K. Singh and J. Narayan, J. Appl. Phys., 67 (1990) 1562.
[16] H.G. Lee, S.D. Park, S.W. Yong, H.S. Shin and D.Y. Won, Jpn. J. Appl. Phys., 31 (1992) L157.
[17] S. Matsumo, F. Uchikawa and S. Utsunomiya, Appl. Phys. Lett., 60 (1992) 2427.
[18] Y.Q. Li, J. Zhao, C.S. Chern, P. Lu, T.R. Chien, B. Gallois, P. Norris, B. Kear and F. Cosandey, Appl. Phys. Lett., 60 (1992) 2430.
[19] H.M. Manasevit, Appl. Phys. Lett., 12 (1968) 156.
[20] J.B. Mullin, S.J.C. Irvine and J. Tunnicliffe, J. Cryst. Growth, 68 (1984) 214.
[21] B. Cockayne and P.J. Wright, J. Cryst. Growth, 68 (1984) 223.
[22] M.J. Ludowise, J. Appl. Phys., 58 (1985) R31.
[23] K. Watanabe, H. Yamane, H. Kurosawa, T. Hirai, N. Kobayashi, H. Iwasaki, K. Noto and Y. Muto, Appl. Phys. Lett., 54 (1989) 575.
[24] J. Zhao, K.H. Dahmen, H.O. Marcy, L.M. Tonge, B.W. Wessels, T.J. Marks and C.R. Kannewurf, Solid State Commun., 69 (1989) 187.
[25] J. Zhang, J. Zhao, H.O. Marcy, L.M. Tonge, B.W. Wessels, T.J. Marks and C.R. Kannewurf, Appl. Phys. Lett., 54 (1989) 1166.
[26] P.H. Dickinson, A. Sanjurjo, T.H. Geballe, D. Hildenbrandt, C. Craig, M. Zisk, J. Collman, S.A. Banning and R.E. Sievers, J. Appl. Phys., 66 (1989) 444.
[27] D.S. Richeson, L.M. Tonge, J. Zhao, J. Zhang, H.O. Marcy, T.J. Marks, B.W. Wessels and C.R. Kannewurf, Appl. Phys. Lett., 54 (1989) 2154.
[28] F. Schmaderer, R. Huber, H. Oetzmann and G. Wahl, Appl. Surf. Sci., 46 (1990) 53.
[29] A.P. Purdy, A.D. Berry, R.T. Holm, M. Fatemi and D.K. Gaskill, Inorg. Chem., 28 (1989) 2799.
[30] G. Malandrino, D.S. Richeson, T.J. Marks, D.C. Degroot, J.L. Shindler and C.R. Kannerwurf, Appl. Phys. Lett., 58 (1991) 182.
[31] T. Nakamori, H. Abe, T. Kanamori and S. Shibata, Jpn. J. Appl. Phys., 27 (1988) L1265.
[32] G.S. Hammond, D.C. Nonhebel and C.S. Wu, Inorg. Chem., 2 (1963) 73.
[33] J.E. Schwarberg, R.E. Sievers and R.W. Moshier, Anal. Chem., 42 (1970) 1828.
[34] R. Belcher, C.R. Cranley, J.R. Majer, W.I. Stephen and P.C. Uden, Anal. Chim. Acta, 60 (1972) 109.
[35] S. Matsuno, F. Uchikawa and K. Yoshizaki, Jpn. J. Appl. Phys., 23 (1990) L947.

[36] K.G. Caulton, M.H. Chisholm, S.R. Drake and J.C. Huffman, J. Chem. Soc., Chem. Commun., (1990) 1498.
[37] W.S. Rees and D.A. Moreno, J. Chem. Soc., Chem. Commun., (1991) 1759.
[38] W.S. Rees, M.W. Carris and W. Hesse, Inorg. Chem., 30 (1991) 4479.
[39] L.A. Wills, B.W. Wessels, D.S. Richeson and T.J. Marks, Appl. Phys. Lett., 60 (1992) 41.
[40] R. Gardiner, D.W. Brown, P.S. Kirlin and A.L. Rheingold, Chem. Mater., 3 (1991) 1053.
[41] J. Zhao, H.O. Marcy, L.M. Tonge, B.W. Wessels, T.J. Marks and C.R. Kannewurf, Physica C, 159 (1989) 710.
[42] K. Timmer and H.A. Meinema, Inorg. Chim. Acta, 187 (1991) 99.
[43] P. van der Sluis, A.L. Spek, K. Timmer and H.A. Meinema, Acta. Cryst., C46 (1990) 1741.
[44] K. Timmer, K. Spee, A. Mackor, H.A. Meinema, A.L. Spek and P. van der Sluis, Inorg. Chim. Acta, 190 (1991) 109.
[45] J.A.T. Norman and G.P. Pez, J. Chem. Soc., Chem. Commun. (1991) 971.
[46] H.D. Inerowicz, M.A. Khan, G. Atkinson and R.L. White, Acta Cryst., in press.
[47] M. Herceg and R. Weiss, Bull. Soc. Chim. Fr., (1972) 549.
[48] D.C. Bradley, M. Hasan, M.B. Hursthouse, M. Motevalli, O.F.Z. Khan, R.G. Pritchard and J.O. Williams, J. Chem. Soc., Chem. Commun., (1992) 575.

ELSEVIER

Analytica Chimica Acta 289 (1994) 259–260

ANALYTICA CHIMICA ACTA

Regular mixtures

Erik Högfeldt [1]

Department of Inorganic Chemistry, The Royal Institute of Technology, S-100 44 Stockholm, Sweden

(Received 4th January 1994)

Abstract

It is shown that Guggenheim's zeroth approximation is consistent with two kinds of solutions, one where the characteristic parameter b is independent of temperature and one dependent of temperature. The first case has tacitly been assumed to be the only one. The second one is new and is here illustrated by data on the liquid ion exchanger dinonylnaphthalene sulfonic acid.

Key words: Ion exchange; Regular mixtures

1. Introduction

The three-parameter model introduced by the present author has recently been illustrated in various kinds of ion-exchange equilibria [1–3]. The model offers a simple way to correct for non-ideality in the ion exchanger. The three-parameter model corresponds to a second degree polynomial in the plot of log κ versus x. Here κ is the equilibrium quotient of the ion-exchange reaction considered, and x a suitable composition variable in the ion exchanger. If the curve degenerates into a straight line, the system behaves as a regular mixture. Recently, Förland et al. [4] showed that activity coefficients for a regular mixture give rise to a straight line in the plot above, thus a confirmation of the results of the three-parameter model. For Guggenheim's zeroth approximation they showed that plots of the kind mentioned above should give parallel curves for different temperatures and give experimental curves illustrating this.

In the present paper it is shown that straight lines with different slopes are also consistent with Guggenheim's zeroth approximation.

2. The model

The model has been discussed elsewhere [1–3]. According to the model an ion-exchange reaction with equilibrium quotient κ is given by

$$\log \kappa = \log \kappa(1)x^2 + \log \kappa(0)(1-x)^2 + 2 \log \kappa_m x(1-x) \quad (1)$$

The model assumes that the kind of nearest neighbours influences the property studied. In a mixture of A and B it has one value when surrounded by A only, another when surrounded by

[1] Address for correspondence: Rättviksvägen 21, S-191 71 Sollentuna, Sweden.

SSDI 0003-2670(94)00042-K

B only and a third value when both components are present. This leads to Eq. 1 above.

Eq. 1 is a second degree polynomial and can for simplicity be written

$$\log \kappa = a + bx + cx^2 \quad (2)$$

From Eqs. 1 and 2 the empirical parameters a, b and c be expressed in terms of the parameters of the model. We consider for simplicity ion exchange between monovalent ions. The equilibrium constant K is related to the equilibrium quotient by

$$K = \kappa(f_2/f_1) \quad (3)$$

Here f_1 and f_2 are the activity coefficients of the two components on the mole fraction scale and K the thermodynamic equilibrium constant of the reaction

$$A_2 + A_1X = A_2X + A_1 \quad (4)$$

From the Gibbs-Duhem equation and Eq. 3 integration gives

$$\log f_1 = (1/2)bx^2 + (2/3)cx^3 \quad (5a)$$

$$\log f_2 = (1/2)\left[(b + 2c)(1-x)^2 - (2/3)c(1-x)^3\right] \quad (5b)$$

For $c = 0$ Eqs. 5a and b reduce to

$$\log f_1 = (1/2)bx^2 \quad (6a)$$

$$\log f_2 = (1/2)b(1-x)^2 \quad (6b)$$

i.e., those for a regular solution.

3. The interchange energy

According to Guggenheim [5] for the zeroth approximation the enthalpy of mixing can be written

$$\Delta H = (1/2)bx(1-x) \quad (7)$$

where b is given in Eqs. 6a and b as shown by Förland et al. [4]. According to Guggenheim, b is the interchange energy per mole. For ideal solutions $b = 0$, for the zeroth approximation $b \neq 0$.

If b is independent of temperature it is seen from Eq. 2 with $c = 0$ that plots of log κ vs. x give a set of parallel curves as illustrated in the paper by Förland et al. [4].

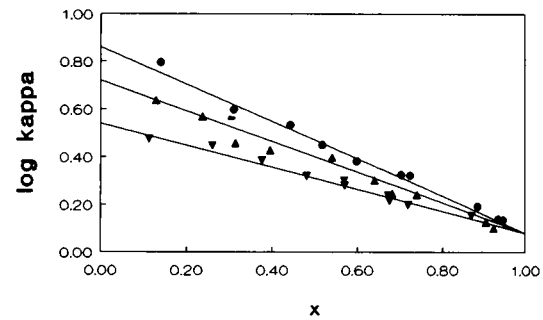

Fig. 1. log κ plotted vs. $x_{CH_3NH_3D}$ for reaction 8 at three temperatures: ●, 273 K; ▲, 298 K; ▼ 336 K.

The possibility with b dependent upon temperature is illustrated in Fig. 1 where log κ is plotted versus x ($= x_{CH_3NH_3D}$) for the reaction

$$CH_3NH_3^+(aq) + HD(org) = CH_3NH_3D(org) + H^+(aq) \quad (8)$$

where HD is dinonylnaphthalene sulfonic acid dissolved in heptane.

The reaction was studied at 273, 298 and 336 K. Three straight lines can be fitted to the data. The interchange energy could be fitted to $1/T$ by

$$b = 0.46 - 233/T \quad (9)$$

4. Concluding remark

In the systems studied here straight line plots with parallel curves are more rare than those with b dependent of temperature, as might be expected.

5. References

[1] E. Högfeldt, J. Phys. Chem., 92 (1988) 6475.
[2] E. Högfeldt, React. Polym., Ion Exch., Sorbents, 11 (1989) 6475.
[3] E. Högfeldt, in J.A. Marinsky and Y. Marcus (Eds.), Ion Exchange and Solvent Extraction, Vol. 11, 1993, pp. 109–150.
[4] K.S. Förland, T. Okada and S.K. Ratkje, J. Electrochem. Soc., 140 (1993) 634.
[5] E.A. Guggenheim, Mixtures, Clarendon, Oxford, 1952, Chap. 4.

Send your article on floppy disk!

All articles may now be submitted on computer disk, with the eventual aim of reducing production times and improving the reliability of proofs still further. Please follow the guidelines below.

With revision, your disk plus one final, printed and exactly matching version (as a printout) should be submitted together to the editor. **It is important that the file on disk to be processed and the printout are identical.** Both will then be forwarded by the editor to Elsevier.

The accepted article will be regarded as final and the files will be processed as such. Proofs are for checking typesetting/editing: only printer's errors may be corrected. No changes in, or additions to the edited manuscript will be accepted.

Illustrations should be provided in the usual manner and, if possible, on a **separate** floppy disk as well.

Please follow the general instructions on style/arrangement and, in particular, the reference style of this journal as given in the "Guide for Authors".

The preferred storage medium is a 5¼ or 3½ inch disk in MS-DOS or Macintosh format, although other systems are also welcome.

Please label the disk with your name, the software & hardware used and the name of the file to be processed.

For further information on the preparation of compuscripts please contact:

Elsevier Science B.V.
Analytica Chimica Acta
P.O. Box 330
1000 AH Amsterdam, The Netherlands
Phone: (+31-20) 5862 791 Fax: (+31-20) 5862459

ELSEVIER SCIENCE

Electrochemical and Electrocatalytic Reactions of Carbon Dioxide

edited by **B.P. Sullivan**, University of Wyoming, Laramie, WY, USA, **K. Krist**, Gas Research Institute, Chicago, IL, USA and **H.E. Guard**, Office of Naval Research, Department of the Navy, Arlington, VA, USA

The recycling of atmospheric molecules for use as fuels and chemicals is a goal which can only be achieved through a deeper understanding of catalytic processes, particularly electrocatalysis whereby redox transformations can be interfaced with solar or nuclear energy input. Carbon dioxide is a prototypical small molecule in many regards since it is chemically inert. In addition, because of the likely role of carbon dioxide in global temperature cycles, it will be imperative in the future to regulate the output from industrial processes. The purpose of this book is to present a unified discussion of the carbon dioxide chemistry which is necessary for the understanding and design of electrochemically-driven processes for the reduction of carbon dioxide and to provide an impetus for the further development of electrocatalytic carbon dioxide chemistry.

Contents:

1993 xiv + 300 pages
Price: US $ 212.50 / Dfl. 340.00
ISBN 0-444-88316-9

ELSEVIER
SCIENCE

ORDER INFORMATION

For USA and Canada
ELSEVIER SCIENCE

Judy Weislogel
P.O. Box 945
Madison Square Station,
New York, NY 10160-0757
Tel: (212) 989 5800
Fax: (212) 633 3880

In all other countries
ELSEVIER SCIENCE

P.O. Box 211
1000 AE Amsterdam
The Netherlands
Tel: (+31-20) 5803 753
Fax: (+31-20) 5803 705

US$ prices are valid only for the USA & Canada and are subject to exchange rate fluctuations; in all other countries the Dutch guilder price (Dfl.) is definitive. Books are sent postfree if prepaid.

711/414\140\0001-00

PUBLICATION SCHEDULE FOR 1994

	S'93	O'93	N'93	D'93	J	F	M	A	M	J	J	A
Analytica Chimica Acta	281/1 281/2 281/3	282/1 282/2 282/3	283/1 283/2	283/3 284/1 284/2	284/3 285/1–2 285/3	286/1 286/2 286/3	287/1–2 287/3 288/1–2	288/3 289/1 289/2	289/3 290/1–2 290/3	291/1–2 291/3 292/1	292/2 292/3 293/1–2	293/3 294/1–2 294/3
Vibrational Spectroscopy		6/1			6/2		6/3		7/1		7/2	

INFORMATION FOR AUTHORS

Detailed "Instructions to Authors" for *Analytica Chimica Acta* was published in Volume 256, No. 2, pp. 373–376. Free reprints of the "Instructions to Authors" of *Analytica Chimica Acta* and *Vibrational Spectroscopy* are available from the Editors or from: Elsevier Science B.V., P.O. Box 330, 1000 AH Amsterdam, The Netherlands. Telefax: (+31-20) 5862459.

Manuscripts. The language of the journal is English. English linguistic improvement is provided as part of the normal editorial processing. Authors should submit three copies of the manuscript in clear double-spaced typing on one side of the paper only. *Vibrational Spectroscopy* also accepts papers in English only.

Rapid publication letters. *Letters* are short papers that describe innovative research. Criteria for letters are novelty, quality, significance, urgency and brevity. Submission data: max. of 2 printed pages (incl. Figs., Tables, Abstr., Refs.); short abstract (e.g., 3 lines); *no* proofs will be sent to the authors; submission on floppy disc; *no* revision will be possible.

Abstract. All papers and reviews begin with an Abstract (50–250 words) which should comprise a factual account of the contents of the paper, with emphasis on new information.

Figures. Figures should be prepared in black waterproof drawing ink on drawing or tracing paper of the same size as that on which the manuscript is typed. One original (or sharp glossy print) and two photostat (or other) copies are required. Attention should be given to line thickness, lettering (which should be kept to a minimum) and spacing on axes of graphs, to ensure suitability for reduction in size on printing. Axes of a graph should be clearly labelled, along the axes, outside the graph itself. All figures should be numbered with Arabic numerals, and require descriptive legends which should be typed on a separate sheet of paper. Simple straight-line graphs are not acceptable, because they can readily be described in the text by means of an equation or a sentence. Claims of linearity should be supported by regression data that include slope, intercept, standard deviations of the slope and intercept, standard error and the number of data points; correlation coefficients are optional.

Photographs should be glossy prints and be as rich in contrast as possible; colour photographs cannot be accepted. Line diagrams are generally preferred to photographs of equipment. Computer outputs for reproduction as figures must be good quality on blank paper, and should preferably be submitted as glossy prints.

Nomenclature, abbreviations and symbols. In general, the recommendations of IUPAC should be followed, and attention should be given to the recommendations of the Analytical Chemistry Division in the journal *Pure and Applied Chemistry* (see also *IUPAC Compendium of Analytical Nomenclature, Definitive Rules*, 1987).

References. The references should be collected at the end of the paper, numbered in the order of their appearance in the text (*not* alphabetically) and typed on a separate sheet.

Reprints. Fifty reprints will be supplied free of charge. Additional reprints (minimum 100) can be ordered. An order form containing price quotations will be sent to the authors together with the proofs of their article.

Papers dealing with vibrational spectroscopy should be sent to: Dr J.G. Grasselli, 150 Greentree Road, Chagrin Falls, OH 44022, U.S.A. Telefax: (+1-216) 2473360 (Americas, Canada, Australia and New Zealand) or Dr J.H. van der Maas, Department of Analytical Molecular Spectrometry, Faculty of Chemistry, University of Utrecht, P.O. Box 80083, 3508 TB Utrecht, The Netherlands. Telefax: (+31-30) 518219 (all other countries).

0003-2670/94/$07.00

This issue is printed on acid-free paper.

PRINTED IN THE NETHERLANDS

TrAC - Trends in Analytical Chemistry: Reference Edition Volume 12: 1993

TrAC Compendium Series Volume 12

The Reference Edition of *Trends in Analytical Chemistry (TrAC)* is a compilation of the archival material reprinted from the regular issues of the journal. *TrAC* provides a topical digest of current developments and new ideas in the analytical sciences. It does so in the form of broadly-based, easy-to-read scientific reviews, backed up by news and other features of interest to the international analytical chemistry community. For subscribers to the library edition of *TrAC*, the reference edition forms an integral part of the annual subscription, but for others it can be purchased individually. It provides informative and stimulating reading for all those who use analytical methods.

This latest volume contains all the archival material published in 1993. It covers a wide range of analytical techniques and applications of interest to academic and research workers in chemistry, biochemistry, clinical chemistry, pharmaceutical chemistry and toxicology.

Contents: *A selection of the Contents.* Single-cell analysis at the level of a single human erythrocyte (B.L. Hogan, E.S. Yeung). Charge-remote fragmentations for structural determination of lipids (J. Adams, M.J. Songer). Recent advances in speciation analysis by capillary gas chromatography-microwave induced plasma atomic emission spectrometry (R. Lobinski, F.C. Adams). Pyrolysis-mass spectrometry under soft ionization conditions (A.C. Tas, J. van der Greef). New developments in glow discharge mass spectrometry (Y. Mei, R.K. Marcus). Enantiomeric separation by micellar electrokinetic chromatography (K. Otsuka, S. Terabe). Liquid chromatographic methods for the chiral separation of β-adrenergic blocking agents (C. Vandenbosch *et al.*). Capillary gel electrophoresis of biopolymers (A.S. Cohen, D.L. Smisek, P. Keohavong). Vibrational spectroscopy - where are we and where are we going? (J.L. Koenig). Capillary electrophoresis of inorganic ions and low-molecular-mass ionic solutes (P.E. Jackson, P.R. Haddad). Mass spectrometric analysis of a GPI-anchored protein: the scrapie prion protein (M.A. Baldwin, A.L. Burlingame, S.B. Prusiner). *In vivo* blood-gas and electrolyte sensors: progress and challenges (M.E. Meyerhoff). Trace analysis in capillary supercritical fluid chromatography: sample introduction (T. Greibrokk, B.E. Berg). Analytical applications of electrified interfaces between two immiscible solutions (P. Vanysek). The use of gas chromatographic detectors in column liquid chromatography (Ch.E. Kientz, U.A.Th. Brinkman). Imaging applications for chemical analysis utilizing charge coupled device array detectors (C.W. Earle *et al.*). Mass spectrometry of proteins (P. Roepstorff).

© 1993 592 pages Hardbound
Price: Dfl. 675.00 (US$ 385.75)
ISBN 0-444-81805-7

*An extra supplement is included in this edition - **Directory of Capillary Electrophoresis**:*

- **Over 450 V.I.P.s Worldwide**
- **Complete Addresses, Fax and Phone Numbers, and E-Mail Addresses (where available)**
- **Many Techniques, Applications and Research Topics**
- **Extensive Subject Index.**

This directory forms an integral part of the 1993 subscription to the Library Edition and is also available as a separate publication.

ORDER INFORMATION
ELSEVIER SCIENCE B.V.
P.O. Box 330
1000 AH Amsterdam
The Netherlands
Fax: (+31-20) 5862 845

For USA and Canada
P.O. Box 945
Madison Square Station
New York, NY 10159-0945
Fax: (212) 633 3680

US$ prices are valid only for the USA & Canada and are subject to exchange rate fluctuations; in all other countries the Dutch guilder price (Dfl.) is definitive. Customers in the European Union should add the appropriate VAT rate applicable in their country to the price(s). Books are sent post-free if prepaid.

ELSEVIER SCIENCE

0003-2670(19940429)289:2;1-Y